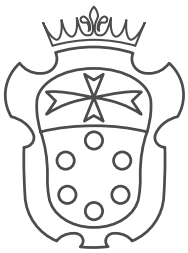

SCUOLA
NORMALE
SUPERIORE

Classe di Scienze

Corso di perfezionamento in
Metodi computazionali e modelli matematici
per le scienze e la finanza

XXXVI ciclo

Noise perturbations of Point Vortex model

Settore Scientifico Disciplinare **MAT/06**

Candidata
dr.ssa Silvia Morlacchi

Supervisione

Prof. Franco Flandoli

Co-supervisione

Prof.ssa Alessandra Caraceni

Anno accademico 2025–2026

Contents

List of Figures

List of Tables

Extended Abstract

The investigation of stochastic perturbations in fluid dynamics has been a standard procedure in the physical and mathematical literature. In particular, we recall the use of transport-type noise (advection by a stochastic velocity field) in the development of the theory of turbulence, due to the work of Kraichnan on stochastic transport of passive scalars.

A very classical particle system in the fluid dynamics context is the Point Vortex model. This system is a discretization of the Euler equation in the vorticity formulation, and it has been introduced and studied by Helmholtz; however, it is due to the investigation on two-dimensional turbulence carried on by Onsager that this model reached popularity and recognition in the context of fluid discretizations. The Point Vortex model is also an object of studies in the context of dynamical systems, due to the Hamiltonian aspects of vortex dynamics. In this thesis, we too focus on the study of two-dimensional models; this is not a limitation in our investigation, as many phenomena in nature can be modeled by almost-two-dimensional systems, examples are atmospheric or geostrophic turbulence; this modelization is possible if the vertical scale of the system is negligible with respect to the horizontal scale or vice-versa.

By investigating both the Point Vortex model in its standard formulation and its stochastic modifications, we explore two long standing problems in fluid dynamics: turbulence modeling by stochastic perturbations of transport type and the long time behavior of an inviscid fluid. In the first case, we investigate both the Point Vortex model with stochastic modification of transport type, and the motion of a passive scalar transported by a stochastic velocity field. This stochastic velocity field is very similar to the one studied in the Point Vortex model context, and it is a sum of independent and compactly supported vector fields. This simplified setting allows us to study more in detail the noise. In the second case, we investigate the long time behavior of a two-dimensional fluid: we study the equilibrium dynamics's temporal structure by computing correlation of local observables, function of the vorticity, of a large number N of point vortices under the invariant measure $dx_1 \dots dx_N$ and we exibit evidence of persistence in time correlations, in the form of power law decay of the latter.

Introduction

In this thesis, we explore stochastic modifications of a very classical fluid dynamics model, the Point Vortex model. The Point Vortex model has been studied by Helmholtz [77] and it gained a prominent role among other fluid discretizations due to Onsager's work on two-dimensional turbulence [109], however, it is also well-known on its own as a Hamiltonian system. This thesis is based on the works [59, 58, 13, 68], as described in more detail below.

In all the chapters of this thesis, we will focus exclusively on two-dimensional models. A system can be described by a two-dimensional fluid model if the vertical scale is negligible with respect to the horizontal scale. In nature, there is an abundance of almost-two-dimensional systems, for example, atmospheric or geostrophic turbulence.

The first three chapters recall some known facts, respectively, on the Point Vortex model and its Hamiltonian dynamics, on the numerical methods employed in this thesis, and on the stochastic modifications of the Point Vortex model, the additive noise one and the environmental noise one. In chapter 3 we also compute elements of the environmental noise correlation matrix, to better understand the behavior of the Point Vortex stochastic modification.

We describe stochastic modification of the Point Vortex model as modelization of the fluid turbulent behavior and dissipative effects in the chapter 5 and in the two works [59, 58]: the numerical investigation of stochastic modifications of the Point Vortex model is conducted by studying their effects on a fluid instability, the Kelvin-Helmholtz instability. This system was chosen in order to investigate the dissipation properties of those stochastic modifications of the model.

In chapter 4 and in the related work [13] we give more details on one of the stochastic modifications of the Point Vortex model, more precisely a noise of transport type (advection by stochastic velocity field). We investigate the effects of this noise, under suitable hypothesis, by studying a stochastic viscous transport equation for a passive scalar with noise of transport type, in a simplified context, by exploiting the tools of homogenization theory.

Finally, in chapter 6 and in the related paper [68] we turn back to the standard Point Vortex model, and study the long time behavior of a two-dimensional fluid, investigating the equilibrium dynamics's temporal structure by computing correlation of local observables, function of the vorticity, of a large number N of point vortices under the invariant measure $dx_1 \cdots dx_N$ and exhibiting evidence of persistence in time correlations, in the form of power law decay of the latter.

Thesis outline

In the following, we describe the content of the chapters, explaining the choices made and the motivations that drove us to include the different topics and studies. In this thesis, both an analytical and numerical investigation are present; to mirror this feature, we included two introductory chapters, one on the Point Vortex model itself, and the other on the computational methods used in the numerical investigation.

Chapter 1: the Point Vortex model

In the first chapter, we recall some well-known facts about the Point Vortex model. Starting from the equations of motion of N vortices on an unbounded plane, of strengths (circulations) γ_i, spatial coordinates $(x_1^{(i)}, x_2^{(i)})$, with $i = 1 \dots N$,

$$\frac{dx_1^{(i)}}{dt} = -\frac{1}{2\pi}\sum_{\substack{j=1\\ j\neq i}}^{N} \gamma_j \frac{x_2^{(i)} - x_2^{(j)}}{d_{ij}^2}, \qquad \frac{dx_2^{(i)}}{dt} = \frac{1}{2\pi}\sum_{\substack{j=1\\ j\neq i}}^{N} \gamma_j \frac{x_1^{(i)} - x_1^{(j)}}{d_{ij}^2} \ ,$$

and d_{ij} the distance computed on the domain, we describe the Hamiltonian formulation of the dynamics,

$$\gamma_i \frac{dx_1^{(i)}}{dt} = \frac{\partial H}{\partial x_2^{(i)}}, \qquad \gamma_i \frac{dx_2^{(i)}}{dt} = -\frac{\partial H}{\partial x_1^{(i)}};$$

by introducing the Green function G. We then discuss its properties, at first in the simple case of the unbounded plane, then moving to generic bounded domains. In particular, we focus on the behavior of the function near the singularities, i.e. the vortices positions. After this discussion, we move to other aspects of the Point Vortex model, and we describe the link with the Euler equations and the fluid motion. To this end, we introduce the following quantities: the fluid velocity, u, the stream function ψ, and the fluid vorticity, ω, explaining the relations between all those quantities. After recalling some definition to express the fluid velocity in terms of the Green function, we finally write the Euler equation in the so called vorticity formulation,

$$\begin{aligned} \frac{\partial \omega}{\partial t}(\mathbf{x},t) + (\mathbf{u}\cdot\nabla)\omega(\mathbf{x},t) &= 0 \\ \mathbf{u}(\mathbf{x},t) &= \int_{\mathcal{D}} \nabla^{\perp} G(\mathbf{x},\mathbf{y})\omega(\mathbf{y},t)d\mathbf{y} \\ \nabla\cdot\mathbf{u} &= 0 \\ \omega(\mathbf{x},0) &= \omega_0(\mathbf{x}), \quad \mathbf{x}\in\mathcal{D}, \quad t\geq 0, \end{aligned}$$

with $\mathbf{u}\cdot\hat{\nu} = 0$ on bounded domains or the condition on unbounded domain that prescribe null velocity for $|\mathbf{x}| \to \infty$ verified (assuming that ω allows that). We end the first section of the chapter by expressing the vorticity of the fluid as a Point Vortex distribution, obtaining the Hamiltonian system which was introduced at the beginning of the chapter.

The second part of the chapter is devoted to an extended derivation of the Euler equation from the Point Vortex model, well-known in the literature. The derivation we choose to present is the one due to [62, 61, 74]; this derivation was selected due to the fact that the Point Vortex model is derived without the infinite contribution due to the self interaction of the vortices. This derivation uses the complex formulation of the Point Vortex model, together with the Green function decomposition

near the singularities. The original computation was reported in full and expanded with comments; it is worth to note that the absence of the auto-interaction term from the Point Vortex Hamiltonian implies that all the quantities to compute are finite.

In the third section of the chapter, we start by discussing the conserved quantities of the model; the starting point is once again the Hamiltonian on an unbounded plane: we list the transformations which leave the Hamiltonian invariant and, from Noether's theorem, we deduce the corresponding conserved quantities, the so-called integrals of motion of the system. We then give some general consideration on the integrability of the system.

We finally discuss the invariant measures and equilibrium states of the Euler equation and, in turn, of the Point Vortex model, and we report the explicit expression of the energy spectrum computed on the torus domain, which is the domain considered for most of the thesis discussions. In particular, following the computation of [108] on the unbounded plane, we compute the energy spectrum in terms of the vorticity also on the torus.

Chapter 2: numerical tools

As anticipated before, this thesis heavily relies on numerical studies which complement the analytical ones. An example of code written for the development of this thesis, in relation to the paper [59], is given in [106]; another example is given in [12] in relation to the work [13]. For this reason, in this second chapter we briefly sum up the different numerical method employed. The majority of them are standard numerical discretization methods or statistical methods for data analysis; however, the coexistence of numerical and analytical analysis calls for a rapid summary of those methods. The first section is devoted to algorithms for integration of equations; we first briefly recall the ODE version of the improved Euler method. We then focus on more advanced integration methods, the family of Runge-Kutta methods for ODE; we also describe the improved Euler method for SDE; we do not describe higher order methods for SDE, but we include a discussion on how those methods could improve the results. We finally discuss other possibilities which were not included in this thesis: the use of an adaptative timestep and symplectic algorithms which guaranty the conservation of one or more quantities.

In the second section of the chapter, we focus on algorithms used for the integration of PDE in space. This family of algorithms will be of use in the fourth chapter, where, in the process of studying the stochastic modification of the Point Vortex model, we study first a SPDE and then we numerically solve a PDE obtained via the so called *homogenization* procedure. A more detailed explanation will follow in the subsection devoted to chapter four. To solve the linear system associated to the discretized PDE, we employ two different kind of solvers, direct and iterative, depending on the dimension of the matrix: if the matrix is very large ($\sim 10^6 \times 10^6$), and ill-conditioned, iterative solvers like GMRES could become favored over direct solvers like Gaussian elimination. In this section, both solvers are discussed and summarized, together with other useful methods like preconditioning of the matrix, restarting and fillfactor employment.

The third section is devoted to the statistical analysis of data. In this thesis, we will compute observables by averaging, for example, on random initial conditions of the vortices positions, sampled from a probability distribution, or on different noise realizations, if noise is added in the equations of motion. This implies that the expectation value of the observable under consideration can be computed via Montecarlo methods, by sampling different configurations:

$$\langle O \rangle = \frac{1}{N} \sum_{i=1}^{N} O(\{X_i\}) + \mathcal{O}\left(\frac{1}{\sqrt{N}}\right)$$

To correctly estimate the errors of the measurements, one has to take into account correlations between different measures, or ensure that the different measures are statistically independent, and this issue is explained in the rest of the section. In the last paragraphs, we finally describe how to estimate the errors of the measurements. Standard error propagation rules are not always applicable in the case of observables not directly computed from the simulation's configurations (i.e. the so-called secondary quantities): in this case, the different quantities to be combined are correlated, moreover their estimator is biased. For this reason, we introduce two well-know techniques, the bootstrap and the jackknife, which will be used in the rest of the thesis to estimate uncertainties on the observables measurement.

In the final section of the chapter, we focus on a specific domain: the torus, as this domain is the one which will be considered in the rest of the thesis. After commenting on some general properties of this domain, we focus on a specific task: how to approximate the infinite sum which is present in the torus's Green function. In this thesis, we considered two different approximations of this infinite sum to compute the Biot-Savart kernel $\mathbf{K}(\mathbf{x})$, one previously introduced in [124], and the other being an adaptation on the torus of the corresponding expression on the plane, valid for $x \to 0$. We report the first one, $\mathbf{K}(\mathbf{x}) = (-S(x_2, x_1), S(x_1, x_2))$ with

$$S(x_1, x_2) \sum_{m=-\infty}^{\infty} \frac{\sin(x_1)}{\cosh(x_2 - 2\pi m) - \cos(x_1)} \ ,$$

or

$$S(x_1, x_2) \sum_{n=-\infty}^{\infty} \frac{\sinh(x_1 - 2\pi n)}{\cosh(x_1 - 2\pi m) - \cos(x_2)} \ ,$$

expanding the derivation with comments, and we describe and introduce the second one,

$$\mathbf{K}(\mathbf{x}) = \frac{1}{4\pi} \frac{\mathbf{x}^{\perp}}{d(\mathbf{x})^2} \ ,$$

where $d(\mathbf{x}^2)$ denotes the periodic distance on the torus; finally, we numerically study the convergence of the approximations.

Chapter 3: internal and environmental noise

In this chapter, we bounce back to the Point Vortex model, adding first additive and then multiplicative noise to the equations of motion. This operation requires some care, as we are introducing perturbations in the Point Vortex model's Hamiltonian, leading to the loss of conserved quantities: the Hamiltonian of the Point Vortex model (in principle) is not conserved under perturbations of this kind. The first section is devoted to the additive (i.e. internal) noise; it is well-known that the addition of this kind of noise to the equations of motion leads to the loss of kinetic energy's conservation. Moreover, the equation of motion of the single point vortex is, with this modification, a diffusion process for the dynamics,

$$d\mathbf{x}^{(i)}(t) = \sum_{\substack{j=1 \\ j \neq i}}^{N} \gamma_j \mathbf{K}\left(\mathbf{x}^{(i)}(t), \mathbf{x}^{(j)}(t)\right) dt + \beta d\mathbf{W}^{(i)}(t)$$

where $\beta > 0$, $i, j = 1, \cdots, N$, and $\mathbf{W}^{(i)}(t)$ are mutually independent two-dimensional Brownian motions. We then summarize some known results on the introduction of the additive noise, in particular regarding effects analogous to fluid viscosity.

In the next section, we introduce the so-called *environmental noise*, and its relation to turbulence in fluids. We start our discussion by specifying the model we investigate; this model is build from the idea that small-scale turbulence could have a dissipative effect on the mean flow, and it is related to Bousinnesq's studies. The natural implication of this intuition is that small-scales and large-scale are mutually influenced. From the Navier-Stokes equation in vorticity formulation,

$$\partial_t \mathbf{u} + \mathbf{u} \cdot \nabla \mathbf{u} = \nu \Delta \mathbf{u}$$
$$\nabla \cdot \mathbf{u} = 0;$$

we summarize the filtering procedure used to derive a closed equation for the small-scale vorticity, obtained by performing the filtering procedure on the initial condition. This intuition comes from the idea of [99], where the initial condition is decomposed in vortex structures. After a summary of known-results, we introduce a stochastic parametrization of the small-scale vorticity, by taking into account that we are making a strong assumption: the artificial vorticity structures which model the small-scale vorticity will not move in the time interval under consideration. In this parametrization, the small-scale velocity $\mathbf{u}'$ is modeled as a stochastic process, a sum of noises of transport type (advection by stochastic vector fields). We understand $\omega'(t=0)$ as a collection of small vorticity structures located in positions $\mathbf{y}^{(k)}$ at $t=0$, with intensities $\Gamma(M)$, such that

$$\mathbf{u}'(t,\mathbf{x}) \cdot \nabla \omega_\ell = \sum_{k=1}^{M} \Gamma(M) \mathbf{K}(\mathbf{x}(t) - \mathbf{y}^{(k)}) \cdot \nabla \omega_\ell \circ dW^k(t),$$

where $W^k(t)$ are $k = 1 \dots M$ one-dimensional Brownian motions. We point out that the Stratonovich differentiation is used in the dynamics.

In the third section of this chapter, we introduce in the Point Vortex model dynamics the environmental noise we just constructed. In the model we study, the advection field is made by a sum of M vorticity blobs of random intensity,

$$d\mathbf{x}^{(i)}(t) = \sum_{\substack{j=1 \\ j \neq i}}^{N} \gamma_j \mathbf{K}\left(\mathbf{x}^{(i)}(t), \mathbf{x}^{(j)}(t)\right) dt + \Gamma(M) \sum_{k=1}^{M} \mathbf{K}\left(\mathbf{x}^{(i)}(t), \mathbf{y}^{(k)}\right) \circ dW^k(t)$$

where $W^k(t)$ are $k = 1 \dots M$ one-dimensional Brownian motions, $\mathbf{x}^{(i)}(t)$ is the position of the i-th point vortex, $\mathbf{y}^{(k)}$ is the position of the k-th vorticity blob, and the coefficient $\Gamma(M)$ correspond to the vorticity blobs intensity. This coefficient has to be determined and it is the equivalent of the strengths γ_i of the point vortices; for the sake of simplicity, we take it to be the same for all M vorticity blobs. The equation of motion is written with the Stratonovich formulation; this choice is briefly commented. We then turn to the characterization of the model parameters; their choice is important, especially because based on the choice of the stochastic advection field, it is possible to distinguish between two different regimes of interest. In the first, the advection field is characterized by large spatial scales and intensities comparable to vortex interactions, while in the second regime the advection field has spatial scales so small and intensities so weak that it becomes a second order operator in the so-called Itô-Stratonovich diffusion limit. To investigate those two regimes, we introduce the empirical measure of a system of point vortices,

$$\mu(t) = \frac{1}{N} \sum_{i}^{N} \delta(\mathbf{x} - \mathbf{x}^{(i)}(t))$$

to study the corresponding mean field equations. We formally derive the two equations, by writing the advection field as a second order operator, plus a correction term. We obtain the two equations,

$$\partial_t \omega + \mathbf{u} \cdot \nabla \omega - \operatorname{div}(Q(\mathbf{x}) \nabla \omega) = 0$$

with $Q(\mathbf{x})$ the covariance of the noise, and

$$\partial_t \omega + \mathbf{u} \cdot \nabla \omega - \Gamma(M) \sum_{k=1}^{M} \mathbf{K}\left(x - \mathbf{y}^{(k)}\right) \nabla \omega \circ dW_t^k = 0 \ .$$

Then, we turn to describing some known results in the literature, about the convergence of the Point Vortex model with environmental noise to a stochastic partial differential equation. We start by introducing a more general environmental noise,

$$d\mathbf{x}^{(i,N)}(t) = \sum_{\substack{j=1 \\ j \neq i}}^{N} \gamma_j \mathbf{K}\left(\mathbf{x}^{(i,N)}(t), \mathbf{x}^{(j)}(t)\right) dt + \sum_{k=1} \boldsymbol{\sigma}_k \left(\mathbf{x}^{(i)}(t)\right) \circ dW^k(t)$$

studied on the two-dimensional torus, $\mathbb{T}^2$. $\mathbf{K}^\varepsilon$ is the regularized kernel, and $\varepsilon = \varepsilon(N)$. $\boldsymbol{\sigma}_k$ is a vector field, $\boldsymbol{\sigma}_k : \mathbb{T}^2 \to \mathbb{R}^2$, $k \in \mathbb{N}$. We recall the appropriate definition of the space covariance, make some assumptions needed to prove the convergence, and report the theorem which proves that the empirical measure of the Point Vortex system solves the associated stochastic partial differential equation for the vorticity in a distributional sense, following [29].

In the fifth section, we briefly explain the procedure of the so called Itô-Stratonovich diffusion limit, which is studied in the work [13] and in chapter 4: following [51], the stochastic two-dimensional Euler equation with environmental noise, written in a similar fashion as in the previous section, but with finite sum on k, converges weakly to the deterministic two-dimensional Navier–Stokes equation, under suitable noises scaling.

In the next section, we study the covariance matrix of the environmental blobs noise in a specific configuration of the vortex blobs which constitute the advection field, the one in which all the vortex blobs are arranged on a lattice. After defining the lattice, we compute the elements of the covariance matrix, in which the Biot-Savart kernel approximation of [124] (the introduced in chapter 1) is used.

Finally, in the last section we turn to the case in which we place the vortex blobs in positions which are independent, uniform and random, as in chapter 5. The covariance matrix is computed by averaging on different samples of the blobs configuration, so that we recover isotropy.

Chapter 4: anisotropic noise effect on passive scalar

This chapter is slightly different from the rest of the thesis, as it is not focused on the Point Vortex model. However, it represents a digression to investigate the effects of the advection by the stochastic velocity field we introduced in chapter 3. To do that, we study the stochastic advection of a passive scalar, considering its SPDE. The results of this chapter are collected in the work [13].

In the first section, we describe the notation and the setting of the model, together with the stochastic viscous transport equation for a passive scalar u_t^N on $\mathbb{R}_+ \times \mathbb{T}^2$, which is the subject of the investigation:

$$du_t^N = \sqrt{2} \sum_{k \in \mathbb{Z}^2} \sigma_k^N \cdot \nabla u_t^N \circ dW_t^k + \kappa \Delta u_t^N dt \ .$$

σ_k^N are divergence-free vector fields, with $k \in \mathbb{Z}^2$, $\{W_t^k\}$ is a sequence of i.i.d standard brownian motions, κ is the molecular diffusivity. We describe the stochastic advecting field, which is made of locally supported vortex patches arranged on a lattice indexed by a parameter, $N \in \mathbb{N}$, which

regulates the resolution of the noise; another parameter, c, regulates the overlap between the patches. We define the matrix field A^N as:

$$A^N(x,y) \coloneqq \sum_{k\in\mathbb{Z}^2} \sigma_k^N(x)\otimes\sigma_k^N(y)\ ; \tag{0.1}$$

this matrix field corresponds to the correlation matrix of the noise under appropriate hypothesis. We define $A(x) \coloneqq A^1(x,x)$.

We are interested in investigating the limit $N\to\infty$ in the small molecular diffusivity regime ($\kappa \ll 1$), the so-called Itô-Stratonovich diffusion limit introduced in the previous chapter; then, tools from homogenization theory are employed to study the effective diffusivity of the system, together with numerical simulations.

In the next section, we turn to the study of the scaling limit $N\to\infty$: the distance between the centers of the patches goes to zero, their intensities are sent to zero, and the stochastic system is described by a deterministic parabolic system. We focus on the behavior of two quantities:

$$\varepsilon_N := \sup\left\{\int\int_{\mathbb{T}^4} (\nabla v(x))^t A^N(x,y)\nabla v(y)\mathrm{d}x\mathrm{d}y :\ v\in\mathcal{H}^1(\mathbb{T}^2),\ \|\nabla v\|_{L^2}=1\right\}\ ,$$

related to the stochastic fluctuations of the solution of the equation, and

$$\pi_N^\kappa \coloneqq \inf\left\{\frac{\int_{\mathbb{T}^2}(\nabla v)^\top(x)(\kappa I + A^N(x,x))\nabla v(x)\mathrm{d}x}{\int_{\mathbb{T}^2}|v(x)|^2\mathrm{d}x} :\ v\in\dot{\mathcal{H}}^1, v\neq 0\right\}\ ,$$

which is the first eigenvalue of an elliptic operator,

$$\mathcal{L}_\kappa^N f = \mathrm{div}\left((\kappa I + A^N(x)\nabla)f\right)\ ,$$

and it is related to the dissipation of the deterministic part of the Itô equation.

In the Itô formulation, the equation we investigate becomes:

$$du_t^N = \sqrt{2}\sum_{k\in\mathbb{Z}^2}\sigma_k^N\cdot\nabla u_t^N dW_t^k + \left(\nabla\cdot(A^N\nabla u_t^N) + \kappa\Delta u_t^N\right)dt\ .$$

We enunciate a martingale estimate: in the case of N large, the noise introduced is so small that the solution is close to the solution of a deterministic equation,

$$\partial_t\tilde{u}_t^N = \nabla\cdot\left(\left(\kappa I + A^N(x)\right)\nabla\tilde{u}_t^N\right)\ ,$$

in which the parameter N is finite,

Proposition 0.1. *Let $u_0^N\in L^2(\Omega,\mathcal{F}_0,H)$, $T>0$ and u^N, $\tilde{u}^N$ be weak solutions to the Itô formulation of our equation and the deterministic equation, with u_0 as initial data. With proper assumptions, there exists a constant $C\coloneqq C(c)>0$ such that for every $\phi\in C_0^\infty(\mathbb{T}^2)$*

$$\sup_{t\in[0,T]}\mathbb{E}\left[\langle u_t^N-\tilde{u}_t^N,\phi\rangle^2\right]\le\frac{Cr^2}{\kappa}\|\phi\|_{L^\infty}^2\mathbb{E}\left[\|u_0^N\|_{L^2}^2\right]$$

In the third section, we first recall some elements and definitions from homogenization theory; then, we study the homogenization of the solutions $\tilde{u}_t^N$ of the deterministic equation obtained in the previous section: any solution converges for $N\to\infty$ to the solution of the homogenized PDE

$$\partial_t\tilde{u} = C(c,\kappa)\Delta\tilde{u}$$

with $C(c,\kappa) \geq \kappa$ constant. For $\tilde{u}_t^N$, the deterministic equation is

$$\partial_t \tilde{u}^N(t,x) = \nabla \cdot \Big(H_\kappa(Nx) \nabla \tilde{u}^N(t,x) \Big) \ ,$$

where

$$H_\kappa(x) := \kappa I + A(x).$$

We study the homogenization of the Stratonovich corrector, and put together results from the Itô-Stratonovich diffusion limit and the homogenized limit:

Proposition 0.2. *Let $u_0 \in \dot{L}^2(\mathbb{T}^2)$, $\kappa > 0$, $T > 0$ and $\tilde{u}^N$ be the associated unique weak solution of the deterministic equation in the weak sense. Under appropriate assumption and the scaling $\theta_\cdot^N \equiv r = \frac{1}{N}$, for $i = 1, 2$ and $e_1 = (1,0)$, $e_2 = (0,1)$, and ϕ_i the unique solutions of*

$$\begin{cases} \nabla \cdot \Big(H_\kappa e_i + H_\kappa \nabla \phi_i \Big) = 0 \\ \phi_i \in \dot{\mathcal{H}}^1(\mathbb{T}^2) \ , \end{cases}$$

with the matrix $\bar{H}_\kappa$ defined by

$$(\bar{H}_\kappa)_{ij} := \int_{\mathbb{T}^2} (H_\kappa(e_j + \nabla \phi_j)) \cdot e_i \ , \tag{0.2}$$

and $\bar{u} \in L^2(0,T; \dot{\mathcal{H}}^1(\mathbb{T}^2))$ the unique weak solution to the initial value problem

$$\partial_t \bar{u} = \nabla \cdot (\bar{H} \nabla \bar{u}), \qquad \bar{u}(0,x) = u_0$$

one has the limits

$$\tilde{u}^N \to \bar{u} \quad \text{in } L^2([0,T]; L^2(\mathbb{T}^2)) \quad \text{and} \quad \tilde{u}^N \rightharpoonup \bar{u} \text{ in } L^2([0,T]; \mathcal{H}^1(\mathbb{T}^2)).$$

Moreover, we obtain the following result:

Theorem 0.3. *Let $u_0 \in L_0^2(\mathbb{T}^2)$, $T > 0$ and $\bar{u}$ be the associated weak solution to the homogenized PDE. Under appropriate assumptions and our fixed scaling ($\theta_\cdot^N \equiv r = \frac{1}{N}$), if u^N is the unique weak solution to the Itô formulation of our equation on $[0,T]$ with initial condition u_0, then, for every $\phi \in C^\infty(\mathbb{T}^2)$, it holds that*

$$\lim_{N \to +\infty} \sup_{t \in [0,T]} \mathbb{E} \left[\left| \langle u_t^N - \bar{u}_t, \phi \rangle \right|^2 \right] = 0 \ .$$

In the fourth section, we turn to the investigation and estimate of the diffusivity $C(c,\kappa)$, a function of the parameter which regulates the overlap between the patches and the molecular diffusivity, for different values of c and in the limit $\kappa \to 0$. We study the properties of the correlation matrix of the noise, the matrix A^N, defined as the periodization of one vortex patch; its support is plotted in figure 1 for different values of the parameter c.

Then, we introduce the variational functional formulation of the diffusivity. As H_κ is a symmetric matrix and ϕ_ξ is the solution of (4.33),

$$C(c,\kappa) = \int_{\mathbb{T}^2} |H_\kappa^{1/2}(x)(\xi + \nabla \phi_\xi(x))|^2 dx$$

and the convex functional $\mathcal{E}_k$ is defined as

$$\mathcal{H}^1(\mathbb{T}^2) \ni u \mapsto \mathcal{E}_\kappa(u) = \int_{\mathbb{T}^2} |H_\kappa^{1/2}(x)(\xi + \nabla u)|^2 dx \ ,$$

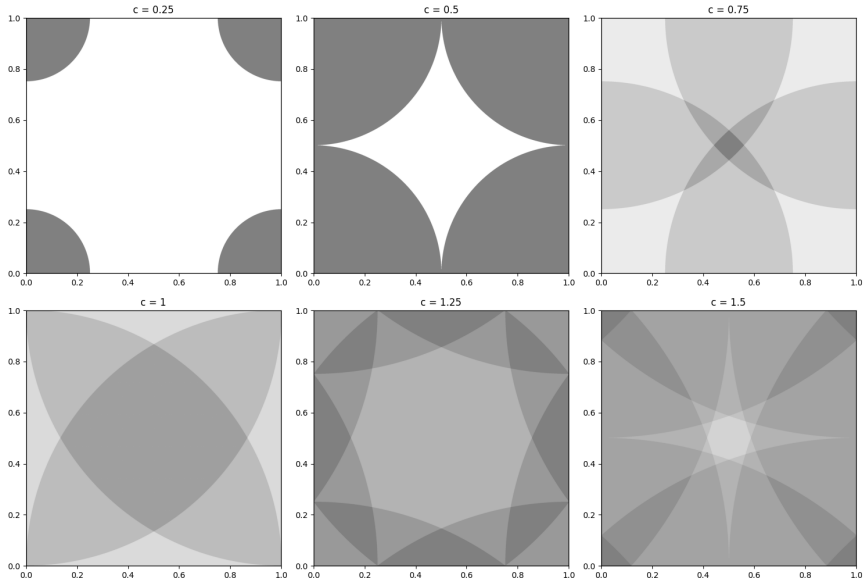

Figure 1: Supports of $A(x)$ for $c \in \{0.25, 0.5, 0.75, 1, 1.25, 1.5\}$. Darker shading represent multiple overlaps.

for any $\xi \in \mathbb{S}^1$. From the Euler-Lagrange equation associated with $\mathcal{E}_\kappa$, the solution of the cell problem ϕ_ξ is the minimizer of $\mathcal{E}_\kappa$, and $\mathcal{E}_\kappa(\phi_\xi)$ is obtained as the minimum of the functional $\mathcal{E}_\kappa(u)$.

We compute the *additional diffusivity* ν_κ of our system, which is defined as the diffusivity $C(c,\kappa)$ minus the molecular diffusivity κ. In the homogenized limit,

$$\nu_\kappa \coloneqq C(c,\kappa) - \kappa = \left(\bar{H}_\kappa \xi \cdot \xi - \kappa\right), \qquad \xi \in \mathbb{S}^1 \ .$$

The additional diffusivity does not depend on the choice of ξ. We study the behavior of ν_κ as a function of the parameter c, obtaining the following results.

Theorem 0.4. *Under suitable assumptions the following statements hold:*

i) If $c \in (0, \frac{1}{2})$ (i.e. the vorticity patches are completely separated) there exists a constant $L > 1$, depending only on c such that

$$\kappa \leq C(c,\kappa) \leq L\kappa \quad \text{for all } \kappa > 0. \tag{0.3}$$

The constant L does not depend on the specific choice of the radial function ψ.

ii) If $c = \frac{1}{2}$ for any $n \geq \frac{7}{2}$ there exists a $p \coloneqq p(n) \geq 1$ and a constant $L' \coloneqq L'(c, \|\psi\|_{W_x^{p+1,\infty}}) > 0$ such that

$$\kappa \leq C(c,\kappa) \leq L'(\kappa + \kappa^{1-\frac{1}{n}}) \quad \text{for all } \kappa > 0.$$

iii) If $c \geq \sqrt{2}/2$, then there exists a constant $m > 0$ such that

$$C(c,\kappa) \geq \kappa + m \quad \text{for all } \kappa > 0.$$

The constant m can be made arbitrarily large by a suitable choice of the stream function ψ.

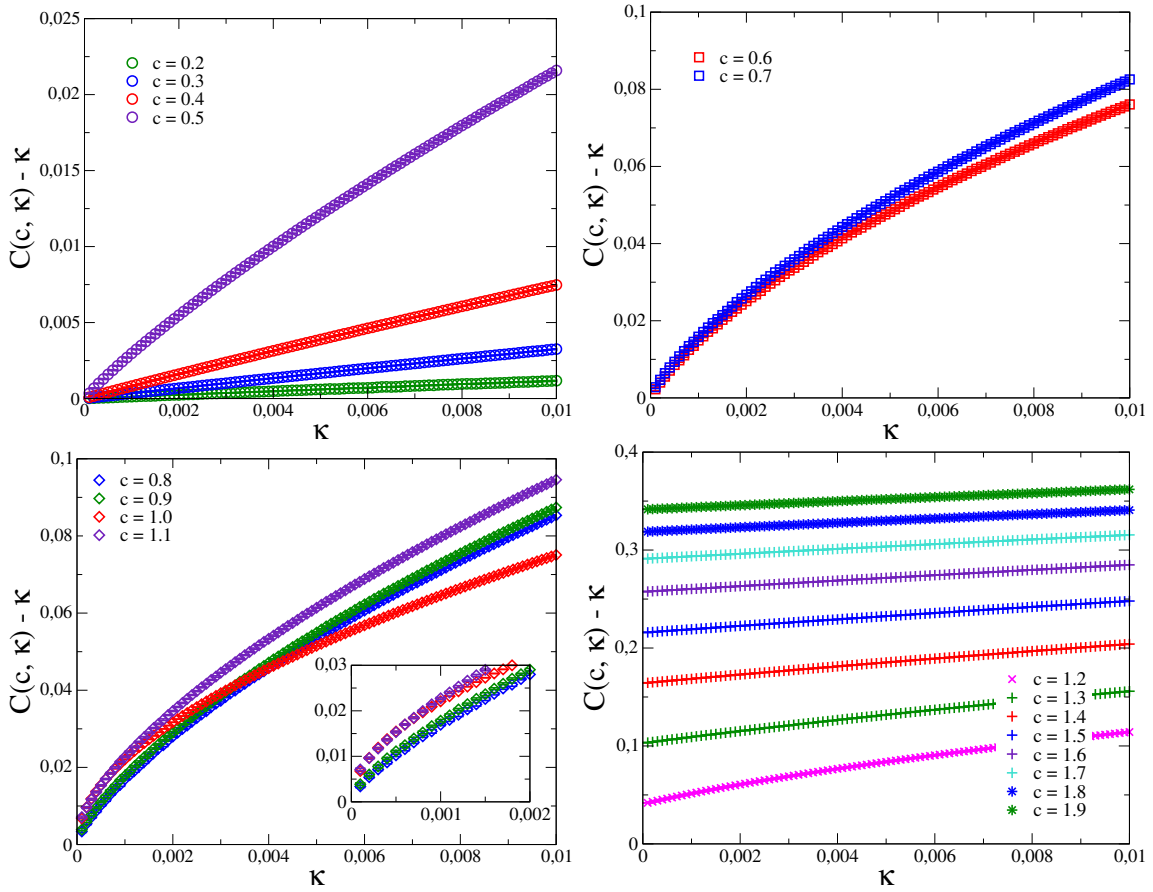

Figure 2: Plot of additional diffusivity $C(c, \kappa)$, for different values of c, from left to right and top to bottom: $c \in (0, \frac{1}{2}]$,$c \in (\frac{1}{2}, \frac{\sqrt{2}}{2})$, $c \in (\frac{\sqrt{2}}{2}, \frac{\sqrt{5}}{2})$, $c > \frac{\sqrt{5}}{2}$ (with zoom at $\kappa \to 0$ if needed). The profile function used is $\varphi(x)$, with $a_1 = 0.05$, $a_2 = 0.3$. The top right panel exhibits values of c in the range $c \in (\frac{1}{2}, \frac{\sqrt{2}}{2})$, which we highlight lies outside the statements of the main theorem.

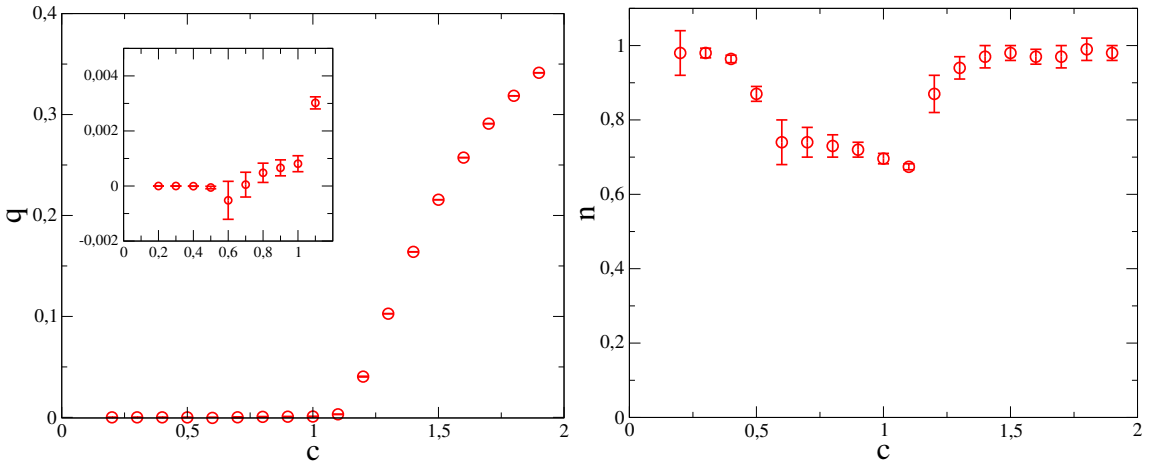

Figure 3: Intercept estimate (left) and power law exponent estimate (right) as a function of the parameter c. The profile function used is $\varphi(x)$, with $a_1 = 0.05$, $a_2 = 0.3$.

Then, we turn to the numerical investigation: we numerically estimate the corrector of the homogenized equation, ϕ_e, to compute the additional viscosity of the system. Our setting is a two-dimensional lattice, with different grid-steps; we comment on our parametric choice of the stream function ψ orthogonal gradient, the so-called profile function,

$$\nabla^{\perp}\psi(x) = \frac{x^{\perp}}{|x|}\frac{\varphi(|x|)}{\|\varphi\|_{L^2_x}},$$

with $x \in \mathbb{T}^2$, and $\varphi(r)$, $r \in \mathbb{R}_+$ defined as

$$\varphi(x) = \frac{1}{r^2}\exp\left(-\frac{a_1}{r^2}\right)\exp\left(-\frac{a_2 r^2}{|r-c|}\right)$$

with a_1, a_2 parameters. We summarize briefly the discretized operator and our notation: we define the second order elliptic operator T in divergence form as:

$$T\phi_e := -\frac{1}{2}\left(\sum_{i=1}^{2} D_i^- \left(\sum_{j=1}^{2} H_{ij} D_j^+ \phi_e\right) + \sum_{i=1}^{2} D_i^+ \left(\sum_{j=1}^{2} H_{ij} D_j^- \phi_e\right)\right) \ ,$$

where $i = 1, 2$ and D_i^- and D_i^+ are, respectively, the forward and backward difference operators. The corresponding divergence operator is defined as:

$$\mathrm{div} f := \frac{1}{2}\sum_{i=1}^{n}(D_i^- + D_i^+)f_i.$$

Then, we turn to the solution of the two linear systems

$$T\phi_1 = \mathrm{div}\,(A \cdot e_1) \ ; \quad T\phi_2 = \mathrm{div}\,(A \cdot e_2)$$

In the next sections, we present our numerical results: we first investigate the dependence of our profile function from its parameters, then we study the behavior of the additional diffusivity

$C(c,\kappa)-\kappa$ as a function of the molecular diffusivity κ. For different values of the support of the profile function, the additional diffusivity can have a linear behavior in κ, or exhibit a power law behavior, as it is possible to see from the data in figure 2. We fit a power law function to our data, to extract information on the power law exponent (equal to one in the case of a linear function of κ) and the intercept. We report our results in figure 3. Our numerical investigation confirms previous analytical results and expands our knowledge in the regimes of the parameter c for which we do not have rigorous analytical results.

In the end, we also investigate the sensitivity of our results with respect to different choices of the profile function.

Chapter 5: testing noise under Kelvin-Helmholtz instability

After the digression on the effects of the stochastic advection field on a passive scalar, in this chapter we focus on the use of the Point Vortex model, together with its stochastic modifications, as a fluid discretization. Note that the stochastic modification we are mainly interested in investigating is the case of the advection by a stochastic velocity field term, which is introduced in chapter 3 and studied from a different point of view in chapter 4 and more in detail in the work [13].

To do so, we firstly introduce a simple example of a system where turbulence develops: the Kelvin-Helmholtz instability, an instability which occurs between transition layers at the boundary of streams of different velocities or densities; small perturbations can trigger huge oscillations. In the turbulent regime, it is possible to observe the so-called inverse cascade: energy flows from small scales to large scales and large structure develops at the transition layer. We summarize some well-known results and formal computations on this model; we also comment on the possibility of delaying the structure formation. In this chapter, we will investigate the effects of the Point Vortex model stochastic modification on this instability, to check how and when instability can be delayed. The results of this chapter are presented in the work [59].

After the brief introduction, we turn to the qualitative numerical investigation of the model: we first investigate the classic deterministic setting and the additive noise setting. The deterministic dynamics is given by the following differential equations:

$$\frac{dX_t^i}{dt}=\sum_{j\neq i}\Gamma_j K\left(X_t^i,X_t^j\right)\ ,$$

where $X_t^1,...,X_t^N$ are the positions of the vortices with intensities (circulations) $\Gamma_1,...,\Gamma_N$, K is the vector-valued kernel $K(x,y)$, the Biot-Savart kernel, equal to

$$K(x,y)=\frac{1}{2\pi}\frac{(x-y)^\perp}{|x-y|^2}$$

in full space, suitably modified on a torus or in a bounded domain. The additive noise stochastic modification of the Point Vortex model is obtained by modifying the previous scheme by adding independent 2D Brownian motions $W_t^1,...,W_t^N$ to the equations:

$$dX_t^i=\sum_{j\neq i}\Gamma_j K\left(X_t^i,X_t^j\right)dt+\sqrt{2\nu}dW_t^i\quad ,$$

see [25, 81, 103]; this model is used to investigate viscous flows.

By investigating those two models, we can both test the qualitative resemblance of our point vortex discretization to the expected behavior of the fluid and also show delay of the instability. The fluid configuration of two shear flows allows us to do that, as it develops instability without viscosity and delays it when viscosity is present. In the beginning of the section, we describe our setting and we discuss the initial condition chosen, together with the numerical discretization used to solve the Point Vortex model dynamics. The initial condition chosen is of uniformly distributed point vortices in a strip of small width, half of it being in the positive part of the domain, half in the negative. Our domain is the torus $\mathbb{T}^2$, equal to the set $[-1,1]^2 / \sim$ with coordinates $x = (x_1, x_2)$ and identified boundaries at $x_1, x_2 = \pm 1$; all fields are periodic in the x_1 and x_2 direction. The initial condition for the velocity field u_0 is of the form

$$u^0(x_1, x_2) = \left(u_1^0(x_2), 0\right)$$

and vorticity $\omega_0 = \partial_{x_2} u_1^0(x_2)$. We choose

$$u_1^0(x_2) = \begin{cases} -1 & \text{if} \quad x_2 \leq -\delta \\ \frac{x_2}{\delta} & \text{if} \quad -\delta \leq x_2 \leq \delta \\ 1 & \text{if} \quad \delta \leq x_2 \end{cases} \tag{0.4}$$

and we fix the parameter $\delta = 0.02$.

We also recall the approximation of the Green function employed, the second of the two described at the end of Chapter 1. Then, we briefly discuss qualitative numerical results on the onset of the instability in the case of the standard Point Vortex model, and we add some formal considerations on the fluid velocity to comment the numerical study of the stochastic Point Vortex model with additive noise, which corresponds to the viscous fluid case.

In the next section, we focus on our results on the stochastic Point Vortex model with environmental noise, with the following dynamics:

$$dX_t^i = \frac{1}{N} \sum_{j \neq i} K\left(X_t^i, X_t^j\right) dt + \sum_{k \in K} \sigma_k\left(X_t^i\right) \circ dB_t^k \ ,$$

where the one dimensional brownian motions B_t^k are the same for all particles, while in the additive noise case each point vortex is affected by an independent brownian motion W_t^i. The divergence-free fields $\sigma_j(X_t^i)$ are defined as

$$\sigma_j(X_t^i) := a_j^{N,M} K\left(X_t^i - Y^j\right), \quad j = 1, ..., M \ ,$$

where the intensities $a_j^{N,M}$ are linked to the scaling limit process we are interested in investigating.

We first describe the stochastic advection field, which is made by a sum of vortex structures, and we discuss the choices we made in our implementation: how to choose the positions of the vortex structure and their intensity. The first ones are taken at each timestep as uniformly distributed on a strip, with width greater than the width of the point vortices strip, while the intensity is formally estimate with an heuristic computation, in order to emphasize the regime where the environmental nose could produce effects similar to viscous ones. To follow the scaling limit procedure, we consider a large number of small intensity vortex structures and we present different simulations, with different choices of the parameters, and comment on the outcomes, comparing with the results obtained for the standard Point Vortex model and the stochastic Point Vortex model with additive noise.

Then, we turn to some statistical analysis on the configurations generated. We focus on the computation of two different quantities, the vorticity of the fluid and the histogram of the positions

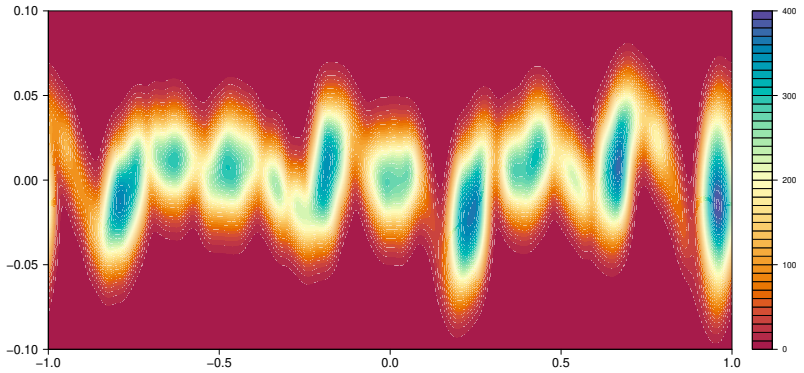

(a)

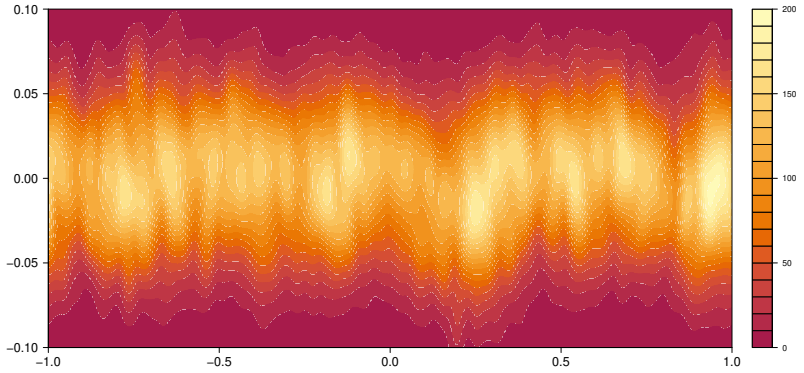

(b)

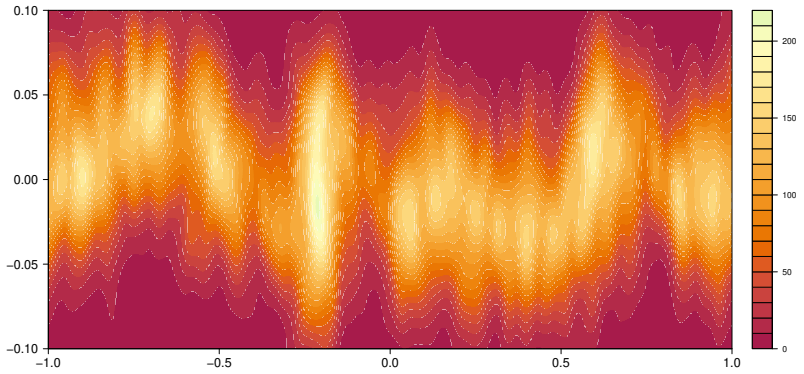

(c)

Figure 4: Vorticity ω_ϵ in the case (a) inviscid, (b) viscous and (c) transport noise, showing macroscopic structures formation or delay of instability.

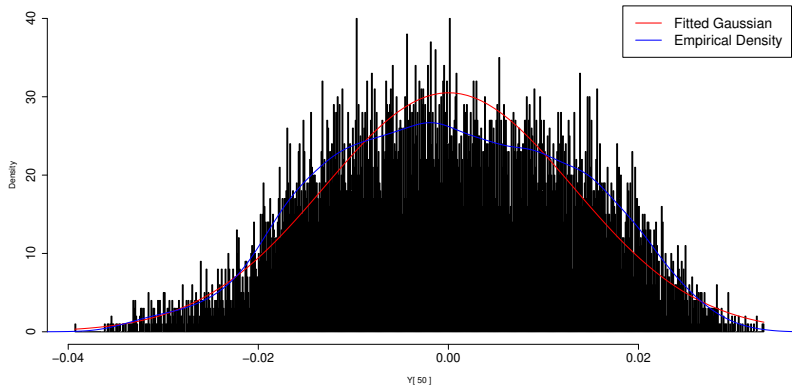

(a)

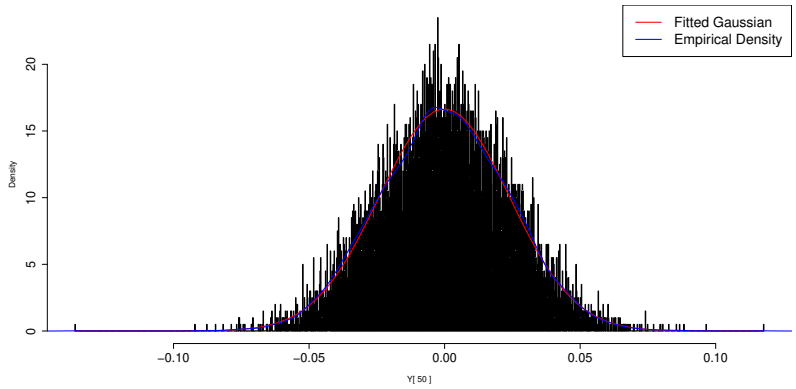

(b)

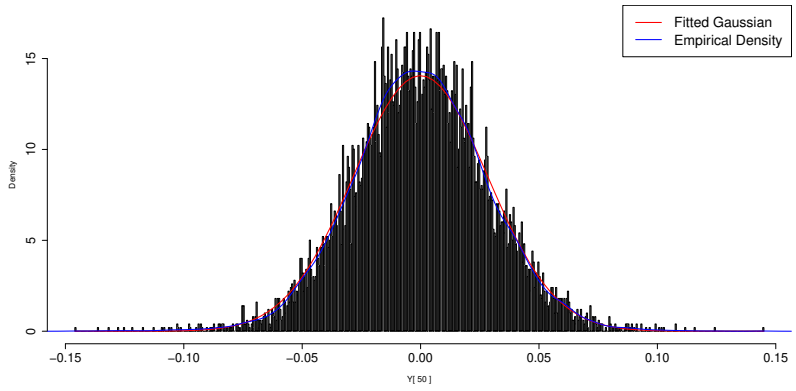

(c)

Figure 5: Histograms of y-positions and empirical density in the case (a) inviscid, (b) viscous and (c) transport noise, showing different density profiles.

on the x and y axis of the point vortices, together with their qq-plots. The vorticity is computed via a mollification process, and compared between the three different models studied, see figures 4a, 4b 4c.

From the positions on x-axis in the three configuration, we obtain the empirical density and compare it with a uniform distribution. In the case of the y-axis, reported in the plot in figure 5, well-known theoretical results states that the fluid velocity solves the heat equation for viscous fluids, namely that the empirical density maintains a Gaussian profile through time. In the case of the stochastic Point Vortex model with additive noise, we expect this result to hold, while we test it for the environmental noise case. To this end, a Kolmogorov-Smirnov test is performed on the different configurations under consideration.

In the last section, we investigate once again the same stochastic modification to the Point Vortex model dynamics studied in the rest of the chapter; the main difference with the previous sections is in the choice of the divergence-free vector fields σ_k: while in the previous section their coefficient was selected according to heuristic arguments, here we base our choice on considerations made in chapter 3, and we consider the following vector fields:

$$\sigma_k(X^{(i)}(t)) := \frac{2\Gamma}{\sqrt{M}} \frac{1}{\|K_\varepsilon\|_2} K_\varepsilon \left(X^{(i)}(t) - Y^{(k)} \right), \quad k = 1, ..., M \ .$$

As before, the vector fields represent small-scale vortex structures located at positions $Y^{(k)}$. Their interaction kernel is regularized, the regularization parameter being ε; this parameter was taken very small in the previous section and in [59], however in this section we take a larger value for this parameter, according to considerations in chapter 3. We fix the parameter $\Gamma = 0.5$ in the following numerical investigation.

Instead of taking a tick strip of vortices as initial condition and investigate a smoothed instability, here we take as initial condition N point vortices uniformly distributed on the line $y = 0$:

$$u(t=0)(x,y) = \left(u_x^0(y), 0 \right) \ ,$$

with

$$u_x^0(y) = \begin{cases} -1 & \text{if} \quad y \leq -\delta \\ 1 & \text{if} \quad \delta \leq y \end{cases}$$

As a preliminary step, we repeat some of the analysis done in the previous sections, and to this end we study the vorticity distribution of the three different Point Vortex model. Then, we investigate the energy conservation in the three different Point Vortex model settings: we compute the Hamiltonian of the Point Vortex model,

$$H = -\frac{1}{2\pi} \sum_{i \neq j} \gamma_i \gamma_j \log d(x_i, x_j) \ ,$$

where we take $\gamma_i = N^{-1}$, the mean-field scaling, x_i is the position of the i vortex, and $d(x_i, x_j)$ is the distance computed on the chosen domain, in our case the two-dimensional torus $\mathbb{T}^2$; as commented before, we are exploiting the second approximation of the Biot–Savart kernel described in chapter 1.

The case of the standard Point Vortex model is used as a benchmark for the rest of the investigation: we estimate the numerical error of our method, as we expect the Hamiltonian to be conserved up to numerical error. We investigate both the case of the additive noise stochastic modification and the transport noise stochastic modification. In the latter case, we consider positions of the fixed vortices random and uniformly distributed on the torus, and placed on a lattice as described

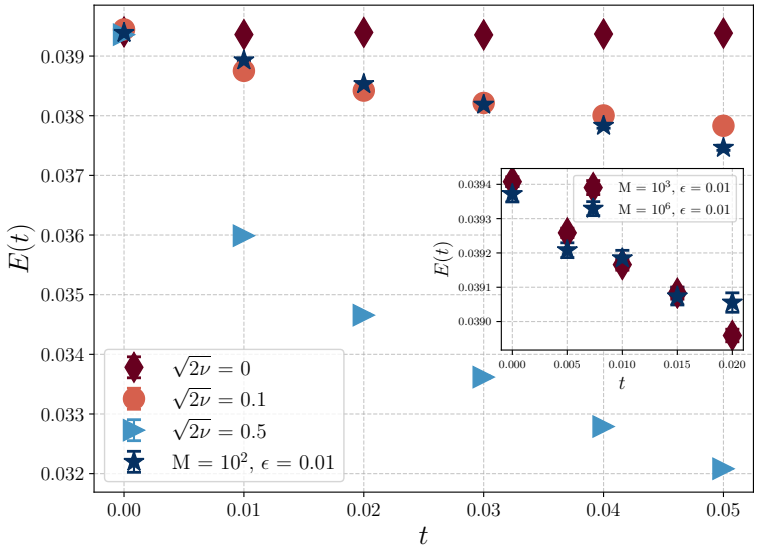

Figure 6: Hamiltonian $E(t)$, with $dt = 10^{-5}$ and $N = 10^2$ point vortices. Datapoints are averaged on different samples with different initial conditions for the positions $X^{(i)}$ and positions of noisy structures. Small plot: all datapoints are averaged on different samples with different initial conditions for the positions $X^{(i)}$ but same positions of noisy structures (on a lattice), for comparison.

in section 3.6 of chapter 3; the results are reported in figure 6 and show that the environmental noise stochastic modification of the Point Vortex model could have non-conservative effects on the Hamiltonian of the system; moreover with the scaling of the vector field σ_k which we are studying, different values of the total numbers of vector fields M, with $k = 1 \dots M$, have comparable effect.

Finally, we investigate the velocity profile: in the case of our initial condition, the velocity of the fluid satisfies the diffusion equation, and we are able to describe our system with the heat equation, obtaining the following relation:

$$u(\eta) = -U_0 \mathrm{erf}\left(\frac{\eta}{2\sqrt{\nu}}\right)$$

where the parameter η is defined as

$$\eta = \frac{y}{\sqrt{t}} \ .$$

We compare the two stochastic modifications of the Point Vortex model's dynamics, the additive noise stochastic modification and the transport noise stochastic modification, both with positions of the fixed vortices random and uniformly distributed on the torus, and placed on a lattice, as before. In figure 7, we report results for the velocity profile as a function of the variable η, for the two different stochastic modifications studied and different parameters. In the case of the stochastic modification of transport noise, we explore different values of M, for which we see once again that different M have comparable effect, and two different settings. First, we average our data on different samples, with different initial positions of the point vortices $X^{(i)}$, with same positions of noisy structures $Y^{(k)}$, placed on on a lattice, then we study the case of averaging on different samples with different initial conditions for the positions $Y^{(k)}$. While there is qualitative agreement between the curves

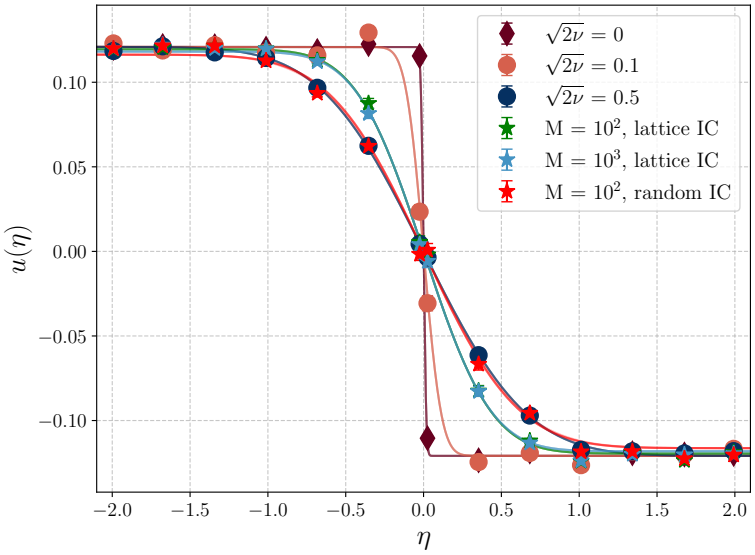

Figure 7: Velocity profile $u(\eta)$, with $dt = 10^{-5}$ and $N = 10^2$ point vortices. We average on different initial conditions for the positions $X^{(i)}$. In the environmental noise case, we consider datapoints averaged on different samples with same positions (on lattice) of noisy structures $Y^{(k)}$, and datapoints averaged on different samples with different positions $Y^{(k)}$.

drawn according to the model and the data, we obtain quantitative agreement (acceptable χ^2/dof) from fitting the model only for the case of the additive noise with larger viscosity parameter.

Chapter 6: statistical correlations

The final chapter is devoted to the investigation of the temporal structure of the equilibrium dynamics of the Point Vortex model. The results of this chapter are contained in the paper [68]. As the Point Vortex model is a simple discretization of the Euler equations, it allows us to perform studies related to one of the open problems of fluid dynamics, the long time behavior of the fluid. To do so, we investigate the equilibrium dynamics of the system and its temporal structure, by computing the statistical correlations in time of local observables, functions of the vorticity, of a large number N of point vortices under the invariant measure $dx_1 \cdots dx_N$.

In the first section, we recall the notation and the model's parameters; we specify the domain, the computed observables and we enunciate our results.

We study the Point Vortex model, with Hamiltonian

$$H = -\frac{1}{2\pi} \sum_{i \neq j} \gamma_i \gamma_j \log d(x_i, x_j),$$

where $\gamma_i \in \mathbb{R} \setminus \{0\}$ are the vortex's circulations, with $|\gamma_i| = 1$. We are allowed to fix γ, as rescaling the intensity corresponds to fix the time scale dynamics. $d(x_i, x_j)$ is the periodic distance between the point vortices in positions x_i, x_j, on the periodic square domain, the torus $\mathbb{T}^2 = [-1, 1] \times [1, 1]$.

The equations of motion are

$$\dot{x}_i = \sum_{j \neq i}^{N} \gamma_j K(x_i - x_j), \quad i = 1, \dots, N,$$

where the Biot-Savart kernel $K(\mathbf{x})$ is defined as

$$K(x) = (-\partial_{x_2}, \partial_{x_1}) G(x),$$
$$-(\partial_{x_1}^2 + \partial_{x_2}^2) G(x) = \delta_0(x) - 1,$$

where G is the zero-averaged fundamental solution of Laplace's equation on the torus. The vorticity distribution is defined as

$$\omega(x) = \sum_{i=1}^{N} \gamma_i (\delta_0(x - x_i(t)) - 1).$$

and under periodic boundary conditions it is solution of the two-dimensional Euler equation in vorticity form.

After a brief introduction on the model, we introduce the computed local observables,

$$F_\sigma^L(t) = \sum_{i=1}^{N} \gamma_i \phi_\sigma^L(x_i(t)),$$

where

$$\phi_\sigma^L(x) = \frac{1}{2\pi\sigma^2} \exp(-d(x, (L,0))^2 / 2\sigma^2)$$

is a function of $\mathbb{T}$ concentrated around the point $(L, 0)$, the shape of which is not relevant, $L \geq 0$ and $d(\cdot, \cdot)$ denotes the (periodic) distance on $\mathbb{T}$, and in our setting

$$0 = \left\langle F_\sigma^L(0) \right\rangle = \left\langle F_\sigma^L(t) \right\rangle \ , \quad t > 0 \ ;$$

where brackets denote integration with respect to initial data with distribution $dx_1 \cdots dx_N$. We study local averages of the vorticity distribution

$$\omega(x) = \sum_{i=1}^{N} \gamma_i \delta_0(x - x_i(t)) \ ,$$

instead of observables of the velocity field u, as this quantities are numerically more stable, and compute the correlations ($L > 0$) of two observables for $L > 0$ and autocorrelation ($L = 0$) of a single observable

$$\rho_\sigma^L(t) = \frac{\left\langle F_\sigma^L(0) F_\sigma^L(t) \right\rangle}{\sqrt{\left\langle F_\sigma^L(0)^2 \right\rangle \left\langle F_\sigma^L(t)^2 \right\rangle}},$$

at times 0 and t.

Then, we recall some well-known information on the object of our investigation, by summarizing the main results in the literature. We first start by highlighting the importance of the convergence of a distribution of point vortices at independent uniform random positions on a torus to white noise in the context of our study. More precisely, the results we obtain in our setting should hold in the limiting regime $N \to \infty$, if the point vortices intensities are scaled as $\gamma_i \sim 1/\sqrt{N}$. This is the case of flows of 2D Euler equations preserving the Gaussian *enstrophy measure*,

$$\frac{1}{Z} \exp^{-\gamma S} d\omega \ ,$$

where we indicate with S the enstrophy,

$$S = \frac{1}{2}\int_T \omega^2(x)dx \ .$$

In this setting, the gaussianity at fixed time is a product of the Central Limit scaling and equidistribution and independence of point vortices positions. On the other hand, the scaling $\gamma_i \sim 1/N$, which we studied in the rest of the thesis, in this setup would lead to a trivial stationary solution of Euler's equations). Then, we turn to some literature review and we comment on the ergodicity of the Point Vortex model, which was conjectured by Onsager [109] and disproved by Khanin [82] in the case of a system with a small number of point vortices. We also remark that the equilibrium state we are investigating, or the Gibbsian ensembles absolutely continuous with respect to it, is not suited for describing the vortex aggregation in turbulent flows as portrayed by Onsager. However, it might constitute a valid model for small, unresolved scales of more complex fluid dynamics systems.

In the second section, we describe in details our setting, and we specify the Green function approximation used for the numerical results of this chapter. The advecting vector field can be represented via the Fourier series expansion

$$K(x) = \frac{1}{4\pi}\sum_{k\in\mathbb{Z}^2_0} \frac{ik^\perp e^{i\pi k\cdot x}}{|k|^2}, \quad x \in \mathbb{T}. \tag{0.5}$$

The latter is singular at $x \to 0$, as it is the (orthogonal) gradient of the Green function G of $\mathbb{T}^2$, which has a logarithmic singularity. In fact, the periodic boundary does not affect asymptotic behavior of G at $x \to 0$, which is the same of the free Green function $-\frac{1}{2\pi}\log|x|$. For this reason, the numerical approximation used in the simulations of the dynamics is the following the regularized interaction kernel

$$K_\epsilon(x,y) = \frac{(y_2 - x_2, x_1 - y_1)}{2\pi(d(x,y)+\epsilon)^2},$$

where $d(x,y)$ denotes the periodic distance on the 2D torus $\mathbb{T} = [-1,1]^2$. This approximation is the second of the two described at the end of Chapter 1, as in the statistical ensemble under consideration the most relevant interactions of point vortices take place at close distance.

Then, we describe the numerical discretization of the equations of motion of the Point Vortex system. The Point Vortex dynamics is numerically solved by means of 4th order Runge-Kutta method, and accuracy of the numerical method was checked by computing the Hamiltonian of the regularized Point Vortex system,

$$H_\epsilon = -\frac{1}{2\pi}\sum_{i\neq j}\gamma_i\gamma_j \log\left(d(x_i,x_j)+\epsilon\right),$$

which is a first integral of the regularized motion; the relative error $H_\epsilon(t)/H_\epsilon(t=0)$ is of order at most 10^{-7} for time $0 \le t \le 0.5$, uniformly with respect to the (random) initial conditions under consideration.

The stability of our result and of our numerical method is also checked by solving the dynamics for different choices of the time step and the regularization parameter of the Green function.

In the next section, we turn to the computation of the observables and the discussion of our results. We estimate the correlations $\rho^L_\sigma(t)$ via the standard Pearson estimator, and report the quantity $\log\rho^L_\sigma(t)$ in figure 8, in the case of self-correlation $L = 0$ and correlation between distinct observables $L > 0$.

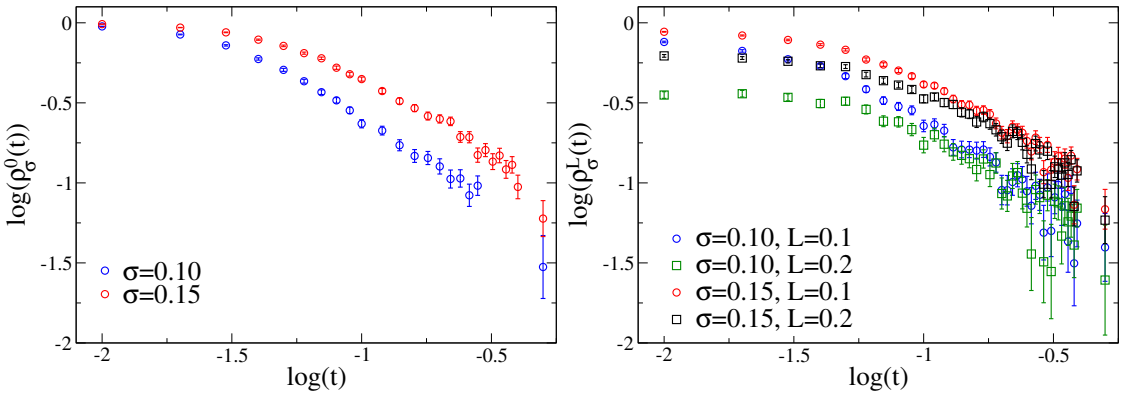

Figure 8: Logarithm of $\rho_\sigma^L(t)$ as a function of the logarithm of t; $\rho_\sigma^{L=0}(t)$ represents the Pearson autocorrelation ($L = 0$, on the left) and correlation ($L > 0$, on the right) coefficient between the observables $F(0, 0, \phi(\sigma))$ and $F(t, L, \phi(\sigma))$. The dynamics is integrated with timestep $\delta t = 10^4$ and machine ϵ regularization, for different values of σ and L.

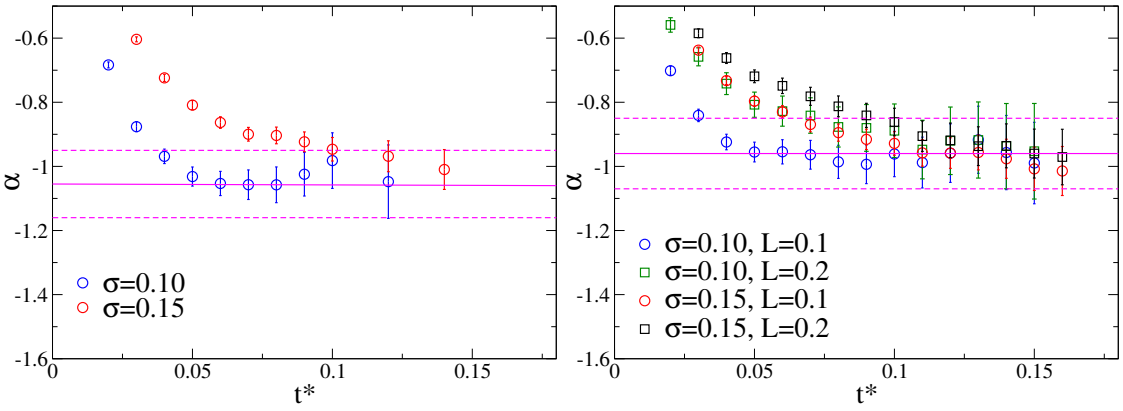

Figure 9: Estimates of the power law exponent α, computed by fitting the logarithm of $\rho_\sigma^L(t)$ for different values of σ and various different fitting ranges $[t^*, t^{**}]$. Horizontal bands denotes the final confidence interval $\alpha = -1.06(11)$ (obtained by taking into account fit systematics) for the self-correlation coefficient, $L = 0$, and $\alpha = -1.02(14)$ for the correlation coefficient, $L > 0$, the two values being compatible.

First, we rule out the exponential decay of correlations, by checking the fit's χ^2 score, then we estimate the power law parametric model Ct^α's exponent α via least square error fit of the logarithm $\log \rho_\sigma^L(t)$ (with C remaining a free parameter). We report our results for the case of self-correlation $L = 0$ and correlation between distinct observables $L > 0$ of the observable $\log \rho_\sigma^L(t)$ in figure 9.

We carry out the same procedure for different choices of the parameters σ and L, and for all the simulations we estimate data points computed at different times and parameters (the regularization parameter ϵ and the time step δt) by using different samples, so that they are independent from each other, and we estimate statistical errors by means of bootstrap procedures.

Finally, as we expect our result to hold in the limit of $N \to \infty$ point vortices, we check the dependence of our results on the parameter N, and we discuss the implications of our findings in relation to the Point Vortex model ergodicity. Our results show that the equilibrium state corresponding to the invariant measure $dx_1 \cdots dx_N$ for a system of many point vortices exhibits mixing behavior; in spite of the existence of singular solutions and (quasi-)periodic orbits, our results may signal that, in the limit $N \to \infty$, they become an increasingly smaller set of phase space, and ergodicity might be recovered.

Chapter 1

The Point Vortex Model: Hamiltonian structure and energy conservation

In this chapter, we introduce the notation and the definitions that will be used in the other chapters of this thesis. We describe the Point Vortex model, which will be investigated in this thesis, and explain its role as a Hamiltonian system and as a discretization of the Euler equation exploited in the context of statistical physics.

1.1 Point vortex dynamics: Hamiltonian system

In this thesis, we consider in most of the chapters a two-dimensional double-periodic domain, a torus $\mathbb{T}^2 = [a, b] \times [a, b], a, b \in \mathbb{R}$, but we will keep this section general. For a more exhaustive discussion, see for example the standard references [107], [117] and [101], the lecture notes [98], the papers [91] and [92], while see [3] for a brief introduction.

We consider N interacting point vortices of strengths (circulations) γ_i and spatial coordinates

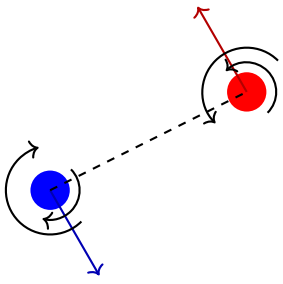

Figure 1.1: Sketch of two point vortices of opposite circulation.

$(x_1^{(i)}, x_2^{(i)})$, with $i = 1 \dots N$. In figure 1.1 we draw two point vortices of opposite circulations in two different colors, and we sketch their respective interaction forces and motion.

On the unbounded plane, $\mathbb{R}^2$, the equations of motion of the system are $2N$ non-linear ordinary differential equations of first order:

$$\frac{dx_1^{(i)}}{dt} = -\frac{1}{2\pi} \sum_{\substack{j=1 \\ j \neq i}}^{N} \gamma_j \frac{x_2^{(i)} - x_2^{(j)}}{d_{ij}^2}, \qquad \frac{dx_2^{(i)}}{dt} = \frac{1}{2\pi} \sum_{\substack{j=1 \\ j \neq i}}^{N} \gamma_j \frac{x_1^{(i)} - x_1^{(j)}}{d_{ij}^2}. \tag{1.1}$$

Note that in the sum the singular term $j = i$ has to be neglected, as it represents the infinite contribution due to the self-energy. More details on why one cannot include this term will be given in the following. The symbol d_{ij} indicates the distance computed on the specific domain that we are investigating, in this case the distance between the point vortices i and j on the unbounded plane $\mathbb{R}^2$. On a different domain, for example on the torus $\mathbb{T}^2$, the definition of distance has to be modified accordingly.

The Hamiltonian formulation of the dynamics (1.1) is due to Kirchhoff [84]; the dynamics can equivalently be derived from a Lagrangian formulation. Seminal works are also Poincaré's monograph on vorticity [111] and Routh's contribution [114]. The conjugate variables are $\sqrt{|\gamma_i|}x_1^{(i)}$ and $\sqrt{|\gamma_i|}x_2^{(i)}(\gamma_i)/(|\gamma_i|)$, both proportional to each coordinate of the two-dimensional system. The dynamics (1.1) can then be formulated in terms of the Hamiltonian function H:

$$\gamma_i \frac{dx_1^{(i)}}{dt} = \frac{\partial H}{\partial x_2^{(i)}}, \qquad \gamma_i \frac{dx_2^{(i)}}{dt} = -\frac{\partial H}{\partial x_1^{(i)}}; \tag{1.2}$$

In turn, if we define the Green function on the unbounded plane $\mathbb{R}^2$, $G_{\mathbb{R}^2}$, as the fundamental solution of the Poisson equation,

$$\Delta_{\mathbf{x}} G_{\mathbb{R}^2}(\mathbf{x} - \mathbf{y}) = \delta(\mathbf{y}), \tag{1.3}$$

with Dirichlet boundary conditions, it is possible to write the Hamiltonian function H in terms of $G_{\mathbb{R}^2}$. We have:

$$H = \sum_{i \neq j} \gamma_i \gamma_j G_{\mathbb{R}^2}\left(\mathbf{x}_i, \mathbf{x}_j\right). \tag{1.4}$$

For the unbounded plane, the Green function is

$$G_{\mathbb{R}^2}(\mathbf{x} - \mathbf{y}) = -\frac{1}{2\pi} \ln |\mathbf{x} - \mathbf{y}|. \tag{1.5}$$

In the case of different domains, the Hamiltonian of the point vortex system is simply written as

$$H = \sum_{i \neq j} \gamma_i \gamma_j G\left(\mathbf{x}_i, \mathbf{x}_j\right). \tag{1.6}$$

where with G we indicate the Green function in a generic domain $\mathcal{D}$. For the two-dimensional torus, $\mathcal{D} = \mathbb{T}^2$, the Green function has an explicit expression in the Fourier space,

$$G_{\mathbb{T}^2}(\mathbf{x}-\mathbf{y}) = -\frac{1}{(2\pi)^2}\sum_{\substack{\mathbf{k}\in\mathbb{Z}^2\\ \mathbf{k}\neq 0}} \frac{1}{k^2}\exp i2\pi\ \mathbf{k}\cdot(\mathbf{x}-\mathbf{y}). \tag{1.7}$$

In the case of generic bounded domains $\mathcal{D}\subseteq\mathbb{R}^2$, without loss of generality, it is possible to assume $G(\mathbf{x}-\mathbf{y})$ to be zero in the case $\mathbf{x}$ or $\mathbf{y}$ lie on the boundary of the domain. This additional property is needed if we want the Point Vortex model to be a discretization of the Euler equations: in this case, the component of the fluid velocity perpendicular to the domain's boundary has to be zero, and this generates conditions on the Green function; in particular, the Green function has to be constant at the boundary. More precisely, if we consider a single vortex with unitary circulation, $\gamma = 1$, located at $p = (x_1, x_2)$, and we give some conditions on the domain, we can define the *hydrodynamic* Green function as the solution of a problem with a singularity in the point p and give some conditions on G; we will follow the definitions from [62], also [107] describes this topic in detail. We consider a finitely connected domain with a boundary which satisfies the following condition

$$\partial\mathcal{D} = \bigcup_{i=1}^{K}\Gamma_i$$

and the uniform exterior ball condition holds for this boundary, while every Γ_i is topologically equivalent to a circle. We now define the periods of the Point Vortex system's Green function as

$$\tau_j = \frac{c_j}{\sum_{i=1}^{N}\gamma_i}$$

where the coefficients c_j represents the circulations around each of the boundary components. The total sum of the periods is a constant and it has to be -1, as we are considering a point vortex with $\gamma = 1$. Now, the Green function will be constant on every Γ_i, and the problem is written as

$$\begin{aligned} -\Delta G(\mathbf{p}) &= \delta(\mathbf{p}) \quad \text{in } \mathcal{D}\\ \partial_\tau G(\mathbf{p}) &= 0 \quad \text{on } \partial\mathcal{D}\\ \int_{\Gamma_i}\partial_\nu G(\mathbf{p}) &= \tau_i \quad \forall\ i\\ \int_{\partial\mathcal{D}} G(\mathbf{p_1})\partial_\nu G(\mathbf{p_2}) &= 0 \quad \forall\ \mathbf{p_1},\mathbf{p_2}\in\mathcal{D} \end{aligned}$$

where we indicate with $\partial\tau$ the tangential derivative and with $\partial\nu$ the normal derivative. While the first three equations allow us to write the Green function plus a constant, the fourth equation gives a unique solution. It is important to note that the Green function as defined before is symmetric. More details, for example on multiply connected domains, can be found in [91, 92]. The link between the Euler equation and the Point Vortex model will be explained in the following section.

In general, the explicit expression for the Green function is not known for every bounded domain. The Green function in open regions with smooth boundary is a generalization of (1.5), and in [98] it is written in the simple form:

$$G(\mathbf{p_1},\mathbf{p_2}) = -\frac{1}{2\pi}\ln|\mathbf{p_1}-\mathbf{p_2}| + f(\mathbf{p_1},\mathbf{p_2}). \tag{1.8}$$

Note that the Green function G can be decomposed in two terms: one is simply the Green function of the unbounded plane, $G_{\mathbb{R}^2}$ Here, we indicate with $f \in \mathcal{D} \times \mathcal{D}$ a smooth function, which is zero if the domain in consideration is the full plane. The Green function can then in general be written as a sum of a logarithmic singularity, the fundamental solution, which has radial symmetry, and a smooth function, which is harmonic in the domain $\mathcal{D}$. From [62, 61, 39], this function is called *Robin function* when computed at the singularity (i.e., $f(\mathbf{p_1}, \mathbf{p_1})$) and it takes into account the interaction between each vortex and the domain boundary; at the boundary it diverges. In some domains, it is possible to formulate an expression for the Robin function in term of the contribution of image vortices, located outside of the domain.

It is possible to expand the Green function close to the point p_1 (where the point vortex is located), by making use of its decomposition:

$$G(\mathbf{p_1}, \mathbf{p_2}) = -\frac{1}{2\pi} \ln |\mathbf{p_1} - \mathbf{p_2}| - t_{\mathcal{D}}(\mathbf{p_1}) + O(|\mathbf{p_1} - \mathbf{p_2}|), \tag{1.9}$$

where we have expanded the function $f(\mathbf{p_1}, \mathbf{p_2}) = -t_{\mathcal{D}}(\mathbf{p_1}) + O(|\mathbf{p_1} - \mathbf{p_2}|)$ near the singularity. For other important properties of the hydrodynamic Green function, its comparison with the Dirichlet Green function and properties of the Robin function, see for example [62, 61, 74, 107].

1.1.1 Link with Euler equation

In the previous section, we anticipated conditions on the Green function which originate from the link between the Point Vortex model and the Euler equations. In the following discussion we will explain this connection, which is one of the reasons of interest for the dynamical system of point vortices. We refer to the lecture notes [98]; also the classic textbooks [4], [107] give a nice explanation of this connection, and both of those references' notation will be followed in this exposition. First of all, we will introduce and explain the two concepts of *stream function* and *vorticity*, then turn to the definition of the *vorticity* in terms of a distribution of N point vortices.

If we consider a fluid element in motion, with position vector $\mathbf{x}$ and velocity $\mathbf{u}$ at time t, and observe the same fluid element again after a small interval of time δt, the position of the fluid element becomes $\mathbf{x} + \mathbf{u}\ \delta t$. The velocity at second order in the time interval is expressed as:

$$\mathbf{u}(\mathbf{x} + \mathbf{u}\ \delta t, t + \delta t) = \mathbf{u}(\mathbf{x}, t) + \left(\frac{\partial \mathbf{u}}{\partial t} + \mathbf{u} \cdot \nabla \mathbf{u} \right) + O\left(\delta t^2\right) \tag{1.10}$$

where the term inside the parenthesis at second member represents the acceleration of the fluid element and can be rewritten in a different notation as $D\mathbf{u}/Dt$, by introducing the notion of material derivative of the velocity.

In this thesis, only two-dimensional incompressible fluids (i.e. the divergence of the velocity field $\mathbf{u}(\mathbf{x}, t)$ of the fluid is equal to zero) will be taken into account: in this case, each infinitesimal volume element subjected to the velocity field has constant density in time, i.e. the material derivative of the density ρ is zero, due to the conservation of mass. As already anticipated, if we take into account a domain $\mathcal{D}$ with boundary, it is necessary to specify the value of the velocity at the domain's boundary, as the fluid has to be constrained inside. The condition on the velocity field is then $\mathbf{u} \cdot \hat{\nu} = 0$, where $\hat{\nu}$ is the outward normal to the boundary. For the unbounded plane or other unbounded domains, it is necessary to prescribe the behavior of the velocity field as $|\mathbf{x}|$ goes to infinity. In general, this is

done by adding to the velocity a gradient of an harmonic function and use this function's behavior as $|\mathbf{x}| \to \infty$ to specify the velocity behavior.

Stream function

Again from the conservation of mass, if we consider two-dimensional flows, we are able to write the components of the velocity field $\mathbf{u} = (u_1, u_2)$ as derivatives of a scalar function $\psi = \psi(x_1, x_2, t)$, the stream function: namely, the mass conservation equation reduces to:

$$\frac{\partial u_1}{\partial x_1} + \frac{\partial u_2}{\partial x_2} = 0, \quad \text{with} \quad u_1 = \frac{\partial \psi}{\partial x_1}, \quad u_2 = \frac{\partial \psi}{\partial x_2}, \quad \mathbf{u} = \nabla^{\perp}\psi.$$

Another way to look at the stream function is to write the field velocity $\mathbf{u}$ as the curl of a three-dimensional vector potential $\mathbf{A}$, as done in the electromagnetism formalism, and note that two components of this vector are zero and the last one is the stream function. Moreover, if we are dealing with a bounded domain $\mathcal{D}$, as a consequence of the fact that the fluid cannot go outside the boundary, the value of the stream function is constant on $\partial\mathcal{D}$.

A general decomposition for the velocity field (the *Helmholtz decomposition*) is the sum of a potential part, which will specify the behavior of the velocity at $|\mathbf{x}| \to \infty$, and a solenoidal vector potential part, in terms of the curl of the stream function:

$$\mathbf{u} = \nabla\phi + \nabla \times \psi \tag{1.11}$$

where the second term will be explained in detail in the following paragraph; it represents the contribution of the vorticity distribution to the velocity field. Finally, if we consider a fluid particle with velocity $\mathbf{u}(\mathbf{x}, t)$, its equation of motion for the two coordinates can be rewritten in the form of Hamilton equations:

$$\dot{x_1} = \frac{\partial H}{\partial x_2}$$
$$\dot{x_2} = -\frac{\partial H}{\partial x_1}$$

where the Hamiltonian function is time dependent and is the stream function ψ.

Vorticity

We now turn to the introduction of the concept of *vorticity* of a fluid. We start by focusing on the analysis of the force that one fluid element with position vector $\mathbf{x}$ exerts on an adjacent one with position vector $\mathbf{x} + \mathbf{r}$, in a similar fashion to what is done in deformation theory. To do so, we write the velocity of the adjacent fluid element as $\mathbf{u} + \delta\mathbf{u}$, where the components of the velocity increment can be written as

$$\delta u_i = r_j \frac{\partial u_i}{\partial x_j} + \{\text{second order in the distance } \mathbf{r}\} = \delta u_i^{symm} + \delta u_i^{asymm} = r_j \left(S_{ij} + A_{ij}\right)$$

where we decomposed the increment in a symmetric and anti-symmetric part. The symmetric part, S_{ij} is not of interest in the present discussion; we only note that it can always be chosen a reference frame where its not-diagonal elements are zero and it has null trace in the case of an incompressible fluid. On the contrary, the antisymmetric part $r_j A_{ij}$ is the one we focus on: as we are considering three-dimensional tensors, it can be written as

$$r_j A_{ij} = -\frac{1}{2}\varepsilon_{ijk} r_j \omega_k.$$

where ω is the vorticity of the fluid. The antisymmetric contribution to $\delta\mathbf{u}$ in this framework represents the velocity due to a rigid rotation of angular velocity $1/2\omega$ at a relative distance $\mathbf{r}$. From the anti-symmetrization of $\delta\mathbf{u}$, the vorticity can also be defined as the curl of the velocity,

$$\omega = \nabla \times \mathbf{u}. \tag{1.12}$$

Moreover, we recall that our focus is on two-dimensional fluids: in this case, only the $\hat{\mathbf{x}}_3$ component survives; and in the following the symbol ω will be used to indicate the scalar function which is the non-null component of the vorticity vector. As a final remark, it is possible to express the vorticity in terms of the streaming function by making use of their definitions, obtaining the following relation:

$$\Delta\psi = -\omega.$$

From the relation between the stream function and the vorticity, and the stream function and the Green function, it is finally possible to express the velocity field in terms of the vorticity field. For a general bounded domain $\mathcal{D}$,

$$\mathbf{u}(\mathbf{x}, t) = \int_{\mathcal{D}} \nabla^{\perp} G(\mathbf{x}, \mathbf{y}) \omega(\mathbf{y}, t) d\mathbf{y} \tag{1.13}$$

where in general the behavior at infinity of the velocity has to be specified, as said in the previous discussion. For example, in the case of the unbounded plane $\mathbb{R}^2$, the velocity field goes to zero if $\omega \in L_1 \cap L_\infty(\mathbb{R}^2)$.

Euler equation in vorticity formulation

The vorticity formulation allows to write the equation of motion for an infinitesimal fluid element in a simple form, by making use of the curl operator and some assumptions; in giving a very brief outline of this formulation, we will mainly follow the notation of [98] and [101]; see also [89].

In the following, we only consider *ideal* fluids, where no dissipation of energy takes place; we also assume the density ρ of the fluid to be constant. We start from equation (1.10), where we wrote the acceleration for a fluid element, and we write the equation of motion for a fluid element as

$$\begin{aligned} \rho \frac{D\mathbf{u}}{Dt} + \nabla P - \rho \mathbf{F} &= 0 \\ \nabla \cdot \mathbf{u} &= 0 \end{aligned} \tag{1.14}$$

where $\mathbf{F}$ is an external force on the fluid and we obtained the gradient of the pression P in the following way: in the integral form, the total force on the fluid element is the integral on the

surface volume element of the pression; this integral can be rewritten as a volume integral of the pression gradient. Moreover, the mass conservation is encoded in the divergence-free condition for the velocity field.

In addition, we have to specify a boundary condition for the velocity, in the case of bounded domains, or the velocity behavior at infinity, in the case of unbounded domains. For the sake of simplicity, we suppose that the force for unit volume $\mathbf{F}$ can be written as a gradient field. By making use of this assumption, if we now apply the curl operator to the first equation in (1.14), we obtain the Euler equation in the vorticity formulation:

$$\begin{aligned} \frac{\partial \omega}{\partial t}(\mathbf{x},t) + (\mathbf{u}\cdot\nabla)\omega(\mathbf{x},t) &= 0 \\ \mathbf{u}(\mathbf{x},t) &= \int_{\mathcal{D}} \nabla^{\perp} G(\mathbf{x},\mathbf{y})\omega(\mathbf{y},t)d\mathbf{y} \\ \nabla\cdot\mathbf{u} &= 0 \\ \omega(\mathbf{x},0) &= \omega_0(\mathbf{x}), \quad \mathbf{x}\in\mathcal{D}, \quad t\geq 0, \end{aligned} \tag{1.15}$$

with $\mathbf{u}\cdot\hat{\nu} = 0$ on bounded domains or the condition on unbounded domain that prescribe null velocity for $|\mathbf{x}|\to\infty$ verified (assuming that ω allows that).

We recall that in the previous discussion we were able to write the evolution for a Lagrangian fluid particle with the Hamiltonian formalism. Now that we have introduced the vorticity ω, the Euler equation becomes:

$$\begin{aligned} \frac{\partial \omega}{\partial t}(\mathbf{x},t) + \frac{\partial \omega}{\partial x_1}\frac{\partial H}{\partial x_2} - \frac{\partial \omega}{\partial x_2}\frac{\partial H}{\partial x_1} &= 0 \\ \Delta H &= -\omega. \end{aligned} \tag{1.16}$$

Vorticity as point vortices distribution

If we now consider a three-dimensional space and restrict our analysis to the case where the vorticity is concentrated along straight vortex filaments, we are able to study a two-dimensional section of this system, where the vorticity is concentrated in points in the two-dimensional slice. This means that the vorticity distribution we are interested in is of the form (see [107]):

$$\omega(\mathbf{x}) = \sum_{i=1}^{N} \gamma_i \phi_\varepsilon(\mathbf{x}-\mathbf{x}_i) \ ,$$

where ϕ_ϵ is a mollifier of the form:

$$\phi_\varepsilon(\mathbf{x}) = \frac{1}{\varepsilon^2}\phi\left(\frac{\mathbf{x}}{\varepsilon}\right)$$

where ϕ is a radially symmetric function of unitary integral and ε is a very small parameter (strictly smaller than one), which can be interpreted as the vortex core. The choice of $\phi_\varepsilon\mathbf{x} = \delta(\mathbf{x})$ represents the idealization of vorticity as decomposed into singular sources, the point vortices.

The Point Vortex system can then be regarded as a discretization of the fluid, where the vorticity is concentrated in the N positions of the point vortices:

$$\omega(\mathbf{x}) = \sum_{i=1}^{N} \gamma_i \delta(\mathbf{x} - \mathbf{x}_i), \tag{1.17}$$

and in this way we finally obtain the Hamiltonian system (1.6) from the Euler equation in vorticity formulation. We point out that this discretization of the Euler equation, beside its use in analytical purposes, can also be of interest in the context of a numerical investigation, which will be one of the focuses of this thesis.

1.2 Euler equation and Point Vortex model

There are many different perspective in the literature where the link between the Euler equation and the Point Vortex model is made explicit, we point out the one due to [99, 98], where it is shown that a L^∞ solution ω of the vorticity formulation of the Euler equation, which has support on disjoint blobs of radius $r \to 0$ is close in the sense of measures to the PV empirical measure (1.17) for short times. More precisely, the following theorem is enunciated in [98].

Theorem 1.1. *Let Λ_i^ε be disjoint open regions with measure equal to $\pi\varepsilon^2$. Define*

$$\omega^\varepsilon(\mathbf{x}) = \frac{1}{\pi\varepsilon^2} \sum_{i=1}^{N} a_i \chi_{\Lambda_i^\varepsilon}(\mathbf{x}) \ .$$

For bounded and continuous functions f, suppose

$$\lim_{\varepsilon \to 0} \omega^\varepsilon(f) = \sum_{i=1}^{N} f(\tilde{\mathbf{x}}_i) \ , \tilde{\mathbf{x}}_i \in \mathbb{R}^2$$

and assume

$$\Lambda_i^\varepsilon \subset \sum_{\alpha_i^\varepsilon} (\tilde{\mathbf{x}}_i), \ \alpha > 0 \ ,$$

where $\sum_R(\mathbf{x})$ indicates the circle of radius R, with center in $\mathbf{x}$. Then, there exists a t^* for which

$$\lim_{\varepsilon \to 0} \omega_t^\varepsilon = \sum_{i=1}^{N} a_i f(\mathbf{x}_i(t)) \ ,$$

for $t < t^*$. Here, ω_t^ε is the weak solution of the Euler equation with ω^ε as initial datum, and $\mathbf{x}_i(t)$ is the solution of the vortex dynamics $(a_i, \mathbf{x}_i(t))$ which starts from $\tilde{\mathbf{x}}_i$ at $t = 0$.

See the above references for a detailed explanation. However, in this section, we will describe another well-known point of view on the link between the Euler equation and the Point Vortex model, which consist in writing a weak formulation of the Euler equation in terms of the stream function and showing that the PV system's stream function satisfies it. We choose to recall this specific viewpoint because from it follows considerations on the self-interaction between vortices. Indeed, if we consider a initial condition for the vorticity of the form (1.17) and we focus on equation (1.15), we see that the singularity in the point vortices positions at time $t = 0$ cause the velocity field not to be properly defined. To avoid this problem, we have to neglect the contribution of the interaction between each vortex and itself. A rigorous treatment of this topic is done in [62, 61, 74], in the following we will only summarize the main ideas behind it.

First of all, we note that in computing the kinetic energy of the Point Vortex system, even for a single vortex, we encounter a divergence, namely the integral on the domain $\mathcal{D}$ of the squared velocity (the gradient of the Green function) is infinite. In particular, if the vortex is located in position $\mathbf{x_i}$, the integral diverges due to the contribution of that specific point. More specifically, the kinetic energy E on the domain $\mathcal{D}$ for a fluid of constant density where the vorticity consist in a single vortex of unitary strength in position $\mathbf{x_i}$ is given by the following expression:

$$E = \frac{1}{2}\rho \int_{\mathcal{D}} \mathbf{u}^2 = \frac{1}{2}\rho \int_{\mathcal{D}} \left(\nabla^{\perp}\psi\right)^2 = \frac{1}{2}\rho \int_{\mathcal{D}} |\sum_i \gamma_i \nabla^{\perp} G(\mathbf{x} - \mathbf{x_i}) + \psi_0|^2 \ ,$$

where we used the definition of the velocity field in terms of the stream function and the Green function of the system. Here, ψ_0 is the stream function of a stationary flow, as defined in [62], [61], harmonic on the domain $\mathcal{D}$. Clearly, this quantity diverges, due to the contribution of the point $\mathbf{x_i}$. The main idea of how to solve this problem is to isolate the divergency from the finite part of the energy. The infinite contribution is the same in every domain, while the remaining part is different, as it takes into account the contribution of the domain's boundary.

To obtain the Point Vortex model without the infinite contribution, the starting point in [62, 61] is the Euler equation in the velocity formulation (1.14); their goal is to formulate it in the form of residual integrals. The rigorous derivation is carried out in [74] with a different notation and formalism. Here, we will explicit some computations and manipulations following [62, 61]. In the following, we will consider a domain $\mathcal{D}$ with smooth boundary. The unbounded plane $\mathbb{R}^2$ is the sub-case with no boundary, while the torus $\mathbb{T}^2$ is a sub-case of the unbounded plane but where the Green function is the periodic solution to the Poisson equation (1.7).

We recall the Euler equation written in terms of the velocity field:

$$\frac{\partial \mathbf{u}}{\partial t} + (\mathbf{u}\cdot\nabla)\mathbf{u} + \frac{1}{\rho}\nabla P = 0$$

where the material derivative of the velocity has been written explicitly and the forcing term is taken to be equal to zero. Taking into account that we are considering a two-dimensional space, we can write $(\mathbf{u}\cdot\nabla)\mathbf{u}$ with the tensor index formalism:

$$(\mathbf{u}\cdot\nabla)\mathbf{u} = u_j\partial_j u_i = u_j\partial_j u_i - u_j\partial_i u_j + u_j\partial_i u_j$$

where we sum and subtract the quantity $u_j\partial_i u_j$. Using the properties of the Kronecker delta and the Levi-Civita symbol in two dimensions,

$$-(u_j\partial_j u_i - u_j\partial_i u_j) = (\partial_i u_j)u_j - (\partial_j u_i)u_j = (\delta_{im}\delta_{jn} - \delta_{in}\delta_{jm})(\partial_m u_n)u_j = (\varepsilon_{ij}\varepsilon_{mn})(\partial_m u_n)(u_j).$$

Rearranging the product,

$$-(u_j\partial_j u_i - u_j\partial_i u_j) = (\varepsilon_{mn}\partial_m u_n)(\varepsilon_{ij}u_j).$$

However, as we are focused on two-dimensional systems, the quantity above is just the vector $\omega(\mathbf{u}^{\perp})$. The remaining term can be rewritten as

$$u_j \partial_i u_j = \frac{1}{2} \partial_i u_j u_j$$

and finally we obtain for the Euler equation:

$$\partial_t \mathbf{u} + \frac{1}{2} \nabla |\mathbf{u}|^2 - \omega \mathbf{u}^\perp + \frac{1}{\rho} \nabla P = 0 \ .$$

If we now replace the velocity $\mathbf{u}$ with its expression in term of the stream function ψ, we obtain

$$\nabla^\perp (\partial_t \psi) + \frac{1}{2} \nabla |\nabla^\perp \psi|^2 + (\Delta \psi)(\nabla^\perp \psi)^\perp + \frac{1}{\rho} \nabla P = 0$$

where we exchanged temporal and spatial derivatives. Once again from the properties of the Kronecker delta and the Levi-Civita symbol in two dimensions, we have

$$\begin{aligned} |\nabla^\perp \psi|^2 &= (\varepsilon_{ij} \partial_j \psi)(\varepsilon_{ik} \partial_k \psi) = \delta_{jk} (\partial_j \psi)(\partial_k \psi) = (\partial_j \psi)(\partial_j \psi) = |\nabla \psi|^2 \\ (\nabla^\perp \psi)^\perp &= \varepsilon_{ij} (\varepsilon_{jk} \partial_k \psi) = -\varepsilon_{ji} \varepsilon_{jk} \partial_k \psi) = -\delta_{ik} \partial_k \psi = -\partial_i \psi = -\nabla \psi. \end{aligned}$$

The Euler equation then becomes

$$\nabla^\perp (\partial_t \psi) + \frac{1}{2} \nabla |\nabla \psi|^2 + (\Delta \psi)(-\nabla \psi) + \frac{1}{\rho} \nabla P = 0. \tag{1.18}$$

Following [62, 61, 74], we replace the Cartesian notation with a complex notation in terms of $z = x_1 + i x_2$ and its conjugate $\bar{z} = x_1 - i x_2$, obtaining two different equations for the new variables z and $\bar{z}$. The procedure to derive, for example, the equation for $\bar{z}$ is the following: we take the projection on $\hat{\mathbf{x}}_\mathbf{1}$ of equation (1.18) and we sum it to the projection of same equation on $\hat{\mathbf{x}}_\mathbf{2}$ multiplied by (i). Using the expressions for the partial derivatives in the complex notation,

$$\partial_1 = \partial_z + \partial_{\bar{z}}, \quad \partial_2 = i(\partial_z - \partial_{\bar{z}}),$$

we get

$$\begin{aligned} |\nabla \psi|^2 &= (\partial_1 \psi)^2 + (\partial_2 \psi)^2 = (\partial_z \psi + \partial_{\bar{z}} \psi)^2 - (\partial_z \psi - \partial_{\bar{z}} \psi)^2 = 4(\partial_z \psi)(\partial_{\bar{z}} \psi) \\ \Delta \psi &= (\partial_1 \partial_1 + \partial_2 \partial_2) = 4 \partial_z \partial_{\bar{z}}, \end{aligned}$$

The projection on the first and second coordinate of equation (1.18) are, respectively,

$$\partial_2 (\partial_t \psi) + \frac{1}{2} \partial_1 |\nabla \psi|^2 + (\Delta \psi)(-\partial_1 \psi) + \frac{1}{\rho} \partial_1 P = 0, \tag{1.19}$$

$$-\partial_1 (\partial_t \psi) + \frac{1}{2} \partial_2 |\nabla \psi|^2 + (\Delta \psi)(-\partial_2 \psi) + \frac{1}{\rho} \partial_2 P = 0. \tag{1.20}$$

The sum of equation (1.19) and equation (1.20) multiplied by i gives the following expression:

$$(-i\partial_1 + \partial_2)(\partial_t \psi) + \frac{1}{2}(\partial_1 + i\partial_2)|\nabla \psi|^2 + (\Delta \psi)(-(\partial_1 + i\partial_2)\psi) + \frac{1}{\rho}(\partial_1 + i\partial_2) P = 0 \ ,$$

which, in turn, can be expressed in terms of z and $\bar{z}$,

$$-2i\partial_{\bar{z}}\partial_t\psi + \partial_{\bar{z}}(4(\partial_z\psi)(\partial_{\bar{z}}\psi)) - 8(\partial_z\partial_{\bar{z}}\psi)\partial_{\bar{z}}\psi + 2\frac{1}{\rho}\partial_{\bar{z}}P = 0$$

Using the identities:

$$8(\partial_z\partial_{\bar{z}}\psi)\partial_{\bar{z}}\psi = 4\partial_z(\partial_{\bar{z}}\psi)^2$$
$$-2i\partial_{\bar{z}}\partial_t\psi + \partial_{\bar{z}}(4(\partial_z\psi)(\partial_{\bar{z}}\psi)) + 2\frac{1}{\rho}\partial_{\bar{z}}P = \partial_{\bar{z}}\left(-2i\partial_t\psi + (4(\partial_z\psi)(\partial_{\bar{z}}\psi)) + 2\frac{1}{\rho}P\right) ,$$

we rewrite the Euler equation in the form:

$$\partial_{\bar{z}}\left(-i\partial_t\psi + (2(\partial_z\psi)(\partial_{\bar{z}}\psi)) + \frac{1}{\rho}P\right) = 2\partial_z(\partial_{\bar{z}}\psi)^2. \tag{1.21}$$

In [62, 61], the idea is to rewrite this equation to obtain the equation of motion of the Point Vortex system,

$$\dot{z}_i = -2i\frac{1}{\gamma_i}\partial_{\bar{z}_i}E \tag{1.22}$$

where E is the renormalized kinetic energy,

$$E := \sum_{i,j,\ j>i}\gamma_i\gamma_j G(z_j, z_i) - \frac{1}{2}\gamma_i^2 t_{\mathcal{D}}(z_i), \tag{1.23}$$

where $t_{\mathcal{D}}(z_i)$ is the Robin function. To rewrite (1.21), we express it as the curl of a two-dimensional vector,

$$\mathbf{H} = \left(-i\partial_t\psi + (2(\partial_z\psi)(\partial_{\bar{z}}\psi)) + \frac{1}{\rho}P, 2(\partial_{\bar{z}}\psi)^2\right)$$

obtaining

$$\frac{\partial}{\partial\bar{z}}\left(-i\partial_t\psi + (2(\partial_z\psi)(\partial_{\bar{z}}\psi)) + \frac{1}{\rho}P\right) - \frac{\partial}{\partial z}\left(2(\partial_{\bar{z}}\psi)^2\right) = (\nabla\times\mathbf{H})\cdot\hat{\mathbf{x_3}} = 0$$

and we took the only non-zero component, the one along the $\hat{\mathbf{x_3}}$ axis. If $\mathcal{B}\subset\mathcal{D}$ is an arbitrary subdomain of $\mathcal{D}$, we can integrate on $\mathcal{B}$ the curl of H and apply the Stokes theorem, obtaining:

$$\begin{aligned}\int\int_{\mathcal{B}}\left(\frac{\partial}{\partial\bar{z}}\left(-i\partial_t\psi + (2(\partial_z\psi)(\partial_{\bar{z}}\psi)) + \frac{1}{\rho}P\right) - \frac{\partial}{\partial z}\left(2(\partial_{\bar{z}}\psi)^2\right)\right)d\bar{z}dz = \\ \int_{\partial\mathcal{B}}\left(-i\partial_t\psi + (2(\partial_z\psi)(\partial_{\bar{z}}\psi)) + \frac{1}{\rho}P\right)dz + \int_{\partial\mathcal{B}}\left(2(\partial_{\bar{z}}\psi)^2\right)d\bar{z} = 0\end{aligned} \tag{1.24}$$

As we took an arbitrary subdomain $\mathcal{B}\subset\mathcal{D}$, we assume that there are no vortices on the boundary of this subdomain. We recall equations (1.8) and (1.9), which expressed the Green function of a generic domain, computed for two generic points $\mathbf{p_1}, \mathbf{p_2}$, as the sum of the Green function on an unbounded plane plus a regular part, $f\in\mathcal{D}\times\mathcal{D}$, a smooth function, which is zero if the domain in consideration is the full plane. We also recall the decomposition of f near the singularity, namely $f(\mathbf{p_1},\mathbf{p_2}) = -t_{\mathcal{D}}(\mathbf{p_1}) + O(|\mathbf{p_1}-\mathbf{p_2}|)$. Exploiting this relation, we obtain the following expression for the stream function:

$$\psi = -\frac{1}{2\pi}\sum_i\gamma_i\log|z - z_i(t)| + \sum_i\gamma_i f(z, z_i(t)).$$

We drop the time dependence and compute $\partial_z\psi$ and $(\partial_z\psi)^2$:

$$\begin{aligned}\partial_z\psi &= -\frac{1}{2\pi}\sum_i \gamma_i \partial_z \log|z-z_i| + \sum_i \gamma_i \partial_z f(z,z_i)\\ &= -\frac{1}{4\pi}\sum_i \gamma_i \frac{1}{z-z_i} + \sum_i \gamma_i \partial_z f(z,z_i)\end{aligned}$$

$$\begin{aligned}(\partial_z\psi)^2 = \left(\sum_i \gamma_i \left(-\frac{1}{4\pi}\frac{1}{z-z_i} + \partial_z f(z,z_i)\right)\right)^2 &= \sum_i \gamma_i^2 \left(-\frac{1}{4\pi}\frac{1}{z-z_i} + \partial_z f(z,z_i)\right)^2\\ + \sum_i \sum_{j\neq i} \gamma_i\gamma_j \left(-\frac{1}{4\pi}\frac{1}{z-z_i} + \partial_z f(z,z_i)\right)&\left(-\frac{1}{4\pi}\frac{1}{z-z_j} + \partial_z f(z,z_j)\right)\end{aligned}$$

At the same time,

$$\begin{aligned}\partial_{\bar z}\psi &= -\frac{1}{2\pi}\sum_i \gamma_i \partial_{\bar z} \log|z-z_i| + \sum_i \gamma_i \partial_{\bar z} f(z,z_i)\\ &= -\frac{1}{4\pi}\sum_i \gamma_i \frac{1}{\bar z-\bar z_i} + \sum_i \gamma_i \partial_z f(z,z_i)\end{aligned}$$

$$\begin{aligned}(\partial_{\bar z}\psi)^2 = \left(\sum_i \gamma_i \left(-\frac{1}{4\pi}\frac{1}{\bar z-\bar z_i} + \partial_{\bar z} f(z,z_i)\right)\right)^2 &= \sum_i \gamma_i^2 \left(-\frac{1}{4\pi}\frac{1}{\bar z-\bar z_i} + \partial_{\bar z} f(z,z_i)\right)^2\\ + \sum_i \sum_{j\neq i} \gamma_i\gamma_j \left(-\frac{1}{4\pi}\frac{1}{\bar z-\bar z_i} + \partial_{\bar z} f(z,z_i)\right)&\left(-\frac{1}{4\pi}\frac{1}{\bar z-\bar z_j} + \partial_{\bar z} f(z,z_j)\right)\end{aligned}$$

As for the partial derivative of ψ with respect to time, we have

$$\begin{aligned}\partial_t\psi &= -\frac{1}{2\pi}\sum_i \gamma_i \partial_t \log|z-z_i| + \sum_i \gamma_i \partial_t f(z,z_i)\\ &= \frac{1}{4\pi}\sum_i \gamma_i \frac{\dot z_i}{z-z_i} + \frac{1}{4\pi}\sum_i \gamma_i \frac{\dot{\bar z}_i}{\bar z-\bar z_i} + \sum_i \gamma_i \partial_t f(z,z_i)\end{aligned}$$

We now have

$$-i\partial_t\psi + 2(\partial_z\psi)(\partial_{\bar z}\psi) + \frac{1}{\rho}P = 2(\partial_z\psi)(\partial_{\bar z}\psi) + \frac{1}{\rho}P + i(\partial_t\psi),$$

where we wrote the same quantity in a different fashion, to emphasize that the first two terms represent the real part of the function, while $i(\partial_t\psi)$ is the imaginary part. This follows from the fact that the stream function ψ is defined as $\psi : \mathbb{C} \to \mathbb{R}$, so it is a real function, and the combination of its derivatives $(\partial_z\psi)(\partial_{\bar z}\psi)$ can be written as:

$$(\partial_z\psi)(\partial_{\bar z}\psi) = \frac{1}{4}\left((\partial_x - i\partial_y)\psi\right)\left((\partial_x + i\partial_y)\psi\right) = \frac{1}{4}\left(\partial_x\psi\partial_x\psi + \partial_y\psi\partial_y\psi\right) = \frac{1}{4}\left((\partial_x\psi)^2 + (\partial_y\psi)^2\right)$$

which is again real. We recall that our aim is to simplify relation (1.24). To do so, we make some manipulations on the partial time derivative of the stream function. In particular, it holds

$$\frac{\dot z_i}{z-z_i} + \frac{\dot{\bar z}_i}{\bar z-\bar z_i} = 2\ \mathrm{Re}\left(\frac{\dot z_i}{z-z_i}\right).$$

From the definition of f, $\partial_t f(z, z_i)$ is an holomorphic function. Then, for the partial time derivative of the stream function, we have:

$$\partial_t \psi = \frac{1}{4\pi} \sum_i \gamma_i \frac{\dot{z_i}}{z - z_i} + \frac{1}{4\pi} \sum_i \gamma_i \frac{\dot{\bar{z}}_i}{\bar{z} - \bar{z_i}} + \sum_i \gamma_i \partial_t f(z, z_i) = \mathrm{Re}\,(g)$$

where the function g is holomorphic too, in an open set $\mathcal{B} \setminus \{z_i, i = 1 \cdots N\}$ where there are no vortices. Then:

$$\mathrm{Re}\left(i \left(-i\partial_t \psi + 2(\partial_z \psi)(\partial_{\bar{z}} \psi) + \frac{1}{\rho} P \right) \right) = \mathrm{Re}\,(g)$$

again on $\mathcal{B} \setminus \{z_i, i = 1 \cdots N\}$, so

$$\mathrm{Re}\left(i \left(-i\partial_t \psi + 2(\partial_z \psi)(\partial_{\bar{z}} \psi) + \frac{1}{\rho} P \right) - g \right) = 0 \tag{1.25}$$

From [14], if a function $h : \Omega \to \mathbb{C}$ is holomorphic and its real part is zero on Ω, then $h = ic$ where c is a constant and $\arg g = \pi/2$. We define the function h as

$$h = i \left(-i\partial_t \psi + 2(\partial_z \psi)(\partial_{\bar{z}} \psi) + \frac{1}{\rho} P \right) - g,$$

and we have that

$$i \left(-i\partial_t \psi + 2(\partial_z \psi)(\partial_{\bar{z}} \psi) + \frac{1}{\rho} P \right) - g = ic_1 + c_2.$$

The real part of h, the constant c_2, is however zero, from (1.25), so for the function h it holds:

$$i \left(-i\partial_t \psi + 2(\partial_z \psi)(\partial_{\bar{z}} \psi) + \frac{1}{\rho} P \right) - g = ic_1,$$

Then, we can apply the Residue theorem to the first integral in (1.24):

$$\int_{\partial \mathcal{B}} \left(-i\partial_t \psi + (2(\partial_z \psi)(\partial_{\bar{z}} \psi)) + \frac{1}{\rho} P \right) dz = 2\pi i \; 2i \frac{1}{4\pi} (-1) \sum_{z_i \in \mathcal{B}} \gamma_i \dot{z}_i = \sum_{z_i \in \mathcal{B}} \gamma_i \dot{z}_i. \tag{1.26}$$

What is left is to compute the second integral in (1.24). Its conjugate can be expressed as

$$2 \overline{\int_{\partial \mathcal{B}} (\partial_{\bar{z}} \psi)^2 d\bar{z}} = 2 \int_{\partial \mathcal{B}} (\partial_z \psi)^2 dz$$

Moreover,

$$\overline{i \partial_{\bar{z}_i} E} = i \partial_{z_i} E,$$

as E is a real function, so if we show that

$$\int_{\partial \mathcal{B}} \left(2(\partial_z \psi)^2 \right) dz = -2i \sum_{z_i \in \mathcal{B}} \gamma_i \partial_{z_i} \left(\sum_{j \neq i} \gamma_j G(z_i, z_j) - \frac{1}{2} \gamma_i t_{\mathcal{D}}(z_i) \right) \tag{1.27}$$

holds, then we obtain (1.22) by taking the complex conjugate. Note that in equation (1.27) we have substituted the expression for E. We already computed

$$\begin{aligned} (\partial_z \psi)^2 = &\sum_i \left(\frac{1}{16\pi} \gamma_i^2 \frac{1}{(z - z_i)^2} - \gamma_i^2 \frac{1}{2\pi} \frac{1}{(z - z_i)} \partial_z f(z, z_i) - \gamma_i^2 (\partial_z f(z, z_i))^2 \right) \\ &+ \sum_i \sum_{j \neq i} \gamma_i \gamma_j \partial_z G(z, z_i) \partial_z G(z, z_j) \end{aligned}$$

We now want, once again, to use the Residue theorem. The squared terms (the first and the third terms) have zero residues, while for the remaining ones we have

$$\mathrm{Res}\left(-\gamma_i^2\frac{1}{2\pi}\frac{1}{(z-z_i)}\partial_z f(z,z_i),z_i\right)=\gamma_i^2\frac{1}{2\pi}\partial_z f(z_i,z_i)$$

$$\begin{aligned}\mathrm{Res}\left(\sum_{j\neq i}\gamma_i\gamma_j\partial_z G(z,z_i)\partial_z G(z,z_j),z_i\right)&=2\sum_{j\neq i}\gamma_i\gamma_j\partial_{z_i}G(z_i,z_j)\mathrm{Res}\left(\partial_z G(z,z_i),z_i\right)\\&=2\sum_{j\neq i}\gamma_i\gamma_j\partial_{z_i}G(z_i,z_j)\mathrm{Res}\left(\frac{1}{2\pi}\partial_z\log|z-z_i|,z_i\right)\\&=-2\frac{1}{4\pi}\sum_{j\neq i}\gamma_i\gamma_j\partial_{z_i}G(z_i,z_j)\end{aligned}$$

Finally,

$$\int_{\partial\mathcal{B}}\left(2(\partial_z\psi)^2\right)dz=-2i\sum_{z_i\in\mathcal{B}}\gamma_i\partial_{z_i}\left(\frac{1}{2}\sum_{j\neq i}\gamma_j G(z_i,z_j)-\frac{1}{2}\gamma_i t_{\mathcal{D}}(z_i)\right)$$

In the end, putting together (1.26) and (1.27), we obtain a derivation of the Point Vortex system from the Euler equation; we note that, in this derivation, the auto-interaction term is automatically excluded from the Hamiltonian of the Point Vortex system, as it should; this implies that all the quantities to compute are finite.

1.3 Conservation laws

In order to determine the conserved quantities of the Point Vortex system, we have to apply Noether's theorem: for every continuous symmetry of the action of a system, a conservation law holds. The Point Vortex system's Hamiltonian possesses various symmetries, depending on what the domain $\mathcal{D}$ considered is. In the following discussion, we will make use of the complex notation as in [107] and we start by considering the Hamiltonian of the Point Vortex system on an unbounded plane $\mathbb{R}^2$, as in (1.4). This Hamiltonian is invariant to translations of all the vortices centers, $z_i \to z_i + a$ and also to global rotations $z_i \to e^{i\phi}z_i$. Moreover, we also mention invariance under time translation, which corresponds the conservation of the Point Vortex Hamiltonian.

We explicitly write the linear momentum, integral of motion for the Point Vortex system, which is also preserved on the torus and is due to invariance under translations in space.

$$\mathbf{M}=\sum_{i=1}^{N}\gamma_i\mathbf{x}_i\ .$$

where we indicate with $\mathbf{x}_i$ the vortices coordinates.

A definition of integral of motion can be given in the Poisson brackets formalism. If we take two functions $f(z_i,t), g(z_i,t)\in C^1$, defined on the $2N$ dimensional phase space, the canonical Poisson brackets are defined as:

$$\{f,g\}=\sum_{i=1}^{N}\left(\frac{\partial f}{\partial z_i}\frac{\partial g}{\partial \bar{z}_i}-\frac{\partial f}{\partial \bar{z}_i}\frac{\partial g}{\partial z_i}\right)$$

and it holds

$$\frac{df}{dt} = \{f, H\} + \frac{\partial f}{\partial t}.$$

If the function f does not depend explicitly on time and its Poisson bracket with the Hamiltonian vanishes, then it is an integral of motion of the system, i.e. it is conserved. Note that those integrals of motion are not in *mutual involution*, as their Poisson brackets are not mutually zero.

The *Liuville-Arnold theorem* gives a condition for a system's integrability: if in a Hamiltonian system with N generalized coordinates N integrals of motions K_α exists and are independent, with $\{K_\alpha, K_\beta\} = 0 \ \forall(\alpha, \beta)$, the system is integrable. This condition is necessary and sufficient to ensure the system's integrability. For a nice discussion of this topic, one may consult [32]. Regarding the integrability of the Point Vortex system, the three-vortex problem is integrable, while it is possible to prove the non-integrability of the four-vortex problem. The integrability of the Point Vortex system is discussed in details in [107].

1.3.1 Invariant measures and equilibrium states

The long time behavior of the fluid (or, in our case, of the Point Vortex model seen as a discretization of the Euler equation) can be investigated by studying the equilibrium states of the system, the *invariant measures*. We stress that *singular configurations*, namely configurations where there is collapse of the vortices, are a negligible set of phase space with respect to absolutely continuous invariant measures of the system. In particular, the dynamics is well-posed for almost all initial configurations, see [35]. More details on this topic will be given in chapter 6. Focusing on the equilibrium states of the system, another important consequence of the Point Vortex system being an Hamiltonian system is that volumes of the phase space are conserved, due to Liouville's theorem. The *volume* (Lebesgue) *measure* $dx_1 \cdots dx_N$ of $\mathbb{T}^{2N}$ is preserved by the dynamics: a distribution of PVs at independent uniform random positions is an equilibrium state of the system. A study on the volume measure as the distribution for the initial condition of a system of point vortices will be described in chapter 6, and more details will be given.

We recall another invariant measure of the system, the *canonical Gibbs measure* for the vortex model,

$$\frac{1}{Z} e^{-\beta H} dx_1 \cdots dx_N$$

which is an invariant measure for the Euler flow. We also recall that flows of two-dimensional Euler equations preserving the Gaussian *enstrophy measure* (white noise)

$$\frac{1}{Z} e^{-\gamma S} d\omega \ , \quad S = \frac{1}{2} \int_{\mathbb{T}^2} \omega^2(\mathbf{x}) d\mathbf{x}$$

can be obtained as limit of PV system; in this equation, we indicate with S the enstrophy. We note that fixing enstrophy is equivalent to fixing the number of vortices N, and correspond to the **canonical ensemble**. When the energy, the Hamiltonian of the system, (H) is also fixed, the ensemble under consideration is the **micro-canonical ensemble**. In chapter 6 and in the work [68], we are interested in fixing only the enstrophy, however we focus on the study of the invariant volume measure, which is not the appropriate ensemble to describe turbulent fluid behavior. Finally, we recall that a distribution of point vortices at independent uniform random positions on a torus converges to white noise (Gaussian measure) for $N \to \infty$, if intensities scale as $\gamma_i \sim \gamma/\sqrt{N}$, as a consequence of the Central Limit Theorem, see for example [48]. More details on invariant measures will be given in chapter 6.

1.3.2 Energy spectrum

An observable which is often used to study the behavior of a fluid is the energy spectrum; in particular, it is possible to investigate the so-called phenomena of *energy cascade*, the transfer of energy from large to small scales or vice-versa. We want to compute the energy spectrum of a system of point vortices. We start from the energy spectrum of the velocity, written in Fourier space:

$$E(k) = \pi k \langle |(\mathbf{u}(\mathbf{k}))|^2 \rangle$$

where the average is over all $|\mathbf{k}| = k$. Then, $\hat{\omega}(\mathbf{k})$ can be obtained from the Fourier transform of the velocity, $\hat{\mathbf{u}}(\mathbf{k})$, by making use of (1.12):

$$\hat{\omega}(\mathbf{k}) = |i\mathbf{k} \times \hat{\mathbf{u}}(\mathbf{k})|; \quad |\hat{\mathbf{u}}(\mathbf{k})|^2 = \frac{1}{k^2}|\hat{\omega}(\mathbf{k})|^2$$

The vorticity for a system of N point vortices is written as

$$\omega(\mathbf{x}) = \sum_{i=1}^{N} \Gamma_i \delta(\mathbf{x}_i - \mathbf{x}),$$

where $\mathbf{x}_i = (x_{1,i}, x_{2,i})$ are the positions of the vortices. The Fourier transform of the vorticity is then

$$\begin{aligned} \hat{\omega}(\mathbf{k}) &= \frac{1}{2\pi} \int \sum_{i=1}^{N} \Gamma_i \delta(\mathbf{x}_i - \mathbf{x}) e^{i\mathbf{k}\mathbf{x}} dx_1 dx_2 \\ &= \frac{1}{2\pi} \sum_i \Gamma_i e^{i\mathbf{k}\mathbf{x}^{(i)}} \end{aligned}$$

We specialize to the case of $\mathcal{D} = \mathbb{R}^2$, so the Fourier transform of the vorticity can be obtained by integrating over the full plane, obtaining:

$$|\hat{\omega}(\mathbf{k})|^2 = \frac{1}{(2\pi)^2} \left(\sum_i \Gamma_i^2 + 2 \sum_{i<j} \Gamma_i \Gamma_j \cos\left(\mathbf{k}(\mathbf{x}^{(i)} - \mathbf{x}^{(j)})\right) \right).$$

On the torus $\mathbb{T}^2$, the computation of the energy spectrum yields a different result. If we consider the doubly periodic domain $[-1, 1] \times [-1, 1]$, the wavevectors are $\mathbf{k} = \mathbf{k}_{m,n} = (m, n)$, with the pair $(m, n) \in \mathbb{Z}_0^2$. The Fourier coefficients $\omega_{m,n}(\mathbf{k})$ are given by the following expression:

$$\omega_{m,n}(\mathbf{k}) = \frac{1}{2\pi} \int_{-1}^{1} \int_{-1}^{1} \omega(\mathbf{x}) e^{i\mathbf{k}_{m,n}\cdot\mathbf{x}} dx_1 dx_2 = \frac{1}{2\pi} \sum_{i=1}^{N} \Gamma_i e^{i(m x_1^{(i)} + n x_2^{(i)})}.$$

and, in the same fashion as the plane case, we obtain

$$|\hat{\omega}(\mathbf{k})|^2 = \frac{1}{(2\pi)^2} \left(\sum_i \Gamma_i^2 + 2 \sum_{i<j} \Gamma_i \Gamma_j \cos(m(x_1^{(i)} - x_1^{(j)}) + n(x_2^{(i)} - x_2^{(j)})) \right).$$

Chapter 2

Numerical methods

In this chapter, we summarize the numerical methods used to solve SDEs, PDEs and ODEs, together with procedures employed for statistical analysis of data. In the following chapters, 5 and 6, we will make frequent use of numerical methods to study the Point Vortex model, both in its standard form and also its stochastic modifications. Moreover, we will solve a grid-discretized PDE in chapter 4. For this reason, this chapter will be devoted to the explanation and check of the various numerical methods employed. As a first step, we will describe the algorithm used to simulate the Point Vortex model in [59], see the related code [106]. Then, we will briefly explain how we solved a grid-discretized PDE, as done in the work [13] and the related code [12]. Finally, we will explain how the statistical analysis of data was performed to compute the various observables investigated in [68, 13, 58].

2.1 Time integration

To get an approximate solution for the ODEs of the point vortex model, we need to solve simultaneously all the N equations up to high precision. In this thesis, we will employ for the most part explicit iterative methods, the Runge-Kutta methods, to integrate the point vortices ODEs in time. On the other hand, we only need to employ the improved Euler's method (also called Heun's method) to solve SDEs. The influence of the noise on the integration procedure will be discussed in the following.

2.1.1 Runge-Kutta method for ODE

In the following, we will briefly describe the Runge-Kutta method, see [112] for a detailed description. We will follow the notation of [112]. The Runge-Kutta method allows us to obtain a numerical approximation for an ordinary differential equation discretized in time, in an interval, by combining results from different application of Euler's method to match a Taylor expansion to some chosen higher order. We will focus as an example on RK4 method, i.e. the Runge-Kutta method of order four, the one which will be used the most in the numerical simulations, for example in the paper [68]. A fourth-order method has a local truncation order of $\mathcal{O}(dt^5)$, where we indicated with dt the timestep. The total error is of order $\mathcal{O}(dt^4)$. This method is explicit; the general N-order

Runge-Kutta method is designed to solve the differential equation

$$\frac{dy}{dt} = f(t, x, y)$$

and its discretization takes the general form:

$$y_{n+1} = y_n + h \sum_{i=1}^{N} b_i k_i$$

The fourth-order Runge-Kutta can be formulated in terms of four different evaluations of the function, for each timestep h. The full formula is reported below:

$$\begin{aligned} k_1 &= hf(x_n, y_n) \\ k_2 &= h\left(x_n + \frac{1}{2}h, y_n + \frac{1}{2}k_1\right) \\ k_3 &= h\left(x_n + \frac{1}{2}h, y_n + \frac{1}{2}k_2\right) \\ k_4 &= h\left(x_n + h, y_n + k_3\right) \\ y_{n+1} &= y_n + \frac{k_1}{6} + \frac{k_2}{3} + \frac{k_3}{3} + \frac{k_4}{6} + O(h^5) \end{aligned}$$

This algorithm is employed to discretize the equation of motions of a system of N point vortices, in the paper [68] and in chapter 6.

2.1.2 Heun's method for SDE

This method is also known as improved or modified Euler method; it is a *predictor-corrector* method which can be also used to approximate ODEs, however, in this thesis and in the works [59, 58] (and the code [106]) we employed this algorithm to approximate SDEs, as we are interested in studying stochastic modifications of the Point Vortex model. In the following, we will adopt the notation from [95] and follow its discussion. Predictor-corrector methods are a class of methods which compute and store the solution; this result is then used to extrapolate the solution at the next step. Finally, the resulting extrapolation is corrected by means of results at the next discretization step, see [112] for more details. In this paragraph, we will use the notation

$$dW_t = \xi(t)dt \tag{2.1}$$

with ξ Gaussian, zero-mean and delta-correlated in time. The Heun method employs a predictor of order zero and a corrector of order one. To integrate the stochastic differential equation

$$dx = f(x)dt + g(x) \circ dW \ ,$$

which employs the Stratonovich calculus, we cannot use directly the Euler method for SDE as we will in the case of the Itô calculus. More precisely, the Itô SDE

$$dx = f(x)dt + g(x)dW \ ,$$

can be discretized via the Euler method,

$$x_{n+1} = x_n + f(x_n)h + g(x_n)\sqrt{h}\ \Delta W_n$$

with random variables $\Delta W_n \sim N(0,1)$ independent and identically distributed. However, for the case of a SDE written in the Stratonovich we would have to explicitly write the Itô-Stratonovich term. This is not necessary if we employ a predictor-corrector method like the Heun method, as in this case the Stratonovich calculus is automatically implemented. The full formula for the Heun method is reported below:

$$\tilde{x}_{n+1} = x_n + f(x_n)h + g(x_n)\sqrt{h}\ \Delta W_n$$
$$x_{n+1} = x_n + \frac{1}{2}\left(x_n + \tilde{x}_{n+1}\right) + \frac{1}{2}\left(g(x_n) + g(\tilde{x}_{n+1})\right)\sqrt{h}\ \Delta W_n$$

See [95, 96] for a thorough discussion on why higher order methods could be less suitable to solve SDEs. See [85] for an extensive analysis of various methods of solutions of SDEs.

2.1.3 Other possibilities

Both the Runge-Kutta algorithm and the implicit Euler algorithm can be used in combination with an *adapted timestep* technique: the timestep is halved (or reduced with some criterion) inside the algorithm if some condition is not met, for example if some quantities computed during the simulation are not conserved up to a chosen tolerance.

Another possibility is to apply *symplectic* algorithms which guarantee the conservation of one or more quantities. The simplest option is the *symplectic Euler*; to apply more sophisticated methods, the Hamiltonian of the system needs to be separable, i.e. it has to be possible to split it in a kinetic part and a potential part. A nice discussion on symplectic methods for separable Hamiltonian can be found in [34]. However, the Point Vortex model Hamiltonian is not separable, so those kind of methods are not available. A tentative of adapting the symplectic algorithm presented in [122] has been done in the progress of drafting the paper [68], however it has not been reported in this thesis as in the end the standard high precision Runge-Kutta methods were chosen.

2.2 Algorithms for integration of PDE in space

In this thesis, the Point Vortex model, both with and without stochastic modifications, will be investigated. The most relevant stochastic modification, which will be summarized in chapter 3, is to add to the vortices dynamics an enviromental noise, namely an advection by stochastic vector field. In order to understand this stochastic modifications, in chapter 4 and in the work [13] the noise added to the vortices dynamics will be investigated in the context of a stochastic advection-diffusion equation for a passive scalar; this SPDE will be in turn investigated via a homogenization procedure. This will consist in numerically solve a so called *cell equation*, a linear system.

In order to do so, we need to employ different techniques from numerical analysis. In particular, we will focus on the iterative method GMRES, which was used together with the standard direct method implemented in MATLAB. In the end, the work [13] reports only results for the MATLAB direct method implementation, but compatibility with the GMRES method results were checked. The scope and application of the GMRES method in the context of this study is briefly explained below. For an outline of iterative methods currently used to solve large systems, the context and their scope, see the detailed review [116] or the book [115].

In this thesis, we will solve the linear system

$$T\phi = b\ ;$$

where T is a matrix, which will be specified in chapter 4 together with ϕ and the right hand side b. We recall that the size of the matrix T is $n^2 \times n^2$, where n is the number of gridsteps in the $n \times n$ grid which is used to discretize the $[0,1]^2$ domain. Typical values of n employed in numerical simulations are in the range $n = 100$, $n = 800$. For some of this values, T becomes a very large, ill conditioned matrix; it is also a sparse, diagonally dominant matrix, however the variety of parameters does not guarantee that the diagonally dominant property remains valid throughout the simulations. Iterative solvers are usually favored over direct solvers (Gaussian elimination), due to the very high memory requirements of the latter, hence we employed an iterative method.

2.2.1 GMRES method

We consider for the sake of simplicity the square linear system $Ax = b$. The $n-th$ Krilov subspace for the vector $r_0 = b - Ax_0$ is defined as:

$$K_N = \text{span}\{r_0, Ar_0, \dots, A^{n-1}r_0\} \ . \tag{2.2}$$

The iterative method GMRES produces an approximate solution $x_n \in x_0 + K_n$ for the linear system $Ax = b$, with x_0 initial guess. This approximate solution is such that the Euclidean norm of $b - Ax_n$ is minimized. If we take a generic vector $y_n \in \mathbb{R}^n$, it is more convenient to express x_n as

$$x_n = x_0 + Q_n y_n \ , \tag{2.3}$$

where Q_n is a matrix of column vectors $q_1, \dots q_n$, orthonormal basis for K_n with $q_1 = \|r_0\|_2^{-1} r_0$. Those vectors are constructed via Arnoldi iteration and they are the preferred choice over the basis (2.2), as the latter have the drawback of possibly being almost linearly dependent. The Arnoldi iteration also allows to rewrite AQ_n as:

$$AQ_n = Q_{n+1} H_n$$

where H_n is a $(n+1) \times n$ upper Heissenberg matrix.

Rewriting x_n as (2.3) reduces the problem to the one of finding y_n; this vector minimizes the Euclidean norm of the residual $b - Ax_n$, as the latter can be rewritten in terms of y_n:

$$\|b - Ax_n\| = \|r_0 - AQ_n y_n\| = \|\alpha q_1 - AQ_n y_n\|.$$

where to avoid confusion we write $\alpha = \|r_0\|_2$.

Using the definition of H_n in (2.2.1), we obtain a linear least square problem:

$$\|b - Ax_n\| = \|\alpha q_1 - Q_{n+1} H_n y_n\| = \|Q_{n+1}(\alpha e_1 - H_n y_n\|),$$

in which we denote with e_k a vector of the canonical basis. After finding y_n, we can compute x_n via (2.3) and check the residual: if it is less than a tolerance threshold, the approximation computed is the final one, otherwise the process can be repeated to find x_{n+1}.

In the code [12], the two options *fillfactor* and *restart* are employed: the first one fills the matrix by a factor which can be indicated in the input file; the second one restarts the algorithm after a certain number of iterations.

Preconditioning

To efficiently solve a system with the GMRES method, we employ a precondition method; namely, by preconditioning the matrix T we apply a transformation to it. The goal of this operation is to reduce the matrix's condition number, producing a new form for the original problem, more convenient for numerical simulations. Finally, the system is solved via another method (usually, an iterative method, in our case the GMRES method itself). There are different kinds of preconditioning methods, the one employed in our case is the ILU (incomplete LU) preconditioning, a sparse approximation of the LU factorization.

2.3 Statistical analysis of data

In this thesis, there will be frequently sources of stochasticity in the computation of the observables of interest; for this reason, it will be necessary to perform a statistical analysis of the data that are produced by our numerical simulations, see for example the works [13, 68]. More information on this topic can be found in the very detailed lecture notes [10] and in the references therein.

Some of the cases that will be considered will be random initial conditions of the vortices positions, sampled from a probability distribution (usually the vortex are *iid* in some subset of the considered domain), or the addition of a noise of some form to the equation of motion of the vortex centers. We consider for example the first case: at time zero, we want to compute the expectation value of the observable O, which is a function of the vortex positions $\mathbf{x}_j$. The vortex positions at time $t = 0$ are a set of stochastic variables with some *pdf*; the expectation value of the observable $\langle O \rangle$ can then be written as a mean computed on N different configurations $\{X_i\}$ of point vortex, generated by means of Montecarlo methods,

$$\langle O \rangle = \frac{1}{N} \sum_{i=1}^{N} O(\{X_i\}) + \mathcal{O}\left(\frac{1}{\sqrt{N}}\right)$$

and in the limit $N \to \infty$ the mean of O computed on the different N configurations converges to the expectation value of the operator of interest. After $t = 0$, the positions of the vortices evolve with their corresponding Hamilton equation; the computation of the observables at different times follows this evolution. Another way to compute mean values of observables without taking into account the evolution of the point vortex positions is to decide that their distribution is stationary in time and use the technique of *importance sampling*. In the context of the point vortex model, this approach is followed especially for sampling *negative temperature* states; some more details will be given in the last chapter and in the conclusion as this kind of investigation is a natural extension of some of the work of this thesis, namely chapter 6 and the paper [68].

Statistical independence

After computing the values of the observable for different $t = t_1, t_2, \ldots$, we have to evaluate the uncertainties, i.e. the errors of our numerical estimations. There are two possibilities: the different measures can be statistically independent, or be correlated. In particular, it is of the utmost importance to ensure that any correlation is taken into account in the error estimate. To avoid complications, the best practice is to avoid correlations between the different measures at different times as much as possible. To ensure independence of the mean values of the observable computed at

different times, we choose to perform every computation $\langle O(t) \rangle$ for each different t from a different set of configurations, thus eliminating correlations between the measures at times t_i. A drawback of this procedure is that we have to perform a huge number of numerical simulations, as if we want to compute $\langle O \rangle$ by simulating n different configurations and measure k different times, the number of different configurations needed is nk.

2.3.1 Estimate of errors of secondary quantities

When estimating the error associated to the measures of the observable O in consideration, we have to be careful if the quantities estimated are not directly computed from the configurations $\{X_i\}$ as mean values (i.e. *primary quantities*): they can be function of those primary quantities themselves (*secondary quantities*). In this case, it is not possible to simply exploit propagation of error rules to estimate the uncertainty on the measures: one has to resort to more refined methods to avoid *bias* on the estimators. In this thesis, we applied the *bootstrap* method and the *jackknife* method. We refer to [10] for a detailed discussion on this methods, its application and other alternatives and perspectives; here, we will only briefly explain the two methods and the contest they where employed in.

Bootstrap

The idea of the bootstrap procedure to estimate the variance of an estimator (in this case, the sample mean of the observable) is to mimic the estimation of the sample variance from k different groups of N samples each. From each group of sample, the mean of the observable is computed and the variance is estimated as

$$\overline{\sigma}^2_{\overline{O}} = \frac{k}{k-1} \left(\frac{1}{R} \sum_{i=1}^{k} \left(\overline{O}^{(i)} \right)^2 - \left(\frac{1}{k} \sum_{i=1}^{k} \overline{O}^{(i)} \right)^2 \right)$$

where we indicated with $\overline{O}$ the sample mean of the observable computed on the k-th group of samples. In our case, the k different groups of samples will not come from numerical simulations, but it will be artificially put together by resampling from the original sample. What we would like to achieve is, in some sense, to approximate the probability distribution function of the original sample with an empirical distribution of samples randomly drawn from it. Those new samples will be drawn with replacement and each drawn will have an uniform probability distribution function. To compute secondary observables, we need to evaluate the primary observables needed by using the same bootstrap sample, otherwise it would not be possible to take into account correlations between observables (and for example, in the last chapter (6) temporal correlations are the quantities that we want to investigate).

Jackknife

In a similar fashion, also the Jackknife is used to mimic the estimator of the sample variance from different groups of samples. However, the groups of samples are constructed via an algorithm and not from random extraction; more precisely, they are build in the following way: each new sample is made by removing one (or more) elements, so that in the end the number of artificially generated groups is $N - 1$ if we removed only one element at a time, or $N - k$ if we removed a block of k

elements at a time. In this way, N estimates of the original quantities are produced,

$$O_{jack,i} = \frac{1}{N-k}\sum_{j\neq i} O(x_i), \quad j = 1, \dots, N$$

and the variance becomes

$$\overline{\sigma}^2_{\overline{O}} = \frac{N-k}{N}\sum_{i=1}^{N/k}\left(\overline{O}^{(i)} - \overline{O}_J\right)^2$$

where $\overline{O}_J$ is the mean of the the sample of the N estimates. In [13] and in the corresponding chapter 4, the jackknife was also employed to correct the bias of the estimators of fit parameters, here indicated with $\overline{O}$. The fit was computed different times, each time removing k points from the interval, and then the bias corrected jackknife estimator was expressed as

$$\overline{O}^*_J = N\overline{O} - (N-k)\overline{O}_J$$

In the case under consideration, we have only one sample to estimate the quantity $\overline{O}$.

2.4 The torus domain: Green function approximations

In this final section of the chapter, we will introduce the problem of numerically approximating the Green function of the Point Vortex model, which will be tackled many times in this thesis. We focus on the torus domain, as it is the domain we investigate in this thesis, and we will discuss how to rewrite the Green function of the torus, (1.7), or how to approximate it, in order to be able to use the resulting expression in numerical simulations. First of all, we recall that every observable computed on the torus, for example the vorticity of the fluid, has to have zero mean. We now move to the discussion on Green function. When working on the torus $\mathbb{T}^2$, as done in most of the numerical simulation of this thesis, one should in principle use in the computations the Green function (1.7) and, consequently, the corresponding Hamiltonian. However, we are interested in the most efficient way of approximating the Green function, as in this thesis for the most part we will be focused on studying the behavior of large systems of point vortices (i.e. large N), and the use of the orthogonal derivative of (1.7) at each step of the numerical integration of the ODEs requires either a very aggressive sum truncation or expensive computations.

First approximation: from two sums to one

We note that in (1.7) a double sum is present: an important simplification can be made to reduce the computations needed to just one sum. In the following, we will refer to [124] for a more extensive treatment. To perform an approximation of the Green function on the torus, we start by noting that to write the dynamics on a two-dimensional domain with periodic boundary conditions, one has to take into account the contribution of the image vortices, which are infinite. To be consistent with the notation exploited in [124], we consider a domain with one-dimensional length 2π. In that work, the Green function (more precisely, the Hamiltonian of the Point Vortex system) is obtained from the equations of motion for the point vortices. Taking into account the images contribution, the Biot-Savart kernel as a function of the vector $\mathbf{x} = (x_1, x_2)$ can be expressed as a double sum, $\mathbf{K}(\mathbf{x}) = (-S(x_2, x_1), S(x_1, x_2))$, with

$$S(x_1, x_2)\sum_{m=-\infty}^{\infty}\sum_{n=-\infty}^{\infty}\frac{x_1 - 2\pi n}{(x_1 - 2\pi n)^2 + (x_2 - 2\pi m)^2},$$

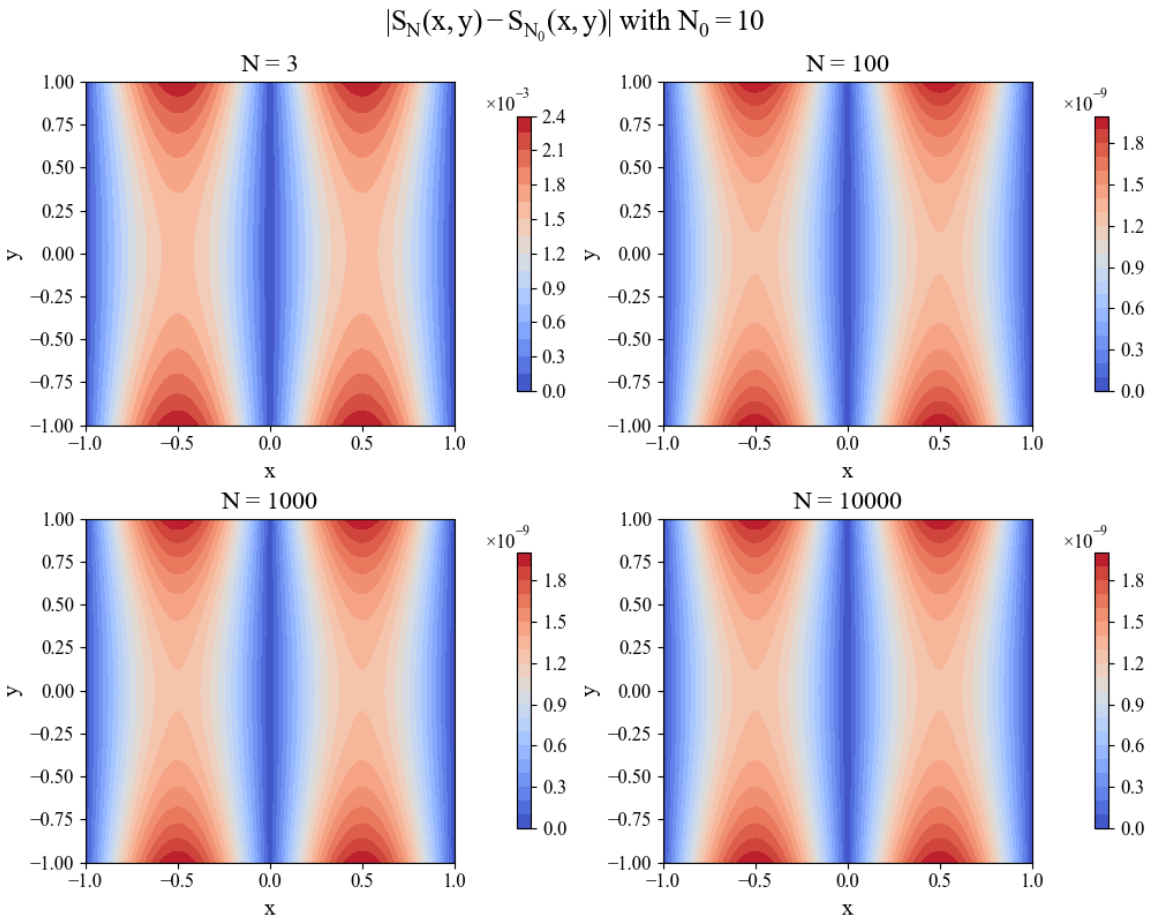

Figure 2.1: Convergence of series $S_N(x_1, x_2)$ for different values of N to series $S_{N_0}(x_1, x_2)$, the truncation of (1.7) for $N_0 = 10$.

see [124] for a discussion on the convergence over m or n. Applying the Laplace transform to the finite sum $S_{M,N}(x_1, x_2)$ over n, we get after some computations the expression:

$$S(x_1, x_2) \sum_{m=-\infty}^{\infty} \frac{\sin(x_1)}{\cosh(x_2 - 2\pi m) - \cos(x_1)} \ .$$

If instead the Laplace transform is applied to m we obtain:

$$S(x_1, x_2) \sum_{n=-\infty}^{\infty} \frac{\sinh(x_1 - 2\pi n)}{\cosh(x_1 - 2\pi m) - \cos(x_2)} \ .$$

Second approximation: no sums

Another option to approximate (1.7) near the discontinuity is to take the Green function on the plane, (1.5), but taking the distance on the torus (here $\mathbb{T}^2 = [-1, 1] \times [-1, 1]$) instead the distance

on the plane,

$$\mathbf{K}(\mathbf{x}) = \frac{1}{4\pi} \frac{\mathbf{x}^{\perp}}{d(\mathbf{x})^2} \ ,$$

where $d(\mathbf{x}^2)$ denotes the periodic distance on the torus. In this case, the vorticity field on the torus domain has a discontinuity. This approximation was used in chapters 5 and 6 and in the works [68, 59]. More details on how this approximation performs near the singularity are given in the chapter 6 and in the paper [68]: in the statistical ensemble under consideration in that work, the most relevant interactions of point vortices take place at close distances, and thus this approximation is appropriate.

Chapter 3

Non-conservative perturbations: internal and environmental noise

In this chapter, we will study the Point Vortex model introduced in the previous chapter, and add to its dynamics two different kind of perturbations, the first one being an *internal* noise, the second one an *environmental* noise. Those perturbations can be *non-conservative*: the notion of 'non-conservativeness' is linked to the loss of conserved quantities associated to the introduction of those perturbations; in particular, the Hamiltonian of the Point Vortex system is not conserved under perturbation of those kind; it is well established that the introduction of additive noise in the Point Vortex dynamics leads to the loss of kinetic energy's conservation, while we have some mild numerical evidence (see chapter 5) of energy decay for environmental noise of the form studied in this thesis.

The additive noise has been extensively studied in the literature, as its Point Vortex approximation solves the deterministic Navier-Stokes equation in the limit $N \to \infty$, where N is the number of vortices, see [26]. The study of the environmental (i.e. common) noise effect on the Euler or Navier Stokes equation is mainly motivated by the interest in turbulence models, and if this stochastic modification can model turbulent phenomena, by appropriately tuning parameters. In this thesis, we do not focus on exploring the link between real world data and the Navier Stokes equation driven by environmental noise: we only study some properties of this model.

The link between additive noise and noise of transport type has been established and investigated in [60]: small-scale random perturbation effect is studied both on a large-scale passive scalar and on the large-scale fluid itself, and the introduction of additive noise is shown to lead the dynamics to converge to one with noise of transport type. However, in this thesis we are concerned with the opposite, namely in showing that, under suitable assumptions and in certain limit regimes, if we add the environmental noise we investigate to the deterministic Point Vortex model dynamics, there are dissipation effects qualitatively similar to additive noise and to the behavior of a discretized viscous fluid.

3.1 Point Vortex model with internal noise

In this section, we introduce additive (internal) noise in the Point Vortex model dynamics and summarize some well-known results, concerning the analytical approach in the literature. In the following, we will use the notation from [35] to introduce the so called '*internal noise*' (additive noise). We will restrict our brief analysis to domains with periodic boundary conditions, as in [35]. We consider the equation of motion (1.1) in a generic domain, and insert in the dynamics an additive noise in the following way:

$$d\mathbf{x}^{(i)}(t) = \sum_{\substack{j=1 \\ j\neq i}}^{N} \gamma_j \mathbf{K}\left(\mathbf{x}^{(i)}(t), \mathbf{x}^{(j)}(t)\right) dt + \beta d\mathbf{W}^{(i)}(t) \tag{3.1}$$

where $\beta > 0$, $i, j = 1, \cdots, N$, and $\mathbf{W}^{(i)}(t)$ are mutually independent two-dimensional Brownian motions. Moreover, in this notation $\mathbf{K}\left(\mathbf{x}^{(i)}(t), \mathbf{x}^{(j)}(t)\right)$ is the orthogonal gradient of the appropriate Green function, depending on the chosen domain, in this case, (1.7), the Green function on a torus $\mathbb{T}^2$. This Green function has to be combined with the assumption of total null vorticity, i.e. the sum of the intensities γ_i of the point vortices has to be zero, see section 2.4. Additive noise has no effect on the point vortices intensities, so the discussion previously made still holds. Equation (3.1) describes a diffusion process for the dynamics of each point vortex, β being its diffusion constant.

The regularized dynamics of $\mathbf{x}^{(i)\varepsilon}(t)$ is introduced: this dynamics is identical to (3.1), except for the presence of the regularized kernel $\mathbf{K}^{\varepsilon}(\mathbf{x}, \mathbf{y})$, the orthogonal gradient of a regularized Green function, identical to the original Green function if $|\mathbf{x}-\mathbf{y}| > \varepsilon$. With the use of the regularized dynamics of $\mathbf{x}^{(i)\varepsilon}(t)$, the existence and uniqueness of the solution of (3.1) is proven; see [35] for the details of the proof. See [79] for convergence of this stochastic system to two-dimensional incompressible Navier-Stokes. This result shows that the introduction of additive noise in the deterministic PV dynamics of N vortices produces, in the limit of $N \to \infty$, effect analogous to viscosity in fluids.

3.2 Environmental noise: vorticity blobs and turbulence

The study of turbulence has always been a long-standing research problem, to the point that one of the seven Millennium Prize problems in mathematics relates the understanding of the Navier–Stokes equations, as a first step to understanding turbulence. There is a a huge amount of studies devoted to the study of turbulence and its modeling; see [121] for a review on the case of two-dimensional turbulence, the only case we will handle in this thesis. The models we ought to investigate originate from the intuition that small-scale turbulence could be dissipative on the mean flow. This idea is linked to Bousinnesq's research [11] and it implies a mutual influence of small scales and large scales.

The separation of scales is often done by *filtering* the velocity field $\mathbf{u}$, via a mollification operation on the velocity or by taking only the firsts Fourier components of $\mathbf{u}$'s Fourier decomposition. However, one drawback of filtering $\mathbf{u}$ is that the resulting equation for the filtered velocity is not closed. There are many techniques to perform the closure of this equation, see for example [43] and references therein, but those procedures will not be the focus of this thesis.

In the following, we will give a brief introduction and some motivations concerning the choice of the model studied in this thesis; the starting point is the Navier-Stokes equation for an incompressible fluid of constant density, while the particle discretization of the model will follow in the next section.

The particle discretization of the vorticity form of the 2D Euler equation with environmental noise is described in [29]: the authors study a mean field limit, where the number of vortices N is sent to infinity, $N \to \infty$, while a regularization parameter ε in the regularized Biot-Savart kernel is sent to zero as a function of the number of vortices N, $\varepsilon(N) \to 0$.

We recall the Navier-Stokes equation in velocity formulation,

$$\begin{aligned} \partial_t \mathbf{u} + \mathbf{u} \cdot \nabla \mathbf{u} &= \nu \Delta \mathbf{u} \\ \nabla \cdot \mathbf{u} &= 0; \end{aligned} \tag{3.2}$$

where for the sake of simplicity we assume the pressure gradient to be zero and the absence of forcing. In vorticity formulation,

$$\partial_t \omega + \mathbf{u} \cdot \nabla \omega = \nu \Delta \omega \tag{3.3}$$

where the scalar function ω indicates the only non-zero component of the velocity curl in 2D and we obtain a non-linear transport equation for ω. We define a family of filters, Λ_ℓ, where we indicate with ℓ a length scale of the system. We define Λ_ℓ as filters which commute with the space derivative. Fourier filters can be used in place of Λ_ℓ, but we use the general definition

$$\left(\Lambda_\ell f\right)(\mathbf{x}) = \int \theta_\ell(\mathbf{x} - \mathbf{y}) f(\mathbf{y}) d\mathbf{y}.$$

In this definition, we introduced the density functions $\theta_\ell(\mathbf{x})$; we take them to be smooth, centered at zero and invariant under rotation. Their support is the ball of radius of order ℓ. One can now take a classical approach and define the filtered velocity $\mathbf{u}_\ell = \Lambda_\ell \mathbf{u}$, while the difference between the original velocity and the filtered velocity is indicated with $\mathbf{u}'$. Then, if we apply the filter to equation (3.2), we obtain the following equation for the filtered velocity $\mathbf{u}_\ell$:

$$\begin{aligned} \partial_t \mathbf{u}_\ell + \mathbf{u}_\ell \cdot \nabla \mathbf{u}_\ell &= \nu \Delta \mathbf{u}_\ell - \mathrm{div} R_\ell \\ \nabla \cdot \mathbf{u}_\ell &= 0; \end{aligned}$$

where $R_\ell = \Lambda_\ell(\mathbf{u} \otimes \mathbf{u}) - \mathbf{u}_\ell \otimes \mathbf{u}_\ell$ is the Reynolds stress tensor. Note that the velocity is filtered at all times if one follows this procedure; moreover, the filtered velocity can be expressed in terms of the filtered vorticity by means of the Biot-Savart kernel K, $\mathbf{u}_\ell = \mathbf{K} * \omega_\ell$.

Alternatively, the filtering procedure can be performed only on the initial condition; this procedure is based on the intuition of [99], where the vorticity formulation of the Euler equation is studied and the initial condition is decomposed in *vortex structures*. This idea is the origin of the noise term studied in this chapter and in chapters 4, 5. In the following, we change the meaning of ω_ℓ and, subsequently, ω'. More precisely, $\omega_\ell = \omega_\ell(t)$ is now the evolution in time of the decomposed initial condition. In this formulation, $\omega = \omega_\ell + \omega'$ is the solution of the Navier-Stokes equation, without any loss of information, but the evolution of its addends is described by the following system:

$$\begin{aligned} \partial_t \omega_\ell + \mathbf{u}_\ell \cdot \nabla \omega_\ell + \mathbf{u}' \cdot \nabla \omega_\ell &= \nu \Delta \omega_\ell \\ \omega_\ell(t=0) &= \Lambda_\ell \omega_0 \\ \omega'(t=0) &= \Lambda'_\ell \omega_0; \end{aligned} \tag{3.4}$$

where we have used the symbol $\mathbf{u}' = \mathbf{K} * \omega'$. The evolution in time of the decomposed vorticity is supposed to mix the scales and thus equations (3.4) will not in principle hold for $t > 0$. However, we suppose that for small t the decomposed model is still able to describe the vorticity evolution. Note that this decomposition is based on the proof of Marchioro and Pulvirenti: they show that point

vortices are the limit of small-scale vortex blobs; following their consideration, one could suppose that, for short times, the large-scale and small-scale decomposition of the vorticity field holds.

We now turn to a stochastic parametrization of the small scales of the vorticity ω': first of all, we decompose it as a sum of vorticity 'components' at $t = 0$,

$$\omega(t=0) = \omega_\ell(t=0) + \omega'(t=0) = \omega_\ell(t=0) + \sum_{k=1}^{M} \omega'^{(k)}(t=0).$$

The main goal of this procedure is to be able to model some turbulent phenomenon, and we are making the assumption that turbulence is mainly generated by the effect of many small-scale viscosity structures, the $\omega'^{(k)}$s. In equation (3.4) we already selected the large-scale equation, however there still is dependence on the small scales. To perform a closure of the equation, we model the small-scale velocity $\mathbf{u}'$ via a stochastic process; we understand $\omega'(t=0)$ as a collection of small vorticity structures located in positions $\mathbf{y}^{(k)}$ at $t = 0$, with intensities $\Gamma(M)$, such that

$$\mathbf{u}'(t,\mathbf{x}) \cdot \nabla\omega_\ell = \sum_{k=1}^{M} \Gamma(M)\mathbf{K}(\mathbf{x}(t) - \mathbf{y}^{(k)}) \cdot \nabla\omega_\ell \circ dW^k(t),$$

where $W^k(t)$ are $k = 1 \dots M$ one-dimensional Brownian motions. Note that we are making the strong assumption that the artificial vorticity structures which model the small-scale vorticity will not move in the time interval we are considering. This parametrization is a specific way to model the small-scale velocity; it is not general and it is the one we use in this thesis. In the next section, we focus on the application of this parametrization in the context of the Point Vortex model and its implications.

3.3 Point Vortex model and environmental noise

In this section, we consider the following domain, a torus $\mathbb{T}^2 = [-1,1] \times [-1,1]$. We study a stochastic modification of the Point Vortex system, in which an environmental noise is added to the deterministic dynamics of the vortices. More precisely, the environmental noise introduced represents an advection by stochastic vector field term in the equation of motion. The advection field is the sum of M vorticity blobs of random intensity and, for the time being, fixed position. The case in which the vorticity blobs coordinates are uniformly distributed on the domain and change in time is investigated in chapter 5 and in the work [59] with numerical simulations.

The Point Vortex dynamics with stochastic advection obeys the following equation:

$$d\mathbf{x}^{(i)}(t) = \sum_{\substack{j=1 \\ j\neq i}}^{N} \gamma_j \mathbf{K}\left(\mathbf{x}^{(i)}(t), \mathbf{x}^{(j)}(t)\right) dt + \Gamma(M) \sum_{k=1}^{M} \mathbf{K}\left(\mathbf{x}^{(i)}(t), \mathbf{y}^{(k)}\right) \circ dW^k(t) \tag{3.5}$$

where $W^k(t)$ are $k = 1 \dots M$ one-dimensional Brownian motions, $\mathbf{x}^{(i)}(t)$ is the position of the i-th point vortex, $\mathbf{y}^{(k)}$ is the position of the k-th vorticity blob, and the coefficient $\Gamma(M)$ correspond to the vorticity blobs intensity. This coefficient has to be determined and it is the equivalent of the strengths γ_i of the point vortices; for the sake of simplicity, we take it to be the same for all M vorticity blobs.

Note that the stochastic advection field in (3.5) has the form of a sum of interaction kernel between the point vortex i and M point vortices k of intensity $\Gamma(M)$, $\mathbf{K}\left(\mathbf{x}^{(i)}(t), \mathbf{y}^{(k)}\right)$ with the Stratonovich differentiation. In the previous section, the regularized kernel $\mathbf{K}^{\varepsilon}\left(\mathbf{x}^{(i)}(t), \mathbf{x}^{(j)}(t)\right)$ was introduced. In the following, we will consider different regularization parameters ε and $\varepsilon(M)$, the former concerning the deterministic term in the equation of motion, and the latter concerning the stochastic term.

The choice of the Stratonovich formulation in the stochastic term is due to the fact that the helicity of vortex field lines,

$$H = \int_V dV \ \mathbf{u} \cdot (\nabla \times \mathbf{u}), \quad \omega = (\nabla \times \mathbf{u}) \cdot e_3 \tag{3.6}$$

is conserved if we move along paths of the Stratonovich stochastic equation of motion. The Itô integration does not allow this important property to manifest, because of the quadratic covariation. For a comprehensive discussion on this topic, see [78], where a derivation of stochastic partial differential equation from a stochastic variational principle, in the fluid dynamics context, is performed. Note that in the definition (3.6) we indicate with dV the volume element; in this thesis, we will consider only two-dimensional systems, however this simplification is made possible by the fact that systems of interest in fluid dynamics can be described by two-dimensional fluids if vertical scale is negligible with respect to the horizontal scale. Finally, we assume the solution of (3.5) to be sufficiently smooth so that the Stratonovich integration makes sense.

3.3.1 Limit mean field equations

Depending on the choice of the stochastic advection field, it is possible to identify two different effects on the deterministic fluid equation, which we are interested in studying. The first one corresponds to insert in the equation an environmental noise which acts on large spatial scales and has intensity comparable to the one of the vortex interactions. The second one corresponds to the case where the environmental noise acts at spatial scales so small and intensities so weak that it becomes a second order operator in the so-called Itô-Stratonovich diffusion limit [63]. In the following, we will briefly comment on the mean field limit equations for this two cases. To this end, we define the empirical measure of a system of N point vortices as:

$$\mu(t) = \frac{1}{N} \sum_{i}^{N} \delta(\mathbf{x} - \mathbf{x}^{(i)}(t)) \tag{3.7}$$

and we study deterministic or stochastic differential equations for the vorticity field for which the empirical measure (3.7) is a solution (under certain hypotheses). Note that in equation (3.7) and in the following, we will take $\gamma_i = 1/N$ for each i; this choice is needed to obtain the mean field limit equation.

Finding the limit mean field equation for a Point Vortex system with multiplicative noise is a active topic of research; we recall for example the work [29]. For a very large number of vortex blobs M, namely in the limit $M \to \infty$ and with proper assumptions on the stochastic advected field, the empirical measure may converge to the solution of the following deterministic vorticity equation,

$$\partial_t \omega + \mathbf{u} \cdot \nabla \omega - \operatorname{div}(Q(\mathbf{x}) \nabla \omega) = 0 \tag{3.8}$$

where $Q(\mathbf{x})$ is a generic $d \times d$ covariance matrix of the noise with $d = 2$, for which the proper

assumptions holds. In our case,

$$Q(\mathbf{x}) = \frac{(\Gamma(M))^2}{2} \begin{bmatrix} K_1(\mathbf{x})K_1(\mathbf{x}) & K_1(\mathbf{x})K_2(\mathbf{x}) \\ K_1(\mathbf{x})K_2(\mathbf{x}) & K_2(\mathbf{x})K_2(\mathbf{x}) \end{bmatrix}. \tag{3.9}$$

In this definition, the kernel components, $\mathbf{K}(\mathbf{x}) = (K_1(\mathbf{x}), K_2(\mathbf{x}))$, are explicitly written. In the special case in which $Q(\mathbf{x})$ is proportional to the identity matrix in some limit, the divergence term becomes, in the limit, a laplacian operator. The goal of the following sections will be to explore the hypothesis under which it is possible to find an appropriate scaling and find a coefficient $\Gamma(M)$, if it exists, for which the limit $M \to \infty$ shows similar behavior.

On the other hand, if M is not large, the limit mean field equation for the vorticity is a SPDE with the same noise,

$$\partial_t \omega + \mathbf{u} \cdot \nabla \omega - \Gamma(M) \sum_{k=1}^{M} \mathbf{K}\left(x - \mathbf{y}^{(k)}\right) \nabla \omega \circ dW_t^k = 0 \tag{3.10}$$

or equivalently, using Itô integration,

$$\partial_t \omega + \mathbf{u} \cdot \nabla \omega - \operatorname{div}\left(Q(\mathbf{x}) \nabla \omega\right) - \Gamma(M) \sum_{k=1}^{M} \mathbf{K}\left(x - \mathbf{y}^{(k)}\right) \nabla \omega \; dW_t^k = 0 \tag{3.11}$$

An equation similar to equation (3.10) (or, equivalently, equation (3.11)) will be studied in detail, in chapter 4. More precisely, we will consider the stochastic advection and diffusion of a passive scalar, so the non-linear term will not appear in the equation. Instead, a diffusion term will be introduced. In the following section, we will make some deductions on the behavior of the system in the limit $M \to \infty$, to understand what conditions have to be met to reproduce equation (3.8).

3.4 From stochastic Point Vortex model to SPDE

In this section, we briefly recall some known results about the convergence of the Point Vortex model with environmental noise to equation (3.10), see [29]. We introduce a more general environmental noise, and explain under what assumptions whose results apply to our case. We follow notation from [29], where the following stochastic modification of the Point Vortex system,

$$d\mathbf{x}^{(i,N)}(t) = \sum_{\substack{j=1 \\ j \neq i}}^{N} \gamma_j \mathbf{K}^{\varepsilon}\left(\mathbf{x}^{(i,N)}(t), \mathbf{x}^{(j)}(t)\right) dt + \sum_{k=1}^{\infty} \boldsymbol{\sigma}_k \left(\mathbf{x}^{(i)}(t)\right) \circ dW^k(t) \tag{3.12}$$

is studied on the two-dimensional torus, $\mathbb{T}^2$. In (3.12), $\mathbf{K}^{\varepsilon}$ is the regularized kernel, and $\varepsilon = \varepsilon(N)$. $\boldsymbol{\sigma}_k$ is a vector field, $\boldsymbol{\sigma}_k : \mathbb{T}^2 \to \mathbb{R}^2$, $k \in \mathbb{N}$. The space covariance of the noise is defined as:

$$Q_{ij}(\mathbf{x}, \mathbf{y}) = \sum_{k=1}^{\infty} \boldsymbol{\sigma}_{k,i}(\mathbf{x}) \boldsymbol{\sigma}_{k,j}(\mathbf{y}) \tag{3.13}$$

where $Q : \mathbb{T}^2 \times \mathbb{T}^2 \to \mathbb{R}^{2\times 2}$. We make the following assumptions on the fields $\boldsymbol{\sigma}_k$:

1. $\boldsymbol{\sigma}_k$ is C^2 and
$$\sum_{k=1}^{\infty} ||\boldsymbol{\sigma}_k||_{C^2} < \infty \ .$$
2. div $\boldsymbol{\sigma}_k = 0$ for all $k \geq 1$.
3. $Q(\mathbf{x}, \mathbf{y}) = Q(\mathbf{x} - \mathbf{y})$.
4. $Q(0) = aI$ for some $a \geq 0$.

The empirical measure, defined as in (3.7), solves the equation in a distributional sense. The following theorem is proved in [29]:

Theorem 3.1. *If ω_0 is a bounded initial condition for the vorticity, we assume that the empirical measure converges to the initial vorticity with rate ζ_N,*
$$\lim_{N\to\infty} \frac{1}{N} \sum_{i}^{N} \gamma_{i,N} \delta(\mathbf{x} - \mathbf{x}^{(i,N)}) = \omega_0 \ .$$
Moreover, we take
$$\varepsilon(N) \approx (-\log \zeta_N)^{-\delta} \quad \delta \in \mathbb{R}_+ \ .$$
and $\mathbf{x}^{(i,N)}(t)$ is the solution of (3.12) with initial condition $\mathbf{x}^{(i,N)}$. Then, if the fields $\boldsymbol{\sigma}_k$ satisfy the assumptions above, the path of empirical measures converges in $W^{1,\infty}(\mathbb{T}^2)^*$, as $N \to \infty$ to the unique bounded solution of
$$\partial_t \omega + \mathbf{u} \cdot \nabla \omega + \sum_{k=1} \boldsymbol{\sigma}_k \cdot \nabla \omega \circ dW_t^k = 0 \ , \tag{3.14}$$
or, equivalently, in the Itô formulation,
$$\partial_t \omega + \mathbf{u} \cdot \nabla \omega + div(Q \ \nabla \omega) + \sum_{k=1} \boldsymbol{\sigma}_k \cdot \nabla \omega \ dW_t^k = 0 \ .$$

In the case of our environmental blobs noise, the space covariance matrix $Q(\mathbf{x}, \mathbf{y})$ defined in (3.9) is not proportional to the identity, or isotropic. Those two properties are used to write the regularized Euler equation in vorticity form, in the Itô formulation, as in [28]:
$$\partial_t \mu + \operatorname{div}(b(\mu)\mu) + \sum_k \operatorname{div}(\boldsymbol{\sigma}_k \mu) \ dW_t^k = \frac{1}{2} \Delta \mu$$
where μ is a measure in $\mathcal{M}(\mathbb{T}^2)$, the space of finite, signed Borel measures on $\mathbb{T}^2$. For a measurable function $\phi : \mathbb{T}^2 \to \mathbb{R}$
$$\mu(\phi) = \int_{\mathbb{T}^2} \phi(\mathbf{x}) \mu(\mathrm{d}\mathbf{x}) \ .$$
Moreover, $b(\mathbf{x}, \mu)$ is defined as
$$b(\mathbf{x}, \mu) = \int_{\mathbb{T}^2} \mathbf{K}^{\varepsilon}(\mathbf{x} - \mathbf{y}) \mu(d\mathbf{y}) \ .$$

However, in the case of our environmental blobs noise, for a test function $\phi \in C^2(\mathbb{T}^2)$ and a Point Vortex position $\mathbf{X}^{(i)}$ the regularized Euler equation reads:

$$d\phi(\mathbf{X}^{(i)}) = \frac{1}{N}\sum_{j\neq i} (\partial_\mu \phi)\ K_\mu^{\varepsilon(i,j)}\ dt + \gamma\ (\partial_\mu\phi)\ K_\mu^{(i,k)}\ dW_t^k$$
$$+ \frac{\gamma^2}{2}\left((\partial_\nu\phi)\ (K_\mu^{(i,k)})\partial_\mu K_\nu^{(i,k)} + (\partial_\mu\partial_\nu\phi)((K_\mu^{(i,k)})(K_\nu^{(i,k)}))\right) dt$$

where we make use of the tensor notation. If we integrate and write the same equation for μ, the first term at right-hand side is zero by using the divergence free property of our stochastic fields and integration by part, and in the same way we can recover the third term of the regularized Euler equation, however the laplacian becomes a second-order elliptic operator. Translation invariance can be recovered as in section 3.6.

3.5 Itô-Stratonovich diffusion limit

In this section, we follow [51], where it is proved that the stochastic two-dimensional Euler equation with environmental noise, in a form very similar to equation (3.14), but with finite sum on k, converges weakly to the deterministic two-dimensional Navier–Stokes equation, under suitable noises scaling, the so called *Ito-Stratonovich diffusion limit*. The stochastic Euler equation studied in [51] is the following:

$$\partial_t\omega^N + \mathbf{u}^N\cdot\nabla\omega^N = \ \varepsilon_N \sum_{k\in\mathbb{Z}_0^2} \theta_k^N \boldsymbol{\sigma}_k\cdot\nabla\omega^N \circ dW_t^k = 0\ , \tag{3.15}$$

with

$$\varepsilon_N = \frac{2\sqrt{\nu}}{||\theta^N||_{\ell^2}}$$

where with $\ell^p (p\in[1,\infty])$ we indicate the spaces of real sequences indexed by $\mathbb{Z}_0^2$, $\theta^N \in \ell^2$ with $N\geq 1$ is a sequence for which the two following properties hold:

$$\theta_k^N = \theta_j^N \quad \text{if} \quad |\mathbf{k}| = |\mathbf{j}|$$

and

$$\lim_{N\to\infty} \frac{||\theta^N||_{\ell^\infty}}{||\theta^N||_{\ell^2}} = 0\ .$$

In this case, if we take $\omega_0^N = \omega_0 \in L^2(\mathbb{T}^2)$ zero mean, in [51] it is proved that equation (3.15) has a weak solution ω^N,

$$\sup_{t\in[0,T]} \int_{\mathbb{T}^{\not\in}} |\omega^N(t,\mathbf{x})|^2 \mathrm{d}x < +\infty$$

and such more regular solutions converge to the unique solution of the two-dimensional Navier-Stokes equation with same initial data.

In [13] and in chapter 4, the *Itô-Stratonovich diffusion limit* is studied in the case of a stochastic viscous transport equation for a passive scalar u_t^N on $\mathbb{R}_+\times\mathbb{T}^2$,

$$du_t^N = \sqrt{2}\sum_{k\in\mathbb{Z}^2} \boldsymbol{\sigma}_k^N\cdot\nabla u_t^N \circ dW_t^k + \kappa\Delta u_t^N dt\ ,$$

where u indicates the passive scalar, $N\in\mathbb{N}$ is a parameter which regulates the resolution of the noise, for each $N\in\mathbb{N}$ and $k\in\mathbb{Z}^2$ $\boldsymbol{\sigma}_k^N$ are divergence-free vector fields, with support inside the ball of radius $c>0$, $\{W_t^k\}$ is a sequence of i.i.d standard brownian motions, κ is the molecular diffusivity. The effective diffusivity behavior is then investigated.

3.6 Environmental blobs noise as sum on lattice: covariance matrix

In this section we study the covariance matrix (3.9) of the environmental blobs noise. The more general way to place the points $\mathbf{X}^{(k)}$ on the torus is to put them as uniformly distributed on the whole torus. A simpler way is to start from a special configuration and arrange all the points in a lattice. In this way, the coordinates of the points $\mathbf{X}^{(k)}$ will be unequivocally chosen and it will be possible to compute the sum in the noise term as a function of the total number of points M. Moreover, it will be possible to associate to each coordinate a function $g : \mathbb{N} \to \mathbb{R}$, which from a pair of natural numbers, a vector $\mathbf{k} = (i, j)$ produces coordinates on the torus $(X^{(k)}, Y^{(k)})$. This configuration will be used in the second part of chapter 5 and, in a slightly different fashion, in chapter 4.

3.6.1 Lattice definition

In the following, we indicate with $\mathbf{X} = (X, Y)$ the coordinates of a generic point vortex, previously indexed with i (or also j). Now, the index i (and also j) is going to be used for a different purpose, so the generic point vortex's coordinate will not be written as $(X^{(i)}, Y^{(i)})$ (or the same with j) anymore. The function $g(i, M)$ depends on the total number of lattice point, as well as the lattice coordinate in one direction, i, and it is defined as:

$$g(i, M) = -1 + \frac{1}{\sqrt{M}} + i\frac{2}{\sqrt{M}} \ .$$

The fixed points on the lattice are chosen in the following way: we recall that we are working on the torus $\mathbb{T}^2 = [-1, 1] \times [-1, 1]$; for the sake of simplicity, we consider only one space dimension, and in this framework we are looking to a way to place $\sqrt{M}$ points on a line, equidistant and periodic. To do that, one has to divide the interval into $\sqrt{M}$ sub-intervals, and take the midpoint of each one. The first point is located at -1 (the left extreme) plus $1/\sqrt{M}$, half of the distance between two points (length of the total interval, 2, divided by the number of points, $\sqrt{M}$). We define the auxiliary function $h(i, M)$ as:

$$h(i, M) \equiv 2 + g(i, M) = 2 - 1 + \frac{1}{\sqrt{M}} + i\frac{2}{\sqrt{M}} = 1 + \frac{1}{\sqrt{M}} + i\frac{2}{\sqrt{M}} \ .$$

3.6.2 Sums to be computed

Rewriting its elements as explicit summations, the matrix elements of the matrix $Q(X, Y)$ read as

$$Q_{11}(X, Y) = \sum_{i=0}^{\sqrt{M}-1} \sum_{j=0}^{\sqrt{M}-1} (K_1^{((X,Y),(i,j,M))})^2$$

$$Q_{22}(X, Y) = \sum_{i=0}^{\sqrt{M}-1} \sum_{j=0}^{\sqrt{M}-1} (K_2^{((X,Y),(i,j,M))})^2$$

$$Q_{12}(X, Y) = Q_{21}(X, Y) = \sum_{i=0}^{\sqrt{M}-1} \sum_{j=0}^{\sqrt{M}-1} (K_1^{((X,Y),(i,j,M))})(K_2^{((X,Y),(i,j,M))})$$

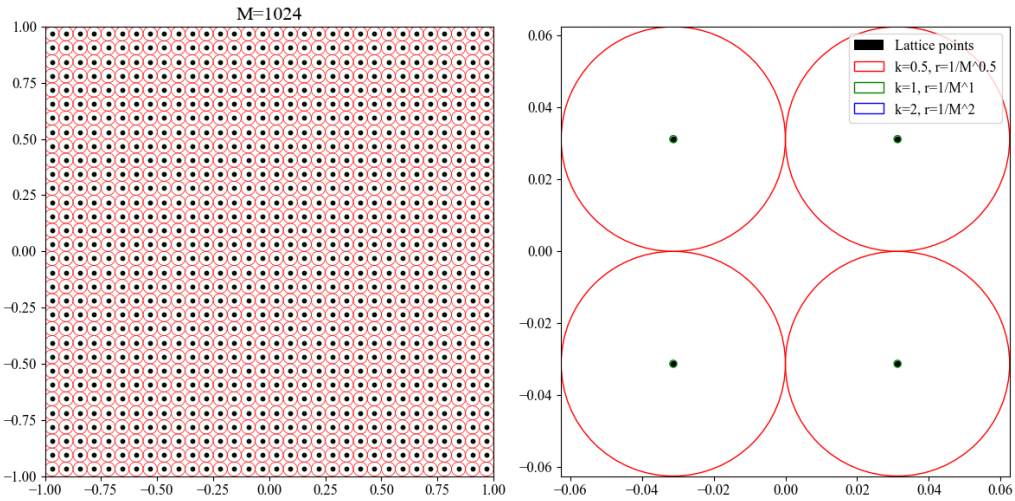

Figure 3.1: Lattice configuration for different values of κ.

where

$$Q(X,Y) = \frac{\gamma^2}{2}\begin{bmatrix} Q_{11}(X,Y) & Q_{12}(X,Y) \\ Q_{21}(X,Y) & Q_{22}(X,Y) \end{bmatrix}$$

Our expectation, based on previous remarks, is that in their asymptotic limit in $M \to \infty$ and under appropriate conditions, the diagonal matrix elements should have the same zero or first order coefficient of the expansion, while the non diagonal elements should be negligible with respect to the diagonal elements. Another problem to be tackled is the behavior of the summation when the point vortex of coordinates (X, Y) is located at a very small distance with respect one of the lattice points. In this situation, we could choose to introduce a regularization parameter ε to regularize the kernel $\mathbf{K}(x, y)$. We take $\varepsilon = \varepsilon(M)$ such that $\sqrt{\varepsilon} = M^{-\kappa}$. We report in figure 3.1 the plot of the lattice points, together with different radius κ. We recall that also the coefficient γ has to be chosen as a function of M, in a form $\gamma \propto (1/M)^{\alpha}$. For the sake of simplicity, in the following series manipulation we will only write the generic expression

$$\sum_{i=0}^{\sqrt{M}-1} \sum_{j=0}^{\sqrt{M}-1} f\left(X - g(i,M), Y - g(j,M)\right)$$

and we report in the Appendix (section 6.4) for all the computations.

For the case of the exact kernel, expressed as in [124], the kernel components are reported below.

$$K_1(x,y) = \sum_{n=-N}^{N} \frac{-\sin(\pi y)}{\cosh(x-2n) - \cos(\pi y) + \varepsilon} \quad ;$$

$$K_2(x,y) = \sum_{n=-N}^{N} \frac{-\sin(\pi x)}{\cosh(y-2n) - \cos(\pi x) + \varepsilon} \quad ,$$

where again we dropped the tildas and introduced the regularization parameter $\varepsilon(M)$, written as ε

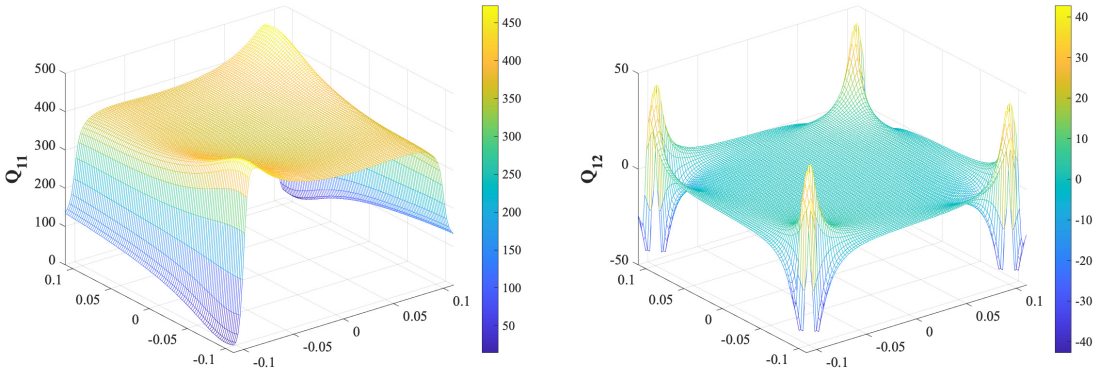

Figure 3.2: Covariance matrix elements computed for $X \in (-1.1/\sqrt{M}, 1.1/\sqrt{M})$ and $Y \in (-1.1/\sqrt{M}, 1.1/\sqrt{M})$ and $M = 100$, $\kappa = 1$, $\gamma^2/2 = 1/M$, $N = 10$.

for brevity. The elements Q_{ij} of the covariance matrix are:

$$
\begin{aligned}
Q_{11}(i,j,M,X,Y,\varepsilon) &= \sum_{i=0}^{\sqrt{M}-1}\sum_{j=0}^{\sqrt{M}-1}\left(\sum_{n=-N}^{N}\frac{-\sin(\pi(Y-g(j,M)))}{\cosh(X-g(i,M)-2n)-\cos(\pi(Y-g(j,M)))+\varepsilon}\right)^2 ; \\
Q_{22}(i,j,M,X,Y,\varepsilon) &= \sum_{i=0}^{\sqrt{M}-1}\sum_{j=0}^{\sqrt{M}-1}\left(\sum_{n=-N}^{N}\frac{-\sin(\pi(X-g(i,M)))}{\cosh((Y-g(j,M))-2n)-\cos(\pi(X-g(i,M)))+\varepsilon}\right)^2 ; \\
Q_{12}(i,j,M,X,Y,\varepsilon) &= Q_{21}(i,j,M,X,Y,\varepsilon) \\
&= \sum_{i=0}^{\sqrt{M}-1}\sum_{j=0}^{\sqrt{M}-1}\left(\sum_{n_1=-N}^{N}\frac{-\sin(\pi(Y-g(j,M)))}{\cosh(X-g(i,M)-2n_1)-\cos(\pi(Y-g(j,M)))+\varepsilon}\right) \\
&\quad\times\left(\sum_{n_2=-N}^{N}\frac{-\sin(\pi(X-g(i,M)))}{\cosh(Y-g(j,M)-2n_2)-\cos(\pi(X-g(i,M)))+\varepsilon}\right).
\end{aligned}
$$

We report in figure 3.2 and figure 3.3, as an example, the two elements of the covariance matrix Q_{11} and Q_{12}, zoomed around lattice points, respectively for $M = 100$ and $M = 500$. From this plots, it is evident that the matrix is not diagonal for every (X, Y). Note that the isotropy property does not hold in the case of blobs located on a lattice.

3.7 Environmental blob noise with independent uniform random positions: covariance matrix

We now turn to the case in which the blobs positions are independent, uniform and random, as in chapter 5. In this case, if we compute the covariance matrix averaging on different samples of the configuration of the blobs, the isotropy property of the covariance matrix is recovered. The elements

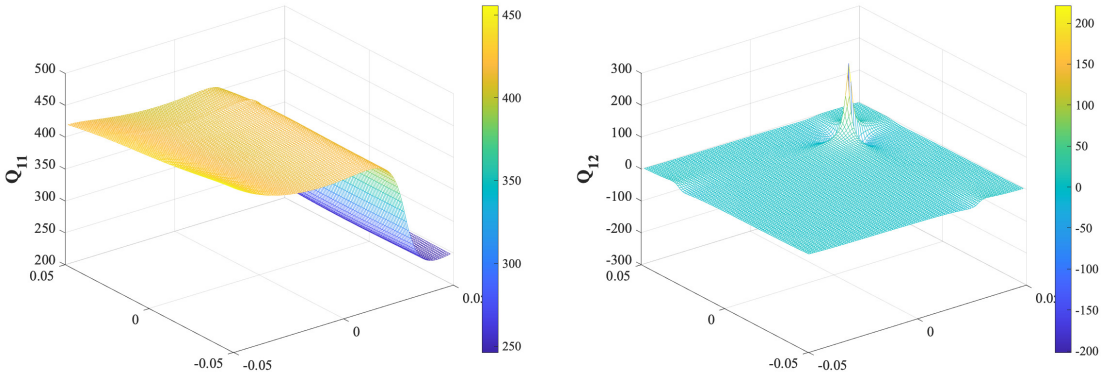

Figure 3.3: Covariance matrix elements computed for $X \in (-1.1/\sqrt{M}, 1.1/\sqrt{M})$ and $Y \in (-1.1/\sqrt{M}, 1.1/\sqrt{M})$ and $M = 500$, $\kappa = 1$, $\gamma^2/2 = 1/M$, $N = 10$.

of the covariance matrix are:

$$Q_{11}(X,Y) = \sum_{k=1}^{M} (K_1^{((X,Y),(x_k,y_k,M))})^2$$

$$Q_{22}(X,Y) = \sum_{k=1}^{M} (K_2^{((X,Y),(x_k,y_k,M))})^2$$

$$Q_{12}(X,Y) = Q_{21}(X,Y) = \sum_{k=1}^{M} (K_1^{((X,Y),(x_k,y_k,M))})(K_2^{((X,Y),(x_k,y_k,M))})$$

where $x_k, y_k \sim U(-1,1)$ are the coordinates of the M blobs. Using the same exact kernel in [124] as before,

$$Q_{11}(M,X,Y,\varepsilon) = \sum_{k=1}^{M} \left(\sum_{n=-N}^{N} \frac{-\sin(\pi(Y-y_k))}{\cosh(X-x_k-2n) - \cos(\pi(Y-y_k)) + \varepsilon} \right)^2 ;$$

$$Q_{22}(M,X,Y,\varepsilon) = \sum_{k=1}^{M} \left(\sum_{n=-N}^{N} \frac{-\sin(\pi(X-x_k))}{\cosh((Y-y_k)-2n) - \cos(\pi(X-x_k)) + \varepsilon} \right)^2 ;$$

$$\begin{aligned} Q_{12}(M,X,Y,\varepsilon) &= Q_{21}(M,X,Y,\varepsilon) \\ &= \sum_{k=1}^{M} \left(\sum_{n_1=-N}^{N} \frac{-\sin(\pi(Y-y_k))}{\cosh(X-x_k-2n_1) - \cos(\pi(Y-y_k)) + \varepsilon} \right) \\ &\quad \times \left(\sum_{n_2=-N}^{N} \frac{-\sin(\pi(X-x_k))}{\cosh(Y-y_k-2n_2) - \cos(\pi(X-x_k)) + \varepsilon} \right). \end{aligned}$$

We do not report the plots of the zoomed covariance matrix elements as in the previous section: we expect the zoom around the blobs to be the same, with the only difference in the positions of the regularized singularities. However, in this case we can compute the average value of $Q_{11}(M, X = 0, Y = 0)$ and $Q_{12}(M, X = 0, Y = 0)$, for different values of M, where the average is taken with respect to different configurations of the blobs (i.e. different x_k, y_k). We can take a single point

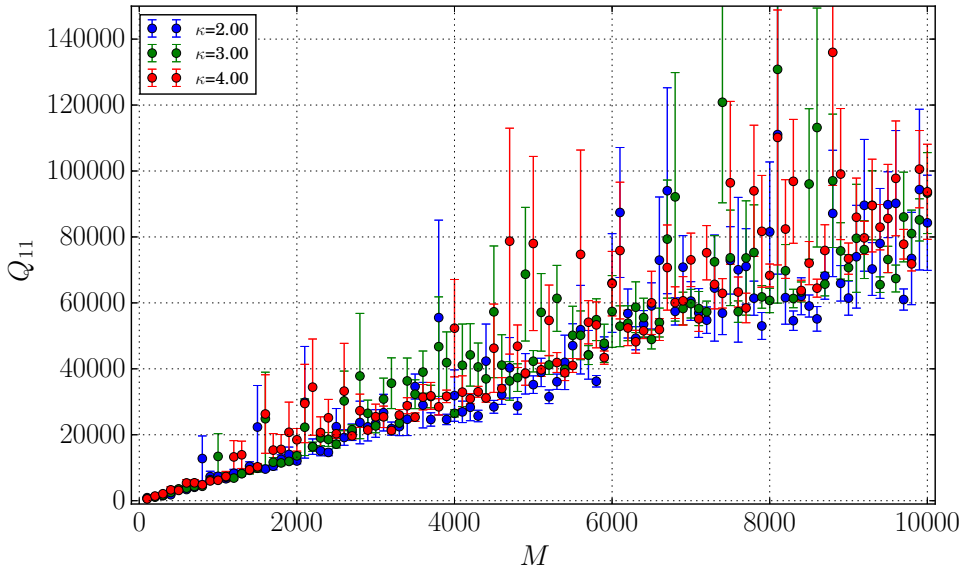

Figure 3.4: Covariance matrix element Q_{11} computed for $X = 0$ and $Y = 0$ and $M = 500$, different values of κ, $\gamma^2/2 = 1$, $N = 10$.

(X, Y) as reference point: in the average with respect to different samples of $\{(x_k, y_k)\}$, the isotropy of the covariance matrix is recovered.

We report in figure 3.4 the covariance matrix element Q_{11}, as a function of M. The plot is very noisy, and even with a large statistic ($n \sim 10000$, with n number of samples) it is hard to evaluate correction of a linear behavior in M. A qualitative exploration of the dissipative properties of this noise, linked with the Itô-Stratonovich diffusion limit, will be performed in chapter 5.

Chapter 4

Anisotropic noise effect on passive scalar

In the previous chapter, we introduced a noise of transport type (advection by stochastic velocity field) in the equation of motion of the Point Vortex model. In this chapter, our goal is to investigate the effects of this noise, under suitable hypothesis, by studying a stochastic viscous transport equation for a passive scalar with noise of transport type, in a simplified context; in particular, some simplifications arises when we introduce molecular diffusivity into the equation. As in chapter 3, we take the noise coefficient as a sum of *vorticity blobs*. The transport-type noise introduced represents the effect of turbulent motion due to small-scales velocities which influences the behavior of a fluid, and the stream function of each vorticity blob is taken to be a smooth compactly supported approximation of a Point Vortex's Green function on the full plane near zero. This choice is a simplified version of the one performed in Chapter 3 to study the vorticity formulation of a similar equation, but with no molecular diffusivity. However, for the reasons explained above, in this chapter we will not study a Point Vortex discretization of the fluid, while we investigate the stochastic transport equation and its scaling limit. The Point Vortex discretization for this system is left to investigate for future studies. The contents of this chapter are presented in the work [13]. The code used for the numerical investigation is [12].

4.1 Context and setting

In this chapter, we will adopt a slightly different notation; for this reason, we will dedicate this first section to introduce it and explain the goals of this study.

The equation we investigate is a stochastic viscous transport equation for a passive scalar u_t^N on $\mathbb{R}_+ \times \mathbb{T}^2$,

$$du_t^N = \sqrt{2} \sum_{k \in \mathbb{Z}^2} \sigma_k^N \cdot \nabla u_t^N \circ dW_t^k + \kappa \Delta u_t^N dt. \tag{4.1}$$

In this equation, u indicates the passive scalar, $N \in \mathbb{N}$ is a parameter which regulates the resolution of the noise, for each $N \in \mathbb{N}$ and $k \in \mathbb{Z}^2$ σ_k^N are divergence-free vector fields, vortices patches, with support inside the ball of radius $c > 0$, $\{W_t^k\}$ is a sequence of Brownian motions, κ is the molecular diffusivity. The parameter c tunes the overlap between the vortices patches: if c is small, the field

is constituted of sparse patches, while if c takes large values the space domain is covered by the patches.

Our main interest is to investigate the behavior of the effective diffusivity of this model, as in [52] the authors show that for an appropriate choice of vector fields and N sufficiently large, solutions to (4.1) are arbitrarily close, in mean square, to solutions of an 'enhanced' divergence form parabolic equation, depending on N, see also [94, Sec. 4.1].

We study equation (4.1) in the limit $N \to \infty$ and in the small molecular diffusivity regime, $\kappa \ll 1$. More precisely, we study the so-called *Itô-Stratonovich diffusion limit* of the equation, as seen in [52]. We then apply homogenization theory to study the effective diffusivity of the system. Finally, we numerically solve the elliptic equation obtained via homogenization to obtain a finer control on the behavior of the effective diffusivity.

4.1.1 Notation and definitions

We define $x = (x_1, x_2) \in \mathbb{R}^2$ and $x^\perp = (-x_2, x_1)$, a counter-clockwise rotation of x through $\frac{\pi}{2}$. Moreover, in this chapter we sometimes set $L^2(\mathbb{T}^2) = L^2(\mathbb{T}^2; \mathbb{R})$ or analogous notation in the case of other function spaces.

In this chapter, we indicate with the symbol:

$$\square_n^2(k) := \mathbb{Z}^2 \cap ([k_1, n] \times [k_2, n])\square_n^2 \quad := \square_n^2((0,0))$$

the finite box with side length $n \in \mathbb{N}$ and bottom left corner $k \in \mathbb{Z}^2$.

The domain considered in this chapter is the torus $\mathbb{T}^2$; it is set as $\mathbb{T}^2 := \mathbb{R}^2/\mathbb{Z}$, and identified as $\mathbb{T}^2 = [0,1]^2$ with periodic boundary conditions across this section. We indicate the domain of operators $\mathcal{L}$, linear and possibly unbounded, between Banach space, with $\mathcal{D}(\mathcal{L})$. The L^p-norm is defined as:

$$\|f\|_{L^p_x} := \begin{cases} \left(\int_{\mathbb{T}^2} |f(x)|^p \, \mathrm{d}x\right)^{\frac{1}{p}}, & p \in [1, +\infty), \\ \operatorname{ess\,sup}_{x \in \mathbb{T}^2} |f(x)|, & p = +\infty, \end{cases}$$

with $n \geq 1$ and $f : \mathbb{T}^2 \to \mathbb{R}^n$ a measurable map. The following notation is then used:

$$L^p(\mathbb{T}^2; \mathbb{R}^n) := \{ f : \mathbb{T}^2 \to \mathbb{R}^n \, : \, \|f\|_{L^p_x} < \infty \}$$
$$L^p_0(\mathbb{T}^2; \mathbb{R}^n) := \{ f \in L^p(\mathbb{T}^2; \mathbb{R}^n) \, : \, \langle f, 1 \rangle_{L^2(\mathbb{T}^2)} = 0 \, \}.$$

The Sobolev spaces of periodic functions are denoted with $\mathcal{H}^k(\mathbb{T}^2 : \mathbb{R}^n)$, for $k \in \mathbb{R}$, while the subspace of $\mathcal{H}^k(\mathbb{T}^2 : \mathbb{R}^n)$ constitued by zero-mean functions, endowed with the homogeneous norm, is denoted with $\mathcal{H}^k_0(\mathbb{T}^2; \mathbb{R}^n)$.

We use the following notation regarding the Fréchet spaces:

- $C^\infty(\mathbb{T}^2; \mathbb{R}^d)$ is the Fréchet space of smooth periodic functions.
- $C^\infty_0(\mathbb{T}^2; \mathbb{R}^d)$ is the Fréchet space of smooth periodic functions which are mean free: $\phi \in C^\infty(\mathbb{T}^2; \mathbb{R}^d)$ such that $\langle \phi_i, 1 \rangle_{L^2(\mathbb{T}^2)} = 0$ for all $i = 1, \ldots, d$.

We consider Banach space valued stochastic processes, $X, Y : \Omega \times \mathbb{R}_+ \to E$. The quadratic variation is expressed as

$$\mathbb{R}_+ \ni t \mapsto [X]_t \, ,$$

while the covariation as

$$\mathbb{R}_+ \ni t \mapsto [X, Y]_t \ .$$

We denote with E a separable Hilbert space. If $I \subseteq \mathbb{R}_+$ is an interval, $\mathbb{F} \coloneqq \{\mathcal{F}_t\}_{t\in I}$ is a filtration. Then:

- $L^2_{\mathbb{F}}(I; E)$ is the space of progressively measurable processes $Z : \Omega \times I \to X$ such that

$$\mathbb{E}\left[\int_0^T \|Z_t\|_X^2 dt\right] < +\infty$$

- $C_{\mathbb{F}}(I; X)$ is the subspace of continuous adapted processes such that

$$\mathbb{E}\left[\sup_{t\in[0,T]} \|Z_t\|_X^2\right] < \infty \ .$$

Finally, if M is a 2×2 matrix, which can possibly depend on $x \in \mathbb{T}^2$, M is λ-*elliptic* or *elliptic* if for every unitary vector $\xi \in \mathbb{S}^1$ it holds:

$$\lambda \leq \xi \cdot M\xi \leq \frac{1}{\lambda}$$

If M depends on the space parameter $x \in \mathbb{T}^2$ and it is λ-elliptic for every $x \in \mathbb{T}^2$ for some λ independent of x, M is *uniformly* elliptic.

4.1.2 Stochastic advecting field

The stochastic field in equation (4.1) is made of locally supported vortex patches σ_k, arranged on a lattice indexed by the parameter $N \in \mathbb{N}$, Λ^N. This lattice is an integer lattice of $\mathbb{R}^2$, with resolution N^{-1},

$$\Lambda^N = \left(\frac{1}{N}\mathbb{Z} \times \frac{1}{N}\mathbb{Z}\right).$$

A point on the lattice, $x_k^n \in \Lambda^N$, is identified as:

$$x_k^n = \frac{k}{N} \ , k \in \mathbb{Z}^2.$$

Each vortex patch is centered on the lattice nodes, and the vorticity is specified via the stream function. To define the stream function ψ, we introduce the constant $c \in (0, +\infty)$. We fix $\psi \in C^\infty(\mathbb{R}^2; \mathbb{R})$ with $\mathrm{supp}(\psi) \in B(0, c)$ and such that there exists a smooth scalar function $f \in C^\infty(\mathbb{R}; \mathbb{R})$ for which the following relation holds:

$$\psi(x) = f(|x|). \tag{4.2}$$

Then, we define the vector fields σ_k^N as:

$$\sigma_k^N(x) \coloneqq \theta_k^N \frac{1}{r}(\nabla^\perp \psi)\left(\frac{x - x_k^N}{r}\right) = \theta_k^N \frac{1}{r} f'\left(\frac{|x - x_k^N|}{r}\right) \frac{(x - x_k^N)^\perp}{|x - x_k^N|}.$$

where $\{\theta^N\}_{N\in\mathbb{N}} \subset \ell^\infty(\mathbb{Z}^2;\mathbb{R})$ is a fixed family of sequences, $r > 1$ is a radius, $N \in \mathbb{N}$ and $k \in \mathbb{Z}^2$. $c > 0$ is a finite quantity, so there exists $n(c) \in \mathbb{N}$ such that the following relation holds:

$$\operatorname{supp}\left(\sum_{|k|\geq n(c)} \sigma_k^N\right) \cap \mathbb{T}^2 = \emptyset.$$

We model the time fluctuations as time varying stochastic weights, which are the intensities of the vortex patches. The stochastic advecting field has to be periodic on the torus $\mathbb{T}^2$; this requirement holds if the weight agree for nodes x_k^N, $x_{k'}^N \in \Lambda^N$ such that $x_k^N - x_{k'}^N \in \mathbb{Z}^2$. A choice of the weights which agrees with this condition is of a sequence of $\mathbb{R}$ valued Brownian motions $\{W_t^k\}_k$, of filtration $\mathbb{F} = \{\mathcal{F}_t\}_{t\geq 0}$, such that

$$\left[W^k, W^{k'}\right]_t = \begin{cases} t, & \text{if } x_k - x_{k'} \in \mathbb{Z}^2 \\ 0 & \text{otherwise.} \end{cases}$$

To satisfy the periodicity requirement, we also need to fix the sequence $\{\theta_k^N\}_{k\in\mathbb{Z}^2}$,

$$\theta_k^N = \theta_{k'}^N \qquad \text{if } x_k - x_{k'} \in \mathbb{Z}^2.$$

The correlation matrix of the noise is defined as:

$$A^N(x,y) \coloneqq \sum_{k\in\mathbb{Z}^2} \sigma_k^N(x) \otimes \sigma_k^N(y). \tag{4.3}$$

for $r < (2c)^{-1}$, which we will always assume in the rest of the chapter, as r will be sent to zero. We indicate with $A(x)$ the matrix $A^1(x,x)$. Note that if we take $L \in \mathbb{Z}_0^2$ and $k' = k - NL$, for all $x \in \mathbb{T}^2$, $x - x_k$ and $x - x_{k'}$ cannot be both in $B(0, rc)$, so one of $\sigma_k(x)$ or $\sigma_{k'}(x)$ is zero and also the correlation is zero.

Moreover, the following scaling relation and lemma hold.

$$\|(f)_r\|_{L_x^2(r\mathbb{T}^2)} = \|f\|_{L_x^2(\mathbb{T}^2)} \quad \text{with} \quad (f)_r(\,\cdot\,) \coloneqq \frac{1}{r} f\left(\frac{\cdot}{r}\right).$$

Lemma 4.1. *If*

$$\theta_k^N = \frac{1}{N} \text{ for all } k \in \mathbb{Z}^2, \tag{4.4}$$

then

$$A^N(x) = (A(Nx))_{Nr} = \sum_{k\in\mathbb{Z}^2} (\nabla^\perp\psi)_{Nr}(Nx - k) \otimes (\nabla^\perp\psi)_{Nr}(Nx - k). \tag{4.5}$$

In particular, if

$$\theta_k^N = r = \frac{1}{N} \text{ for all } k \in \mathbb{Z}^2 \tag{4.6}$$

then

$$A^N(x) = A^1(Nx) \tag{4.7}$$

We refer to [13] for the proof of this lemma.

4.2 Scaling Limit

In this section, we will investigate the scaling limit $N \to \infty$, for any sequence of solutions $\{u^N\}_{N\in\mathbb{N}}$ to (4.1), in terms of the scaling parameter $r := r(N) > 0$. In this limit, the distance between the centers of the vortex patches goes to zero, their radii r and intensities $\{\theta_k^N\}_{k\in\mathbb{Z}^2}$ are sent to zero, and we give an effective description of the stochastic system in terms of a deterministic parabolic system. Then, we investigate the effective diffusivity of the parabolic system, in the limit of small molecular diffusivity, $\kappa \to 0$.

We investigate two quantities, ε_N and π_N^κ, which have been introduced in the literature, see [63, 49, 54, 52]. ε_N is related to the stochastic fluctuations of the solution and is defined as

$$\varepsilon_N := \sup\left\{ \int\int_{\mathbb{T}^4} (\nabla v(x))^t A^N(x,y)\nabla v(y)\,\mathrm{d}x\,\mathrm{d}y : \ v\in\mathcal{H}^1(\mathbb{T}^2),\ \|\nabla v\|_{L^2}=1 \right\}. \tag{4.8}$$

Note that the fluctuation have to be small (*c.f.* Lemma 4.6). We define the elliptic operator:

$$\mathcal{L}_\kappa^N f = \operatorname{div}\left((\kappa I + A^N(x)\nabla) f\right).$$

π_N^κ is then defined as the first eigenvalue of the operator $-\mathcal{L}_\kappa^N$,

$$\pi_N^\kappa := \inf\left\{ \frac{\int_{\mathbb{T}^2}(\nabla v)^\top(x)(\kappa I + A^N(x,x))\nabla v(x)\,\mathrm{d}x}{\int_{\mathbb{T}^2}|v(x)|^2\,\mathrm{d}x} : \ v\in\dot{\mathcal{H}}^1, v\neq 0 \right\}. \tag{4.9}$$

and it is related to the dissipation of the deterministic part of the Itô equation. A non-trivial scaling limit is obtained for π_N^κ of fixed magnitude and $\varepsilon_N \searrow 0$ (*c.f.* section 4.3.2), see [63, 52].

Remark 4.1. If the uniform ellipticity inequality

$$\inf_{x\in\mathbb{T}^2}\inf_{\xi\neq 0}\frac{\xi^T A^N(x)\xi^T}{|\xi|^2} \geq M \tag{4.10}$$

holds, then

$$\pi_N^\kappa \geq C(\kappa + M)$$

with C the Poincaré constant of $\mathbb{T}^2$. In previous works, see [63, 49, 50, 52], to the best of our knowledge, (4.10) holds. However, the use of homogenization theory allows us to treat cases in which (4.10) does not hold, as in Lemma 4.15 and Remark 4.4.

In the rest of the section, we first write the Itô formulation of (4.1), then we enunciate a martingale estimate: in the case of N large enough, the noise introduced in equation (4.11) is so small that the solution is close to the solution of a deterministic equation in which the parameter N is finite. We assume that the scaling relation (4.4) holds.

4.2.1 Itô formulation of (4.1)

To write the Itô formulation of (4.1), we compute the Itô-Stratonovich corrector given by the covariation

$$\frac{\sqrt{2}}{2}\sum_{k\in\mathbb{Z}^2} d[\sigma_k^N\cdot\nabla u^N, W^k]_t\ .$$

We assume $r \leq (2c)^{-1}$. As σ_k is divergence-free,

$$d(\sigma_k^N \cdot \nabla u^N) = \operatorname{div}(\sigma_k^N du^N) = dV_t + \sqrt{2}\operatorname{div}((\sigma_k^N \otimes \sigma_l^N)\nabla u) dW_t^l$$

with V_t a process with bounded variation. Then, the Itô formulation of (4.1) is

$$du_t^N = \sqrt{2}\sum_{k\in\mathbb{Z}^2} \sigma_k^N \cdot \nabla u_t^N dW_t^k + \Big(\nabla \cdot (A^N \nabla u_t^N) + \kappa \Delta u_t^N\Big) dt \tag{4.11}$$

Definition 4.2. Given $u_0 \in L^2_0(\mathbb{T}^2)$ and $T > 0$, we say that a process $u^N \in C_{\mathbb{F}}(0,T; L^2_0(\mathbb{T}^2)) \cap L^2_{\mathbb{F}}(0,T; \mathcal{H}^1_0(\mathbb{T}^2))$ is a weak solution of (4.1) on $[0,T]$ if, for every $\phi \in C^\infty(\mathbb{T}^2)$ it holds that

$$\begin{aligned} \langle u_t^N, \phi\rangle = \langle u_0, \phi\rangle + \int_0^t \langle u_s^N, \nabla \cdot (\kappa I + A^N)\nabla\phi\rangle \, ds \\ + \sum_{k\in\mathbb{Z}^2} \int_0^t \sqrt{2}\langle u_s^N, \sigma_k^N \cdot \nabla\phi\rangle \, dW_s^k, \quad \mathbb{P}\text{-a.s.} \end{aligned} \tag{4.12}$$

Remark 4.2 (Mean Free Test Functions)**.** For any weak solution in the sense of Definition 4.2

$$\langle u_t^N, 1\rangle_{L^2_x} = \langle u_0, 1\rangle_{L^2_x} \, , \tag{4.13}$$

as (4.1) and (4.11) are in divergence form. We then require the test function ϕ in 4.2 to be mean free.

Proposition 4.3 (Energy Estimate)**.** *Let $u_0 \in L^2_0(\mathbb{T}^2)$ and $T > 0$. Then, there exists a unique solution to (4.1) in the sense of 4.2. Moreover it holds that*

$$\|u^N\|^2_{L^\infty_T L^2_x} + 2\kappa \int_0^T \|\nabla u_s^N\|^2_{L^2_x} \, \mathrm{d}x = \|u_0\|^2_{L^2_x}, \quad \mathbb{P}\text{-a.s.} \tag{4.14}$$

This proposition follows from the Itô formula, see [52, Thm. 1.2] [56, Thm. 1.2] and [47, Thm. 5.24].

4.2.2 Martingale estimate

We introduce the deterministic equation

$$\partial_t \tilde{u}_t^N = \nabla \cdot \Big(\big(\kappa I + A^N(x)\big)\nabla \tilde{u}_t^N\Big) \, , \tag{4.15}$$

with the following notion of weak solution.

Definition 4.4. Given $\tilde{u}_0 \in L^2_0(\mathbb{T}^2)$ and $T > 0$, we say that a path $u \in C([0,T]; L^2_0(\mathbb{T}^2))$ is a weak solution of (4.15) on $[0,T]$ if, for every $\phi \in C^\infty(\mathbb{T}^2)$, it holds that

$$\langle \tilde{u}_t^N, \phi\rangle = \langle \tilde{u}_0, \phi\rangle + \kappa \int_0^t \langle \tilde{u}_s^N, \nabla \cdot (\kappa I + A^N)\nabla\phi\rangle ds. \tag{4.16}$$

where the test function ϕ can be required to be mean free, see Definition 4.4. Our goal is to compare equation (4.11), for $N \in \mathbb{N}$ finite, with the deterministic equation (4.15).

Proposition 4.5. *For $N \in \mathbb{N}$, $\kappa > 0$ the following all hold.*

i) The operator $u \mapsto -\mathcal{L}_N^\kappa u := \nabla \cdot ((\kappa I + A^N)\nabla u)$, *for* $u \in \mathcal{D}(\mathcal{L}_N^\kappa) = \dot{H}^2(\mathbb{T}^2)$ *is strongly elliptic.*

ii) The operator $u \mapsto \mathcal{L}_N^\kappa u$ *is the infinitesimal generator of a analytic semigroup of operators on* H *for which we write* $[0, +\infty) \ni t \mapsto e^{t\mathcal{L}_N^\kappa}$. *In particular,*

$$\|e^{t\mathcal{L}_N^\kappa}\phi\|_{L^2_x} \lesssim_T e^{-\pi_N^\kappa t}\|\phi\|_{L^2_x} \quad \text{for all } \phi \in L^2_0(\mathbb{T}^2), \tag{4.17}$$

where π_N^κ *is defined by* (4.9).

iii) Given $T > 0$, *a weak solution* u^N *to* (4.11) *and a weak solution* $\tilde{u}^N$ *to* (4.15) *on* $[0, T]$, *then the following identities hold in the sense of distributions*

$$u_t^N = e^{t\mathcal{L}_N^\kappa}u_0 + \sqrt{2}\sum_{k\in\mathbb{Z}^2}\int_0^t e^{(T-s)\mathcal{L}_N^\kappa}\nabla u_s^N \cdot \sigma_k \, \mathrm{d}W_s^k, \quad \text{for all } t \in [0, T] \tag{4.18}$$

and

$$\tilde{u}_t^N = e^{t\mathcal{L}_N^\kappa}u_0, \quad \text{for all } t \in [0, T]. \tag{4.19}$$

We refer to [110, Sec. 7.2] for the proof of this proposition; see [57, Section 3.2] for the standard results such (4.18) and the uniqueness of the mild formulation.

We define the bi-linear form

$$L^2(\mathbb{T}^2;\mathbb{R}^2)^{\otimes 2} \ni (v, w) \mapsto \mathcal{A}^N(v, w) := \iint_{\mathbb{T}^4} v(x)^\top A^N(x, y)w(y) \, \mathrm{d}x \, \mathrm{d}y \in \mathbb{R} \, , \tag{4.20}$$

for any $N \in \mathbb{N}$. Then,

$$\varepsilon_N = \sup_{v\in\mathcal{H}^1, \|\nabla v\|=1} \mathcal{A}^N(v, v)$$

and from (4.3) and (4.4) we compute $A^N(v, v)$:

$$\mathcal{A}^N(v, v) = \iint_{\mathbb{T}^4} v(x)^\top A^N(x, y)v(y) \, \mathrm{d}x \, \mathrm{d}y \tag{4.21}$$

$$= \frac{1}{N^2 r^2}\sum_{k\in\square_1^2}\left[\int_{\mathbb{T}^2} v(x) \cdot \nabla^\perp \psi\left(\frac{x - k/N}{r}\right) dx\right]^2 . \tag{4.22}$$

Moreover,

$$\mathcal{A}^N(v, v) \geq 0 \, ,$$

as A^N is positive semi-definite.

Lemma 4.6. *Assume* (4.4). *For all* $v \in L^2(\mathbb{T}^2;\mathbb{R}^2)$, *it holds that*

$$\varepsilon_N = \sup_{N\in\mathbb{N}} \mathcal{A}^N(v, v) \lesssim_c r^2\|v\|^2_{L^2_x}\|\nabla^\perp\psi\|^2_{L^2_x}. \tag{4.23}$$

We refer to [13] for the proof of this lemma, which descends from the assumption that the function ψ has compact support.

Proposition 4.7. *Assume* (4.4). *Let* $u_0^N \in L^2(\Omega, \mathcal{F}_0, H)$, $T > 0$ *and* u^N, $\tilde{u}^N$ *be weak solutions to* (4.11) *and* (4.15) *with* u_0 *as initial data. Then, there exists a constant* $C := C(c) > 0$ *such that for every* $\phi \in C_0^\infty(\mathbb{T}^2)$

$$\sup_{t\in[0,T]} \mathbb{E}\left[\langle u_t^N - \tilde{u}_t^N, \phi\rangle^2\right] \leq \frac{Cr^2}{\kappa}\|\phi\|^2_{L^\infty}\mathbb{E}\left[\|u_0^N\|^2_{L^2}\right]$$

We refer to [13] for the proof of this proposition, which is based on the fact that we have the uniform bound of Lemma 4.6; this proposition allows us to have a quantitative mixing-type estimate for u^N for any $u_0 \geq 0$.

Corollary 4.8. *In the setting of Proposition 4.7, for any $\phi \in C_0^\infty(\mathbb{T}^2)$ there exists a constant $C := C(c, \|\phi\|_{L^\infty_x}) > 0$ such that*

$$\mathbb{E}\left[\left(\int_{\mathbb{T}^2} u^N(t,x)\phi(x)dx\right)^2\right] \leq 2\left(\frac{Cr^2}{\kappa} + \exp(-2\pi_N^\kappa t)\right)\mathbb{E}\left[\|u_0^N\|_{L^2}^2\right]. \tag{4.24}$$

We refer to [13] for the proof of this corollary.

Note that π_N^κ depends on the molecular diffusivity κ and on the radius of support of the vortex patches, c. For values of c which are sufficiently large, $A^N(x)$ is uniformly elliptic, see Lemma 4.15 and Proposition 4.17. Then, we have an estimate of π_N^κ, see Remark 4.1, which can be made arbitrarily large by choosing ψ so that for fixed $\kappa > 0$, and every $N > 0$, $c > 0$, it holds $\pi_N^\kappa > \kappa$. As we are interested in the regimes $N \to \infty$ and/or $\kappa \to 0$, we employ homogenization theory in order to obtain sharper estimates.

4.3 Homogenized limit

In this section, we study the homogenization of the solution of the deterministic equation (4.15): we show that it exists a constant $C(c,\kappa) \geq \kappa$ such that any solution of equation (4.15) converges in a suitable sense to the solution of the homogenized equation,

$$\partial_t \tilde{u} = C(c,\kappa)\Delta\tilde{u}$$

and we establish that the homogenized diffusivity matrix is a multiple of the identity matrix.

As a first step, we describe the setting and give some definitions related to Homogenization Theory.

4.3.1 Elements of Homogenization Theory

In this subsection, we recall some elements of Homogenization Theory. We indicate with $M(x)$ a smooth field of symmetric, uniformly elliptic matrices on $\mathbb{T}^2$. For $f^N \in \mathcal{H}^{-1}(\mathbb{T}^2)$ and any $N > 1$ we have the elliptic problem in weak formulation,

$$\nabla \cdot (M(Nx)\nabla u^N(x)) = f^N(x), \qquad u^N \in \dot{\mathcal{H}}^1(\mathbb{T}^2)\ , \tag{4.25}$$

and the elliptic PDE problem with solution ϕ_i,

$$\begin{cases} \nabla \cdot \Big(M(x)e_i + M(x)\nabla\phi_i(x)\Big) = 0 \\ \phi_i \in \dot{\mathcal{H}}^1_{per}(\mathbb{T}^2) \end{cases} \tag{4.26}$$

for $i = 1, 2$, $e_1 = (1,0)$, $e_2 = (0,1)$. (4.26) is well-posed, as $M(x)$ is uniformly elliptic, see [40, Sec. 6.2.1]. We define the matrix $\bar{M}_{ij}$, linked to the effective diffusivity of (4.25) for $N \to \infty$:

$$\begin{aligned} \bar{M}_{ij} = (\bar{M}e_j)\cdot e_i &:= \int_{\mathbb{T}^2} (M(x)(e_j + \nabla\phi_j(x)))\cdot e_i dx \\ &= \int_{\mathbb{T}^2} (M_{ij}(x) + (M(x)\nabla\phi_j(x)))\cdot e_i dx\ , \end{aligned} \tag{4.27}$$

with $\bar{M}$ with constant entries. Any solution u^N to (4.25) converges in $L^2(\mathbb{T}^2)$ to $u(x)$, the unique solution of

$$\nabla \cdot (\bar{M}\nabla u(x)) = f(x), \qquad u \in \dot{\mathcal{H}}^1(\mathbb{T}^2) \ , \tag{4.28}$$

if $f^N \to f \in \dot{\mathcal{H}}^{-1}(\mathbb{T}^2)$, see [6, Chapter 1]. We are interested in investigating the parabolic problem: in our study, the matrix M is time-independent and the homogenization of the parabolic problem reduces to the homogenization of the elliptic problem [6] : if for the initial condition u_0^N it holds $u_0^N \to u_0$ in $L^2(\mathbb{T}^2)$, the solution of the equation

$$\begin{aligned} \partial_t u^N(t,x) &= \nabla \cdot (M(Nx)\nabla u^N(t,x)) \ , \\ u^N(0,\cdot) &= u_0^N \in \dot{\mathcal{H}}^1(\mathbb{T}^2) \ , \\ u^N &\in C(0,T;\dot{\mathcal{H}}^1(\mathbb{T}^2)) \end{aligned}$$

converges in $L^2(0,T;L^2(\mathbb{T}^2))$ to $u(t,x) \in C(0,T;\dot{\mathcal{H}}^1(\mathbb{T}^2))$, unique solution of the equation

$$\begin{aligned} \partial_t u(t,x) &= \nabla \cdot (\bar{M}(x)\nabla u(t,x)) \ , \\ u(0,\cdot) &= u_0 \in \dot{\mathcal{H}}^1(\mathbb{T}^2) \ . \end{aligned}$$

Lemma 4.9. *Let $M(x)$ be a smooth and periodic field of symmetric matrices and let $0 \le \lambda \le \Lambda < +\infty$ be such that*

$$\sup_{x\in\mathbb{T}^2} |M(x)\xi| \le \Lambda\xi \quad \textit{and} \quad \inf_{x\in\mathbb{T}^2} M(x)\xi\cdot\xi \ge \lambda|\xi|^2 \quad \textit{for all } \xi \in \mathbb{R}^2. \tag{4.29}$$

Furthermore, we fix $\phi_i \in \mathcal{H}^1(\mathbb{T}^2)$, for $i = 1, 2$, weak solutions to (4.26). Then:

i) For every $\xi \in \mathbb{R}^2$,

$$|\bar{M}\xi| \le \Lambda|\xi| \left(\sum_{i=1}^{2} \int_{\mathbb{T}^2} |e_i + \nabla\phi_i(x)|^2 \, \mathrm{d}x \right)^{\frac{1}{2}} . \tag{4.30}$$

ii) For every $\xi \in \mathbb{R}^2$,

$$\bar{M}\xi \cdot \xi \ge \lambda|\xi|^2. \tag{4.31}$$

iii) The matrix $\bar{M}$ is symmetric.

We refer to [13] for the proof of this lemma.

4.3.2 Homogenization of the Stratonovich Corrector

In the following, we study the homogenization of solutions $\tilde{u}_t^N$ to (4.15) in the scaling (4.6). More precisely, any solution $\tilde{u}_t^N$ of (4.15) converges (*c.f.* 4.10) for $N \to \infty$ to the solution of the homogenized PDE

$$\partial_t \tilde{u} = C(c,\kappa)\Delta\tilde{u}$$

with $C(c,\kappa) \ge \kappa$ constant. For $\tilde{u}_t^N$, equation (4.15) is

$$\partial_t \tilde{u}^N(t,x) = \nabla \cdot \Big(H_\kappa(Nx)\nabla\tilde{u}^N(t,x) \Big).$$

where

$$H_\kappa(x) := \kappa I + A(x).$$

From Lemma 4.1 and the assumption $\theta^N = r = 1/N$,

$$A^N(x) = A^1(Nx) = A(Nx)$$

so we can employ standard results of homogenization theory; If $\kappa > 0$,

$$H_\kappa(x)\xi \cdot \xi = (\kappa I + A(x))\,\xi \cdot \xi \geq \kappa|\xi|^2 \quad \text{for} \quad \text{a.e.} \quad x \in \mathbb{T}^2 \tag{4.32}$$

(uniform ellipticity). H_κ does not depend on time, thus the homogenization of the parabolic problem reduces to homogenization of the elliptic operator H_κ, see [6, Ch. 2, Rem. 1.6] for details.

The Homogenized Limit

Proposition 4.10. *Assume (4.4). Let $u_0 \in \dot{L}^2(\mathbb{T}^2)$, $\kappa > 0$, $T > 0$ and $\tilde{u}^N$ be the associated unique weak solution of (4.15) in the sense of 4.4. For e_1, e_2 as above and ϕ_i for $i = 1, 2$ the unique solutions of*

$$\begin{cases} \nabla \cdot \Big(H_\kappa e_i + H_\kappa \nabla \phi_i \Big) = 0 \\ \phi_i \in \dot{\mathcal{H}}^1(\mathbb{T}^2). \end{cases} \tag{4.33}$$

we let $\bar{H}_\kappa$ be the matrix defined by

$$(\bar{H}_\kappa)_{ij} := \int_{\mathbb{T}^2} (H_\kappa(e_j + \nabla\phi_j)) \cdot e_i. \tag{4.34}$$

Then, finally, letting $\bar{u} \in L^2(0,T;\dot{\mathcal{H}}^1(\mathbb{T}^2))$ be the unique weak solution to the initial value problem

$$\partial_t \bar{u} = \nabla \cdot (\bar{H}\nabla\bar{u}), \qquad \bar{u}(0,x) = u_0 \tag{4.35}$$

one has the limits

$$\tilde{u}^N \to \bar{u} \quad \text{in } L^2([0,T];L^2(\mathbb{T}^2)) \quad \text{and} \quad \tilde{u}^N \rightharpoonup \bar{u} \text{ in } L^2([0,T];\mathcal{H}^1(\mathbb{T}^2)).$$

We refer to [6, Chapter 2, Thm. 2.1 & Rem. 1.6] for the proof of this proposition.

Corollary 4.11. *In the above setting it also holds that $\tilde{u}^N \to \bar{u}$ in $C([0,T];\mathcal{H}^-(\mathbb{T}^2))$. As a result, for any $\phi \in C^\infty(\mathbb{T}^2;\mathbb{R})$*

$$\lim_{N\to\infty} \sup_{t\in[0,T]} \left|\langle \tilde{u}^N - \bar{u}, \phi\rangle\right| = 0. \tag{4.36}$$

Proof. Since the matrix A is bounded, one has that:

$$\tilde{u}^N_t \in L^\infty([0,T];L^2(\mathbb{T}^2)) \quad , \quad \partial_t \tilde{u}^N \in L^2([0,T];\mathcal{H}^{-1}(\mathbb{T}^2)) \ .$$

Then, from the Aubin-Lions lemma, $\tilde{u}^N_t$ is pre-compact in $C([0,T];\mathcal{H}^{-\varepsilon}(\mathbb{T}^2))$ for every $\varepsilon > 0$. Moreover, the whole sequence converges also in $\mathcal{H}^-(\mathbb{T}^2)$, due to the uniqueness of the limit. □

Proposition 4.12. *For $H_\kappa = \kappa I + A$ and $\bar{H}_\kappa$ as defined by (4.34) it holds that $\bar{H}_k = C(c,\kappa)I$ for some positive constant $C(c,\kappa) \geq \kappa$.*

We refer to [13] for the proof that $\bar{H}$ is diagonal.

4.3.3 Combined Homogenised and Itô-Stratonovich Diffusion Limit

If we now put together results from the Itô-Stratonovich diffusion limit and the homogenized limit, the following theorem can be enunciated.

Theorem 4.13. *Assume (4.6). Let $u_0 \in L^2_0(\mathbb{T}^2)$, $T > 0$ and $\bar{u}$ be the associated weak solution to (4.35) as in 4.10. Under our fixed scaling assumptions ($\theta^N_\cdot \equiv r = \frac{1}{N}$), if u^N is the unique weak solution to (4.11) on $[0,T]$ with initial condition u_0, then, for every $\phi \in C^\infty(\mathbb{T}^2)$, it holds that*

$$\lim_{N\to+\infty} \sup_{t\in[0,T]} \mathbb{E}\left[\left|\langle u^N_t - \bar{u}_t, \phi\rangle\right|^2\right] = 0. \tag{4.37}$$

Proof. If we add and subtract $\tilde{u}^N_t$ in (4.37) and use the following inequality from Proposition 4.7,

$$\sup_{t\in[0,T]} \mathbb{E}\left[\left|\langle u^N_t - \tilde{u}^N_t, \phi\rangle\right|^2\right] \leq \frac{1}{N^2\kappa}\|u_0\|^2_{L^2},$$

we obtain

$$\sup_{t\in[0,T]} \mathbb{E}\left[\left|\langle u^N_t - \bar{u}_t, \phi\rangle\right|^2\right] \leq 2 \sup_{t\in[0,T]} \mathbb{E}\left[\left|\langle u^N_t - \tilde{u}^N_t, \phi\rangle\right|^2\right] + 2 \sup_{t\in[0,T]} \left|\langle \tilde{u}^N_t - \bar{u}_t, \phi\rangle\right|^2 \tag{4.38}$$

$$\lesssim \frac{1}{N^2\kappa}\|u_0\|^2_{L^2} + 2 \sup_{t\in[0,T]} \left|\langle \tilde{u}^N_t - \bar{u}_t, \phi\rangle\right|^2. \tag{4.39}$$

Then, 4.11 ensures that for every $\varepsilon > 0$ exists $N_0 := N_0(\varepsilon) \in \mathbb{N}$ such that for every $N > N_0$,

$$\sup_{t\in[0,T]} \left|\langle \tilde{u}^N_t - \bar{u}_t, \phi\rangle\right|^2 \leq \varepsilon$$

it holds for arbitrary ε that

$$\limsup_{N\to+\infty} \sup_{t\in[0,T]} \mathbb{E}\left[\left|\langle u^N_t - u_t, \phi\rangle\right|^2\right] \leq \varepsilon.$$

□

We refer to [13] for the proof of this theorem. Theorem 4.13 allows us to improve the mixing estimate in 4.8.

Corollary 4.14. *Assume (4.6), then for every $\varepsilon > 0$, there exists N large enough such that*

$$\mathbb{E}\left[\left(\int_{\mathbb{T}^2} u^N(t,x)\phi(x)dx\right)^2\right] \lesssim_\phi 2\left(\varepsilon + \exp(-2C(c,\kappa)t)\right)\mathbb{E}\left[\|u^N_0\|^2_{L^2}\right].$$

We refer to [13] for the proof of this corollary. A quantitative estimate can be obtained as in [126].

Remark 4.3. It holds

$$\pi^\kappa_N \to C(c,\kappa) \quad \text{as} \quad N \to +\infty\ ,$$

see [102, Chapter 24], Thm 24.1.

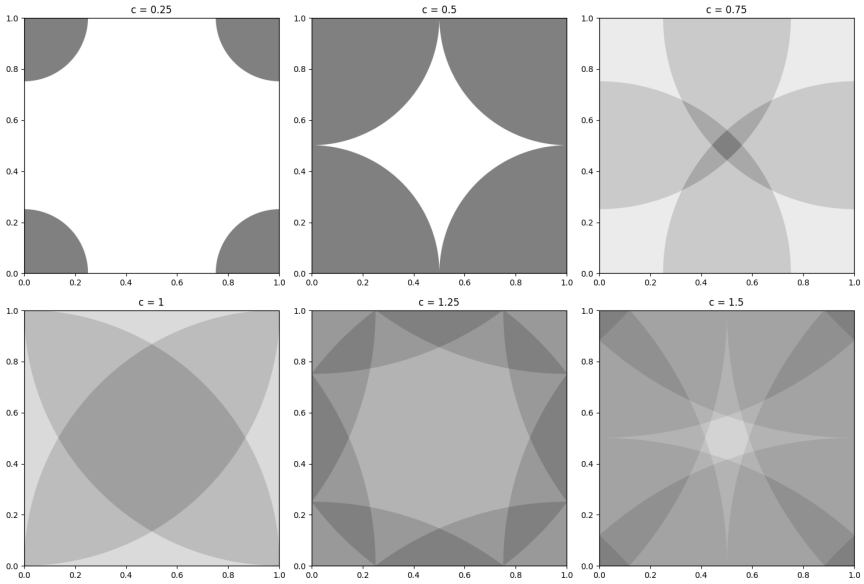

Figure 4.1: Illustration of the supports of $A(x)$ for selected $c \in \{0.25, 0.5, 0.75, 1, 1.25, 1.5\}$. Darker shading represent multiple overlaps.

4.4 Homogenised diffusivity

In this section, we investigate and quantitatively estimate the diffusivity $C(c, \kappa)$. For

$$\lambda_A = \inf_{x \in \mathbb{T}^2} \sup_{\xi \neq 0} \frac{\xi^T A(x) \xi}{|\xi|^2} \ ,$$

one has the following inequality for the diffusivity,

$$C(c, \kappa) \geq (\kappa + \lambda_A) \ . \tag{4.40}$$

Note that the factor λ_A can be made arbitrarily large by acting on the intensities and the supports of the σ_k^N, see 4.17. In the following, we will take into account also the case $\lambda_A = 0$; moreover, we investigate the behavior of $C(c, \kappa)$ distinguishing different regimes for different values of the parameter c, in the limit $\kappa \to 0$. The difference between the behaviors is due to the different overlap of the patches. In [46] a similar system, a cellular transport, is investigated.

4.4.1 Properties of the matrices A^N

The matrix A^N is a positive semi-definite matrix for every $x \in \mathbb{T}^2$. It is defined as the periodicization of one vortex patch; in the case $c \leq 1$ the sum in the definition of A^N has all terms equals to zero, except for $k \in \{(0,0),\ (1,0),\ (0,1),\ (1,1)\}$, and because of the choice of the support of the smooth radial function ψ, $A(k) = 0$ at each lattice points $k \in \mathbb{Z}^2$. Our goal is to understand when $A(x)$ does not have full rank.

Lemma 4.15. *The following situations all hold.*

1. *If $c = 1/2 - \delta$ for some $\delta \in (0, \frac{1}{2})$ then*

$$\left\{(x_1, x_2) \in \mathbb{T}^2 : \min(|x_1 - 1/2|, |x_2 - 1/2|) \leq 2\delta\right\} \subset supp(A)^c.$$

2. *If $1/2 \leq c < \frac{\sqrt{2}}{2}$, then letting $\delta = \frac{\sqrt{2}}{2} - c$, it holds that*

$$\left\{x \in \mathbb{T}^2 : \min_{k \in \{(0,0),(0,1),(1,0),(1,1)\}} (|x - k|) \geq \frac{\sqrt{2}}{2} - \delta\right\} = supp(A)^c.$$

3. *If $\sqrt{2}/2 \leq c \leq 1$ then letting $\delta = 1 - c$ it holds that A has a null eigenvalue in the region*

$$\left\{x \in \mathbb{T}^2 \, : \, |x - k| \geq 1 - \delta \text{ for exactly three } k \text{ out of } (0,0), (0,1), (1,0), (1,1)\right\}$$

and on the edges of the square $\partial([0,1]^2)$, while it has full rank in the rest of $[0,1]^2$.

4. *Let $1 \leq c \leq \frac{\sqrt{5}}{2}$, then setting $\delta = \frac{\sqrt{5}}{2} - c$ it holds that A has full rank outside of the region*

$$\left\{x \in \mathbb{T}^2 \, : \, \exists\, a \in B\left(\frac{1}{2}, \sqrt{\frac{1}{4} + \delta^2 - \sqrt{5}\delta}\right) \text{ s.t. } x \in \{(a,0), (a,1), (0,a), (1,a)\} \right\}. \tag{4.41}$$

Furthermore, in this region it has one null eigenvalue.

5. *If $c > \sqrt{5}/2$ then A is strictly positive definite everywhere on $\mathbb{T}^2$.*

Proof. 1. Since the vortices are located at integer lattice points $k \in \mathbb{Z}^2$ and have support in the ball of radius c, only finitely many vortices contribute at any point $x \in \mathbb{T}^2$. In particular, when $c < 1$, only the contribution of the four patches at the corners of the square is relevant. Only if the torus is not fully covered by the vortex patches we have regions in which $A \equiv 0$. In this first case, the region described in the statement consists of two strips separating the supports of the patches σ_k at the corners of the square.

2. In this case, there is overlap between the supports, however the torus is not fully covered (c is not large enough to reach the center) and in the region described in the statement, $A \equiv 0$.

3. In this case, there is again overlap between the supports, but c is large enough that the torus is fully covered. We recall the definition of $A(x)$,

$$A(x) = \sum_{k \in \square_1^2} \nabla^\perp \psi(x - k) \otimes \nabla^\perp \psi(x - k) \, , \tag{4.42}$$

namely for $k \in \mathbb{Z}^2$, $A(x)$ is the sum of orthogonal projections along $\nabla^\perp \psi(x - k)$. In the region described in the statement, only one of the four vortices contributes to the sum, so A does not have full rank. Outside that region, more than one vortex patch contributes, up to four. If there are two, $x - k_1$ and $x - k_2$ are linearly independent unless x is in the span of $k_1 - k_2$, as ψ is radial, and for every $x \in \mathbb{T}^2$, $\nabla^\perp \psi(x - k)$ is parallel to $(x - k)^\perp$. $x - k_1$ and $x - k_2$ are not linearly independent only on the edges. if there are three or four patches, we argue by contradiction. We suppose there exists $w \in \mathbb{R}^2 \setminus \{0\}$ such that $w \cdot A(x) w = 0$, and thus $\sum_{k \in \square_1^2} |\nabla^\perp \psi(x - k) \cdot w|^2 = 0$. However, this holds if and only if $\omega \perp (x - k)$ for all patches k which contributes. Then, if the k are not all collinear, $w = 0$.

4. In this case, the proof is similar to the previous case. In particular, $\{\nabla^\perp\psi(x-k)\}_{k\in\square_1^2}$ spans $\mathbb{R}^2$ for every $x\in\mathbb{T}^2$ except on the edges of the square. For every $x\in\mathbb{T}^2$, the condition $c>1$ ensures the contribution of at least two or three vortices with non co-linear centres. In the regions where more than two patches contributes, $A(x)$ has full rank, so only the region where two patches contributes is relevant for our discussion; in this region, $A(x)$ has rank 1 only on the segment which connects the vortex centres, a subset of the edges of the square.

5. In this last case, $A(x)$ has full rank at any point $x\in\mathbb{T}^2$, as at least three patches with non co-linear centres contribute.

□

Remark 4.4. The null eigenspace of the matrix for $1\le c<\sqrt{5}/2$ is parallel to $\partial[0,1]^2$, the lattice's boundary:

$$\begin{aligned} A(x)e_1 &= 0 \qquad \text{for } \ x=(x_1,0) \text{ or } \ x=(x_1,1),\\ A(x)e_2 &= 0 \qquad \text{for } \ x=(0,x_2) \ \text{ or } \ x=(1,x_2). \end{aligned}$$

This is a consequence of Lemma 4.15. For $c\ge 1$, if $A(x)$ is invertible, as it is symmetric, its inverse is:

$$A^{-1}(x)=\frac{1}{\det(A(x))}\sum_{k\in\mathbb{Z}^2}\nabla\psi(x-k)\otimes\nabla\psi(x-k)\ . \tag{4.43}$$

Lemma 4.16. *For any $x\in\mathbb{T}^2$ and $v\in\mathbb{S}^1$ it is always possible to find an integer point $\bar{k}\in\square_1^2$ such that*

$$\left| v\cdot\frac{(x-\bar{k})^\perp}{|x-\bar{k}|}\right| > \frac{1}{\sqrt{2}}. \tag{4.44}$$

Moreover, $\bar{k}$ can always be chosen such that $|x-\bar{k}|\le\sqrt{5}/2$.

We refer to [13] for the proof of this lemma.

Proposition 4.17. *Let $\theta_k^N\equiv r=\frac{1}{N}$ and $c>\sqrt{5}/2$. Then, there exists a constant M such that for every $\xi\in\mathbb{R}^2\setminus\{0\}$*

$$A^N(x)\,\xi\cdot\xi\ge M|\xi|^2\ , \tag{4.45}$$

which holds for all $x\in\mathbb{T}^2$. Moreover, it holds that

$$M\ge m:=\inf\left\{|f'(y)|,\ y\in B(0,\sqrt{5}/2)\right\}. \tag{4.46}$$

Proof. From the definition of $A(x)$, we can compute the quantity $A(x)\xi\cdot\xi$,

$$A(x)\xi\cdot\xi:=A^1(x)\xi\cdot\xi=\sum_{k\in\square_1^2}|\nabla^\perp\psi(x-k)\cdot\xi|^2\ .$$

As we took $\theta_k^N\equiv r=\frac{1}{N}$ and $c>\sqrt{5}/2$, it follows from Lemma 4.1 that $A^N(x)=A(Nx)$. Thus, we only need to prove the case $N=1$.

We compute the quantity $A(x)\xi\cdot\xi$,

$$A(x)\xi\cdot\xi=\sum_{k\in\mathbb{Z}^2}\left|\frac{(x-k)^\perp}{|x-k|}\cdot\xi\,f'(|x-k|)\right|^2\ge\frac{1}{2}\inf_{k\in\mathbb{Z}^2}|f'(x-k)|^2\ ,$$

where we used

$$\nabla^{\perp}\psi(x-k) = \frac{(x-k)^{\perp}}{|x-k|} f'(|x-k|)$$

and Lemma 4.16. The assumptions on the support of f ensures that the weakest condition under which the quantity $A(x)\xi \cdot \xi$ does not vanish is $\sup_{k\in\square_2^2} |x-\bar{k}| < c$. This assumption holds, due to Lemma 4.16 and $c > \sqrt{5}/2$; we also obtain the lower bound of M by $m \coloneqq \inf\left\{|f'(y)|,\, y \in B(0,\sqrt{5}/2)\right\}$. □

4.4.2 Variational functional

To investigate the homogenized diffusivity, we employ a variational formulation, made possible by the symmetry of the matrix H_κ. From Proposition 4.12 and (4.34),

$$C(c,\kappa) = \xi \cdot \int_{\mathbb{T}^2} H_\kappa(x)(\xi + \nabla\phi_\xi(x))\ \mathrm{d}x \tag{4.47}$$

where $\xi \in \mathbb{S}^1$ is the unit vector, and ϕ_ξ solves the cell problem (4.33) in which e_i is replaced by ξ. As H_κ is a symmetric matrix and ϕ_ξ is the solution of (4.33),

$$C(c,\kappa) = \int_{\mathbb{T}^2} |H_\kappa^{1/2}(x)(\xi + \nabla\phi_\xi(x))|^2 dx \tag{4.48}$$

where we integrated by parts. We define the convex functional,

$$\mathcal{H}^1(\mathbb{T}^2) \ni u \mapsto \mathcal{E}_\kappa(u) = \int_{\mathbb{T}^2} |H_\kappa^{1/2}(x)(\xi + \nabla u)|^2 dx\ ,$$

for any $\xi \in \mathbb{S}^1$. From the Euler-Lagrange equation associated to $\mathcal{E}_\kappa$, the cell problem solution ϕ_ξ is the minimizer of $\mathcal{E}_\kappa$, and $\mathcal{E}_\kappa(\phi_\xi)$ is obtained as the minimum of the functional $\mathcal{E}_\kappa(u)$:

$$\mathcal{E}_\kappa(\phi_\xi) = \min_{u\in\mathcal{H}^1(\mathbb{T}^2)} \mathcal{E}_\kappa(u) \quad \text{and} \quad \phi_\xi = \operatorname*{arg\,min}_{u\in\mathcal{H}^1(\mathbb{T}^2)} \mathcal{E}_\kappa(u).$$

The energy $\mathcal{E}_\kappa$ admits a unique minimizer, which coincides with the cell problem solution in a given direction ξ. Moreover, the energy evaluated at this minimizer, viewed as a function of ξ, defines the quadratic form associated with the homogenized matrix $\overline{H}_\kappa = C(c,\kappa)I$.

4.4.3 Additional Diffusivity

We define the *additional diffusivity* ν_κ, in the homogenized limit:

$$\nu_\kappa \coloneqq C(c,\kappa) - \kappa = \left(\bar{H}_\kappa \xi \cdot \xi - \kappa\right), \qquad \xi \in \mathbb{S}^1\ . \tag{4.49}$$

The additional diffusivity does not depend on the choice of ξ. The goal of this section is to investigate this quantity for different values of the parameter c. Before stating the main theorem, we enunciate two results on the matrix $\overline{H}_\kappa - \kappa I$:

1. for $c \in (0, \sqrt{2}/2)$ the matrix $\bar{H}_\kappa - \kappa I$ is non-negative definite for all $\kappa > 0$;
2. for $c > \sqrt{5}/2$ the matrix $\bar{H}_\kappa - \kappa I$ is positive definite with a quantifiable lower bound.

Those results follows from Lemma 4.9 and from Lemma 4.15, which characterize the ellipticity properties of the matrix A depending on the value of the parameter c. In particular, $c \in (0, \sqrt{2}/2)$ ensures that the support of A has measure strictly smaller than that of the torus, while $c > \sqrt{5}/2$ ensures that the matrix A is strictly positive definite everywhere on $\mathbb{T}^2$. In this case, a quantifiable lower bound on the ellipticity of A is available (see Proposition 4.17).

Theorem 4.18. *Under the same assumptions of the previous theorem the following statements hold:*

i) If $c \in (0, \frac{1}{2})$ (i.e. the vorticity patches are completely separated) there exists a constant $L > 1$, depending only on c such that

$$\kappa \leq C(c, \kappa) \leq L\kappa \quad \text{for all } \kappa > 0. \tag{4.50}$$

In particular, the constant L does not depend on the specific choice of the radial function ψ.

ii) If $c = \frac{1}{2}$ for any $n \geq \frac{7}{2}$ there exists a $p := p(n) \geq 1$ and a constant $L' := L'(c, \|\psi\|_{W^{p+1,\infty}_x}) > 0$ such that

$$\kappa \leq C(c, \kappa) \leq L'(\kappa + \kappa^{1-\frac{1}{n}}) \quad \text{for all } \kappa > 0. \tag{4.51}$$

iii) If $c \geq \sqrt{2}/2$, then there exists a constant $m > 0$ such that

$$C(c, \kappa) \geq \kappa + m \quad \text{for all } \kappa > 0. \tag{4.52}$$

Moreover, in this case, the constant m can be made arbitrarily large by a suitable choice of the stream function ψ (see Remark 4.5 below).

Remark 4.5. From Theorem 4.18 iii),

a) If $\frac{\sqrt{2}}{2} < c$ then m is 1-homogeneous in ψ (i.e. m^λ associated to $\lambda\psi$ satisfies $m^\lambda = \lambda m^1$.)

b) If $\frac{\sqrt{5}}{2} < c$ then we have $m \geq \inf\{|f'(y)|, y \in B(0, \sqrt{5}/2)\}$.

See Remark 4.7 for the first relation; see Proposition 4.17 and Lemma 4.9 for the second.

The regime $c \in (0, \frac{1}{2})$

From Lemma 4.9,

$$C(c, \kappa) \geq \kappa \quad \Longrightarrow \quad \nu_\kappa \geq 0 \quad ; \quad \lim_{\kappa \to 0} \nu_\kappa(\xi) \geq 0 \, . \tag{4.53}$$

for all $\xi \in \mathbb{R}^2$ and $\kappa > 0$, as A is not uniformly elliptic. Our goal is to compute an upper bound for $\nu_\kappa(\xi)$; in the following, we take $\xi = e_1 = (1, 0)$ and we build approximate solutions of the cell problem for e_1.

Lemma 4.19. *Let $c \in (0, \frac{1}{2}]$. Then, there exists a constant $L > 0$ depending on $c > 0$ alone for $c \in (0, \frac{1}{2})$, such that*

$$\nu_\kappa \leq L\kappa. \tag{4.54}$$

For $c = \frac{1}{2}$ and any $n \geq \frac{7}{2}$ there exists a $p := p(n) \geq 1$ and a constant $L' := L'(c, \|\psi\|_{W^{p+1,\infty}_x}) > 0$ such that

$$\nu_\kappa \leq L' \left(\kappa + \kappa^{1-\frac{1}{n}}\right). \tag{4.55}$$

Proof. In the following, we report only a sketch of the proof; we refer to [13] for the detailed proof.

For any $\xi \in \mathbb{S}^1$,

$$\begin{aligned}\nu_\kappa &= \left(\bar{H}_\kappa \xi \cdot \xi - \kappa\right) \\ &= \inf_{\phi \in H^1_0(\mathbb{T}^2)} \left\{ \int_{\mathbb{T}^2} \left[\kappa |\nabla\phi(x)|^2 + (\nabla\phi(x))^\top A(x) \nabla\phi + 2(\nabla\phi(x))^\top A(x)\xi + \xi A(x)\xi\right] \mathrm{d}x; \right\},\end{aligned}$$

where we used the definition of H_κ and $C(c,\kappa)$, as in (4.48) and Proposition 4.12. This equality implies that for any $\phi \in H^1_0(\mathbb{T}^2)$, the following inequality holds:

$$\nu_\kappa \leq \int_{\mathbb{T}^2} \left[\kappa |\nabla\phi(x)|^2 + (\nabla\phi(x))^\top A(x) \nabla\phi(x) + 2(\nabla\phi(x))^\top A(x)\xi + \xi A(x)\xi\right] \mathrm{d}x. \tag{4.56}$$

Using the definition of $A(x)$, we rewrite

$$(\nabla\phi(x))^\top A(x) \nabla\phi(x) + 2(\nabla\phi(x))^\top A(x)\xi + \xi A(x)\xi = \sum_{k \in \square_1^2} \left|(\nabla\phi(x) + \xi) \cdot \nabla^\perp \psi(x-k)\right|^2, \tag{4.57}$$

and for (4.56) we obtain

$$\nu_\kappa \leq \int_{\mathbb{T}^2} \left[\kappa |\nabla\phi(x)|^2 + \sum_{k \in \square_1^2} \left|(\nabla\phi(x) + \xi) \cdot \nabla^\perp \psi_k(x-k)\right|^2\right] \mathrm{d}x \tag{4.58}$$

We take $\xi = e_1 = (1,0)$ and

$$\phi(x) = \begin{cases} -x_1, & x_1 \in [0,c], \\ \frac{2c}{1-2c} x_1 - \frac{c}{1-2c}, & x_1 \in [c, 1-c], \\ 1 - x_1, & x_1 \in [1-c, 1]. \end{cases} \tag{4.59}$$

for which,

$$\nabla\phi(x) = \begin{cases} -e_1, & x_1 \in (0,c) \cup (1-c,1) \\ \frac{2c}{1-2c} e_1, & x_1 \in (c, 1-c) \end{cases} \tag{4.60}$$

In this case, we obtain the following inequality:

$$\begin{aligned}\nu_\kappa \leq & \kappa \left(2 \int_0^c \int_0^1 \mathrm{d}x_1\, \mathrm{d}x_2 + \int_c^{1-c} \int_0^1 \left|\frac{2c}{1-2c}\right|^2 \mathrm{d}x_1\, \mathrm{d}x_2\right) && (4.61) \\ & + \sum_{k \in \square_1^2} \int_{B(k,c)} \left|(-e_1 + e_1) \cdot \nabla^\perp \psi(x-k)\right|^2 \mathrm{d}x && (4.62) \\ = & 2\kappa \left(c + \frac{4c^2}{(1-2c)^2}\right) && (4.63)\end{aligned}$$

and we conclude the proof for the case $c \in (0, 1/2)$.

However, as $c \to 1/2$, the estimate (4.63) degenerates. To treat the case $c = 1/2$, we define a family of approximate competitors for $\delta \in (0, 1/2)$,

$$\phi^\delta(x) = \begin{cases} -x_1, & x_1 \in [0, 1/2 - \delta], \\ \frac{1-2\delta}{2\delta} x_1 + \frac{2\delta - 1}{4\delta}, & x_1 \in [1/2 - \delta, 1/2 + \delta], \\ 1 - x_1, & x_1 \in [1/2 + \delta, 1]. \end{cases} \tag{4.64}$$

Using the symmetry of the sum and the radial symmetry of ψ, we obtain for every $\delta \in (0, 1/2)$

$$\begin{aligned}\nu_\kappa \leq \kappa &\left(2\int_0^1 \int_0^{1/2-\delta} \mathrm{d}x_1\,\mathrm{d}x_2 + \int_0^1 \int_{1/2-\delta}^{1/2+\delta} \left|\frac{1-4\delta}{8\delta}\right|^2 \mathrm{d}x_1\,\mathrm{d}x_2 \right) \\ &+ \sum_{k\in\square_1^2} \int_{B(k,1/2)\cap([1/2-\delta,1/2+\delta]\times[0,1])} \left| \left(\frac{1-4\delta}{8\delta}+1\right) e_1\cdot\nabla^\perp\psi(x-k)\right|^2 \mathrm{d}x \\ = 2\kappa &\left(\frac{1}{2}-\delta+\frac{(1-4\delta)^2}{8\delta}\right) \\ &+ 4\int_{B(0,1/2)\cap([1/2-\delta,1/2]\times[0,1])} \left| \left(\frac{1-4\delta}{8\delta}+1\right) e_1\cdot\nabla^\perp\psi(x)\right|^2 \mathrm{d}x.\end{aligned}$$

We assume $D^a\nabla^\perp\psi|_{\partial_{B(0,1/2)}} = 0$ for all $a \in \mathbb{N}^2$ and $\nabla^\perp\psi \in C^\infty(\mathbb{T}^2)$, so we may perform a Taylor expansion of arbitrary order about any point $x \in \partial B(0, 1/2)$. We take again $\delta \in (0, 1/2)$, and we define

$$B(0,1/2)\cap\{x_1 = 1/2-\delta\} =: x_\delta = \left(1/2-\delta, \sqrt{\delta(1-\delta)}\right),$$

for which

$$|x_\delta - (1/2, 0)| = \sqrt{\delta},$$

For any $x \in B(0, 1/2) \cap ([1/2-\delta, 1/2]\times[0, 1])$ and $p \geq 0$, it holds

$$\begin{aligned}|\nabla^\perp\psi(x)| &= \left|\nabla^\perp\psi(x) - \sum_{|a|\leq p}\frac{1}{a!}D^a\nabla^\perp\psi((1/2,0))(x-(1/2,0))^a\right| && (4.65)\\ &\leq \sup_{x\in B(0,1/2)\cap[1/2-\delta,1/2]\times[0,1]} |x-(1/2,0)|^{p+1} \max_{|a|=p+1}\|D^a\nabla^\perp\psi_1\|_{L^\infty(\mathbb{T}^2)} && (4.66)\\ &\lesssim \delta^{\frac{p+1}{2}}\|\nabla^\perp\psi\|_{W^{p+1,\infty}(\mathbb{T}^2)}, && (4.67)\end{aligned}$$

where we only reported part of the computations. See [13] for a detailed explanation. It holds the following inequality,

$$\left|B(0,1/2)\cap[1/2-\delta,1/2]\times[0,1]\right| \leq \delta\sqrt{\delta(1-\delta)} \lesssim \delta^{3/2}. \tag{4.68}$$

Then, for any $p \geq 1$,

$$\begin{aligned}\int_{B(k_1,1/2)\cap[\delta,1/2]\times[0,1]} &\left| \left(\frac{1-4\delta}{8\delta}+1\right) e_1\cdot\nabla^\perp\psi(x)\right|^2 \mathrm{d}x \\ &\leq \delta^{\frac{p+4}{2}}\left|\frac{1-4\delta}{8\delta}+1\right|^2 \|\nabla^\perp\psi\|^2_{W^{p+1,\infty}(\mathbb{T}^2)},\end{aligned}$$

again see [13] for the full computation. We obtain

$$\begin{aligned}\nu_\kappa &\leq 2\kappa\left(\frac{1}{2}-\delta+\frac{(1-4\delta)^2}{8\delta}\right) + 2\delta^{\frac{p+4}{2}}\left|\frac{1-4\delta}{8\delta}+1\right|^2\|\nabla^\perp\psi\|^2_{W^{p+1,\infty}(\mathbb{T}^2)} \\ &\lesssim (1+\|\psi\|_{W^{p+1,\infty}})\left(\kappa+\frac{\kappa}{\delta}+\delta^{\frac{p+4}{2}}\right).\end{aligned}$$

We take $\delta = \kappa^\alpha$ for some $\alpha > 0$, and we have

$$\nu_\kappa \lesssim_{\|\psi\|_{W^{p+1,\infty}}} \kappa + \kappa^{1-\alpha} + \kappa^{\frac{\alpha(p+4)}{2}}.$$

We choose the parameter $\alpha > 0$ such that

$$1 - \alpha = \frac{\alpha(p+4)}{2} \qquad \Longleftrightarrow \qquad \alpha = \frac{2}{p+6},$$

obtaining

$$\nu_\kappa \lesssim_{\|\psi\|_{W^{p+1,\infty}}} \kappa + 2\kappa^{1-\frac{2}{p+6}}.$$

Then, for any $n \geq 7/2$ there exists a $p := p(n) \geq 1$, $p(n) = 2n - 6$, such that

$$\nu_\kappa \lesssim_{\|\psi\|_{W^{p(n)+1,\infty}}} \kappa + \kappa^{1-\frac{1}{n}}.$$

and the result follows.

□

Remark 4.6. For $c = \frac{1}{2}$, ψ has to be smooth to perform Taylor expansions of arbitrarily high order. We recall that ψ is compactly supported, thus it cannot be analytic. This implies that it is not possible to take the limits $p(n)$, $n \to +\infty$. In the next section, numerical simulations (see Figure 4.5) will show that the exponent drops from the value one (linear behavior) for $c < \frac{1}{2}$ to strictly less than one for $c = \frac{1}{2}$.

The regime $\frac{1}{2} < c < \frac{\sqrt{2}}{2}$:

In this regime, the torus is not fully covered, so we cannot use the same arguments as the case $c > \sqrt{2}/2$ below. If we try to reason as in the previous case, unfortunately, we are not able to construct competitors $\phi(x)$ such that $\nabla\phi(x) = -\xi = -e_1$ on the support of the patches, due to the regions where there is overlap. For this reason, the quantity $\nabla\phi + \xi$ cannot vanish on the whole support of the matrix A.

The regime $\frac{\sqrt{2}}{2} < c < \frac{\sqrt{5}}{2}$:

For $\frac{\sqrt{2}}{2} < c < \frac{\sqrt{5}}{2}$, there exists a constant m independent of κ such that $C(c,\kappa) \geq m > 0$, as shown below. This implies that the additional diffusivity ν_k is such that $\nu_k > 0$, and this result holds uniformly in $kappa > 0$.

Definition 4.20. Let $\xi \in \mathbb{S}^1$ be given and define the affine space

$$\mathcal{V}_\xi = \left\{ F \in C^\infty(\mathbb{T}^2, \mathbb{R}^2) : \int_{\mathbb{T}^2} F = \xi,\ \nabla^\perp \cdot F = 0 \right\}.$$

V_ξ is the closure of $\mathcal{V}_\xi$ in $L^2(\mathbb{T}^2, \mathbb{R}^2)$.

Let $c > 1$, introduce on V_ξ the quadratic functional

$$\|F\|_A^2 := \int_{\mathbb{T}^2} F^\top(x) A(x) F(x) dx = \sum_{k \in \square_1^2} \int_{\mathbb{T}^2} |F \cdot \nabla^\perp \psi(x-k)|^2 dx$$

Lemma 4.21. *The infimum of $\|\cdot\|_A$ on V_ξ coincides with the infimum on $\mathcal{V}_\xi$.*

We refer to [13] for the proof of this lemma. In the following, we write V, $\mathcal{V}$ instead of V_ξ, $\mathcal{V}_\xi$.

Lemma 4.22. *Let $F \in \mathcal{V}$, defined on $\mathbb{R}^2$, $a \in [0,1]$ and define the curves*

$$\gamma_H(t) = (t, a), \quad \gamma_V(t) = (a, t)$$

and the functions

$$g_H(x) = x_2 - a, \quad g_V(x) = -x_1 + a.$$

Then, it holds that

$$\int_0^1 F_1(t,a)dt = \int_{\gamma_H} g_H F d\tau = \xi_1 \quad \text{and} \quad \int_0^1 F_1(a,t)dt = \int_{\gamma_V} g_V F d\tau = -\xi_2 \ .$$

We refer to [13] for the proof of this lemma.

Corollary 4.23. *Let $c > \frac{\sqrt{2}}{2}$ and $\xi \in \mathbb{S}^1$. Then it holds that,*

i) $\inf_{F \in V} \|F\|_A > 0$.

ii) There exists a constant $m > 0$ such that

$$\inf_{u \in \mathcal{H}^\infty(\mathbb{T}^2)} \mathcal{E}_0(u) = \int (\xi + \nabla u(x))^t A(x)(\xi + \nabla u(x))dx > m$$

iii) For every $k > 0$, if u_k^* is the minimizer of $\mathcal{E}_k$, it holds that

$$\mathcal{E}_k(u_k^*) \geq \kappa + \kappa \|\nabla u_\kappa^*\|_{L^2} + m$$

and thus

$$C(c,\kappa) \geq \kappa + \kappa \|\nabla u_\kappa^*\|_{L^2}^2 + m.$$

Proof. In the following, we report only a sketch of the proof; we refer to [13] for the detailed proof.

Lemma (4.21) allows us to prove i) only over $\mathcal{V}$, and not also on V. We argue by contradiction. We assume that there exists a sequence $F^n \in \mathcal{V}$ such that $\|F^n\|_A \to 0$. We will construct a set of test functions φ, which for $c > \sqrt{2}/2$ will lead to a contradiction. We take φ as an $L^2(\mathbb{T}^2; \mathbb{R}^2)$ function,

$$\varphi(x) := \sum_{k \in \square_1^2} a_k(x) \nabla^\perp \psi(x - k). \tag{4.69}$$

for some $a_k(x) \in L^2(\mathbb{T}^2)$ and where ψ is as in (4.2). We have

$$\left| \int_{\mathbb{T}^2} F^n \cdot \varphi \right| = \left| \sum_{k \in \square_1^2} \int_{\mathbb{T}^2} a_k(x) F^n \cdot \nabla^\perp \psi(x-k) \right| \leq \sum_{k \in \square_1^2} \|a_k\|_{L^2} \left(\int_{\mathbb{T}^2} |F^n \cdot \nabla^\perp \psi(x-k)|^2 \right)^{1/2}.$$

and we obtain

$$\left| \int_{\mathbb{T}^2} F^n \cdot \varphi \right| \lesssim \|F^n\|_A \xrightarrow{n} 0. \tag{4.70}$$

For any $\delta > 0$ and a test function $\hat{\varphi} = (\varphi_1(x_2), 0)$, that is positive and equal to one if $|x_2 - 1/2| \leq \delta/2$ and zero if $|x_2 - 1/2| \geq \delta$,

$$\int_{\mathbb{T}^2} F^n \cdot \hat{\varphi} = \int_{1/2-\delta}^{1/2+\delta} \int_0^1 F_1^n(x_1, x_2)\varphi_1(x_2)\,\mathrm{d}x_1\,\mathrm{d}x_2$$

$$\geq \frac{\delta}{2}\xi_1 \ ,$$

where we used lemma (4.22) and Fubini-Tonelli, see [13] for the full computation. We now take $\xi_1 \neq 0$. Using (4.70), we have a contradiction, if it is possible to express the test function $\hat{\varphi}$ as in (4.69). We now demonstrate that this can be done if $c > \sqrt{2}/2$ and δ is sufficiently small. From Lemma 4.15, we obtained the following results:

1. If $c > \sqrt{2}/2$, there exists a strip
$$S_c = [0,1] \times [1/2 - \delta(c), 1/2 + \delta(c)]$$
for $\delta(c) = \sqrt{c^2 - 1/4} - 1/2 => 0$ where the set of vectors $\mathcal{B}(x) = \{\nabla^\perp \psi(x-k)\}_{k \in \square_1^2}$, contains two or more vectors.
2. If $x \in \mathring{S}_c$ (the interior of S_c), $\mathcal{B}(x)$ spans $\mathbb{R}^2$.

Remark (4.4) establishes that for $x \in \partial[0,1]^2$, $\mathcal{B}(x)$ spans the direction normal to the boundary,

$$\operatorname{span}\mathcal{B}(x) = \operatorname{span}(e_2) \qquad for\ x = (x_1, 0)\ or\ x = (x_1, 1)$$
$$\operatorname{span}\mathcal{B}(x) = \operatorname{span}(e_1) \qquad for\ x = (0, x_2)\ or\ x = (1, x_2).$$

If we now take the strip

$$S_c^{1/2} = [0,1] \times [1/2 - \delta(c)/2, 1/2 + \delta(c)/2],$$

we have that the vector e_1 is in the range of $A(x)$ for every $x \in S_c^{1/2}$. In turn, this implies that there exists functions $\tilde{a}_k(x)$ given by $\tilde{a}_k(x) = \nabla^\perp \psi(x-k) \cdot w(x)$ for $\omega(x)$ such that $A(x)\omega(x) = e_1$ such that $e_1 = \sum_{k \in \square_1^2} \tilde{a}_k(x)\nabla^\perp \psi(x-k)$. We recall that $A(x)$ is smooth, and that $\omega(x) = e_2$ for $x = (0, x_2)$, $(1, x_2)$. For those reasons, we can take coefficients $\tilde{a}_k(x)$ as bounded (even smooth) in the strip $S_c^{1/2}$. If we take $\delta \leq \delta(c)/2$,

$$\hat{\varphi}(x) = \sum_{k \in \square_1^2} \varphi_1(x_2)\tilde{a}_k(x)\nabla^\perp \psi(x-k)$$

.

In the case $\xi_1 = 0$, we have to take $\varphi = (0, \varphi_2)$ with

$$\operatorname{supp}(\varphi) \subset [1/2 - \delta, 1/2 + \delta] \times [0,1].$$

We now take $F = \xi + \nabla u \in V$ and obtain ii). Moreover,

$$\mathcal{E}_\kappa(u) = \kappa + \kappa\|\nabla u\|_{L^2}^2 + \|\xi + \nabla u\|_A^2$$

and we obtain iii). □

Remark 4.7. The functional $\|\cdot\|_A$ is 1−homogeneous in ψ:

$$\|F\|^2_{A_\lambda} = \lambda^2 \sum_{k\in\square_1^2} \int_{\mathbb{T}^2} |F\cdot\nabla^\perp\psi(x-k)|^2 dx > \lambda^2 m$$

where $A_\lambda(x)$ is the matrix $A(x)$ in which ψ is multiplied by λ; the same effect can be achieved with $\theta_k^N = \lambda/N$. Then, if we fix κ, $C(c,\kappa)$ is arbitrarily large.

4.5 Numerical Simulations

As anticipated in the previous sections, the behaviour of the total effective diffusivity $C(c,\kappa)$ as $\kappa\to 0$ is not completely understood. In particular, Theorem 4.18 leaves a gap, the regime in which the parameter c takes value in $(1/2, \sqrt{2}/2)$. To address this issue, we perform a numerical estimate of the total effective diffusivity $C(c,\kappa)$ by solving equation (4.33).

4.5.1 Numerical setup

The equation (4.33) is numerically solved on a two-dimensional lattice $[0,1]\times[0,1]$, discretized on a $n\times n$ grid of grid-space $d = 1/n$, and $H_\kappa(x) = \kappa I + A(x)$ is a $2n\times 2n$ matrix. In our numerical setup, the orthogonal gradient of ψ is taken as:

$$\nabla^\perp\psi(x) = \frac{x^\perp}{|x|}\frac{\varphi(|x|)}{\|\varphi\|_{L^2_x}}, \tag{4.71}$$

with $x\in\mathbb{T}^2$. In order to be able to compare different values of the parameter c, the function $\varphi(x)$ is normalized, so that the following condition holds:

$$\|\nabla\psi\|_{L^2_x} = 1. \tag{4.72}$$

The following choice of $\varphi(r)$, $r\in\mathbb{R}_+$ is used, in order to satisfy conditions (4.2) :

$$\varphi(r) = \frac{1}{r^2}\exp\left(-\frac{a_1}{r^2}\right)\exp\left(-\frac{a_2 r^2}{|r-c|}\right) \tag{4.73}$$

with a_1, a_2 parameters.

The second order elliptic operator T in divergence form is defined as:

$$T\phi_e := -\frac{1}{2}\left(\sum_{i=1}^2 D_i^-\left(\sum_{j=1}^2 H_{ij}D_j^+\phi_e\right) + \sum_{i=1}^2 D_i^+\left(\sum_{j=1}^2 H_{ij}D_j^-\phi_e\right)\right), \tag{4.74}$$

where D_i^- and D_i^+ are, respectively, the forward and backward difference operators. The two directions are denoted by the index $i = 1,2$. This numerical approximation is consistent up to second order, see [64]. In this framework, the corresponding divergence operator is defined as:

$$\mathrm{div} f := \frac{1}{2}\sum_{i=1}^n (D_i^- + D_i^+) f_i.$$

We solve the two linear systems

$$T\phi_1 = \mathrm{div}\,(A \cdot e_1) \;\; ; \quad T\phi_2 = \mathrm{div}\,(A \cdot e_2) \tag{4.75}$$

both employing ILU preconditioned GMRES from Eigen3 library for C++ as a linear solver and the direct solver implemented in MATLAB. The two results obtained via the two different procedures are compatible. In the following, we report results obtained via the direct solver implemented in MATLAB.

After solving the linear systems, we compute the total effective diffusivity, (4.47), for different values of the parameter c. The total diffusivity is extracted from the real part of the leading eigenvalue of the 2×2 matrix obtained by averaging over the entire grid. Computing the total diffusivity using the second eigenvalue leads to consistent results, since the 2×2 matrix is (almost) diagonal. We checked that the imaginary parts of both the eigenvalues are compatible with zero.

In all cases, the data obtained at different values of the molecular diffusivity κ were computed for different values of the gridstep d: $d = 0.0100, 0.00222, 0.00167, 0.00125$. Then, the final estimate for the total diffusivity was obtained by extrapolating for $d \to 0$.

As a consistency check, we also evaluated the total diffusivity by plugging our solution into the definition obtained in the variational setting, (4.48). This second quantity was also extrapolated for $d \to 0$.

4.5.2 Results

In the following, we report our numerical results concerning the behaviour of the additional diffusivity, $C(c, \kappa) - \kappa$, as $\kappa \to 0$, also presented in the work [13]. For most of the section, we focus on a single choice of the profile function $\varphi(x)$. Nevertheless, examining different choices of parameters for the function $\varphi(x)$ is crucial to identify which results depends on the choice of the profile function and how. Based on the previous analysis, we expect our results to be stable under the choice of the profile function for $c \in (0, 1/2)$.

Choice of profile function and corresponding solution of corrector equation

As a first step, we investigate the dependence of the profile function $\varphi(x)$ on the parameters a_1 and a_2. We report our choice for $\varphi(x)$ in the upper plot of Figure 4.2, while in the lower plots of Figure 4.2 we show other possible choices for the two parameters a_1 and a_2. The parameters have to be chosen carefully, as the function could drop dramatically to a value effectively indistinguishable from zero already at $x' < c$, inside the prescribed support radius c.

For the chosen values of the parameters a_1, a_2, we report in Figure 4.3 the corresponding matrix elements $A_{ij}(x)$. In Figure 4.4 we report the solution of the corrector equation (4.33), for the same parameters choice. The matrix T was de-singularized by subtracting to the corrector its mean value.

Additional diffusivity

To investigate the dependence of the additional diffusivity on the parameter c as $\kappa \to 0$, we begin by performing simulations for a fixed single set of parameters: $a_1 = 0.05$, $a_2 = 0.3$. The corresponding results are reported in Figure 4.5: they are grouped into four regimes, $c \in (0, \frac{1}{2}]$, $c \in (\frac{1}{2}, \frac{\sqrt{2}}{2})$,

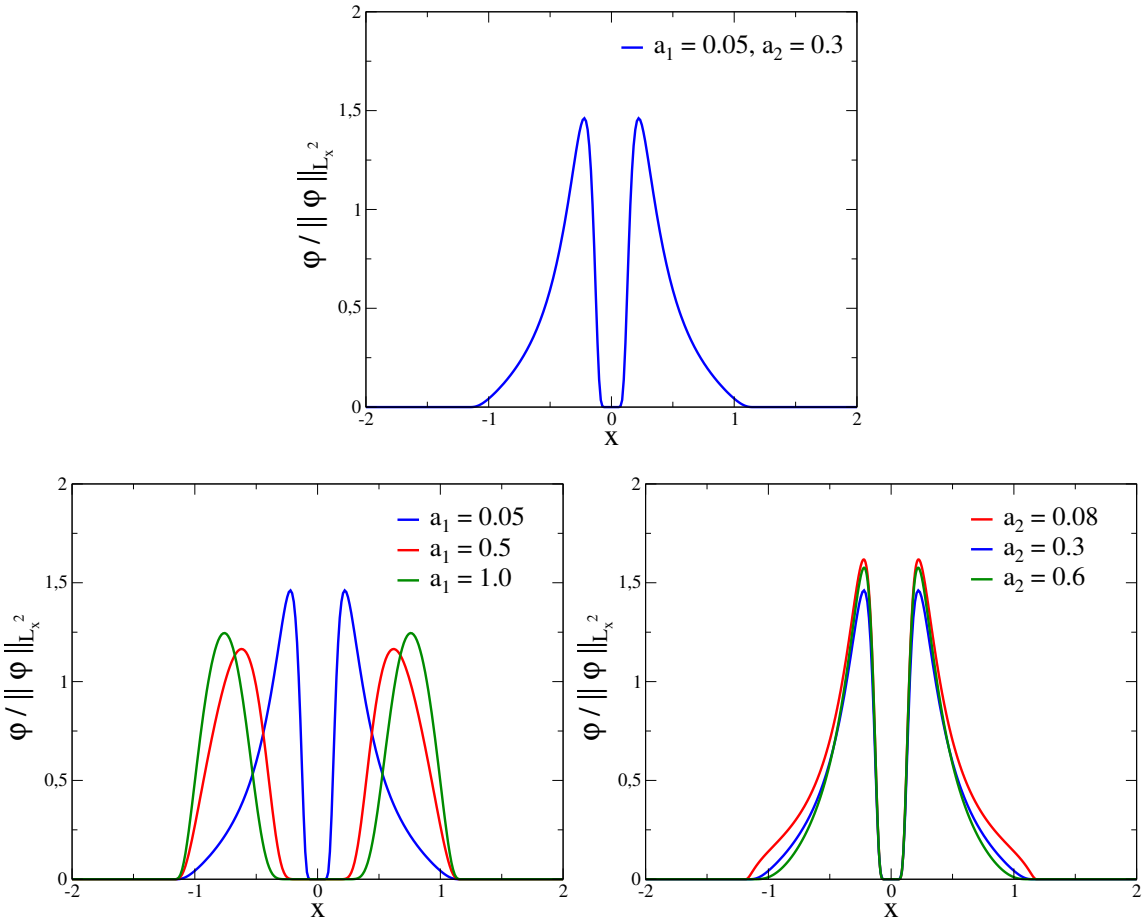

Figure 4.2: Up: plot of $\varphi(x)/\|\varphi\|_{L^2_x}$, with $\varphi(x)$ defined in (4.73), with our choice $a_1 = 0.05$, $a_2 = 0.3$, at $c = 1.2$. This choice of the parameter c shows that for $c > 1$ the profile function is not zero outside the interval [-1,1].
Down: different possible choices of the coefficients a_1 (left, a_2 is held fixed, $a_2 = 0.3$), a_2 (right, a_1 is held fixed, $a_1 = 0.05$), at $c = 1.2$. Choices of parameters employed in numerical simulations are plotted in blue, with $a_1 = 0.05$, $a_2 = 0.3$. Note that the plot on the right hints that for $a_2 > 0.6$ the support of the function drops to a value compatible with zero already before $c = 1.2$.

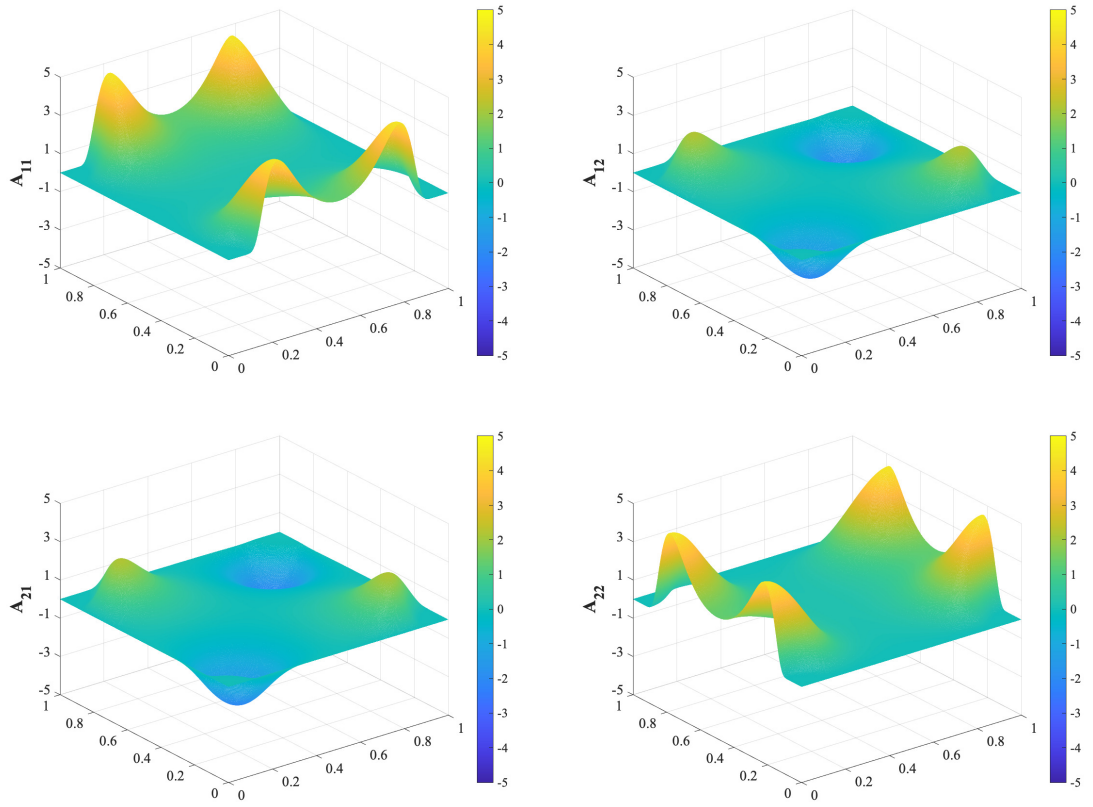

Figure 4.3: Plot of the matrix elements $A_{ij}(x)$, with $\varphi(x)$ defined in (4.73). The parameters used are $a_1 = 0.05$, $a_2 = 0.3$, $c = 1.0$.

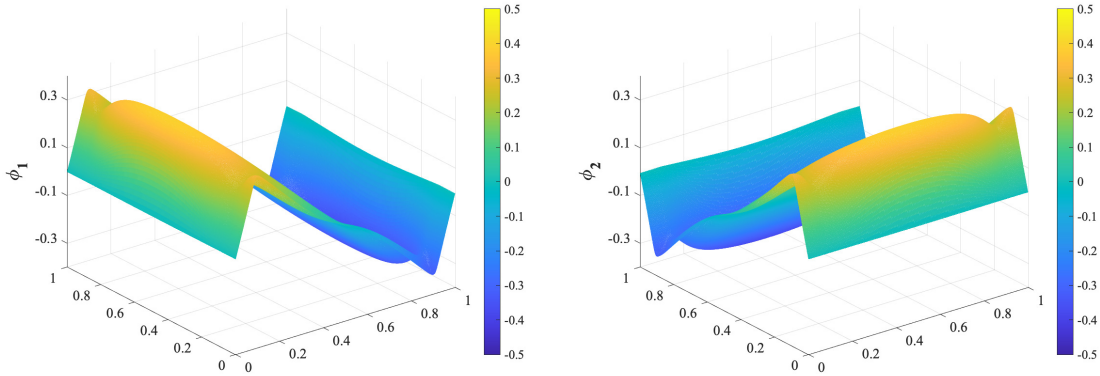

Figure 4.4: Plots of the solution $\phi_1(x)$ (left), $\phi_2(x)$ (right), with $\varphi(x)$ defined in (4.73), $a_1 = 0.05$, $a_2 = 0.3$, $c = 1.0$ and $\kappa = 0.01$.

$c \in (\frac{\sqrt{2}}{2}, \frac{\sqrt{5}}{2})$, $c > \frac{\sqrt{5}}{2}$. From those data, we observe that for $c \in (0, \frac{1}{2})$ the additional diffusivity exhibits a linear dependence on k as $\kappa \to 0$ is linear, with an intercept that is indistinguishable from zero. For values of c in the interval $c \in (\frac{1}{2}, \frac{\sqrt{2}}{2})$, the intercept remains compatible with zero, but the additional diffusivity appears to follow a power law behaviour. A similar power-law behaviour, but with non-zero intercept, is present for $c \in (\frac{\sqrt{2}}{2}, \frac{\sqrt{5}}{2})$. On the contrary, for $c > \frac{\sqrt{5}}{2}$ the intercept seems to be still non-zero, however the behaviour of the additional diffusivity is again linear. We emphasize that these numerical findings are in full agreement with the conclusion of Theorem 4.18, moreover, our simulations provide conclusive evidence also in the regime $c \in (\frac{1}{2}, \frac{\sqrt{2}}{2})$, which was outside the reach of our theorem. The case $c = \frac{1}{2}$ is in-between the two regimes, the power law behaviour and the linear behaviour, probably due to numerical artifacts.

To further investigate the different behaviours of the additional diffusivity for different values of the parameter c, we perform a set of fits in the range $0.0001 < \kappa < \kappa^*$ using the parametric model

$$f(\kappa) = a\kappa^n + q.$$

We consider several choices of κ^*, and report the corresponding estimates for the parameters n and q in Figure 4.6. The fitting procedure is carried out by taking into account constraints for the parameter $a \in [0, +\infty)$, as values outside this interval would be unphysical. This constraint is enforced by fitting the parameter a', with $a = e^{a'}$. No analogous constraint is imposed on the parameter q, in order to allow it to become negative if very small. The stability of the fitting procedure is assessed by performing jackknife procedure for each dataset in the following way: first, the fit was performed for different values of κ^* in the interval $(0, \kappa^*]$, with $\kappa^* \in [0.0016, 0.005]$; then, the jackknife procedure was applied to the fit performed in each interval. To ensure the same effect on each dataset, we removed 95% of the points in each interval, not only one. The jackknife estimate for each interval was used to to reduce bias and estimate uncertainty, in the usual fashion. In general, the estimates of the power-law exponent and the coefficient a remain stable only for relatively small values of k^*, however, in determining the final estimates we also take into account results obtained for moderately larger values of k^*. In particular, the power law exponent has a reduced stability interval for $c > 1.1$. The intercept value, on the other hand, is stable over a wider range of k^*.

As shown in Figure 4.6, for $c \in (0, \frac{1}{2})$ and $c > \frac{\sqrt{5}}{2}$, although our estimates do not yield exactly $n = 1$, the power law exponent approaches the value 1.0 as the fitting interval is restricted to $\kappa \to 0$. In particular, as noted above, the value of $c = \frac{1}{2}$appears to correspond to a transitional regime for the additional diffusivity, probably as a consequences of numerical artifacts. Moreover, for $c \in (0, \frac{1}{2}]$ and $c \in (\frac{1}{2}, \frac{\sqrt{2}}{2})$ the estimated intercept is compatible with zero. In the interval $c \in (\frac{\sqrt{2}}{2}, \frac{\sqrt{5}}{2})$, the intercept estimate does not seems to be compatible with zero for $c = 1.0$ and $c = 1.1$, while for $c = 0.8$ the non-zero value is too small to draw definitive conclusions. For $c > \frac{\sqrt{5}}{2}$, the intercept estimate grows as a function of the parameter c.

Finally, in Figure 4.7 we report the quantity $\|\nabla\phi_1\|^2_{L^2_x}$: the behaviour of the corrector's gradient is linear for $c > \frac{\sqrt{5}}{2}$, but it does not seems to be the case for $c \in (\frac{\sqrt{2}}{2}, \frac{\sqrt{5}}{2})$, however the numerical artifacts become too relevant at lower values of κ to estimate a power law exponent for the curve.

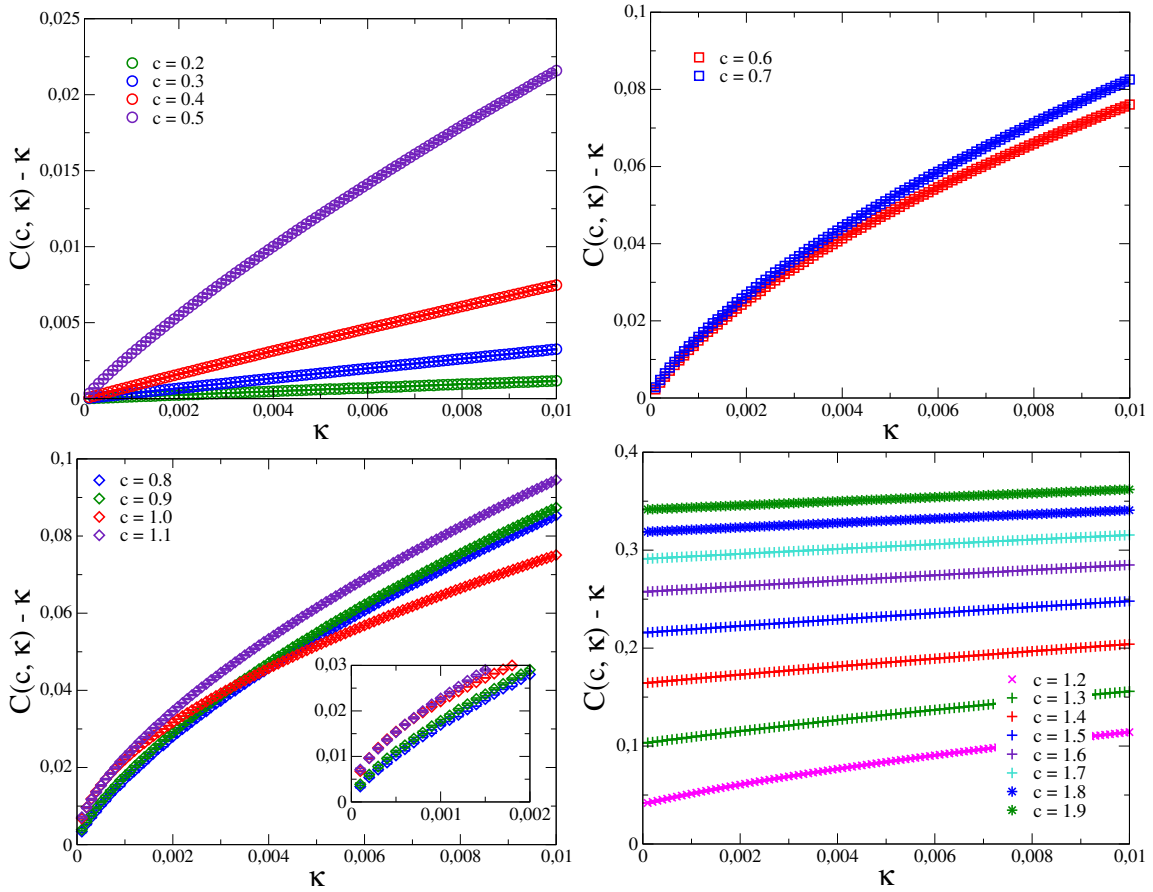

Figure 4.5: Plot of additional diffusivity $C(c,\kappa)$, for different values of c, from left to right and top to bottom: $c \in (0, \frac{1}{2}]$,$c \in (\frac{1}{2}, \frac{\sqrt{2}}{2})$, $c \in (\frac{\sqrt{2}}{2}, \frac{\sqrt{5}}{2})$, $c > \frac{\sqrt{5}}{2}$ (with zoom at $\kappa \to 0$ if needed). The additional diffusivity is computed by means of (4.47). Compatibility with results obtained by using (4.48) was separately checked. The profile function used is $\varphi(x)$, defined in (4.73), with $a_1 = 0.05$, $a_2 = 0.3$. The top right panel exhibits values of c in the range $c \in (\frac{1}{2}, \frac{\sqrt{2}}{2})$, which we highlight lies outside the statements of Theorem 4.18.

c	q	n
0.2	-0.000001(57)	0.98(6)
0.3	-0.0000006(27)	0.980(13)
0.4	-0.0000050(55)	0.964(10)
0.5	-0.000055(45)	0.87(2)
0.6	-0.00052(69)	0.74(6)
0.7	0.000050(45)	0.74(4)
0.8	0.00048(35)	0.73(3)
0.9	0.00066(29)	0.72(2)
1.0	0.00081(29)	0.696(14)
1.1	0.00302(22)	0.674(8)
1.2	0.04036(39)	0.87(5)
1.3	0.10270(12)	0.94(3)
1.4	0.163985(75)	0.97(3)
1.5	0.215595(45)	0.98(2)
1.6	0.257324(40)	0.97(2)
1.7	0.290976(48)	0.97(3)
1.8	0.318566(41)	0.99(3)
1.9	0.341377(29)	0.98(2)

Table 4.1: Results of the fits of the additional viscosity to the power law, for various values of the parameter c, with $a_1 = 0.05$ and $a_2 = 0.3$.

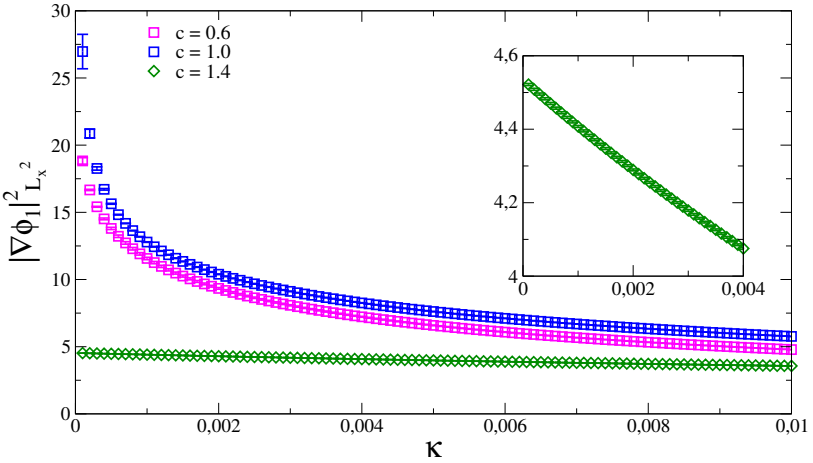

Figure 4.7: Plot of $\|\nabla\phi_1\|^2_{L^2_x}$ for $c = 0.6, 1.0, 1.4$. For $c \in (0, \frac{1}{2})$ no curve was plotted, as the corrector's gradient is not relevant in this regime. The profile function used is $\varphi(x)$, defined in (4.73), with $a_1 = 0.05$, $a_2 = 0.3$. We note that for $c \in [0.6, 1]$ (probably $c \in (\sqrt{2}/2, \sqrt{5}/2)$) the gradient seems to explode at zero.

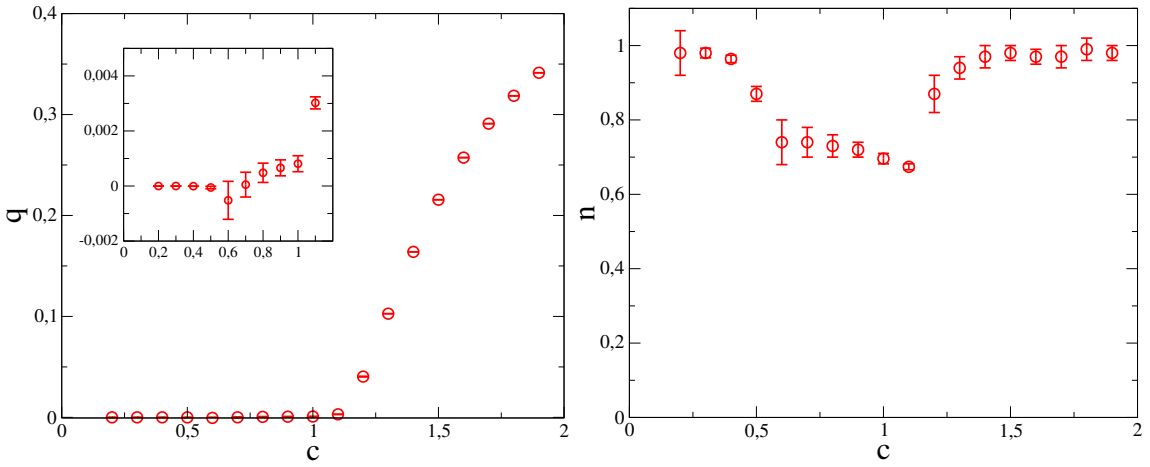

Figure 4.6: Intercept estimate (left) and power law exponent estimate (right) as a function of the parameter c. The profile function used is $\varphi(x)$, defined in (4.73), with $a_1 = 0.05$, $a_2 = 0.3$.

Sensitivity with Respect to Profile Parameters

We conclude this section by investigating the sensitivity of our results to the choice of the two parameters of the profile function $\varphi(x)$, a_1 and a_2. For selected values of the parameter c, one for each of the investigated regimes, we compute the additional diffusivity for three different choices of a_1 and a_2, $a_1 = 0.05, 0.5, 1.0$ and $a_2 = 0.08, 0.3, 0.6$. When varying these parameters, particular care must be taken, since if the function $\varphi(x)$ goes to zero too fast for $x \to c$, numerical artifacts which have the effect of *shrinking* the support radius (see Figure 4.2) will arise. To avoid the introduction of an *effective support*, the parameter values were selected in order to keep the numerical support (i.e. the value of x for which the function φ becomes smaller than a tolerance value) close to c. However, even in this case, complete quantitative agreement between different parameter choices should not be expected. The results obtained for the additional diffusivity for the different choices of the parameters a_1 and a_2 are reported in Figure 4.8. The estimates for the power law exponent and the intercept for the different choices of the parameter a_1 are reported in Figure 4.9, while the results for a_2 are reported in Figure 4.10.

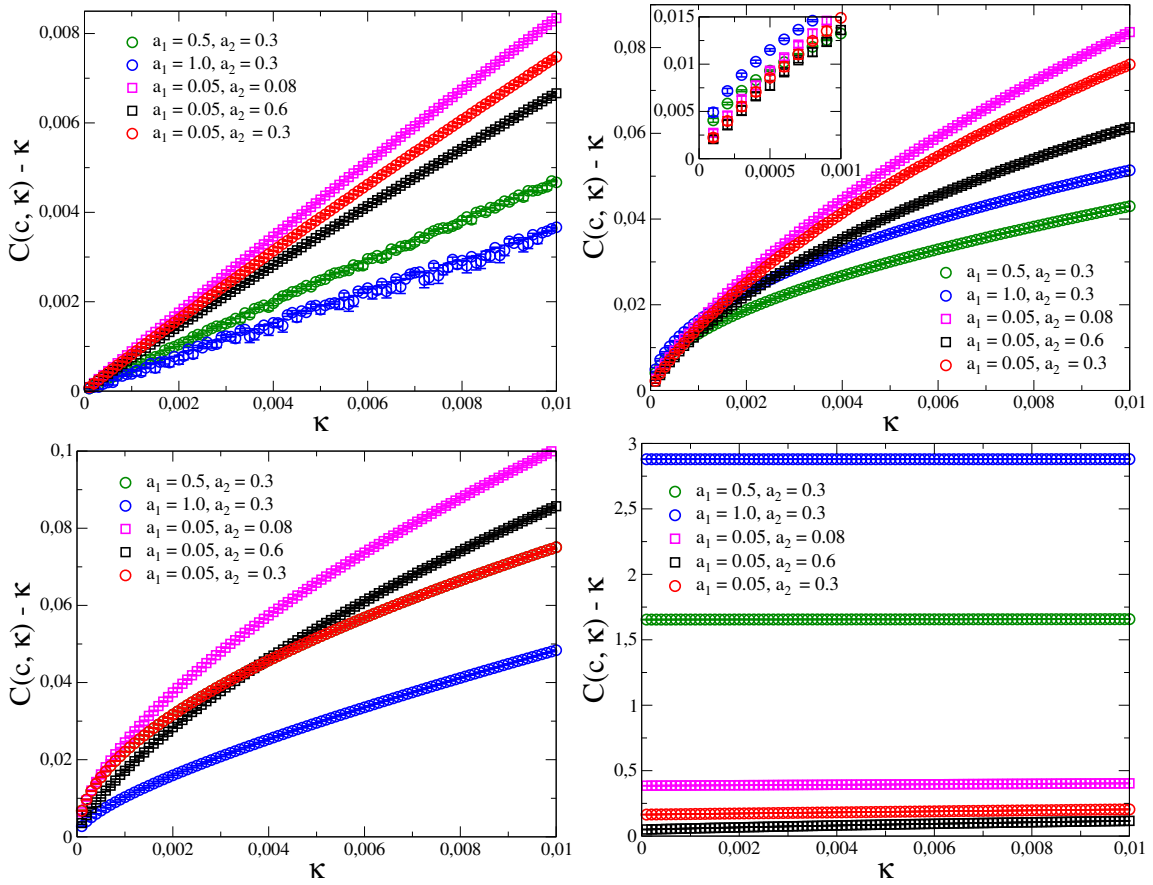

Figure 4.8: Plot of additional diffusivity, for the values of the parameter $c = 0.4$ (up, left), $c = 0.6$ (up, right), $c = 1.0$ (down, left), $c = 1.4$ (down, right), computed as in (4.47). Compatibility with results obtained by using (4.48) was separately checked. The profile function used is $\varphi(x)$, defined in (4.73), with $a_1 = 0.05, 0.5, 1.0$, $a_2 = 0.3$, and $a_1 = 0.05$, $a_2 = 0.08, 0.3, 0.6$.

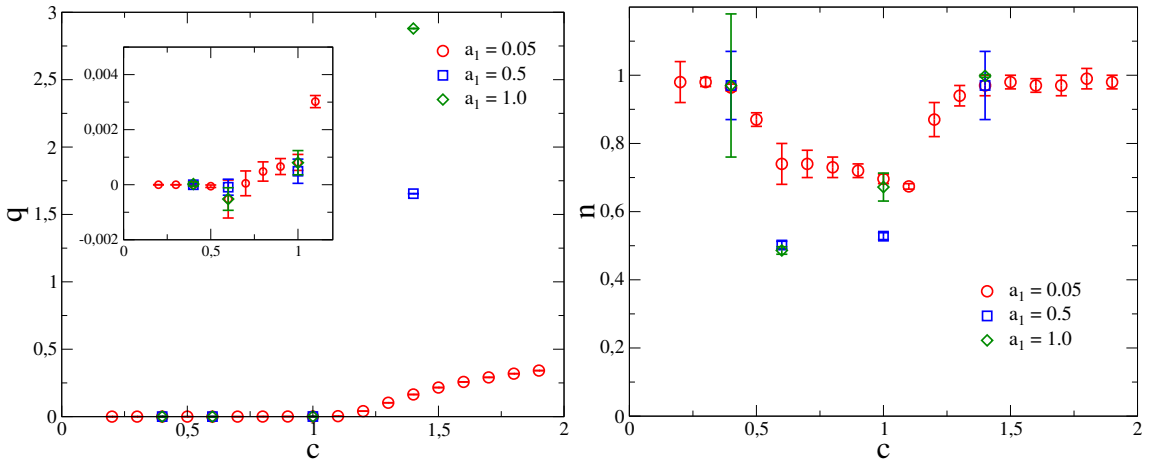

Figure 4.9: Intercept estimate (left) and power law exponent estimate (right) as a function of the parameter c. The profile function used is $\varphi(x)$, defined in (4.73), with $a_1 = 0.05, 0.5, 1.0$, $a_2 = 0.3$.

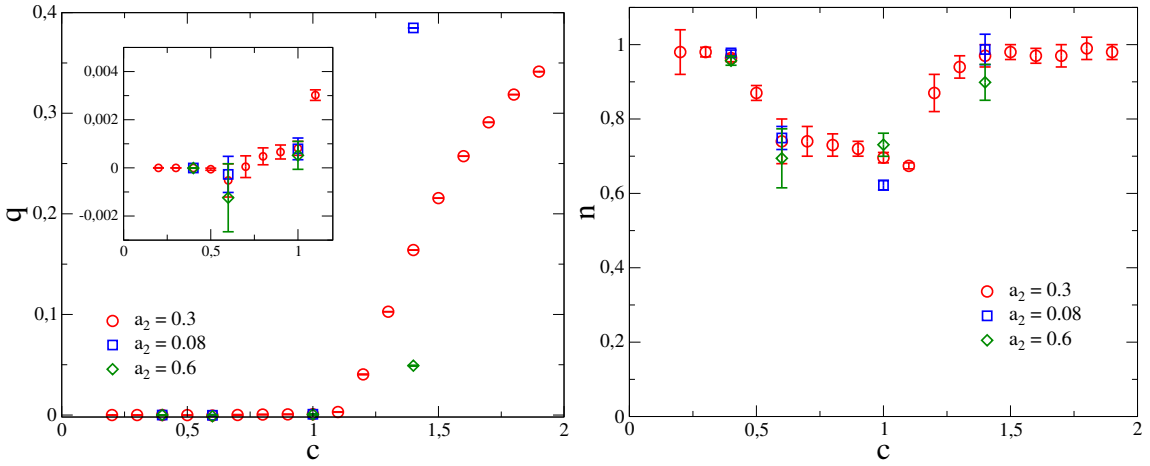

Figure 4.10: Intercept estimate (left) and power law exponent estimate (right) as a function of the parameter c. The profile function used is $\varphi(x)$, defined in (4.73), with $a_1 = 0.05$, $a_2 = 0.3, 0.08, 0.6$.

From the data shown in Figure 4.9, it is evident that for $c \in (0, \frac{1}{2})$ there is not much difference in the (almost linear) behaviour of the additional diffusivity for different values of the parameter a_1. An analogous conclusion can be drawn from Figure 4.10 when varying the parameter a_2. By contrast, the results for n outside of this range seem to depend on the specific choice of the profile parameters, while the zero-valued intercept in the range $c \in (\frac{1}{2}, \frac{\sqrt{2}}{2})$ remains unchanged (see Figure 4.9 and Figure 4.10), indicating that the vanishing intercept in this interval is robust with respect to variations of the parameters a_1, a_2.

Chapter 5

Testing internal and environmental noise under Kelvin-Helmholtz instability

This chapter is devoted to the numerical investigation of stochastic modifications of the Point Vortex model and their effects on a fluid instability, the Kelvin-Helmholtz instability. This system was chosen in order to investigate the dissipation properties of those stochastic modifications of the model. In the first part of this chapter, we briefly summarize what the Kelvin-Helmholtz instability is, where it occurs and how to model it, taking into account turbulent fluid behavior.

Then, we numerically investigate a Point Vortex discretization of a fluid whose initial condition triggers the Kelvin-Helmholtz instability. In addition to the classical Point Vortex system, used to model and inviscid fluid, we will also investigate the well-known stochastic modification of the model in which an additive noise is added to the equations of motion of the point vortices, to model a viscous fluid. Beyond those two models, which will be used for comparison, we will focus on the stochastic modification of the Point Vortex model obtained by adding an environmental noise to the model; this noise was described in chapter 3, 4 and references therein, and in [59, 58, 13]; in particular, in this chapter we focus on investigating its dissipation properties.

In the following, we give some motivations for the investigation of the dissipation properties of the environmental noise stochastic modification, and the choice of the model. It is Joseph Boussinesq's intuition [11] that *turbulent small scales may be be dissipative on the mean flow.* The physical intuition is that fluid particles move so erratically to produce effects similar to the molecular dynamics: as macroscopic kinetic energy transfers to molecular kinetic energy (heat), reducing the macroscopic motion, similarly large-scale kinetic energy moves to small-scale turbulence and reduce the intensity of the mean flow. Numerous attempts have been made to establish the validity of this picture, see for instance [7, 51, 80, 88, 125], but there are not clear conclusions, as sometimes the validity is only partial [80, 118]; in particular, the inverse cascade in 2D seems to break the viscosity effect due to small-scale turbulence [31]. However, this idea is particularly relevant for numerical simulations of fluid dynamics model: it lies at the core of the LES method [7], and, in the context of vorticity equations, of the vortex blob method [27]. The numerical results in this chapter, which investigate the dissipation properties of the environmental noise turbulence model, are presented in [59] and in [58]. Future development of this work will be focused on computing the energy spectrum

of the model, understand the effects of stochastic transport forcing, and on improving the analysis the fluid velocity field.

5.1 Kelvin-Helmholtz instability and vortex sheet model

The *Kelvin-Helmholtz* is a fluid instability which occurs, for example, between free shear layers which are transition layers at the boundary of two streams of different speeds (or densities). The main advantage of investigating system of fluids which develops this kind of instability is that it is possible to make an easy comparison with the Navier-Stokes equation in terms of velocity field evolution (explicit solution) and energy decay. The main idea is that small (both in intensity and scale) stochastic perturbations can trigger huge oscillations at instability. In this section, we briefly describe the vortex sheet model and how its instability develops [76]; we follow the notation of [4] and more information on the topic are to be found there. For the sake of simplicity, in this section we take $\mathcal{D} = \mathbb{R}^2$, the full plane, however in the rest of the chapter we will study the system on the torus $\mathbb{T}^2$. The physical system which we want to study is made of two uniform streams of identical fluid, each one moving with a different velocity,

$$\begin{array}{ll} U_1(t=0) & = \left(-\frac{1}{2}U, 0\right) \quad \text{for } x_2 > 0 \\ U_2(t=0) & = \left(\frac{1}{2}U, 0\right) \quad \text{for } x_2 < 0 \end{array}$$

where U is a constant and the two fluids come into contact on the line $x_2 = 0$. We are interested in the transition from one stream to another adjacent stream, and we want to study the small disturbances which develop at the separation. The layer between the two fluids is a surface across which there is a velocity discontinuity, a jump of magnitude U, and we model its motion in time with a so-called *sheet vortex* of equation

$$x_2 = \eta(x_1, z, t).$$

As the instability occurs locally, this simple model effectively reproduces the physical phenomena, as it accounts of how the sheet vortex changes shape in time. Our focus is on studying the effect of very small perturbation of the velocity field; we assume that the transition layer is a line, so its thickness is negligible with respect to the characteristic length of the sheet vortex perturbation. If we call the disturbance potential ϕ_1 on the upper plane and ϕ_2 on the lower plane, the fluid velocity is obtained, according to (1.11), from the following potential:

$$\Phi(x_1) = \begin{cases} -\frac{1}{2}Ux_1 + \phi_1 & \text{if} \quad x_2 > 0 \\ \frac{1}{2}Ux_1 + \phi_2 & \text{if} \quad x_2 < 0 \end{cases}$$

To show that time evolution of a vortex sheet give rise to instability, we start by considering small perturbation of the flow; following [4], we only take into account corrections up to first order in the perturbation displacement of the vortex sheet. We expect undulations of increasing amplitude at the transition layer, resulting in a *turbulent motion*. The vortex sheet is a boundary of the region $x_2 > 0$, so the partial derivative of the disturbance potential ϕ_1 with respect to the x_2 coordinate, computed at $x_2 = \eta$ is equal to the material derivative of η:

$$\left(\frac{\partial \phi_1}{\partial_y}\right)_{y=\eta} = \frac{D\eta}{Dt} = \frac{\partial \eta}{\partial t} + \left(-\frac{1}{2}U + \frac{\partial \phi_1}{\partial x_1}\right)_{x_2=\eta} \frac{\partial \eta}{\partial x} + \left(\frac{\partial \phi_1}{\partial z}\right)_{x_2=\eta} \frac{\partial \eta}{\partial z} \, .$$

If we compute this quantity at $x_2 = 0$ to first order in ϕ_1, and repeat the same computation for the disturbance potential ϕ_2 we obtain the following two relations:

$$\left(\frac{\partial \phi_1}{\partial_y}\right)_{y=0} = \frac{\partial \eta}{\partial t} - \frac{1}{2}U\frac{\partial \eta}{\partial x}$$
$$\left(\frac{\partial \phi_2}{\partial_y}\right)_{y=0} = \frac{\partial \eta}{\partial t} + \frac{1}{2}U\frac{\partial \eta}{\partial x} \ .$$

In this way, we satisfy conditions related to the forces acting on the common boundary. We now have to satisfy condition related to the pressure of the fluid. As the two streams are made of the same fluid, the pressure across the interface $x_2 = \eta$ is continuous. The following relation holds:

$$\left(\frac{\partial \phi_2}{\partial_t} - \frac{\partial \phi_1}{\partial_t}\right)_{y=0} + \frac{1}{2}U\left(\frac{\partial \phi_2}{\partial_x} + \frac{\partial \phi_1}{\partial_x}\right)_{y=0} = \text{const} \ .$$

The displacement of the vortex sheet, η, can be expressed as a Fourier integral in x and z, and the same can be done for the disturbance potential ϕ_1 and ϕ_2. For this reason, we look for solutions of the form

$$\eta = A(t)e^{i(\alpha x+\beta z)}$$
$$\phi_1 = B_1(t)e^{-ky}e^{i(\alpha x+\beta z)}$$
$$\phi_2 = B_2(t)e^{ky}e^{i(\alpha x+\beta z)} \ ,$$

where α, β satisfy the following relation

$$k = \sqrt{\alpha^2 + \beta^2}$$

and k is the amplitude of a wavenumber vector in the plane (z, x). We recall that the disturbance potentials have to obey Laplace equation and the disturbance has to vanish at large distance from the vortex sheet. We refer to [4] for the explicit computations, and we only report the result obtained for the coefficient A,

$$A \propto e^{\mp \frac{1}{2}\alpha U t} \ .$$

We note that in the case of the positive root, the perturbation is exponentially growing and there is *instability* of the vortex sheet for any disturbance which is periodic with respect x and z, with $\alpha \neq 0$.

In the case of a transition layer of thickness d, which is the case we will investigate in this chapter and in the work [106], if the disturbances are of sinusoidal form and their wavelength is large with respect to d, this simple model is still able to capture the behavior of the vortex sheet. For disturbance of wavelength smaller, we do not see growing of the perturbation, while for wavelength of order d there is a maximum in the growth rate. We refer to [4] for an extensive discussion.

5.1.1 Effect of viscosity

In this subsection, we focus on the effect of viscosity in our simple model, following [4]; we suppose that at time $t = 0$ the thickness d is equal to zero, and the vortex sheet is the plane $y = 0$. The jump of magnitude in the velocity discontinuity is $2U$. We consider the axis in motion with the mean of the velocities of the two different fluids.

If we consider a fluid motion of an unidirectional viscous flow due to the unsteady boundaries in motion, the velocity obeys the diffusion equation,

$$\frac{\partial u}{\partial t} = \nu \left(\frac{\partial^2 u}{\partial y^2} + \frac{\partial^2 u}{\partial z^2} \right) ,$$

and its solution for the velocity u is given by the following expression,

$$u(y,z,t) = \frac{1}{4\pi\nu t} \int_{-\infty}^{+\infty} \int_{-\infty}^{+\infty} u(y',z',0) e^{-\frac{(y-y')^2)}{4\nu t} - \frac{(z-z')^2)}{4\nu t}} dy' dz' .$$

To study the effect of the viscosity ν on our model, we follow the discussion in [4] and take:

$$\begin{aligned} u(y',z',0) &= -U \quad y' < 0 \\ u(y',z',0) &= +U \quad y' > 0 , \end{aligned}$$

obtaining for the velocity

$$u(y,t) = U \ \mathrm{erf} \left(\frac{y}{\sqrt{4\nu t}} \right) .$$

By rescaling the velocity as u/U, it is possible to write a diffusion equation in which the combination

$$\eta^* = \frac{y}{(\nu t)^{1/2}} \tag{5.1}$$

is the only independent variable, thus in the case of viscous flow the onset of the turbulent behavior is delayed to late times.

5.2 Numerical simulations

In this section, we exploit the Point Vortex discretization of a two-dimensional fluid to investigate the shear flow model and the Kelvin–Helmholtz instability. The onset of the instability is also the onset of a turbulent behavior of the fluid and the formation of large vortex structure at the transition layer between the two streams. First, we test our Point Vortex discretization in the classical inviscid case: at the same time, we set a benchmark for which we will show delayed instability in the case of viscous fluid and inviscid fluid with environmental noise, as described briefly below.

We use the notation $X_t^1, ..., X_t^N$ for the positions of the vortices with intensities (circulations) $\Gamma_1, ..., \Gamma_N$; their dynamics is given by the following differential equations:

$$\frac{dX_t^i}{dt} = \sum_{j \neq i} \Gamma_j K \left(X_t^i, X_t^j \right) , \tag{5.2}$$

in the case of the discretization of the two-dimensional inviscid fluid. In this equations, K is the vector-valued kernel $K(x,y)$, the Biot-Savart kernel, equal to

$$K(x,y) = \frac{1}{2\pi} \frac{(x-y)^\perp}{|x-y|^2}$$

in full space, suitably modified on a torus or in a bounded domain.

To investigate viscous flows, following the approaches of [25, 81, 103], we modifying the previous scheme by adding independent 2D Brownian motions $W_t^1, ..., W_t^N$ to the equations of the Point Vortex model:

$$dX_t^i = \sum_{j \neq i} \Gamma_j K\left(X_t^i, X_t^j\right) dt + \sqrt{2\nu} dW_t^i \quad . \tag{5.3}$$

Finally, following [30, 113, 78, 104, 75], and [15], we investigate the following stochastic modification of the Euler equations,

$$d\omega + u \cdot \nabla \omega dt = \sum_{k \in K} \sigma_k \cdot \nabla \omega \circ dB_t^k \ , \tag{5.4}$$

where $\sigma_k = \sigma_k(x)$ are given vector fields, that we assume divergence-free, $\left(B_t^k\right)_{k \in K}$ are independent 1D Brownian motions and the stochastic operation $\circ$ stands for the Stratonovich integral. Due to this, formally, the vorticity is conserved, as it is transported randomly by the field $u\ dt + \sum_{k \in K} \sigma_k \circ dB_t^k$. This stochastic modification was already introduced in chapter 3. This model exhibits similarities with viscous flows; in this section, we will investigate differences and similarities of the elliptic operator arising from such a transport-advection noise. The Point Vortex dynamics associated with the model (5.4) is given by

$$dX_t^i = \frac{1}{N} \sum_{j \neq i} K\left(X_t^i, X_t^j\right) dt + \sum_{k \in K} \sigma_k\left(X_t^i\right) \circ dB_t^k. \tag{5.5}$$

As already pointed out in chapter 3, this is a model of common noise (also called environmental noise): the brownian motions's B_t^k are the same for all particles, in contrast to the model (5.3) where each particle X_t^i is driven by an independent brownian motion W_t^i. We refer to [53] for theoretical results on this model. For similar models, it has been proved (see e.g. [28]) that the empirical measure converges to the solution of the SPDE (5.4). In parallel, in the setting of [63] and subsequent works, the SPDE (5.4) converges to the deterministic equation with additional viscosity

$$\partial_t \omega + u \cdot \nabla \omega = \nu \Delta \omega \ . \tag{5.6}$$

in the case of small-scale noise. In this chapter, we numerically investigate the Point Vortex model dynamics with common noise (5.5). For given fields σ_k, this model would converge to the SPDE (5.4). We choose the fields σ_k such that our model is close to the deterministic equation (5.6).

There are two interpretations for our choice. If we look at the Point Vortex model just as a numerical discretization of the Euler equation, its stochastic modification (5.5) is just like the transport noise stochastic modification of the Euler vorticity dynamics (5.4). Therefore, a numerical realization of the theoretical scaling limit investigated in [51], from the stochastic Euler equation to the deterministic Navier-Stokes equation, could be to choose the coefficients σ_k as more and more concentrated. This could be a test of the validity of Boussinesq hypothesis that small scale turbulence enhances the viscosity.

The second interpretation is related to the fact that the Point Vortex model is a particle system. Consider the particle system (5.5), driven by common noise and compare it with the more classical particle system in which independent noise acts on on each particle. In the scaling limit for the fields σ_k described above, the common noise becomes increasingly spatially decorrelated, approaching the behavior of independent noise at each spatial location. As a consequence, the noise acts almost independently on each particle. Since the Point Vortex system driven by independent noise is known to converge to the Navier-Stokes equations, it is natural to expect that alsoe in the presence of common noise with highly concentration of σ_k the empirical measure of the particle system

remains close to the solution of the Navier-Stokes equations. This perspective has been investigated theoretically in [55]. Moreover, the problem of linking the turbulence stresses to the mean flow, the Boussinesq hypothesis, has been theoretically investigated in [52], where a connection with eddy viscosity and environmental small-scale noise is established.

Noise selection

We recall that our choice for the stochastic modification of environmental noise follows from literature on the study of passive scalar field advected by a stochastic velocity field, see [86]. For this reason, when considering the scaling limit of (5.5) to $\omega(\mathbf{x})$ solution of the viscous Euler equation (5.6), we study a noise delta-correlated in time, a white noise with space dependence:

$$\mathbf{W}(t,\mathbf{x})\,dt = \sum_{k\in K} \sigma_k(\mathbf{x})\,dB_t^k \ , \tag{5.7}$$

where $(\sigma_k(\mathbf{x}))_k$ is a family of smooth, divergence-free vector fields defined on the two-dimensional domain of the equation, and B_t^k are independent one-dimensional Brownian motions. The index set K is finite; however, under suitable assumptions, one may also consider the case of a countable family of smooth vector fields. The term

$$\mathbf{W}(t,\mathbf{x})\cdot\nabla\omega(\mathbf{x})$$

obtained in the convergence result of the Point Vortex model empirical measure, is to be understood as a Stratonovich integral,

$$\sum_{k\in K} \sigma_k(\mathbf{x})\cdot\nabla\omega(\mathbf{x})\circ dB_t^k \ . \tag{5.8}$$

We assume that the solution is sufficiently smooth, so that the Stratonovich integral makes sense, then, (5.8) can be expressed as an Itô-Stratonovich corrector plus an Itô integral:

$$-\frac{1}{2}\sum_{k\in K} \sigma_k(\mathbf{x})\cdot\nabla\left(\sigma_k(\mathbf{x})\cdot\nabla\omega(\mathbf{x},\mathbf{v})\right)dt + dM(t,\mathbf{x})$$

where $M(t,\mathbf{x})$ is a (local) martingale. Then, the Itô-Stratonovich corrector can be written as an elliptic operator:

$$-\frac{1}{2}\operatorname{div}\left(C(\mathbf{x},\mathbf{x})\nabla\omega(\mathbf{x})\right)dt \ ,$$

where $C(\mathbf{x},\mathbf{y})$ is the space-covariance function of the noise, defined as

$$C(\mathbf{x},\mathbf{y}) = \sum_{k\in K} \sigma_k(\mathbf{x})\otimes\sigma_k(\mathbf{y}) \ .$$

If we now make the same choice as [86] for the noise term, and for simplicity, we assume the domain to be $\mathbb{R}^2$ (modifications on $\mathbb{T}^2$ are possible, see for example [51, 55]), we are able to sketch some computations as an example. The covariance function of the noise term in [86] is space-homogeneous, i.e. $C(\mathbf{x},\mathbf{y}) = C(\mathbf{x}-\mathbf{y})$, and it takes the following form:

$$C(\mathbf{z}) = \nu k_0^{\zeta}\int_{k_0\le|\mathbf{k}|<k_1} \frac{1}{|\mathbf{k}|^{d+\zeta}} e^{i\mathbf{k}\cdot\mathbf{z}}\left(I - \frac{\mathbf{k}\otimes\mathbf{k}}{|\mathbf{k}|^2}\right)d\mathbf{k}.$$

For $\zeta = 4/3$ we recover the Kolmogorov K41 law: the model reproduce K41 energy spectrum for appropriate parameter choices. If $k_1 = +\infty$, then $C(\mathbf{0}) = K\sigma^2$ where the constant K is defined as

$$K = \int_{1 \leq |\mathbf{k}| < \infty} \frac{1}{|\mathbf{k}|^{d+\zeta}} \left(I - \frac{\mathbf{k} \otimes \mathbf{k}}{|\mathbf{k}|^2} \right) dk \quad .$$

We consider small-scale turbulent velocity fields depending on a scaling parameter and study the corresponding scaling limit in (5.4), following [55, 63]. In the setting of [86] we have

$$k_0 = k_0^N \to \infty$$

In this regime, the quantity

$$C(\mathbf{0}) = K\nu$$

is independent of N. As a consequence, the Itô-Stratonovich corrector reduces to

$$\nu \Delta \omega(\mathbf{x}),$$

At the same time, the Itô correction may vanish in the limit, recovering (5.6).

In the following, we give some motivations (see [51] for details) to briefly explain why the Itô term vanish in the limit, despite the convergence of the Itô-Stratonovich corrector to a finite, non-zero limit. Let ϕ be a smooth test function, then

$$\mathbb{E}\left[\left(\sum_{k \in K} \int_0^T \langle \sigma_k \cdot \nabla \omega_t, \phi \rangle_{L^2} \, dB_t^k \right)^2 \right] = \mathbb{E}\left[\sum_{k \in K} \int_0^T \langle \sigma_k \cdot \nabla \omega_t, \phi \rangle_{L^2}^2 \, dt \right]$$

by the isometry formula of Itô integrals, we obtain

$$= \mathbb{E}\left[\sum_{k \in K} \int_0^T \langle \omega_t, \sigma_k \cdot \nabla \phi \rangle_{L^2}^2 \, dt \right]$$

Using $\operatorname{div} \sigma_k = 0$,

$$\begin{aligned}
&= \mathbb{E}\left[\int_0^T \int\int \sum_{k \in K} \sigma_k(x) \cdot \nabla \phi(x) \, \sigma_k(y) \cdot \nabla \phi(y) \, \omega(t,x) \, \omega(t,y) \, dxdydt \right] \\
&= \mathbb{E}\left[\int_0^T \int\int \nabla \phi(y)^T \cdot C(x,y) \cdot \nabla \phi(x) \, \omega(t,x) \, \omega(t,y) \, dxdydt \right] \\
&= \mathbb{E} \int_0^T \langle \mathbf{C}\theta_t, \theta_t \rangle_{L^2} \, dt
\end{aligned}$$

In this expression, $\mathbf{C}$ denotes the linear operator acting on vector fields with kernel $C(x,y)$ and

$$\theta_t(x) = \nabla \phi(x) \, \omega(t,x) \quad .$$

Thus, we have

$$\mathbb{E} \int_0^T \langle \mathbf{C}\theta_t, \theta_t \rangle_{L^2} \, dt \leq \|\mathbf{C}\|_{L^2 \to L^2} \, \mathbb{E} \int_0^T \|\theta_t\|_{L^2}^2 \, dt.$$

One can now establish uniform bounds on

$$\mathbb{E} \int_0^T \|\theta_t\|_{L^2}^2 \, dt$$

with respect to the scaling of the noise. Moreover, it is possible to choose the noise in such a way that the operator norm $\|\mathbf{C}\|_{L^2\to L^2}$ vanishes in the limit. We point out that in the Itô-Stratonovich corrector the diagonal $C(x,x)$ dominates, whereas the smallness of $\|\mathbf{C}\|_{L^2\to L^2}$ is related to the smallness of $C(x,y)$ when $x \neq y$.

5.2.1 Setting: Kelvin–Helmholtz instability

In order to test the Point Vortex model in the deterministic case (5.2) and in the additive noise case (5.3), we consider a shear-flow configuration due to its fundamental properties: *developing instability without viscosity and delaying it when viscosity is present* [98].

We consider the following domain: the torus $\mathbb{T}^2$, equal to the set $[-1,1]^2 / \sim$ with coordinates $x = (x_1, x_2)$ and identified boundaries at $x_1, x_2 = \pm 1$; all fields are periodic in the x_1 and x_2 direction. We consider an initial velocity u_0 of the form

$$u^0(x_1,x_2) = \left(u_1^0(x_2), 0\right)$$

and corresponding vorticity $\omega_0 = \partial_{x_2} u_1^0(x_2)$. We take

$$u_1^0(x_2) = \begin{cases} -1 & \text{if} \quad x_2 \leq -\delta \\ \frac{x_2}{\delta} & \text{if} \quad -\delta \leq x_2 \leq \delta \\ 1 & \text{if} \quad \delta \leq x_2 \end{cases} \tag{5.9}$$

and we fix the parameter $\delta = 0.02$ in our numerical simulations.

To compute the vorticity measure of our Point Vortex model, we employ the method of vortex blobs, obtained by spreading the circulation of a Point Vortex over a chosen small area, the vortex core (see e.g. [120]). In this formulation, the vorticity field is approximated by

$$\omega_\varepsilon^N(\mathbf{x},t) \;=\; \sum_i \Gamma_i \, \phi_\varepsilon(\mathbf{x} - X_t^i), \tag{5.10}$$

where the mollifier ϕ_ε describes the vorticity distribution in the vortex core. In our numerical simulations, ϕ_ε is a Gaussian kernel, with width dependent on the subscript ε, the characteristic size of the vortex core. Following standard numerical techniques (see e.g. [2, 5]), the core size ε of the vortices has to be much larger than the average inter-vortex spacing d; the core size is usually chosen as $\varepsilon = d^q$, with $q << 1$.

In (5.10), the vorticity distribution at any time depends on the point vortices X_t^i through the vortex blobs. In our numerical simulations, we investigate a Point Vortex model with $N \sim 10^4$ vortices, following a mean-field scaling. The initial circulation assigned to each vortex is derived from u_1^0 and is equal to $\Gamma_0^i = \frac{1}{2\delta N}$. We refer to chapter 3 for a discussion on the scaling of the model. The Point Vortex system (5.2) is integrated using a 2nd order Runge-Kutta scheme, coupled with a Heun method for the stochastic term, yielding a second-order time discrete approximation. The time step is chosen as $\Delta t \sim 10^{-3}$ to provide a balance between numerical stability and the generation of vortex-like structures in the shear flow configuration. We refer to chapter 2 for a detailed discussion of the numerical techniques.

In our numerical framework, in (5.5) K indicates the Biot-Savart kernel, $K = \nabla^\perp G = (\partial_2 G, -\partial_1 G)$, where G is the Green function on $\mathbb{T}^2$. In the whole plane, the Green function is expressed as $G_{\mathbb{R}^2} = \frac{1}{2\pi}\log|x|$. For the torus, we have instead

$$G(x) = \frac{1}{2\pi}\log|x| + s(x), \;\; \forall x \in \mathbb{T}^2 \setminus \{0\}, \tag{5.11}$$

where $s(x)$ is a smooth function on $\mathbb{T}^2$; see chapter 1 for an extended discussion. As a consequence, K is divergence-free, smooth away from the origin, and symmetric. Moreover, it satisfies the asymptotic behavior

$$|K(x)| \sim \frac{1}{|x|}, \text{ as } |x| \to 0 \quad ,$$

which we extensively exploit in our numerical simulations to approximate the kernel with:

$$K_{\mathbb{R}^2}(x-y) = \frac{1}{2\pi}\frac{(x-y)^\perp}{|x-y|^2} \ .$$

More details on the numerical approximation of K are reported in chapter 2. Finally, without loss of generality, we consider the horizontal and vertical axes as our reference frame, referring to them as the x-axis and y-axis.

The role of intrinsic instability

The initial condition of the fluid velocity in our model, the vector field $u = u^0$, is a (at least formal) solution of Euler equation (1.15). This system is unstable: small perturbations rapidly develop vortex blobs, as described in section 5.1. We investigate the system of point vortices of positions $(X_t^i)_i$ with initial vorticity derived from (5.9),

$$\omega_0(x_1, x_2) := \frac{1}{N}\sum_i \frac{1}{2\delta}\delta_{X_0^i}(x_1, x_2), \tag{5.12}$$

where the circulation of each vortex is equal to $\frac{1}{2\delta N}$ and the initial positions of the vortices $X_0^i \ \forall i = 1, ..., N$ are uniformly distributed on the strip $[-1, 1] \times [-\delta, \delta]$. The randomly generated initial condition represents small perturbationsof the system and is responsible for the emergence of different patterns.

The empirical measure

$$\omega_t^N := \frac{1}{N}\sum_i \delta_{X_t^i}$$

converges in distribution to the scalar vorticity field solving the Euler equation (1.15). In analogy with the continuous setting, figures [5.1a] and [5.1c] show the development of instability in the form of macroscopic vortex-like structure forming along the interface between the two fluid layers.

We remark that both the number and the positions of these macroscopic vortex-like structures depend sensitively on the initial condition. In particular, small perturbations in the randomly generated initial configuration of point vortices may lead to entirely different macroscopic patterns, hence the instability of the two laminar flows profile.

The role of viscosity and stability restoration

The exact solution of the Navier-Stokes equation (3.3), with $\nu > 0$ and initial condition u^0, is given by the following velocity field:

$$u\,(t, x_1, x_2) = (u_1\,(t, x_2)\,, 0) \quad ,$$

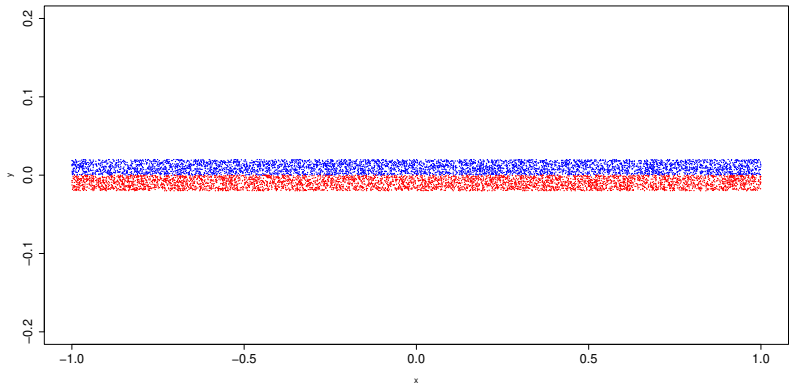

(a)

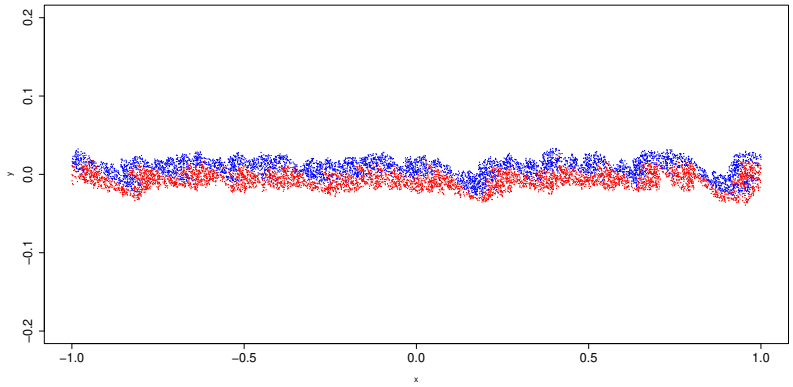

(b)

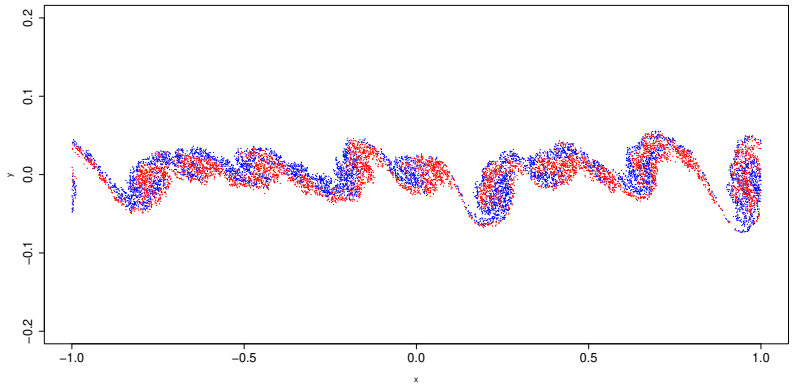

(c)

Figure 5.1: $\nu = 0$. (a): initial configuration, approximating a shear-flow velocity field; (b): iteration $t = 50$, showing the formation of macroscopic vortex structures; (c): iteration $t = 100$, displaying fully developed macroscopic vortex structures.

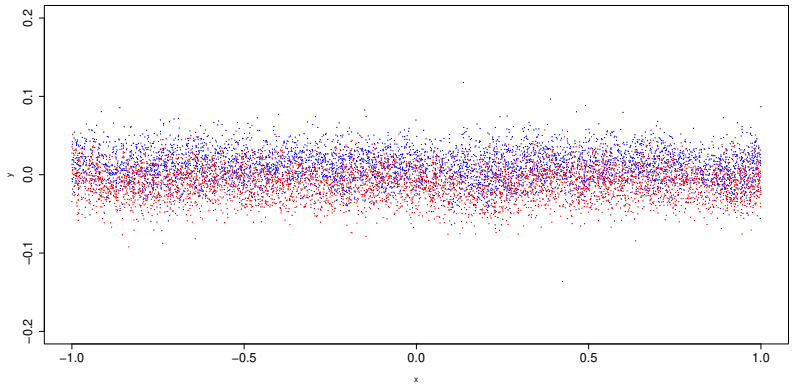

(a)

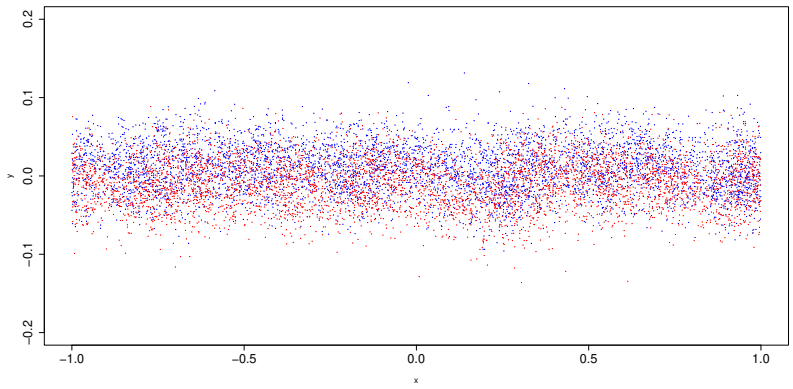

(b)

Figure 5.2: $\nu > 0$. (a): iteration $t = 50$, showing preservation of the strip profile; (b): iteration $t = 100$, initial development of the strip profile instability, and formation of large rotating structures.

where $u_1(t, x_2)$ solves the heat equation,

$$\begin{aligned} \partial_t u_1 &= \nu \partial^2_{x_2} u_1 \\ u_1(0, x_2) &= u_1^0(x_2) \ , \end{aligned} \tag{5.13}$$

see section 5.1 and the subsection therein for more details. Due to the spreading of the profile u_1^0, the solution becomes more stable and the formation of macroscopic vortex-like structures is delayed. In our numerical simulations, we reproduce this effect by perturbing the system (5.2) with independent Brownian motions B_t^i, $i = 1, ..., N$, whose variance is linked to the viscosity parameter, $Var(B_t^i) \sim \sqrt{\nu}$. In the limit $N \to \infty$, this stochastc particle system converges to the exact solution; however, in our numerical study we consider a finite number of vortices. As a consequence, the strip profile remains relatively stable at short times, exhibiting a spreading along the y-axes.

Figures [5.2a] and [5.2b] display a single realization of the system at two different timesteps, $t = 50$ and $t = 100$ respectively. We choose the parameter $\sqrt{\nu}$ as $\sqrt{\nu} = 0.095$ to better highlight the stabilization effect. Our results are consistent with theoretical predictions: comparison with [5.1b-5.1c] shows that when $\nu > 0$, the profile is much more stable and diffused than in the deterministic case, and macroscopic vortex-like structures emerge only at later times.

5.2.2 Numerical results on environmental noise

Starting from the same initial condition (5.9), we consider $N + M$ point vortices, with

$$X_t^1, ..., X_t^N, Y^1, ..., Y^M.$$

being their respective positions on the torus $\mathbb{T}^2$.

In this setup, the vortices Y^i, $i = 1, ..., M$ are fixed in space, and when their interactions with the point vortices became non-negligible, they represent the feedback of small-scale turbulence on the large-scale fluid dynamics.

The vortex dynamics for X_t^i in $\mathbb{T}^2$ as in (5.5), is

$$dX_t^i = \frac{1}{N} \sum_{i' \neq i} \Gamma_{i'} K\left(X_t^i - X_t^{i'}\right) dt + \sum_j \sigma_j(X_t^i) \circ dW_t^j \tag{5.14}$$

where W_t^j are Brownian motions, all independent and uni-dimensional, and they act simultaneously on all particles $i = 1, ..., N$. The environmental noise is interpreted in the Stratonovich sense, which is naturally implemented by Heun's method [95, 96]. We employ periodic boundary conditions as our domain is the torus $\mathbb{T}^2$.

Selection of divergence free field

We choose the divergence-free vector fields σ_j as

$$\sigma_j(X_t^i) := a_j^{N,M} K\left(X_t^i - Y^j\right), \quad j = 1, ..., M \ ,$$

following the theoretical analysis developed in [57, 55]. The coefficients $a_j^{N,M}$ are determined by the scaling limit procedure, which yields an effective viscosity at large scales, while K, the Biot-Savart kernel, models the action of the small-scale vortices. The motivation for this choice is that we want

to exploit the same features of the vortex model, namely the feedback induced by small-scale vortex structures on the overall configuration. In the limit, the dynamics of such small structures, modulated through a Brownian motion, should act on the emerging large scales, perturbing their motion as a consequence of the dissipative properties of the small structures and delaying the formation of the instability.

Positions and intensities of fixed vortices

In this numerical investigaton, the positions of the fixed vortices Y^j and their intensity $a_j^{N,M}$ are chosen according to the convergence of the scaling limit (5.14). At each timestep, we generate $Y^j,\ j = 1, ..., M$, uniformly distributed point vortices; their position on the y-axis is prescribed beforehand in the interval $[-\delta_{FX}, \delta_{FX}]$. The vortices Y^j are generated in a strip of variable height $2\delta_{FX}$. This strip contains the moving vortices X_t^i, and is chosen to have the same height as the boundary fluid layers, or to be one order of magnitude larger. This choice emphasizes that the proposed *small-scale* structures should act on the fluid at all points and in all directions: on average, the contribution of the Y^j to the dynamics of the X_t^i along each direction is intended to mimic a Brownian motion. We explored several setups of positions and intensities; we selected representative realizations, which are reported in table 5.1.

M	δ_{FX}	m	a
200000	0.1	0.0014	0.0005
132000	0.07	0.0014	0.0005
1000	0.07	0.0017	0.005

Table 5.1: Parameters of the transport noise stochastic modification used in the numerical simulations.

We choose the intensity of the *small-scale* perturbations following the heuristic considerations below. The mean inter-particle distance between two fixed point vortices is defined as

$$\langle r \rangle := \frac{1}{\sqrt{m}}$$

where

$$m := \frac{M}{A}$$

is the particle density and A is the total area occupied by the M vortices.

For a single moving vortex, X_t^i, we compute the magnitude of its velocity when X_t^i is at a distance

$$d = \frac{\langle r \rangle}{2}$$

from the nearest fixed vortex, i.e., its position is halfway between two fixed vortices. We obtain the following estimate for the velocity of X_t^i:

$$\sum_j a_j^{N,M} \frac{1}{4\pi} \frac{|X_t^i - Y^j|^\perp}{\|X_t^i - Y^j\|^2} \sim \frac{1}{4\pi} \sum_j \frac{a_j^{N,M}}{d} \sim \frac{a^N}{4\pi} \sum_j \frac{1}{d}.$$

where we assume that the coefficients depend on the configuration $(X_t^i)_i$, and are equal for each $j = 1, ..., M$. We then estimate the number of fixed vortices such that the interaction with X_t^i is not

negligible, K. We obtain:

$$\sum_j a_j^{N,M} \frac{1}{4\pi} \frac{|X_t^i - Y^j|^\perp}{\|X_t^i - Y^j\|^2} \sim \frac{Ka^N}{4\pi d} .$$

We exploit the scaling limit of environmental transport noise (see e.g. [55, 57, 63]) to deduce the following relation for the viscosity ν:

$$\nu \sim \frac{1}{2} \left(\frac{Ka^N}{4\pi d} \right)^2 .$$

Putting together all the previous estimates, we finally obtain for the intensity of the fixed vortices as a function of K:

$$a^N \sim 2\sqrt{2}\pi \frac{\sqrt{A}}{\sqrt{M}} \frac{\sqrt{\nu}}{K} .$$

We now have to estimate the number of the nearest fixed vortices K: to do that, we consider a ball centered in X_t^i with radius d. The area of the ball is

$$A_{near} = \pi d^2 .$$

The nearest vortices are estimated by

$$m \times A_{near} = \frac{M}{A} A_{near} = \frac{\pi}{4} ,$$

where we indicate with m the density of the fixed vortices. Note that, as we are only counting the nearest vortices, the real contribution of all the vortices is being underestimated in this estimate. To obtain a sharper estimate, we should compute such contribution by considering a radius dependent on the effective range of the image of the Biot-Savart kernel. As the Biot-Savart kernel satisfies the following relation:

$$K \sim \frac{\Gamma_i}{|x|^2} ,$$

the contribution of distant vortices is negligible. To take into account such small contribution, in this numerical study we empirically selected a wider radius αd, with $\alpha \sim 3$.

Finally, the estimate for the fixed vortices intensity is given by the following relation:

$$a^N \sim \frac{8\sqrt{2}}{3} \sqrt{\nu} \frac{\sqrt{A}}{\sqrt{N}} .$$

Effect of small scale common noise

In the previous paragraph, we exploited the fact that the scaling limit procedure is valid in the regime in which both N and M are large, and the intensity $a_j^{N,M}$ is small.

For this reason, we do not expect to obtain results too close to the exact solution of the Navier-Stokes equation (3.3), $\nu > 0$, with initial condition u^0, as in the case of the independent noise. However, since the regime tends, in the limit, to the same solution, we expect to see a diffusive effect on the vortices strip in the numerical simulations. We expect a delay in the formation of macroscopic structures, as in the viscous case. However, the small vortex blobs are more dispersed

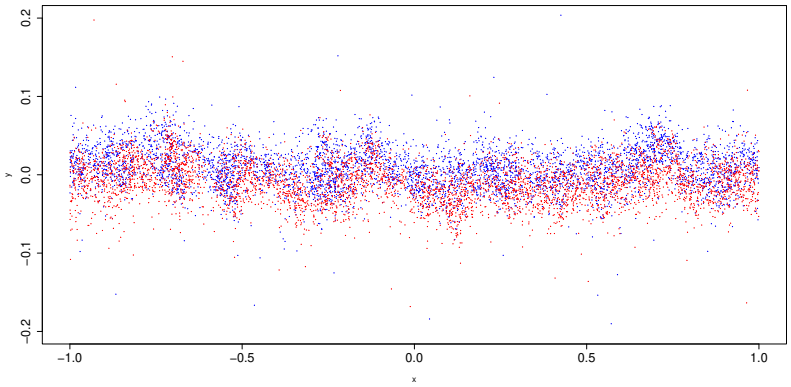

(a)

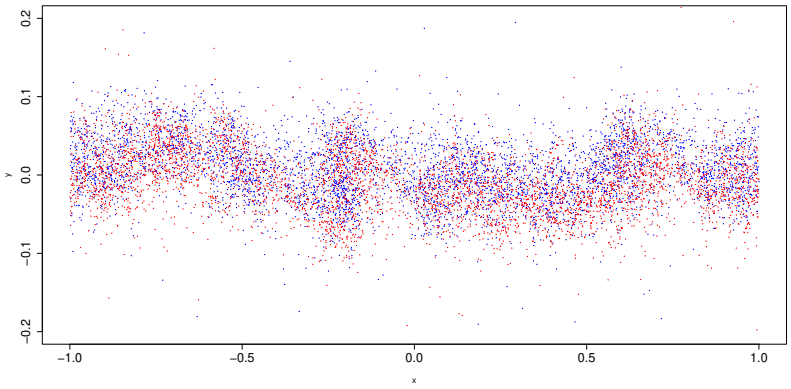

(b)

Figure 5.3: environmental noise. (a): iteration $t = 50$, showing diffusive behaviour of the strip profile; (b): iteration $t = 100$, showing degradation of the profile, and formation of macroscopic structures due to stretching.

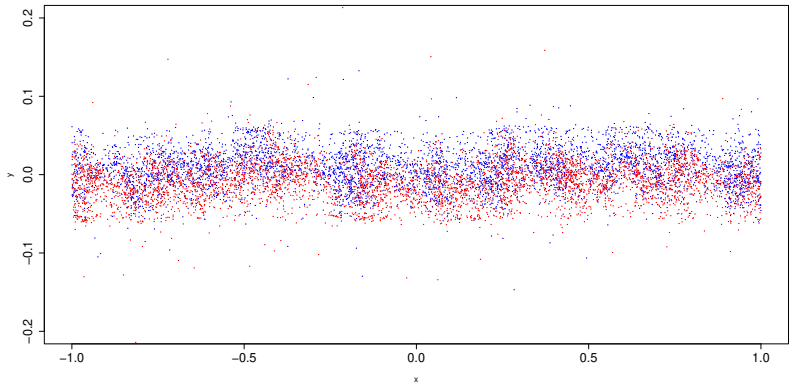

Figure 5.4: environmental noise case, iteration $t = 50$, diffusion of the strip is present for a short time with preservation of its overall configuration.

than in the viscous case, due to the environmental nature of the noise, and they fail to maintain the strip configuration at large times, in contrast to the viscous case.

In the first of our simulations, we generate at each time step $M \sim 2 \cdot 10^5$ fixed vortices, with intensity $a_j^{N,M} \sim 5 \cdot 10^{-4}$, chosen according to the consideration already reported in the previous sections. The fixed vortices are uniformly distributed in a strip $[-1, 1] \times [-0.1, 0.1]$, which contains the initial point vortices configuration.

Our goal in choosing this setup is to study the feedback effect of the small scales on the large vorticity structures which are formed after the onset of the instability; the low-intensity stochastic perturbations of the Point Vortex model's dynamics tend to average out isotropically, due to their distribution in space.

Our numerical results show that the transport noise model reproduces the expected delay of the instability, although it is slightly less effective than the case with independent noise. Snapshots of a representative realization at times $t = 50$ and $t = 100$ are reported in figures [5.3a,5.3b]. By comparison with figures [5.1b,5.2a], we observe that the initial strip configuration is preserved for a longer time than in the deterministic case and that the fluid rotation is milder; however, the profile remains less stablethan in the viscous regime. In the deterministic setting, blob-like structures already form at $t = 50$, whereas in the transport-noise regime such structures are significantly less pronounced and become clearly visible only toward the end of the simulation ($t = 100$). This delay of the instability is evident when comparing the realizations in figures [5.3b], with those in figure [5.1c,5.2b]. We observe a more diffused and homogeneous profile, together with a delayed formation of rotational structures due to the noise-induced spreading of particles along the y-axis. A difference with respect to the viscous case is that the compression along the x-axis is stronger than in the case of the independent noise regime, leading to a more pronounced stretching. This behavior suggests that the transport noise case represents an intermediate regime between the deterministic and viscous cases.

Next, we generate the strip of fixed points Y^j within the same spatial region occupied by the moving point vortices at each timestep. We take $M \sim 1.32 \cdot 10^5$, with the fixed vortices uniformly distributed over $[-1, 1] \times [-\delta - \varepsilon, \delta + \varepsilon]$, with $\varepsilon = 0.03$. The corresponding intensities are chosen according to the heuristic scaling, $a_j^{N,M} \sim 5 \cdot 10^{-4}$. The results are shown in figure [5.4]. We observe

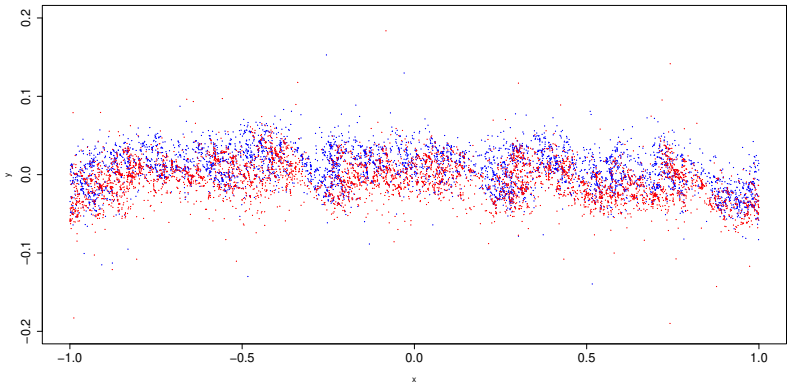

Figure 5.5: environmental noise case, iteration $t = 50$, low density ratio between fixed vortices and moving point vortices, showing the emergence of medium-scale structures.

that diffusion along the y-direction is present at short times, and the strip profile is preserved. A limitation of this configuration, however, is that the analysis can be carried out only over relatively short time intervals: boundary effects of the fixed vortex strip may deteriorate the configuration, making the results unrealistic. In future works, we aim to overcome this limitation by proposing a new method, under investigation, to generate small vortices only in regions activated by the motion of the shear flow.

Finally, we consider a configuration in which the density of fixed vortices is lower than the density of the moving point vortices. In particular, the strip of fixed vortices Y^j is generated in the same region as the moving point vortices at each timestep. We choose $M \sim 10^3$ fixed vortices, uniformly distributed in $[-1, 1] \times [-\delta - \varepsilon, \delta + \varepsilon]$, with $\varepsilon = 0.05$, and intensity $a_j^{N,M} \sim 5 \cdot 10^{-3}$. n this configuration, the diffusive behavior is no longer observed. As shown in [5.5], the strip is already broken at time $t = 50$, showing rotating structures. The combination of a lower density of fixed vortices and higher intensities appears to produce new medium-scale structures, resulting in a substantially different behaviour from both the deterministic and viscous cases. For this reason, a systematic investigation of the link between the ratio of vortex densities and the formation of independent medium-scale structures is in order.

5.2.3 Statistical Analysis

In this section, we perform a statistical analysis of the three configurations considered in this study in order to highlight their differences, the degree of restored stability, and the emergence of new structures.

As a first step, we compute the vorticity field ω_ε obtained via the same mollification procedure adopted by Majda [5], through the vortex blob method applied to each point vortex X_t^i. We report the vorticity field obtained in the deterministic case at $t = 100$ in figure [5.6a]. The vorticity concentration near the fluid boundary layer is localized within the newly formed macroscopic structures. Moreover, a displacement from the initial laminar configuration is present.

By contrast, in the viscous case $\nu > 0$, the vortex blob solution preserves its structure for longer times than in the inviscid case. The delay of the instability is learly visible both in the

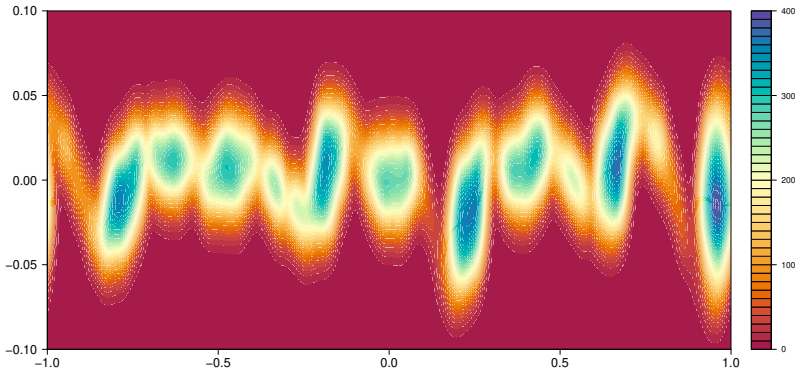

(a)

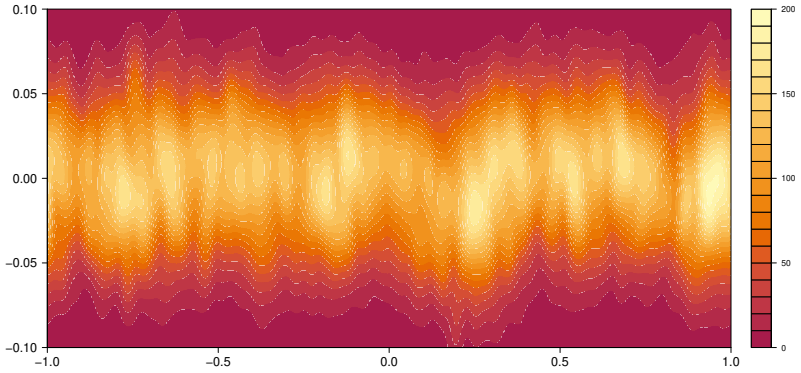

(b)

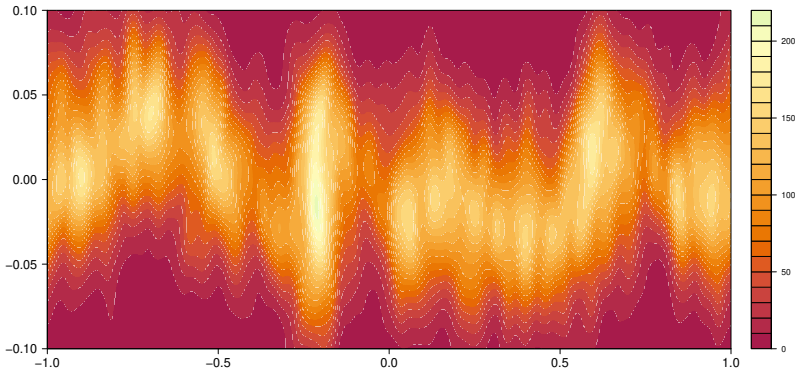

(c)

Figure 5.6: Vorticity ω_ε at $t = 100$ in the case (a) inviscid, (b) viscous and (c) transport noise, showing macroscopic structures formation or delay of instability.

configuration shown in figure [5.2a] and in the vorticity intensity reported in figure [5.6b]: the vorticity concentration at time $t = 100$ is close to the one of the initial strip, with a more diffused profile along the horizontal direction.

Finally, figure [5.6c] shows the vorticity in the environmental noise regime at $t = 100$ for the configuration 5.3b. In contrast to the inviscid case, no macroscopic structures develop in the profile. Although the vorticity distribution is more diffused and exhibits a overall lower density, the stability of the strip is lost at larger times compared to [5.6b] and [5.2b]. This instability at larger times suggests that different behavior, may arise, dependending on the density of fixed vortex Y^j and on the choice of transport noise fields σ_j. For this reason, we focus our analysis on the short-time behavior of the system.

Concerning the formation of large rotating structures, the particles spread in the horizontal direction when a forcing term, either an independent or transport noise, acts on the fluid, in contrast to the solution of the Euler equation with $\nu = 0$. To quantify this effect, we analyze the empirical density obtained from the x-coordinates in the three configurations at $t = 100$, [5.7]. In the deterministic case [5.7a] we observe the formation of distinct blobs with density peaks in the exact locations of the macroscopic structures, in agreement with [5.1c]. By contrast, in both the viscous [5.7b] and transport noise cases [5.7c], the vortices distribution significantly more uniform, resulting in a delayed development of the instability of the fluid layers.

From theoretical results, for the chosen initial condition ω_0, the velocity u_t solves (5.13) when $\nu > 0$. This is essential to understand the short-time behaviour of the system and the persistence of the initial configuration. This result implies that the empirical density obtained from the y-coordinates, when viscosity is present, remains Gaussian in time. In contrast, in the case of $\nu = 0$, the viscosity follows the deterministic Euler equation. As such, the y-position profile deviates from a Gaussian: it behaves like a multi-modal distribution, with mass concentrated near the center of the large structures. This behavior is shown both by the profile of the particle system and by figures [5.8a,5.9a]; the qq-plot shows a deviation from Gaussian behaviour for lower quantiles. The Kolmogorv-Smirnov test estimates a D-statistic of 0.031, with a p-value less than 10^{-9} confirming the rejection of the Gaussianity hypothesis.

Conversely, for $\nu > 0$, as in the case of independent Brownian forcing, the noise's diffusive behaviour allows restoration of the profile in the y-direction, and the strip configuration is preserved for a longer time. From the Point Vortex configuration and figures [5.8b,5.9b], we see that the empirical density approximates well the one of a Gaussian kernel. Moreover, the qq-plot indicates a excellent agreement with a normal distribution, consistent with the preservation of the strip through time, at the expense of increased spreading along the y-axis. Finally, a Kolmogorv-Smirnov test yields a D-statistic of 0.005 and a p-value greater than 0.9 providing strong evidence for the normality hypothesis. This behaviour is preserved throughout the simulation, degrading only at later times when a small number of large-scale structures start to emerge, as in figure [5.2b].

In the transport noise case, under an appropriate scaling limit, one could recover the same viscous Euler equation solved in the independent Brownian motion case. To this end, we expected that the more stable profile shown in figure [5.3a] exibits a diffusion of the y-coordinate density, as in the case of the independent noise. This intuition is confirmed at short times, $t = 50$, by figures [5.8c,5.9c], in which the profile still approximates a Gaussian kernel. We perform a qq-plot and a Kolmogorov-Smirnov test on the y-coordinate; we obtain a D-statistic of 0.011, and a p-value of 0.312; those results support the profile stability and the validity of our hypothesis.

At later times ($t = 100$), although the Kolmogorov–Smirnov statistics remain comparable to those observed in the viscous case, with a D-statistics of 0.008 and a p-value of 0.48, the profile

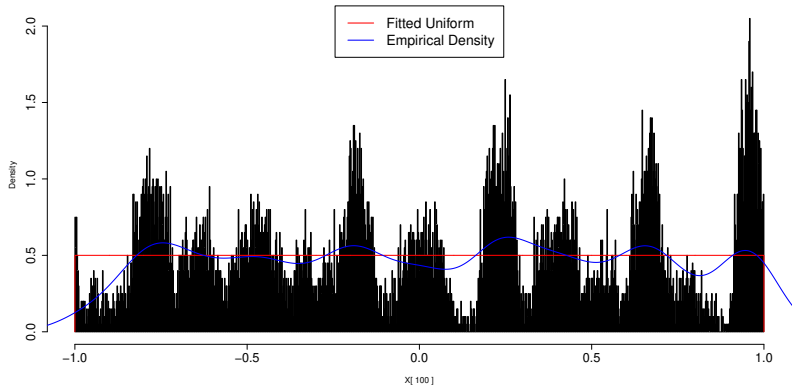

(a)

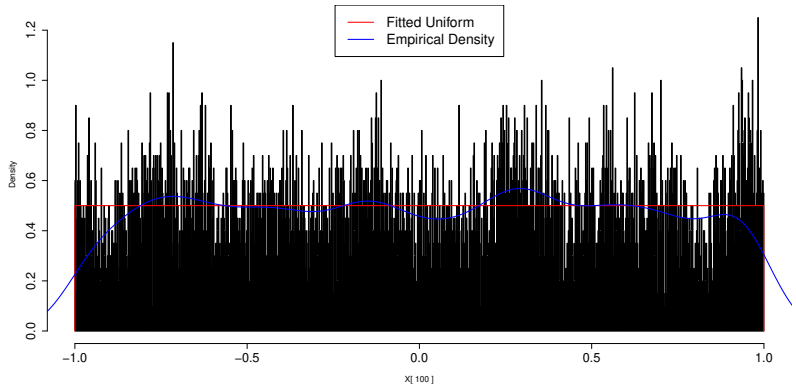

(b)

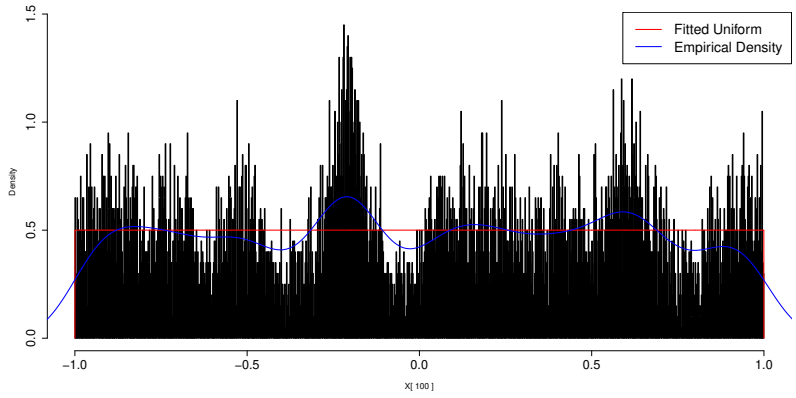

(c)

Figure 5.7: Histograms of x-positions and empirical density at $t = 100$ in the case (a) inviscid, (b) viscous and (c) transport noise, showing formation of macroscopic structures.

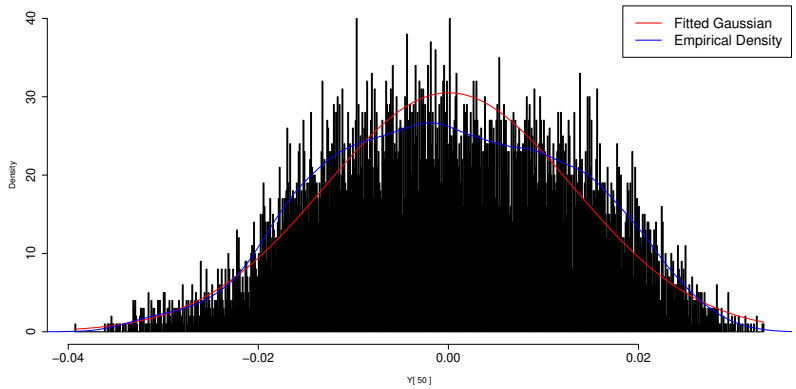

(a)

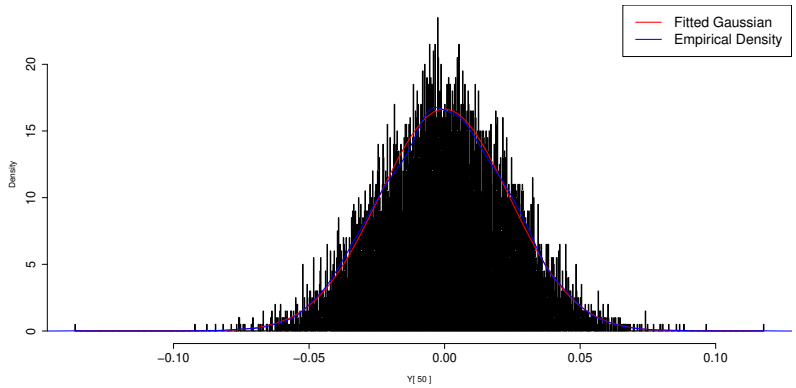

(b)

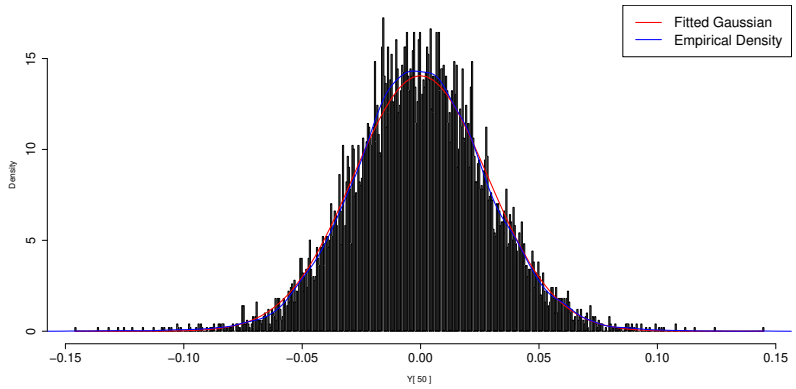

(c)

Figure 5.8: histograms of y-positions and empirical density at $t = 50$ in the case (a) inviscid, (b) viscous and (c) transport noise, showing different density profiles.

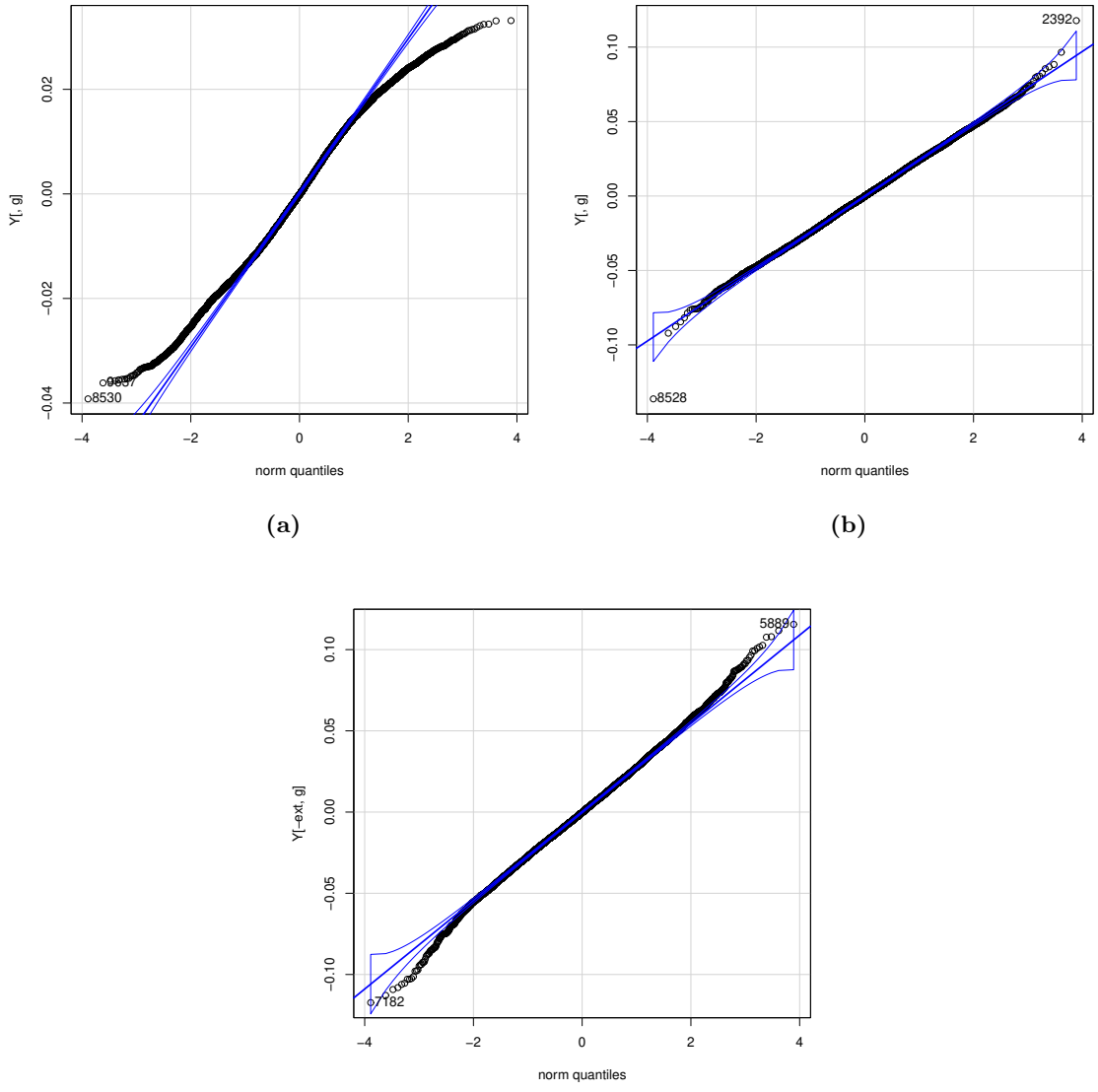

(a) **(b)** **(c)**

Figure 5.9: qq-plot of the empirical density in the y-positions, at $t = 50$ in the case (a) inviscid, (b) viscous and (c) transport noise.

degrades as shown in [5.3b]. Those results show that the strip configuration is not preserved over long times due to transport noise stretching acting on the point vortices. This is evident in the tail of the distribution in figure [5.9c], when compared with the viscous case in [5.9b], which exibits different behaviour already at $t = 50$. This observations suggest that the environmental noise's effect is not only related to the diffusivity of the strip, but is also responsible for the stretching and formation of structures.

5.3 Some further numerical studies on the properties of the environmental noise

In this section, we consider both the Point Vortex model with environmental noise, introduced in the previous section and in the work [59], and the formulation described in detail in chapter 3. The numerical investigation reported in this section is presented in [58]; we focus on the study of the Kelvin-Helmholtz instability, comparing results for inviscid fluid, viscous fluid and inviscid fluid with transport noise, in the numerical framework of point vortices.

In the following, we introduce a minor modification to the Point Vortex model dynamics perturbed by transport noise, motivated by the considerations discussed in chapter 3. We consider the following dynamics:

$$dX^{(i)}(t) = \frac{1}{N}\sum_{j\neq i} K(X^{(i)}(t) - X^{(j)}(t))dt + \sum_k \sigma_k\left(X^{(i)}(t)\right) \circ dB_t^{(k)}$$

which is the same as the previous section, equation (5.14). In this equation, $B_t^{(k)}$ are independent 1D Brownian motions; $B_t^{(k)}$ are the same for each value of i, as opposed to the independent Brownian motions introduced for the viscous flow, as already pointed out in the previous section. The main difference with respect to the previous section is the choice of the divergence-free vector fields σ_k. While in the previous section their intensities were selected according to heuristic arguments, here we focus on the following choice, based on considerations made in chapter 3:

$$\sigma_k(X^{(i)}(t)) := \frac{2\Gamma}{\sqrt{M}}\frac{1}{\|K_\varepsilon\|_2}K_\varepsilon\left(X^{(i)}(t) - Y^{(k)}\right), \quad k = 1, ..., M \ .$$

As before, the vector fields represent small-scale vortex structures located at positions $Y^{(k)}$. Their interaction kernel is regularized, the regularization parameter being ε. While this parameter was taken very small in the previous section and in [59], in this section we consider larger values of ε. Throughout the following numerical investigation, we fix $\Gamma = 0.5$.

Once again, we consider a two-dimensional, doubly periodic domain, a torus $\mathbb{T}^2$, $[-1,1]^2 \,/\, \sim$, with coordinates $x_p = (x, y)$ and identified boundaries at $x, y = \pm 1$ ($L = 2$). In the previous section, we investigated a *smoothed instability*, in this present setting, however, our goal is to study a slightly different setup. We take as initial condition the following velocity field:

$$u(t = 0)\,(x, y) = \left(u_x^0\,(y)\,, 0\right) \ ,$$

but with

$$u_x^0\,(y) = \begin{cases} -1 & \text{if} \quad y < 0 \\ 1 & \text{if} \quad 0 < y \end{cases}$$

Instead of taking a tick strip of point vortices as initial condition, in this section we discretize the layer separating the two streams using N point vortices, uniformly distributed on the line $y = 0$.

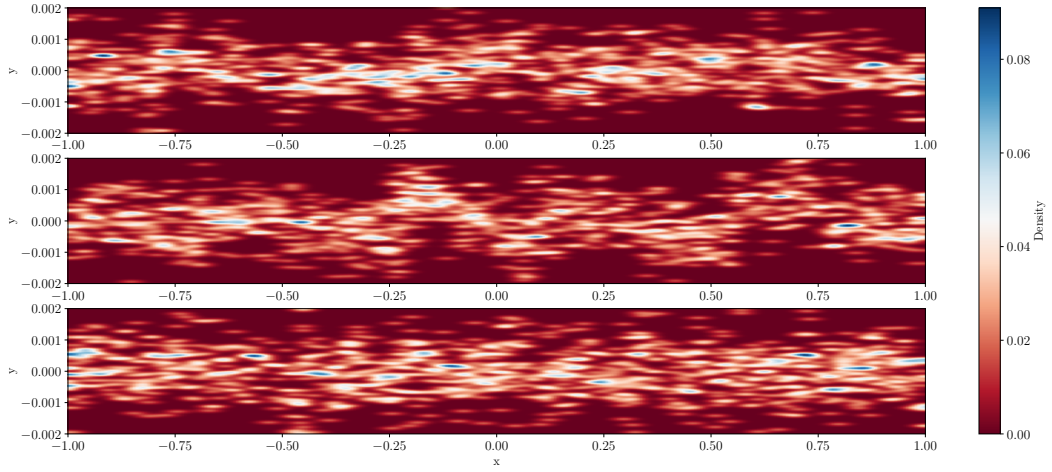

Figure 5.10: Time evolution of $N = 10^3$ point vortices, uniform distributed on $y = 0$ at $t = 0$. From up to down: inviscid fluid ($\nu = 0$), inviscid fluid with transport noise ($\varepsilon = 0.01$, $M = 10^6$), viscous fluid ($\nu = 0.005$). We take $t = 900\ dt$, with $dt = 10^{-5}$.

This numerical setup bears similarities with the one described in the previous section and adopted in [59]. The minor changes are motivated by the specific numerical investigation of the velocity field, which constitutes one of the main objectives of this section and will be described in greater detail below. In this section, we adopt the numerical approximation of the Biot–Savart kernel exploited in [59, 68], namely the second approximation described in chapter 2.

As in the previous section, we numerically solve the dynamics by a 2nd order Runge-Kutta scheme coupled with a Heun techniques for the noise, see chapter 2 for a detailed discussion of the numerical techniques. We thus compute the observables with a second-order time discrete approximation.

5.3.1 Vorticity distribution

As a preliminary step, we repeat part of the analysis carried out in the previous sections, and to this end we study the vorticity distribution for the three different variants of the Point Vortex model, already described in details in the previous sections of this chapter and in chapter 3.

We report in figure 5.10 the vorticity distribution for the time evolution of $N = 10^3$ point vortices, uniform distributed on $y = 0$ at $t = 0$. As in the previous sections, we consider three different models: the inviscid fluid, corresponding to zero viscosity, $\nu = 0$, the inviscid fluid with stochastic modification of transport noise, with parameters $\varepsilon = 0.01$, $M = 10^6$, and the viscous fluid. From this qualitative plot, we can already draw several observations on the effects of the environmental noise on the Kelvin-Helmholtz instability: the environmental noise induces a deformation of the initially straight vortex sheet and appears to act as an additional (low) viscosity. Moreover, we note that macroscopic vortex structures are developed even in this case. Those numerical results further confirm the behavior previously reported in [59] and described in the previous sections. In these simulations, we take $\varepsilon = 0.01$, a larger value compared with the one employed in the previous

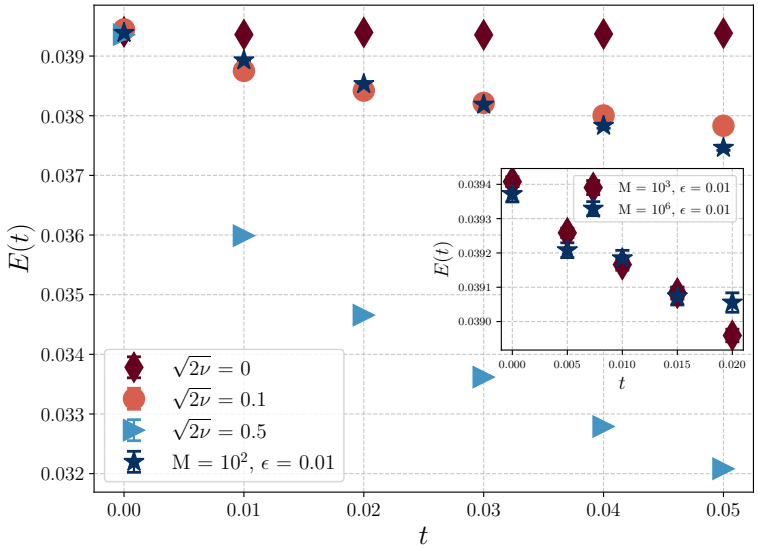

Figure 5.11: Hamiltonian of the Point Vortex system, which in the case of the standard model represents the kinetic energy of the fluid, computed at different times t. We take $dt = 10^{-5}$ and $N = 10^2$ point vortices. Datapoints are averaged on different samples with different initial conditions for the positions $X^{(i)}$ and positions of noisy structures. Inset: all datapoints are averaged on different samples with different initial conditions for the positions $X^{(i)}$ but same positions of noisy structures, for comparison. Different M have comparable effect.

sections and in the work [59]. This choice represents a compromise between the two regimes of very small ε and very large ε, the latter emphasizing large-distance effects of the noise, and it allows us to compare our results on the vorticity distribution with the ones obtained in the previous sections.

We point out that, within our setup, the choice $\delta = 0$ leads to reduced stability of the system, see [87], compared with the case $\delta > 0$ analyzed in the previous sections, or with configurations of point vortices uniformly distributed on the torus, see chapter 6 and [68]. This reduced stability will become apparent in the computation of observables that are expected to be conserved in time, such as the Hamiltonian of the system.

5.3.2 Energy conservation

A further step in the analysis of the effects of noise on the Kelvin-Helmholtz instability is pursued by studying the energy conservation in the different Point Vortex models investigated. In the case of the Point Vortex model, as seen in chapter 1, the kinetic energy of the fluid can be computed via the Hamiltonian of the system, in which the auto-interaction between vortices is not included. More precisely, we compute the quantity $E(t)$, which in the case of the deterministic Point Vortex model coincides with the Hamiltonian of the system,

$$H = -\frac{1}{2\pi} \sum_{i \neq j} \gamma_i \gamma_j \log d(x_i, x_j) \ , \tag{5.15}$$

Table 5.2: Computed values of the Point Vortex model Hamiltonian (inviscid case, $\nu = 0$) at different timesteps, in the case in which there is no stochastic modification in the dynamics. We note that, due to the specific initial configuration chosen ($\delta = 0$), the relative error in the conservation of the Hamiltonian is comparable with the statistical error. The statistical error is computed by performing bootstrap procedure over ~ 10000 samples.

t	$\langle H(t)\rangle$	$\lvert\langle H(t)\rangle - \langle H(0)\rangle/\langle H(0)\rangle\rvert$
0.00	0.039405(14)	-
0.01	0.039360(14)	0.0011
0.02	0.039395(14)	0.0002
0.03	0.039355(14)	0.0013
0.04	0.039369(13)	0.0009
0.05	0.039385(14)	0.0005

Here, we take $\gamma_i = N^{-1}$, the mean-field scaling, x_i is the position of the i vortex, and $d(x_i, x_j)$ is the distance computed on the chosen domain, in our case the two-dimensional torus $\mathbb{T}^2$; as commented before, we are exploiting the second approximation of the Biot–Savart kernel, described in chapter 1.

We report in figure 5.11 the computed values of the Hamiltonian of the system, comparing the two different stochastic modifications of dynamics of the Point Vortex system: the additive noise stochastic modification, characterized by the viscosity parameter ν, and the transport noise stochastic modification, characterized by the regularization kernel parameter ε and by M, the number of fixed vortices in the system. Results are reported for several values of the viscosity, $\sqrt{2\nu} = 0, 0.1, 0.5$, which allows for a quantitative comparison between the effects of additive noise and transport noise on the dynamics of the Point Vortex model. In particular, we observe that, in the stochastic regimes, the Hamiltonian exhibits a decay that is significantly larger than the estimated numerical integration error, suggesting that the stochastic perturbations induce dissipation in the system.

We begin by discussing the main panel of the figure, deferring the analysis of the inset to the end of this section. We first focus on the case $\sqrt{2\nu} = 0$, which corresponds to the deterministic Point Vortex model, for which the Hamiltonian is theoretically conserved up to numerical errors. This case is therefore used to estimate the numerical error associated with our computational approach, and serves as a reference for the subsequent analysis. The numerical error is evaluated as the relative deviation in time from the initial value $H(t = 0)$ over time, since the magnitude of $H(t = 0)$ may vary significantly depending on the initial configuration of the point vortices. We report in table 5.2 the values of the Hamiltonian of the system at different times, together with their statistical uncertainties and the relative variation with respect to the initial value $H(t = 0)$. We emphasize that the objective of this analysis is not to obtain a highly accurate estimate of the Hamiltonian, nor to employ a specialized numerical scheme aimed at minimizing errors in the deterministic dynamics. A quantitative analysis of the numerical error in the Hamiltonian evolution of the deterministic Point Vortex model, computed using a higher order method, is deferred to chapter 6 and to the paper [68]. In that work, it is shown that the relative error in the Hamiltonian decay is, in the worst case, of order 10^{-7}, when the dynamics are discretized using a fourth-order Runge-Kutta scheme.

We next consider two additional cases: the additive noise stochastic modification of the dynamics with $\sqrt{2\nu} = 0.1$, and the transport noise stochastic modification with $M = 10^2$ fixed vortices and regularization parameter $\varepsilon = 0.01$. In the latter case, a larger value of the regularization parameter is deliberately chosen in order to explore a regime different from the one analyzed in the previous

section. The positions $Y^{(k)}$ of the fixed vortices are drawn independently from a uniform distribution on the torus $\mathbb{T}^2$. As discussed in chapter 3, averaging over different realizations of these initial conditions restores isotropy properties in the resulting dynamics. We note that, for times $t < 0.04$, the Hamiltonian decay in the additive noise and transport noise cases appears to be qualitatively compatible. In both cases, the decay is significantly more pronounced than in the inviscid case $\nu = 0$, where the observed variation was attributable solely to numerical error. For comparison, we also report results for $\sqrt{2\nu} = 0.5$, which exhibit a substantially sharper decay of the Hamiltonian.

Finally, in the inset plot of figure 5.11 we present results for the transport noise stochastic modification of the dynamics for larger values of the parameter M, namely $M = 10^3$ and $M = 10^6$, with the regularization parameter fixed at $\varepsilon = 0.01$. In this comparison, we take the same positions of the fixed vortices $Y^{(k)}$ for both values of M. This allows us to isolate the effect of varying the number of vortices and to examine the corresponding scaling behavior in a regime where isotropy is not recovered through averaging over different configurations of $Y^{(k)}$, see chapter 3 for a discussion on this topic. The positions $Y^{(k)}$ taken in this setup are placed on a lattice as described in section 3.6 of chapter 3. We observe that, for the two values of M considered, the Hamiltonian evolution obtained from identical initial configurations of the fixed vortices is compatible, at least for sufficiently small times t.

As a final remark, we observe that the Hamiltonian decay induced by the numerical integration error is negligible when compared with the decay induced by the introduction of stochastic perturbations in the Point Vortex model dynamics. On the basis of our numerical investigation, we conclude that, in the presence of transport noise stochastic modification of the dynamics, the kinetic energy of the model, defined as in equation (5.15), does not appear to be conserved, as the observed decay is significantly steeper than the decay associated with the numerical integration error. Nevertheless, we cannot completely rule out the possibility that part of this behavior arises from additional sources of error related to the implementation of the stochastic perturbations in the dynamics.

5.3.3 Velocity profile

In this final section, we turn to an investigation of the velocity field, focusing on the velocity profile. As discussed in section 5.1.1, when the initial velocity field of a viscous flow exhibits a discontinuity, the velocity evolution satisfies a diffusion equation. In this regime, the Navier–Stokes equations reduce to the considerably simpler heat equation: the evolution of the velocity profile can be written as a function of the variable η, in the following form

$$u(\eta) = -U_0 \mathrm{erf}\left(\frac{\eta}{2\sqrt{\nu}}\right) \tag{5.16}$$

where η is defined as

$$\eta = \frac{y}{\sqrt{t}}$$

as seen before in section 5.1.1; this parameter differs from η^* in equation (5.1), as it does not depends on ν, and it is a combination of the coordinate y and the time t.

In figure 5.12, we plot the velocity profile u as a function of the variable η. As before, we compare the two stochastic modifications of the Point Vortex dynamics, the additive noise stochastic modification and the transport noise stochastic modification. In the case of the additive noise stochastic modification, we study the dependence of our results on the parameter ν, the viscosity of the fluid. We compute the variable η in the following way: we first select a range for the y coordinate, the range being $y \in [-0.1, 0.1]$, and we compute values of η in the following interval,

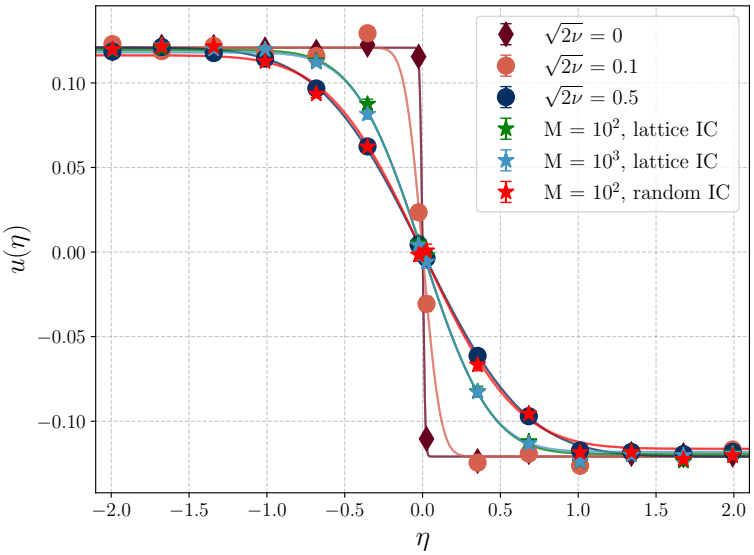

Figure 5.12: Velocity profile as a function of the variable η, for the two different stochastic modifications studied and different parameters. The statistical error is computed by performing bootstrap procedure over $\sim$ 5000 samples. If not visible, errorbars are smaller than the symbols. We take $dt = 10^{-5}$ and $N = 10^2$ point vortices and we average on different initial conditions for the positions $X^{(i)}$. In the case of the stochastic modification of transport noise, we explore different values of M and two different cases: datapoints averaged on different samples with same positions of noisy structures $Y^{(k)}$, placed on on a lattice as described in section 3.6, for which we see that different M have comparable effect, and datapoints averaged on different samples with different initial conditions for the positions of noisy structures $Y^{(k)}$.
We obtain acceptable χ^2/dof, $\chi^2/dof \in [0.9, 0.6]$ for different choice of the fitting interval, with $dof \in [13, 7]$, from fitting the model (5.16) only for the case of the additive noise with viscosity parameter ν taken as $\sqrt{2\nu} \sim 0.5$.

$|\eta| \in [0.025, 2]$, so to avoid numerically unstable values near the value zero. We then compute $u(\eta)$ for all combinations of y, t, at $x = 0$. The velocity component taken into account for this computation is the x-component.

From the datapoints reported in figure 5.12, we can already draw several observations: first of all, all profiles seems to be in agreement with the curves drawn according to the model (5.16). However, a more accurate analysis performed by fitting the model (5.16) to our data reveals that this agreement is qualitative, as we will discuss in the next paragraph.

Moreover, there are some differences with respect to the data in figure 5.11: the energy decay associated to the transport noise stochastic modification with random initial conditions is compatible with the additive noise stochastic modification $\sqrt{2\nu} = 0.1$, while in the plot 5.12 the velocity profile computed in the same regime appears to be compatible with the one of the additive noise stochastic modification with viscosity $\sqrt{2\nu} = 0.5$. Future studies should aim to extend this analysis, in order to clarify the origin and implications of this discrepancy. We stress that averaging over different configurations of $Y^{(k)}$ could restore the isotropy of the system, emphasizing the diffusive behavior.

We comment on the results obtained for the transport noise stochastic modification with datapoints averaged on different samples, with same positions of noisy structures $Y^{(k)}$, placed on a lattice as described in section 3.6. In this setting, we see that different values of M have comparable effect, consistently with what was previously observed for the energy decay.

The case $\nu = 0$ is reported solely for comparison with the other values of ν considered, as it corresponds to the inviscid case and diffusive behavior is not expected.

We conclude our analysis of the velocity profile by fitting the model (5.16) to our data, for both the stochastic modifications studied. Our expectation is as follows: the additive noise model should serve as a reference, to test whether stochastic Point Vortex models are able to capture the diffusive features of the velocity field, and with what limitations. Then, the transport noise stochastic modification could exibit diffusive behavior; however, as we are not able to numerically investigate its diffusive limit at this stage, we do not expect quantitative agreement between the diffusive model and our results.

In the additive noise case, we obtain acceptable values of the χ^2 for our fits only for the value of the viscosity parameter $\sqrt{2\nu} = 0.5$, for which we obtain $\chi^2/dof \in [0.9, 0.6]$ for different choice of the fitting interval, with $dof \in [13, 7]$. For $\sqrt{2\nu} = 0.1$, we obtain a value which is approximately twice as large: one explanation for this result could be that larger values of the viscosity parameter in the additive noise stochastic modification model are needed in order to obtain not only qualitative diffusive behavior, but also quantitative agreement.

Finally, to estimate the impact of the discretization errors, the numerical simulations were repeated for larger values of the timestep, up to 10 dt, and the results were found to be consistent with those obtained using the smaller time step.

Chapter 6

Statistical correlations

In this final chapter, we turn back to the standard Point Vortex model (without any stochastic modification), and we investigate its equilibrium dynamics's temporal structure. The result reported are presented in the paper [68].

The main open problem in the context of incompressible 2D Euler dynamics is the long time behavior of the fluid. The formation of coherent structures and self-organization of the fluid at large scales is a crucial feature of 2D turbulence [121], and it is intimately linked to quantitatively observable phenomena such as the inverse cascade in the energy spectrum [9, 45], anomalous dissipation of energy [42, 44], irreversible mixing [33]. As the Point Vortex model can be regarded as a very simple discretization of the Euler equation, an approach to tackle this open problem is to investigate its equilibrium dynamics's temporal structure.

In this chapter, we first recall some properties of the Point Vortex model (see chapter 1 and reference therein for more details), then we discuss invariant measures of the system and ergodicity of the Point Vortex model. We then turn to a numerical investigation of the correlation of local observables, function of the vorticity, of a large number N of point vortices under the invariant measure $dx_1 \cdots dx_N$ and we exhibit evidence of persistence in time correlations, in the form of power law decay of the latter. In the meantime, we also give some perspectives on this investigation by describing other related studies in the literature.

6.1 Point Vortex model Hamiltonian dynamics, observables and motivations

In this section, we specify our Point Vortex model, and we define the observables we investigate to study the temporal structure of the system. Then, we explore motivations for this investigation, by recalling known results from the literature: the preservation of the Gaussian enstrophy measure for flows of the two-dimensional Euler equation and the Point Vortex model ergodicity conjecture.

6.1.1 Point Vortex model Hamiltonian dynamics

In the following, we recall some Hamiltonian properties of the Point Vortex model. As already anticipated in chapter 1, the Point Vortex system is an Hamiltonian system. The Hamiltonian H corresponds to the kinetic energy of the fluid, as seen in chapter 1, and is expressed as

$$H = -\frac{1}{2\pi}\sum_{i\neq j}\gamma_i\gamma_j \log d(x_i, x_j),$$

where $\gamma_i \in \mathbb{R}\setminus\{0\}$ are the vortex's circulations. As a rescaling in the intensities corresponds to fixing the dynamics' time scale, we will take $|\gamma_i| = 1$ and consider identical vortices. $d(x_i, x_j)$ is the distance between the point vortices in positions x_i, x_j, defined differently on different domains. In this chapter, we will only take into account the doubly periodic square domain, the torus $\mathbb{T}^2 = [-1, 1] \times [1, 1]$; in this case, d is the periodic distance on $\mathbb{T}^2$. This simplification allows us to deal with a finite reference measure and to neglect boundary effects. For the sake of simplicity, we recall both the equations of motion for the Point Vortex system,

$$\dot{x}_i = \sum_{j\neq i}^{N}\gamma_j K(x_i - x_j), \quad i = 1, \dots, N, \tag{6.1}$$

with the Biot-Savart kernel $K(\mathbf{x})$ expressed as

$$K(x) = (-\partial_{x_2}, \partial_{x_1})G(x),$$
$$-(\partial^2_{x_1} + \partial^2_{x_2})G(x) = \delta_0(x) - 1,$$

where G is the zero-averaged fundamental solution of Laplace's equation on the torus. We also recall the expression for the vorticity distribution in this context, which under periodic boundary conditions is solution of the two-dimensional Euler equation in vorticity form (see (1.15)):

$$\omega(x) = \sum_{i=1}^{N}\gamma_i(\delta_0(x - x_i(t)) - 1).$$

The velocity $u(x)$ is expressed via the Biot-Savart law as

$$u(x) = \int K(x - y)\omega(y)dy.$$

This system is almost the same system studied in [35]; in their work, the authors study the dynamics of N point vortices in bounded domains in $\mathbb{R}^2$, and their relevant domain choice is the bounded domain $\mathbb{T}^2 = [-L, L] \times [-L, L]$. They prove that, if the domain considered is bounded, the set of initial positions which lead to a collapse of two or more vortices in finite time has Lebesgue measure zero.

It is important to note that equations (6.1) are not well-posed. In fact, it is possible to show the existence of initial configurations of arbitrary number of vortices where in finite positive time the vortices positions $\mathbf{x}_i$ coincide for different is, i.e. there is the so called phenomenon of vortices collapse. This implies that equations (6.1) do not have meaning in the limit $|\mathbf{x}| \to 0$, where $|K(\mathbf{x})| \sim |\mathbf{x}|^{-1}$. For more details on this topic, see [69].

As equations (6.1) are Hamilton's equations with conjugate coordinates $(x_{i,1}, \gamma_i x_{i,2})_{i=1}^N$, the dynamics is almost complete with respect to natural invariant measures. Then, the Lebesgue measure

(also denoted as the volume measure), $dx_1 \cdots dx_N$ of $(\mathbb{T}^2)^N$, is preserved by the dynamics; moreover, an equilibrium state of the Point Vortex system is given by a distribution of point vortices at independent uniform random positions.

It is a classical result (see [36, 100]) that singular configurations form a negligible set of phase space with respect to absolutely continuous invariant measures of the system. In particular, there exists a measure-preserving flow $\Phi_t : (\mathbb{T}^2)^N \to (\mathbb{T}^2)^N$ consisting of smooth solutions (see [65]).

6.1.2 Computed observables

In the following, we report the numerical investigation done in the paper [68], in which we study the behavior of time correlations of local observables of a large number N of point vortices under the invariant measure $dx_1 \cdots dx_N$.

We first describe the observables computed in the work, then, in the next section, we briefly anticipate our results and comment on its limits of validity and the related literature. The numerical simulation of the system is obtained through a 4th order Runge-Kutta method (see chapter 2 for more details).

We measure local observables of the form

$$F_\sigma^L(t) = \sum_{i=1}^{N} \gamma_i \phi_\sigma^L(x_i(t)), \tag{6.2}$$

where

$$\phi_\sigma^L(x) = \frac{1}{2\pi\sigma^2} \exp(-d(x,(L,0))^2/2\sigma^2)$$

is a function of $\mathbb{T}^2$ concentrated around the point $(L,0)$, the shape of which is not relevant. In the definitions above, $L \geq 0$ and $d(\cdot,\cdot)$ denotes the (periodic) distance on $\mathbb{T}^2$. We investigate the case in which $N = 1000$ point vortices have intensities $\gamma_i = \pm 1$, half of each sign, so that the observables under consideration are zero averaged,

$$0 = \left\langle F_\sigma^L(0) \right\rangle = \left\langle F_\sigma^L(t) \right\rangle \ , \quad t > 0 \ .$$

Throughout this chapter, brackets denote integration with respect to the initial data, distributed according to $dx_1 \cdots dx_N$.

We study local averages of the vorticity distribution

$$\omega(x) = \sum_{i=1}^{N} \gamma_i \delta_0(x - x_i(t)) \ ,$$

instead of observables of the velocity field u. Indeed, since the velocity field induced by a Point Vortex configuration is singular at the vortex locations, measurements of u are subject to strong fluctuations and are therefore less suitable for statistical analysis. On the other hand, we emphasize that the velocity field u is recovered from the vorticity field by means of a linear operation (Biot-Savart law) performed at fixed time. As a consequence, the temporal dependence of correlation functions should not be influenced by such transformation.

The correlation

$$\rho_\sigma^L(t) = \frac{\left\langle F_\sigma^L(0) F_\sigma^L(t) \right\rangle}{\sqrt{\left\langle F_\sigma^L(0)^2 \right\rangle \left\langle F_\sigma^L(t)^2 \right\rangle}}, \tag{6.3}$$

provides for $L = 0$ the autocorrelation of a single observable at times 0 and t, and that of two observables for $L > 0$.

In the following, we anticipate our results and comment on their limits of validity and related literature.

The measurements reported in this chapter provide robust statistical evidence for a power law decay of correlations of the form

$$\rho_\sigma^L(t) \sim \frac{1}{t}, \quad t > 0, \tag{6.4}$$

with an exponent that appears being independent of the parameters of the system, *i.e.* the timestep of the integration scheme δt, the regularization parameter ε required to perform the numerical simulation, the width σ of ϕ_σ^L, the distance L between observables. In particular, the result holds for self-correlations and correlations between distinct observables. In order to support this claim, we performed simulations with increasingly small values of $\delta t, \varepsilon$. We emphasize, however, that the range of validity of eq. (6.4) in t strongly depends on the choice of parameters σ, L. In particular, larger and closer observables require a longer transient before they begin to decay. Moreover, the time threshold beyond which $\rho_\sigma^L(t)$ is too close to 0 to be measurable in our simulation, due to the dominance of numerical errors, is smaller for smaller $\sigma > 0$ and larger $L \geq 0$.

6.1.3 $\sqrt{N}$ scaling and Gaussian enstrophy measure

We expect our result to hold in the limiting regime $N \to \infty$, provided that the vortex intensities scale as $\gamma_i \sim 1/\sqrt{N}$. This scaling corresponds to flows of the two-dimensional Euler equations preserving the Gaussian *enstrophy measure*,

$$\frac{1}{Z} \exp^{-\gamma S} d\omega \ ,$$

where the enstrophy is defined as:

$$S = \frac{1}{2} \int_T \omega^2(x) dx \ .$$

In this setting, Gaussianity at fixed time is a consequence of the Central Limit scaling and equidistribution and independence of Point Vortex positions. By contrast, the scaling $\gamma_i \sim 1/N$ would lead to a trivial stationary solution of Euler's equations.

A series of recent theoretical contributions, see [48, 66, 71, 72, 70], has established the existence of limiting measure-preserving solutions as $N \to \infty$, in the form of analytically very weak solutions of the two-dimensional Euler equations preserving Gaussian Energy-Enstrophy ensembles. As observed in [67], the nonlinearity of the dynamics makes multi-time marginals non-Gaussian. In particular, even a precise control of the correlations investigated in this paper would not completely characterize their distribution, and the description of the necessarily non-Gaussian multi-marginals of equilibrium flows at different times remains an open problem. From a numerical perspective, producing statistically robust data supporting extrapolation in $N \to \infty$ is computationally intensive. In our numerical simulations, we have therefore considered the evolution of systems consisting of up to $N = 1000$ point vortices.

Despite considerable effort, the temporal structure of fluid mechanical models remains only partially understood, and relatively few theoretical results are available for equilibrium flows of the two-dimensional Euler dynamics or its regularizations. We refer to [119, 83] for an overview on relaxation towards simple states in two-dimensional Euler equations, and to [37] for results concerning spatially scale-invariant dynamics. Time correlations of equilibrium dynamics in closely related

dynamical systems have been the subject of seminal works, see [1, 123]. The kinetic approach to relaxation in Point Vortex dynamics has been extensively investigated in a series of works by Chavanis [16, 17, 18, 24, 22, 23], with a primary focus on the dynamics of a tracer vortex in a large ensemble. Diffusive relaxation towards equilibrium of the full vortex system was discussed in [21, Section 3.2], where it is observed that characteristic relaxation time does not depend solely on the number of vortices N, but it is influenced by the whole initial distribution of point vortices, a class of initial conditions that does not include the one considered in the present work. Indeed, relaxation might not even take place [20]. Describing collective effects in Point Vortex dynamics remains a challenging problem [19]: to the best of our knowledge, the results presented in this chapter and in the paper [68] is the first evidence of power law decay of correlation in large Point Vortex systems.

We finally recall that the *canonical Gibbs measure* for the vortex model (in the sense of Onsager),

$$\frac{1}{Z}\exp^{-\beta H}\, dx^1 \cdots dx^N$$

is an invariant measure for the Euler flow. However, this measure is not the one studied in the work [68] and in this chapter.

6.1.4 Ergodicity of Point Vortex system

In the following, we briefly discuss the implications of our results for the ergodicity of the Point Vortex system, which was originally conjectured by Onsager [109] and disproved by Khanin [82] in a system of few point vortices.

Our results, however, indicate that the equilibrium state corresponding to the invariant measure $dx_1 \cdots dx_N$ of eq. (6.1) for a system of many point vortices exhibits mixing behavior. Notwithstanding the existence of singular solutions and (quasi-) periodic orbits [90, 8], this observation suggests that, in the limit $N \to \infty$, such trajectories occupy an increasingly smaller set of phase space, and that ergodicity might be recovered. Indeed, the latter was proposed by [41, p. 865] as a condition much weaker than strict ergodicity that justifies the statistical equilibrium assumption for Point Vortex dynamics, while the rate of approach to equilibrium in ergodic components was indicated as a central issue in the scope of Onsager's theory.

The equilibrium state of the Point Vortex system considered here, or Gibbsian ensembles absolutely continuous with respect to it, is not suited for describing the vortex aggregation in turbulent flows as portrayed by Onsager, but it might provide a valid model for small, unresolved scales of more complex fluid dynamics systems. We also note that integrable and non-integrable behaviors of Point Vortex dynamics as Hamiltonian systems have been extensively studied in the literature, usually in the context of systems with a small number of point vortices; we refer to [105] for a recent survey.

6.2 Point Vortex Dynamics

In this section, we describe the simulated system in details, together with the procedure of desingularization of the Biot-Savart kernel followed in the study, and our parameters choices, commenting on the accuracy of the numerical approximation used.

We consider a system of N identical point vortices with intensities ± 1, half of each sign, evolving on $\mathbb{T}^2$ according to the dynamics of eq. (6.1).

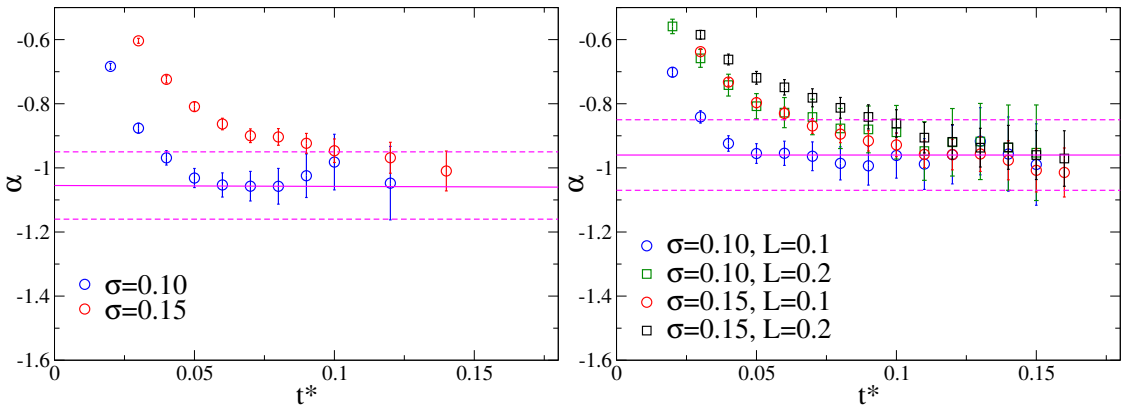

Figure 6.1: Estimates of the power law exponent α, computed by fitting the logarithm of $\rho_\sigma^L(t)$ for different values of σ and various different fitting ranges $[t^*, t^{**}]$. Horizontal bands denotes the final confidence interval $\alpha = -1.06(11)$ (obtained by taking into account fit systematics) for the self-correlation coefficient, $L = 0$, and $\alpha = -1.02(14)$ for the correlation coefficient, $L > 0$, the two values being compatible.

6.2.1 Desingularization of the Interaction Kernel

The advecting vector field in eq. (6.1) can be represented via the Fourier series expansion

$$K(x) = \frac{1}{4\pi} \sum_{k \in \mathbb{Z}_0^2} \frac{ik^\perp e^{i\pi k \cdot x}}{|k|^2}, \quad x \in \mathbb{T}^2. \tag{6.5}$$

This kernel is singular at $x \to 0$, since it is the (orthogonal) gradient of the Green function G of $\mathbb{T}^2$, which exibits a logarithmic singularity. In fact, the periodic boundary does not affect asymptotic behavior of G at $x \to 0$, which is the same of the free Green function $-\frac{1}{2\pi} \log |x|$. Because of the relatively large number of point vortices, the relevant interactions are those occurring at short distances [18]. As a consequence, for computational purposes it is justified to replace K with (a regularization of) the orthogonal gradient of the free Green function.

Numerical simulations of Point Vortex dynamics have been performed using the regularized interaction kernel

$$K_\varepsilon(x, y) = \frac{(y_2 - x_2, x_1 - y_1)}{2\pi(d(x, y) + \varepsilon)^2},$$

where $d(x, y)$ denotes the periodic distance on the two-dimensional torus $\mathbb{T}^2 = [-1, 1]^2$. As we just mentioned, even at the ideal value $\varepsilon = 0$ the kernel still deviates from the original K: the error is negligible at close distances ($|x| < 0.1$) and overall bounded by $|K - K_0| < 0.2$. This error is negligible when compared with the singular behaviour at $x = 0$. Polynomial corrections of K_0 allow to improve the approximation arbitrarily. Nevertheless, numerical tests indicate that already a quadratic correction produces negligible fluctuations in the quantities we have measured. This is again due to the fact that, in the statistical ensemble under consideration, the most relevant interactions of point vortices occur at short range. On the other hand, spectral methods, *i.e.* Fourier truncation of the fluid velocity (thus of K), are not suited for our purposes: they approximate well interactions of distant point vortices, but become computationally inefficient in approximating the more relevant and singular close-range interactions.

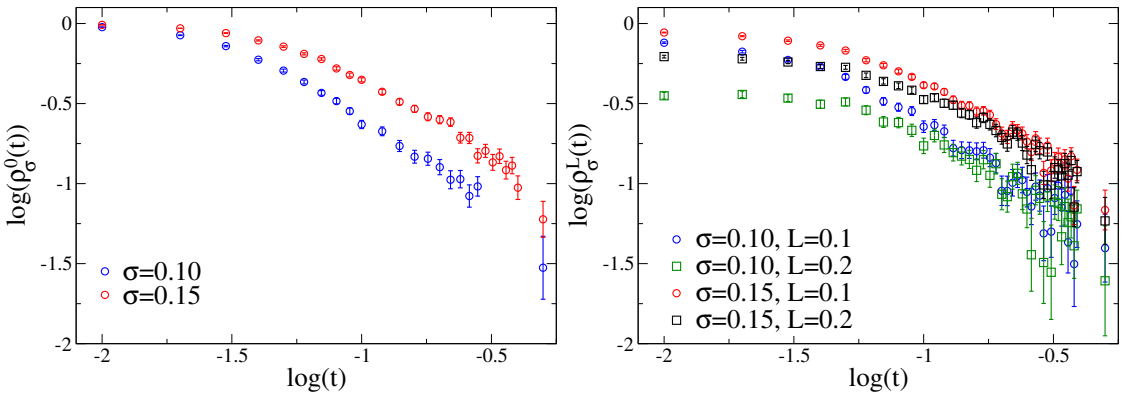

Figure 6.2: Logarithm of $\rho_\sigma^L(t)$ as a function of the logarithm of t; $\rho_\sigma^{L=0}(t)$ represents the Pearson autocorrelation ($L = 0$, on the left) and correlation ($L > 0$, on the right) coefficient between the observables $F(0, 0, \phi(\sigma))$ and $F(t, L, \phi(\sigma))$. The dynamics is integrated with timestep $\delta t = 10^4$ and machine ε regularization, for different values of σ and L.

6.2.2 Accuracy of Numerical Approximations

The dynamics in eq. (6.1) was numerically integrated using a fourth-order Runge–Kutta scheme. To assess the robustness of our measurements, we considered several values of the timestep $\delta t = 10^{-3}, 10^{-4}, 10^{-5}$ and of the regularization parameter $\varepsilon = 10^{-3}, 10^{-6}, 10^{-16}$, the latter value reaching machine epsilon.

For each choice of parameters $\delta t, \varepsilon$ the system was solved up to time $T = 1$, starting from an initial configuration of $N = 1000$ i.i.d. uniformly distributed point vortices. The time interval over which the decay of correlations was observed always remained well below T; in most cases, correlations were close to zero already at half time, so that their fluctuations could not be distinguished from numerical error. For each pair $\delta t, \varepsilon$, numerical simulations were performed for at least 10^4 samples of the initial configuration, ensuring statistical robustness and independent sampling.

To quantify numerical accuracy we computed the energy (Hamiltonian) of the regularized Point Vortex system,

$$H_\varepsilon = -\frac{1}{2\pi} \sum_{i \neq j} \gamma_i \gamma_j \log \left(d(x_i, x_j) + \varepsilon \right),$$

which is a conserved quantity of the regularized motion. Numerical integration of Point Vortex dynamics with any of the above choices of parameters $\delta t, \varepsilon$ led to a relative error $H_\varepsilon(t)/H_\varepsilon(t = 0)$ of order at most 10^{-7} for time $0 \leq t \leq 0.5$, uniformly with respect to the (random) initial conditions under consideration.

6.3 Time Decay of Correlations

In this section, we explain our sampling procedure and comment of dependence of our results from the different parameters of the model.

6.3.1 Sampling procedure

Most of the sampling was performed using $\delta t = 10^{-4}$ and $\varepsilon = 10^{-16}$, after verifying that a smaller timestep ($\delta t = 10^{-5}$) or a larger regularization parameter lead to results compatible with those obtained with the adopted numerical setup.

Correlations $\rho_\sigma^L(t)$ were measured using the standard Pearson estimator. Exponential decay was ruled out due to the large chi-square score of the fit. We therefore estimated the exponent α of the power law parametric model Ct^α for $\rho_\sigma^L(t)$ by performing a least square error fit of the logarithm $\log \rho_\sigma^L(t)$ (with C remaining a free parameter). In fig. 6.2 we report data points for $\log \rho_\sigma^L(t)$ in the case of self-correlation $L = 0$ and correlation between distinct observables $L > 0$. The linear fitting procedure was carried out for several choices of the parameters σ and L, and the corresponding results are reported in tables 6.1 to 6.3. For all the simulations, data points computed at different times and parameters are independent from each other, as they have been estimated using different samples; statistical errors were estimated by means of bootstrap procedures.

6.3.2 Time dependence

For any choice of the parameters, the correlation $\rho_\sigma^L(t)$ starts at $\rho_\sigma^L(0) = 1$ and decays to values close to 0 after a short transient phase. The fitting range $[t^*, t^{**}]$ has to be chosen properly: $t^* > 0$ must be large enough so to neglect the transient phase and $t^{**} > t^*$ should not be too large, since when $\rho_\sigma^L(t)$ is too close to 0 its variations can not be distinguished from numerical error. The choice of t^* was the more sensitive: results obtained for increasing values of t^* are reported in table 6.1, and show that including part of the transient phase, corresponding to for small values of t^*, makes the fit unstable, as indicated by significantly larger χ^2-scores. In our simulations, variations of t^{**} (in the simulated time interval) did not affect the result of the fit except for a slightly larger χ^2-score for larger t^{**}. The dependence of the fit parameter α on the fitting range, specifically on the lower extremum t^*, is illustrated in fig. 6.3.

6.3.3 Results and dependence on parameters

We performed numerical simulations for several values of the width σ of ϕ_σ^L; we report only the results obtained for $\sigma = 0.1$ and $\sigma = 0.15$, since smaller values of σ lead to a shorter time frame in which $\rho_\sigma^L(t)$ drops from values close to 1 to values close to 0, thus making curve fitting procedures less stable.

With regard to the dependence on the timestep δt and the regularization parameter ε, the (negligible) deviations from the reference case $\delta t = 10^{-4}$ and $\varepsilon = 10^{-16}$ for other choices of those parameters are collected in tables 6.2 and 6.3.

Taking into account the systematic uncertainties that arise from the choice of the fitting range, we ultimately estimate $\alpha = -1.06(11)$ for the case $L = 0$ and $\alpha = -1.02(14)$ for the other choices of L, the two estimates for α being fully compatible with -1.

6.3.4 Dependence on the number N of vortices

We compute time correlations using the same procedure for systems of $N = 10$ and $N = 100$ point vortices, rescaling intensities $\gamma_i \sim 1/\sqrt{N}$ in order to obtain comparable characteristic scales of decay.

We report the results in section 6.3.4. While the case of $N = 10$ vortices is not compatible with the case of $N = 1000$ vortices (the former exhibit slower decay rate), results for $N = 100$ are consistent with the power law rate eq. (6.4). Taking into account the relative error, this provides moderate evidence for the robustness of $1/t$ time decay at larger N. The fitting errors for $N = 100$ and $N = 1000$ are of comparable magnitude: even if the case $N = 1000$ is closer to the ideal $N \to \infty$ regime, the numerical error due to the large number of interactions makes a precise estimation of the decay exponent more challenging.

6.4 Some final remarks

In this chapter, we reported the numerical simulations of the Point Vortex flows presented in [68]; their accuracy allowed us to produce strong statistical evidence for a power law decay of time correlations at equilibrium, in agreement with previous theoretical and numerical results obtained for closely related models.

A natural continuation of this work concerns two limitations of the present analysis. The first is the fixed number of point vortices: the large N limit is expected to allow extrapolation toward results for solutions of the two-dimensional Euler equations, but it faces the issue of rapidly increasing computational cost. This limitation cannot be offset by reducing sample sizes without losing statistical robustness, because of the intrinsic instability of the flow. The second limitation is the equilibrium state under consideration, which is not appropriate for describing turbulent phenomena. Within the framework of Onsager's statistical mechanics theory, one should focus on high-energy microcanonical ensembles or negative-temperature canonical ensembles. Consistent sampling from those states presents a challenge on its own [38], and is therefore left to future investigations. Nevertheless, it is worth noting that the system studied in this chapter may provide a meaningful description of small scale dynamics in turbulent flows, and our results can thus be regarded as a first step toward understanding more complex systems.

The persistence of time correlations observed in our simulations indicates that, even under a relatively mixing state, characterized of completely independent vortex positions, the Point Vortex system retains a certain stiffness, although aggregation phenomena cannot be observed in such an equilibrium flow, confirming the indication of [93, 41] that scattered vortices may fail to relax towards equilibrium rapidly. As a consequence, particular care is required in sampling procedures for numerical simulations of similar fluid dynamical models, since repeated sampling at short time intervals from the same evolution may lead to correlated data, unsuitable for statistical analysis.

Finally, we emphasize that the model we considered describes an inviscid fluid. Viscosity can be included in the dynamics through stochastic forcing acting on single vortices, see [97, 73]. The dependence of time correlations on the viscosity parameter (Reynolds number) is expected to be closely related to anomalous dissipation effects observed in the inviscid limit of Navier-Stokes equations, which is most relevant in the study of boundary effects and fluid dynamical instabilities, and it constitutes a further possible future extension of this present work.

Table 6.1: Results of the fit of the angular coefficient α for $\log(\rho_\sigma^L(t))$ data, with $\delta t = 10^{-4}$ and $\varepsilon = 10^{-16}$. We report the estimated values of α and the reduced χ^2-score of the fit, together with the degrees of freedom.

	$L=0$, $\sigma=0.1$			$L=0$, $\sigma=0.15$		
t^*	α	χ^2/dof	dof	α	χ^2/dof	dof
0.02	-0.684(9)	17.4	17	—	—	—
0.03	-0.876(15)	3.0	16	-0.604(8)	16.4	22
0.04	-0.969(23)	1.1	15	-0.724(11)	6.7	21
0.05	-1.032(30)	0.5	14	-0.809(14)	2.7	20
0.06	-1.053(38)	0.4	13	-0.863(18)	1.5	19
0.07	-1.057(46)	0.4	12	-0.900(21)	1.0	18
0.08	-1.058(56)	0.5	11	-0.904(26)	1.1	17
0.09	-1.025(68)	0.5	10	-0.923(31)	1.1	16
0.10	-0.982(87)	0.4	9	-0.947(37)	1.1	15
0.12	-1.048(115)	0.4	8	-0.969(48)	1.1	14
0.14	—	—	—	-1.010(62)	1.1	13
	$L=0.1$, $\sigma=0.1$			$L=0.1$, $\sigma=0.15$		
t^*	α	χ^2/dof	dof	α	χ^2/dof	dof
0.02	-0.702(14)	4.6	37	—	—	—
0.03	-0.841(19)	1.6	36	-0.638(10)	6.9	36
0.04	-0.924(24)	0.7	35	-0.733(12)	2.8	35
0.05	-0.955(31)	0.7	34	-0.797(16)	1.5	34
0.06	-0.955(38)	0.7	33	-0.830(20)	1.3	33
0.07	-0.964(45)	0.7	32	-0.869(23)	1.0	32
0.08	-0.986(52)	0.7	31	-0.895(27)	1.0	31
0.09	-0.994(60)	0.7	30	-0.916(32)	0.9	30
0.10	-0.961(70)	0.7	29	-0.928(37)	0.9	29
0.11	-0.988(79)	0.7	28	-0.958(41)	0.9	28
0.12	-0.959(91)	0.8	27	-0.959(48)	0.9	27
0.13	-0.917(105)	0.8	26	-0.957(54)	1.0	26
0.14	-0.957(116)	0.8	25	-0.976(61)	1.0	25
0.15	-0.990(127)	0.8	24	-1.008(68)	1.0	24
0.16	—	—	—	-1.014(76)	1.0	23
	$L=0.2$, $\sigma=0.1$			$L=0.2$, $\sigma=0.15$		
t^*	α	χ^2/dof	dof	α	χ^2/dof	dof
0.02	-0.559(23)	2.4	37	—	—	—
0.03	-0.658(28)	1.5	36	-0.585(14)	3.9	36
0.04	-0.742(34)	1.0	35	-0.662(17)	2.3	35
0.05	-0.808(39)	0.7	34	-0.719(20)	1.5	34
0.06	-0.828(47)	0.7	33	-0.749(24)	1.4	33
0.07	-0.841(55)	0.7	32	-0.781(28)	1.3	32
0.08	-0.877(63)	0.7	31	-0.813(32)	1.2	31
0.09	-0.880(73)	0.7	30	-0.841(38)	1.1	30
0.10	-0.889(84)	0.7	29	-0.862(43)	1.1	29
0.11	-0.948(91)	0.6	28	-0.906(48)	1.0	28
0.12	-0.920(105)	0.7	27	-0.919(54)	1.0	27
0.13	-0.918(119)	0.7	26	-0.937(60)	1.1	26
0.14	-0.937(133)	0.7	25	-0.936(69)	1.1	25
0.15	-0.953(149)	0.7	24	-0.960(76)	1.1	24
0.16	—	—	—	-0.971(87)	1.2	23

Table 6.2: Correlation $\rho_\sigma^L(t)$ computed for different values of δt; the difference between the results obtained in the setup used for the majority of the simulations ($\delta t = 10^{-4}$) and the results obtained for different values of δt is reported, for different choices of the parameter σ and different values of L. The regularization parameter is taken as $\varepsilon = 10^{-16}$.

	$L = 0$, $\sigma = 0.1$	$L = 0$, $\sigma = 0.15$
δt	$\rho_\sigma^L(t = 0.08, \delta t) - \rho_\sigma^L(t = 0.08, \delta t = 10^{-4})$	$\rho_\sigma^L(t = 0.08, \delta t) - \rho_\sigma^L(t = 0.08, \delta t = 10^{-4})$
10^{-5}	0.004(16)	-0.012(15)
10^{-3}	0.037(16)	-0.005(14)
	$L = 0.1$, $\sigma = 0.1$	$L = 0.1$, $\sigma = 0.15$
δt	$\rho_\sigma^L(t = 0.08, \delta t) - \rho_\sigma^L(t = 0.08, \delta t = 10^{-4}))$	$\rho_\sigma^L(t = 0.08, \delta t) - \rho_\sigma^L(t = 0.08, \delta t = 10^{-4}))$
10^{-5}	-0.000(20)	-0.008(17)
10^{-3}	0.0436(20)	0.002(17)
	$L = 0.2$, $\sigma = 0.1$	$L = 0.2$, $\sigma = 0.15$
δt	$\rho_\sigma^L(t = 0.08, \delta t) - \rho_\sigma^L(t = 0.08, \delta t = 10^{-4}))$	$\rho_\sigma^L(t = 0.08, \delta t) - \rho_\sigma^L(t = 0.08, \delta t = 10^{-4}))$
10^{-5}	-0.004(21)	-0.018(19)
10^{-3}	0.009(21)	-0.020(18)

Table 6.3: Correlation $\rho_\sigma^L(t)$ computed for different values of ε; the difference between the results obtained in the setup used for the majority of the simulations ($\varepsilon = 10^{-16}$) and the results obtained for different values of ε is reported, for different choices of the parameter σ and different values of L. The timestep is taken as $\delta t = 10^{-4}$.

	$L = 0$, $\sigma = 0.1$	$L = 0$, $\sigma = 0.15$
ε	$\rho_\sigma^L(t = 0.08, \varepsilon) - \rho_\sigma^L(t = 0.08, \varepsilon = 10^{-16})$	$\rho_\sigma^L(t = 0.08, \varepsilon) - \rho_\sigma^L(t = 0.08, \varepsilon = 10^{-16})$
10^{-6}	0.001(16)	-0.015(15)
10^{-3}	-0.002(16)	-0.012(15)
	$L = 0.1$, $\sigma = 0.1$	$L = 0.1$, $\sigma = 0.15$
ε	$\rho_\sigma^L(t = 0.08, \varepsilon) - \rho_\sigma^L(t = 0.08, \varepsilon = 10^{-16})$	$\rho_\sigma^L(t = 0.08, \varepsilon) - \rho_\sigma^L(t = 0.08, \varepsilon = 10^{-16})$
10^{-6}	0.018(20)	0.006(17)
10^{-3}	0.003(20)	0.002(17)
	$L = 0.2$, $\sigma = 0.1$	$L = 0.2$, $\sigma = 0.15$
ε	$\rho_\sigma^L(t = 0.08, \varepsilon) - \rho_\sigma^L(t = 0.08, \varepsilon = 10^{-16})$	$\rho_\sigma^L(t = 0.08, \varepsilon) - \rho_\sigma^L(t = 0.08, \varepsilon = 10^{-16})$
10^{-6}	0.051(21)	0.022(20)
10^{-3}	0.011(21)	-0.003(19)

Table 6.4: Results of the fit of the angular coefficient α for $\log(\rho^{L=0}_{\sigma=0.1}(t))$ data, with $\delta t = 10^{-4}$ and $\varepsilon = 10^{-16}$. We report the estimated values of α and the reduced χ^2-score of the fit, together with the degrees of freedom, for different values of N.

	$L=0$, $\sigma=0.1$, $N=10$			$L=0$, $\sigma=0.1$, $N=100$		
t^*	α	χ^2/dof	dof	α	χ^2/dof	dof
0.02	-0.674(12)	8.7	17	-0.678(11)	11.3	17
0.03	-0.820(18)	2.2	16	-0.859(19)	3.5	16
0.04	-0.908(25)	0.6	15	-0.973(27)	1.3	15
0.05	-0.932(32)	0.5	14	-1.036(35)	0.9	14
0.06	-0.923(40)	0.5	13	-1.044(46)	1.0	13
0.07	-0.920(48)	0.6	12	-1.082(55)	0.9	12
0.08	-0.899(57)	0.6	11	-1.075(67)	1.0	11
0.09	-0.920(65)	0.6	10	-1.124(77)	0.9	10
0.10	-0.849(82)	0.5	9	-0.995(99)	0.6	9
0.12	-0.877(109)	0.5	8	-0.955(134)	0.6	8

Table 6.5: Results of the fit of the angular coefficient α for $\log(\rho^{L=0}_{\sigma}(t))$ data, with $\delta t = 10^{-4}$ and $\varepsilon = 10^{-16}$. We report the estimated values of α and the reduced χ^2-score of the fit, together with the degrees of freedom, for different values of N and σ.

	$N=10$, $L=0$, $\sigma=0.1$			$N=10$, $L=0$, $\sigma=0.15$		
t^*	α	χ^2/dof	dof	α	χ^2/dof	dof
0.02	-0.674(12)	8.7	17	—	—	—
0.03	-0.820(18)	2.2	16	-0.562(9)	12.8	22
0.04	-0.908(25)	0.6	15	-0.670(12)	4.9	21
0.05	-0.932(32)	0.5	14	-0.743(15)	2.2	20
0.06	-0.923(40)	0.5	13	-0.794(18)	0.9	19
0.07	-0.920(48)	0.6	12	-0.811(22)	0.8	18
0.08	-0.899(57)	0.6	11	-0.825(26)	0.8	17
0.09	-0.920(65)	0.6	10	-0.850(30)	0.7	16
0.10	-0.849(82)	0.5	9	-0.843(36)	0.7	15
0.12	-0.877(109)	0.5	8	-0.860(46)	0.8	14
0.14	—	—	—	-0.898(59)	0.7	13
	$N=100$, $L=0$, $\sigma=0.1$			$N=100$, $L=0$, $\sigma=0.15$		
t^*	α	χ^2/dof	dof	α	χ^2/dof	dof
0.02	-0.678(11)	11.3	17	—	—	—
0.03	-0.859(19)	3.5	16	-0.587(9)	12.5	22
0.04	-0.973(27)	1.3	15	-0.710(13)	5.0	21
0.05	-1.036(35)	0.9	14	-0.795(17)	2.0	20
0.06	-1.044(46)	1.0	13	-0.833(21)	1.6	19
0.07	-1.082(55)	0.9	12	-0.871(25)	1.3	18
0.08	-1.075(67)	1.0	11	-0.903(30)	1.1	17
0.09	-1.124(77)	0.9	10	-0.945(35)	0.9	16
0.10	-0.995(99)	0.6	9	-0.965(43)	0.9	15
0.12	-0.877(109)	0.5	8	-1.053(54)	0.4	14
0.14	—	—	—	-1.050(70)	0.4	13

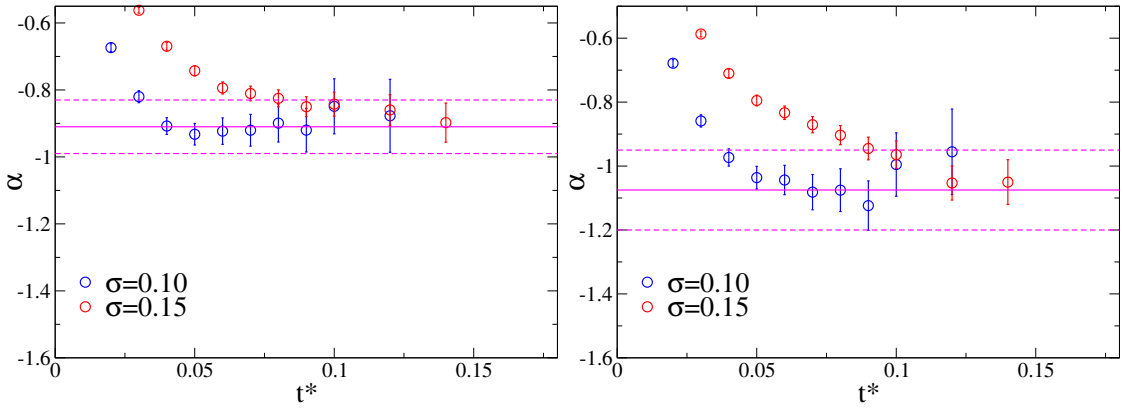

Figure 6.3: Estimates of the power law exponent α, computed by fitting the logarithm of $\rho_\sigma^L(t)$ for different values of σ and various different fitting ranges $[t^*, t^{**}]$, for $N = 10$ and $N = 100$. Horizontal bands denotes the final confidence interval for α (obtained by taking into account fit systematics) for the self-correlation coefficient, $L = 0$.

Appendix

Chapter 4: code

In this section, we report some specifics of the code used to compute the solution of the homogenized equation, both in 4 and in the work [13], see [12]. The specifics reported here are relative to the MATLAB code used to compute the results shown in the thesis, some parameters are however specific to the C++ version of the code. In the following, we specify parameters of the code and available commands.

```
Numerical solution of homogenized equation.


The sigma field on the torus T = [0,1] x [0,1] is computed in the following way:
- if c < 1 only vortex blobs in the red dots contributes
- if c = 1, for the gridpoints (0,n), (n, 0), (0, 0), (n,n)
    also the blue points contribute, but their contribution is zero
- if c > 1 all points (even the green ones) contributes
```

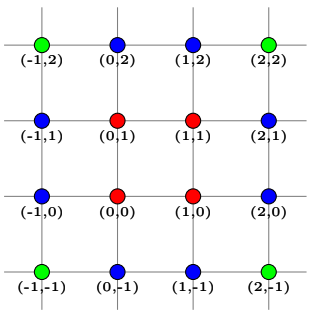


```
get input parameters from input file 'input.in'

L = domain length, default L=1

n =  number of gridpoints
```

```
rand_shift = shift the field so that singularities are not in gridpoints
             could be random but is deterministic

epsilon = regularizing parameter, default set to zero

a1 = varphi parameters
a2 =

c = support of varphi


nu = molecular diffusivity (kappa in the computations)

zoom = multiplicative coefficient of varphi function
         in sigma tensor sigma
         default zoom = 1

write_t_matrix = write operator matrix T on file

write_phi = write corrector phi_1 on file
            not implemented in matlab, only in c++

write_phi_to_plot = write corrector phi_1 on file (plot format)
                    not implemented in matlab, only in c++

write_data = write data on file

write_aone = write matrix Aone on file
             not implemented in matlab, only in c++

write_grad = write norm of gradient of phi_1 and phi_1 derivatives on file
```

Chapter 5: code

In the following, we describe some specifics of the code used to generate configurations of point vortices analyzed in 5 and in the work [59]. The code is available at [106] and is written in C. Here, we specify parameters of the code and available commands.

```
Point vortex system simulation.


Makefile commands:
```

```
make set
creates directories
before launcing simulation
do 'make set' to avoid segmentation fault

make clean
removes ex and .o files

make killdata
removes configurations

make convert-csv
converts files in data from .dat to .csv

make run
run simulations



input file specifications (example is input.in):

input file has to be named input.in

'=' has to be immediately after parameter name, see input.in example

N_1= number of vortices
N_2= if specified, two groups of vortices are simulated (if possible)

TYPE_BLOB_1= intensity of the vortices
TYPE_BLOB_2=

DT= time discretization
PRINT_EVERY= to avoid printing each iteraction
N_T= number of time iteractions

LOAD_SAVED_CONF= if 0, random configuration is generated,
    if 1 a configuration is loaded from the folder 'load'.
    Configuration has to be named conf_0.dat for group 1 and 2,
    or conf2_0.dat for group 3 and 4.

SIGMA_NOISE= brownian motion term (viscous) coefficient

MODEL= 2 torus with fixed vortices randomization, 1 without
    else plane

L= torus lenght on the torus or shear flow lenght if on the plane

for environmental noise:
```

N_FX= number of 'fixed random' vortices, they model the environmental noise

for shear flow:

DELTA= thickness of the shear layer

DELTA_FX= thickness of the fixed vortices (environmental flow model) layer

Bibliography

[1] B. J. Alder and T. E. Wainwright, *Decay of the velocity autocorrelation function*, Phys. Rev. A, 1 (1970), pp. 18–21.

[2] C. Anderson and C. Greengard, *On vortex methods*, SIAM journal on numerical analysis, 22 (1985), pp. 413–440.

[3] H. Aref, *Point vortex dynamics: a classical mathematics playground*, Journal of mathematical Physics, 48 (2007).

[4] G. K. Batchelor, *An introduction to fluid dynamics*, Cambridge university press, 2000.

[5] J. T. Beale and A. Majda, *High order accurate vortex methods with explicit velocity kernels*, Journal of Computational Physics, 58 (1985), pp. 188–208.

[6] A. Bensoussan, J.-L. Lions, and G. Papanicolaou, *Asymptotic Analysis for Periodic Structures*, no. v. 5 in Studies in Mathematics and Its Applications, North-Holland Pub. Co. Sole distributors for the U.S.A. and Canada, Elsevier North-Holland, 1978.

[7] L. C. Berselli, T. Iliescu, and W. J. Layton, *Mathematics of large eddy simulation of turbulent flows*, Springer, 2006.

[8] D. Blackmore and J. Champanerkar, *Periodic and quasiperiodic motion of point vortices*, in Vortex Dominated Flows: A Volume Celebrating Lu Ting's 80th Birthday, World Scientific, 2005, pp. 21–42.

[9] G. Boffetta and R. E. Ecke, *Two-dimensional turbulence*, Annual review of fluid mechanics, 44 (2012), pp. 427–451.

[10] C. Bonati, *Some notes for "numerical methods for physics"*, (2024).

[11] J. Boussinesq, *Essai sur la théorie des eaux courantes*, Impr. nationale, 1877.

[12] F. Butori, A. Mayorcas, and S. Morlacchi, *In preparation (code).*

[13] ——, *Homogenisation of a passive scalar transported by locally supported white noise*, arXiv preprint arXiv:2509.06878, (2025).

[14] H. Cartan, *Elementary theory of analytic functions of one or several complex variables*, Courier Corporation, 1995.

[15] B. Chapron, D. Crisan, D. Holm, E. Mémin, and A. Radomska, *Stochastic transport in upper ocean dynamics. stuod 2021 workshop, london, uk, september 20–23*, (2023).

[16] P.-H. Chavanis, *Systematic drift experienced by a point vortex in two-dimensional turbulence*, Physical Review E, 58 (1998), p. R1199.

[17] ——, *Kinetic theory of point vortices: diffusion coefficient and systematic drift*, Physical Review E, 64 (2001), p. 026309.

[18] ——, *Effective velocity created by a point vortex in two-dimensional hydrodynamics*, Physical Review E, 65 (2002), p. 056302.

[19] ——, *Kinetic theory of 2d point vortices from a bbgky-like hierarchy*, Physica A: Statistical Mechanics and its Applications, 387 (2008), pp. 1123–1154.

[20] ——, *Kinetic theory of onsager's vortices in two-dimensional hydrodynamics*, Physica A: Statistical Mechanics and its Applications, 391 (2012), pp. 3657–3679.

[21] ——, *Kinetic theory of two-dimensional point vortices with collective effects*, Journal of Statistical Mechanics: Theory and Experiment, 2012 (2012), p. P02019.

[22] ——, *Statistical mechanics of two-dimensional point vortices: relaxation equations and strong mixing limit*, The European Physical Journal B, 87 (2014), pp. 1–24.

[23] ——, *Kinetic theory of two-dimensional point vortices and fluctuation–dissipation theorem*, The European Physical Journal Plus, 138 (2023), pp. 1–51.

[24] P.-H. Chavanis and M. Lemou, *Kinetic theory of point vortices in two dimensions: analytical results and numerical simulations*, The European Physical Journal B, 59 (2007), pp. 217–247.

[25] A. J. Chorin, *Numerical study of slightly viscous flow*, Journal of fluid mechanics, 57 (1973), pp. 785–796.

[26] ——, *The evolution of a turbulent vortex*, Communications in Mathematical Physics, 83 (1982), pp. 517–535.

[27] R. Clements and D. J. Maull, *The representation of sheets of vorticity by discrete vortices*, Progress in Aerospace Sciences, 16 (1975), pp. 129–146.

[28] M. Coghi and F. Flandoli, *Propagation of chaos for interacting particles subject to environmental noise*, (2016).

[29] M. Coghi and M. Maurelli, *Regularized vortex approximation for 2d euler equations with transport noise*, Stochastics and Dynamics, 20 (2020), p. 2040002.

[30] C. J. Cotter, G. A. Gottwald, and D. D. Holm, *Stochastic partial differential fluid equations as a diffusive limit of deterministic lagrangian multi-time dynamics*, Proceedings of the Royal Society A: Mathematical, Physical and Engineering Sciences, 473 (2017), p. 20170388.

[31] P. F. Cummins and G. Holloway, *Reynolds stress and eddy viscosity in direct numerical simulations of sheared two-dimensional turbulence*, Journal of fluid mechanics, 657 (2010), pp. 394–412.

[32] M. D'Elia et al., *Lezioni di meccanica classica*, Pisa University Press srl, 2020.

[33] M. Dolce and T. D. Drivas, *On maximally mixed equilibria of two-dimensional perfect fluids*, Arch. Ration. Mech. Anal., 246 (2022), pp. 735–770.

[34] D. Donnelly and E. Rogers, *Symplectic integrators: An introduction*, American Journal of Physics, 73 (2005), pp. 938–945.

[35] D. Dürr and M. Pulvirenti, *On the vortex flow in bounded domains*, Communications in Mathematical Physics, 85 (1982), pp. 265–273.

[36] D. Dürr and M. Pulvirenti, *On the vortex flow in bounded domains*, Comm. Math. Phys., 85 (1982), pp. 265–273.

[37] T. Elgindi, R. Murray, A. Said, et al., *On the long-time behavior of scale-invariant solutions to the 2d euler equation and applications*, arXiv preprint arXiv:2211.08418, (2022).

[38] J. Esler, *Equilibrium energy spectrum of point vortex motion with remarks on ensemble choice and ergodicity*, Physical Review Fluids, 2 (2017), p. 014703.

[39] J. Esler and T. Ashbee, *Universal statistics of point vortex turbulence*, Journal of Fluid Mechanics, 779 (2015), pp. 275–308.

[40] L. C. Evans, *Partial Differential Equations*, American Mathematical Society, 2010.

[41] G. Eyink and H. Spohn, *Negative-temperature states and large-scale, long-lived vortices in two-dimensional turbulence*, Journal of statistical physics, 70 (1993), pp. 833–886.

[42] G. L. Eyink, *Energy dissipation without viscosity in ideal hydrodynamics i. fourier analysis and local energy transfer*, Physica D: Nonlinear Phenomena, 78 (1994), pp. 222–240.

[43] ——, *Turbulence noise*, Journal of statistical physics, 83 (1996), pp. 955–1019.

[44] ——, *Dissipation in turbulent solutions of 2d euler equations*, Nonlinearity, 14 (2001), p. 787.

[45] G. L. Eyink and K. R. Sreenivasan, *Onsager and the theory of hydrodynamic turbulence*, Reviews of modern physics, 78 (2006), p. 87.

[46] A. Fannjiang and G. Papanicolaou, *Convection enhanced diffusion for periodic flows*, SIAM Journal on Applied Mathematics, 54 (1994), pp. 333–408.

[47] F. Flandoli, *Regularity theory and stochastic flows for parabolic SPDEs*, Singapone: Gordon and Breach Publ., 1995.

[48] F. Flandoli, *Weak vorticity formulation of 2D Euler equations with white noise initial condition*, Comm. Partial Differential Equations, 43 (2018), pp. 1102–1149.

[49] F. Flandoli, L. Galeati, and D. Luo, *Delayed blow-up by transport noise*, Comm. Partial Differential Equations, 0 (2021), pp. 1–39.

[50] F. Flandoli, L. Galeati, and D. Luo, *Quantitative convergence rates for scaling limit of SPDEs with transport noise*. arXiv:2104.01740, 2021.

[51] F. Flandoli, L. Galeati, and D. Luo, *Scaling limit of stochastic 2d euler equations with transport noises to the deterministic navier–stokes equations*, Journal of Evolution Equations, 21 (2021), pp. 567–600.

[52] ——, *Eddy heat exchange at the boundary under white noise turbulence*, Philosophical Transactions of the Royal Society A, 380 (2022), p. 20210096.

[53] F. Flandoli, M. Gubinelli, and E. Priola, *Full well-posedness of point vortex dynamics corresponding to stochastic 2D Euler equations*, Stochastic Process. Appl., 121 (2011), pp. 1445–1463.

[54] F. Flandoli and D. Luo, *High mode transport noise improves vorticity blow-up control in 3D Navier–Stokes equations*, Probability Theory and Related Fields, 180 (2021), pp. 309–363.

[55] ——, *Mean field limit of point vortices with environmental noises to deterministic 2d navier–stokes equations*, Communications in Mathematics and Statistics, (2024), pp. 1–22.

[56] F. Flandoli and E. Luongo, *Heat diffusion in a channel under white noise modeling of turbulence*, Math. Eng., 4 (2022), pp. Paper No. 034, 21.

[57] ——, *Stochastic Partial Differential Equations in Fluid Mechanics*, vol. Lecture Notes in Mathematics, 2330, Springer Nature, 2023.

[58] F. Flandoli and S. Morlacchi, *In preparation.*

[59] F. Flandoli, S. Morlacchi, and A. Papini, *Effect of transport noise on kelvin–helmholtz instability*, in Stochastic Transport in Upper Ocean Dynamics Annual Workshop, Springer Nature Switzerland Cham, 2022, pp. 29–52.

[60] F. Flandoli and U. Pappalettera, *From additive to transport noise in 2d fluid dynamics*, Stochastics and Partial Differential Equations: Analysis and Computations, 10 (2022), pp. 964–1004.

[61] M. Flucher and M. Flucher, *Vortex motion in two dimensional hydrodynamics*, Variational Problems with Concentration, (1999), pp. 131–149.

[62] M. Flucher and B. Gustafsson, *Vortex motion in two-dimensional hydrodynamics, energy renormalization and stability of vortex pairs*, Royal Inst. Techn. Stockholm TRITA-MAT-9J-MA-02, (1997).

[63] L. Galeati, *On the convergence of stochastic transport equations to a deterministic parabolic one*, toch PDE: Anal Comp, (2020).

[64] C. Grossmann, *Numerical treatment of partial differential equations*, Springer, 2007.

[65] F. Grotto, *Essential self-adjointness of liouville operator for 2D euler point vortices*, J. Funct. Anal., 279 (2020), pp. 108635, 23.

[66] ——, *Stationary solutions of damped stochastic 2-dimensional Euler's equation*, Electron. J. Probab., 25 (2020), pp. Paper No. 69, 24.

[67] F. Grotto, E. Luongo, and M. Romito, *Gibbs equilibrium fluctuations of point vortex dynamics*, arXiv preprint arXiv:2308.00163, (2023).

[68] F. Grotto and S. Morlacchi, *Decay of time correlations in point vortex systems*, Physica D: Nonlinear Phenomena, 463 (2024), p. 134169.

[69] F. Grotto and U. Pappalettera, *Burst of point vortices and non-uniqueness of 2D Euler equations*, Arch. Ration. Mech. Anal., 245 (2022), pp. 89–126.

[70] F. Grotto and G. Peccati, *Infinitesimal invariance of completely random measures for 2D Euler equations*, Theory Probab. Math. Statist., (2022), pp. 15–35.

[71] F. Grotto and M. Romito, *A central limit theorem for Gibbsian invariant measures of 2D Euler equations*, Comm. Math. Phys., 376 (2020), pp. 2197–2228.

[72] ——, *Decay of correlation rate in the mean field limit of point vortices ensembles*, Stoch. Dyn., 20 (2020), pp. 2040009, 16.

[73] F. Grotto, M. Romito, and M. Viviani, *Zero-noise dynamics after collapse for three point vortices*, Physica D: Nonlinear Phenomena, (2023), p. 133947.

[74] B. Gustafsson, *Vortex motion and geometric function theory: the role of connections*, Philosophical Transactions of the Royal Society A, 377 (2019), p. 20180341.

[75] S. K. Harouna and E. Mémin, *Stochastic representation of the reynolds transport theorem: revisiting large-scale modeling*, Computers & Fluids, 156 (2017), pp. 456–469.

[76] Helmholtz, *Xliii. on discontinuous movements of fluids*, The London, Edinburgh, and Dublin Philosophical Magazine and Journal of Science, 36 (1868), pp. 337–346.

[77] H. Helmholtz, *Über Integrale der hydrodynamischen Gleichungen, welche den Wirbelbewegungen entsprechen*, J. Reine Angew. Math., 55 (1858), pp. 25–55.

[78] D. D. Holm, *Variational principles for stochastic fluid dynamics*, Proceedings of the Royal Society A: Mathematical, Physical and Engineering Sciences, 471 (2015), p. 20140963.

[79] P.-E. Jabin and Z. Wang, *Quantitative estimates of propagation of chaos for stochastic systems with w^-1, ∞ kernels*, Inventiones mathematicae, 214 (2018), pp. 523–591.

[80] N. Jiang, W. Layton, M. McLaughlin, Y. Rong, and H. Zhao, *On the foundations of eddy viscosity models of turbulence*, Fluids, 5 (2020), p. 167.

[81] B. Jourdain and S. Méléard, *Probabilistic interpretation and particle method for vortex equations with neumann's boundary condition*, Proceedings of the Edinburgh Mathematical Society, 47 (2004), pp. 597–624.

[82] K. Khanin, *Quasi-periodic motions of vortex systems*, Physica D: Nonlinear Phenomena, 4 (1982), pp. 261–269.

[83] B. Khesin, G. Misiołek, and A. Shnirelman, *Geometric hydrodynamics in open problems*, Archive for Rational Mechanics and Analysis, 247 (2023), p. 15.

[84] G. Kirchhoff, *Vorlesungen über mathematische Physik*, vol. 1, 1883.

[85] P. K. KPj and E. PLATEN, *Numerical solutions of stochastic differential equations*, 1992.

[86] R. H. Kraichnan, *Convection of a passive scalar by a quasi-uniform random straining field*, Journal of fluid mechanics, 64 (1974), pp. 737–762.

[87] R. Krasny, *A study of singularity formation in a vortex sheet by the point-vortex approximation*, Journal of Fluid Mechanics, 167 (1986), pp. 65–93.

[88] A. Labovsky and W. Layton, *Magnetohydrodynamic flows: Boussinesq conjecture*, Journal of Mathematical Analysis and Applications, 434 (2016), pp. 1665–1675.

[89] L. D. Landau and E. M. Lifshitz, *Fluid Mechanics: Volume 6*, vol. 6, Elsevier, 1987.

[90] C. C. Lim, *Quasi-periodic dynamics of desingularized vortex models*, Physica D: Nonlinear Phenomena, 37 (1989), pp. 497–507.

[91] C. Lin, *On the motion of vortices in two dimensions: i. existence of the kirchhoff-routh function*, Proceedings of the National Academy of Sciences, 27 (1941), pp. 570–575.

[92] ——, *On the motion of vortices in two dimensions: ii. some further investigations on the kirchhoff-routh function*, Proceedings of the National Academy of Sciences of the United States of America, (1941), pp. 575–577.

[93] T. Lundgren and Y. Pointin, *Statistical mechanics of two-dimensional vortices*, Journal of statistical physics, 17 (1977), pp. 323–355.

[94] A. J. Majda and P. R. Kramer, *Simplified models for turbulent diffusion: theory, numerical modelling, and physical phenomena*, Phys. Rep., 314 (1999), pp. 237–574.

[95] R. Mannella, *Numerical integration of stochastic differential equations*, Proc. Euroconf. on Supercomputation in Nonlinear and Disordered Systems, (1997), pp. 100–30.

[96] ——, *Integration of stochastic differential equations on a computer*, International Journal of Modern Physics C, 13 (2002), pp. 1177–1194.

[97] C. Marchioro and M. Pulvirenti, *Hydrodynamics in two dimensions and vortex theory*, Comm. Math. Phys., 84 (1982), pp. 483–503.

[98] C. Marchioro and M. Pulvirenti, *Lecture notes in physics*, 1984.

[99] C. Marchioro and M. Pulvirenti, *Vortices and localization in euler flows*, Communications in mathematical physics, 154 (1993), pp. 49–61.

[100] ——, *Mathematical theory of incompressible nonviscous fluids*, vol. 96 of Applied Mathematical Sciences, Springer-Verlag, New York, 1994.

[101] ——, *Mathematical theory of incompressible nonviscous fluids*, vol. 96, Springer Science & Business Media, 2012.

[102] G. Maso, *An Introduction to [gamma]-convergence*, An Introduction to [gamma]-convergence, Birkhäuser, 1993.

[103] S. Méléard, *Monte-carlo approximations for 2d navier-stokes equations with measure initial data*, Probability Theory and Related Fields, 121 (2001), pp. 367–388.

[104] E. Mémin, *Fluid flow dynamics under location uncertainty*, Geophysical & Astrophysical Fluid Dynamics, 108 (2014), pp. 119–146.

[105] K. Modin and M. Viviani, *Integrability of point-vortex dynamics via symplectic reduction: a survey*, Arnold Math. J., 7 (2021), pp. 357–385.

[106] S. Morlacchi, A. Papini, and F. Flandoli, *Effect of transport noise on kelvin-helmholtz instability*, June 2023.

[107] P. K. Newton and M. Platzer, *N-vortex problem: Analytical techniques*, Appl. Mech. Rev., 55 (2002), pp. B15–B16.

[108] E. Novikov, *Dynamics and statistics of a system of vortices*, Zh. Eksp. Teor. Fiz, 68 (1975), p. 2.

[109] L. Onsager, *Statistical hydrodynamics*, Il Nuovo Cimento (1943-1954), 6 (1949), pp. 279–287.

[110] A. Pazy, *Semigroups of linear operators and applications to partial differential equations*, vol. 44 of Applied Mathematical Sciences, Springer-Verlag, New York, 1983.

[111] H. Poincaré, *Théorie des tourbillons: leçons professées pendant le deuxième semestre 1891-1892*, Gauthier-Villars, 1893.

[112] W. H. Press, *Numerical recipes 3rd edition: The art of scientific computing*, Cambridge university press, 2007.

[113] V. Resseguier, E. Mémin, and B. Chapron, *Geophysical flows under location uncertainty, part i random transport and general models*, Geophysical & Astrophysical Fluid Dynamics, 111 (2017), pp. 149–176.

[114] E. J. Routh, *Some applications of conjugate functions*, Proceedings of the London Mathematical Society, 1 (1880), pp. 73–89.

[115] Y. Saad, *Iterative methods for sparse linear systems*, SIAM, 2003.

[116] Y. Saad and H. A. Van Der Vorst, *Iterative solution of linear systems in the 20th century*, Journal of Computational and Applied Mathematics, 123 (2000), pp. 1–33.

[117] P. G. Saffman, *Vortex dynamics*, Cambridge university press, 1995.

[118] F. G. Schmitt, *About boussinesq's turbulent viscosity hypothesis: historical remarks and a direct evaluation of its validity*, Comptes Rendus Mécanique, 335 (2007), pp. 617–627.

[119] A. Shnirelman, *On the long time behavior of fluid flows*, Procedia IUTAM, 7 (2013), pp. 151–160.

[120] S. Subramaniam, *A new mesh-free vortex method*, The Florida State University, 1996.

[121] P. Tabeling, *Two-dimensional turbulence: a physicist approach*, Physics reports, 362 (2002), pp. 1–62.

[122] M. Tao, *Explicit symplectic approximation of nonseparable hamiltonians: Algorithm and long time performance*, Physical Review E, 94 (2016), p. 043303.

[123] T. E. Wainwright, B. J. Alder, and D. M. Gass, *Decay of time correlations in two dimensions*, Phys. Rev. A, 4 (1971), pp. 233–237.

[124] J. B. Weiss and J. C. McWilliams, *Nonergodicity of point vortices*, Physics of Fluids A: Fluid Dynamics, 3 (1991), pp. 835–844.

[125] A. Wirth, S. Gama, and U. Frisch, *Eddy viscosity of three-dimensional flow*, Journal of Fluid Mechanics, 288 (1995), pp. 249–264.

[126] S. Zhongwei, *Periodic homogenization of elliptic systems, volume 269 of Operator Theory: Advances and Applications*, Advances in Partial Differential Equations, Birkhäuser/Springer, Cham,, 2018.